ПУБЛИКАЦИЈЕ АСТРОНОМСКЕ ОПСЕРВАТОРИЈЕ У БЕОГРАДУ
PUBLICATIONS OF THE ASTRONOMICAL OBSERVATORY OF BELGRADE
Св. 102 No. 102

31st Summer School and International Symposium on the Physics of Ionized Gases

Belgrade, Serbia,
September 5 - 9, 2022

CONTRIBUTED PAPERS

&

ABSTRACTS of INVITED LECTURES, TOPICAL INVITED LECTURES and PROGRESS REPORTS

Editors:
Dragana Ilić, Vladimir Srećković,
Bratislav Obradović and Jovan Cvetić

БЕОГРАД
2022

PUBL. ASTRON. OBS. BELGRADE No. 102, 1 - 302 BELGRADE, AUGUST 2022

31st Summer School and International Symposium on the Physics of Ionized Gases

September 5 – 9, 2022, Belgrade, Serbia

S P I G 2022

CONTRIBUTED PAPERS

&

ABSTRACTS OF INVITED LECTURES,
TOPICAL INVITED LECTURES AND
PROGRESS REPORTS

Editors

Dragana Ilić, Vladimir Srećković,
Bratislav Obradović and Jovan Cvetić

University of Belgrade –
School of Electrical
Engineering

University of Belgrade –
Faculty of Physics

Serbian Academy of
Sciences and Arts

Belgrade, 2022

PUBLICATIONS OF THE ASTRONOMICAL OBSERVATORY OF BELGRADE

FOUNDED IN 1947

All papers in this Publication are peer reviewed.

Director of the Astronomical Observatory: Dr. Gojko Djurašević

Typesetting: Tatjana Milovanov

Internet address http://www.aob.rs

ISSN 0373-3742
ISBN 978-86-82296-02-7

Number of copies / tiraž : 200
Production: Skripta Internacional, Mike Alasa 54, Beograd

CIP - Каталогизација у публикацији - Народна библиотека Србије, Београд

537.56(082)
539.186.2(082)
539.121.7(082)
533.9(082)

SUMMER School and International Symposium on the Physics of Ionized Gases (31 ; 2022 ; Belgrade)

Contributed papers & abstracts of invited lectures, topical invited lectures and progress reports / 31st Summer School and International Symposium on the Physics of Ionized Gases - SPIG 2022, September 5-9, 2022, Belgrade, Serbia ; editors Dragana Ilić ... [et al.]. - Belgrade : Astronomical Observatory, 2022 (Beograd : Skripta Internacional). - 302 str. : ilustr. ; 24 cm. - (Publications of the Astronomical Observatory of Belgrade, ISSN 0373-3742)

Na nasl. str.: University of Belgrade, School of Electrical Engineering; University of Belgrade, Faculty of Physics; Serbian Academy of Sciences and Arts. - Tiraž 200. - Str. 17-18: Preface / editors Dragana Ilić ... [et al.]. - Bibliografija uz svaki rad. - Registar.

ISBN 978-86-82296-02-7

1. Ilić, Dragana, 1978- [уредник] [аутор додатног текста]

а) Јонизовани гасови – Зборници б) Атоми – Интеракција – Зборници в) Плазма – Зборници

COBISS.SR-ID 72751881

SPIG 2022

SCIENTIFIC COMMITTEE

D. Ilić (Co-chair), Serbia
V. Srećković (Co-chair), Serbia

A. Antoniou, Greece
D. Borka, Serbia
J. Burgdörfer, Austria
J. Cvetić, Serbia
V. Guerra, Portugal
M. Ivković, Serbia
K. Kutasi, Hungary
I. Mančev, Serbia
D. Marić, Serbia
N. J. Mason, UK
A. Milosavljević, France
V. Milosavljević, Serbia
K. Mima, Japan
Z. Mišković, Canada
L. Nahon, France
B. Obradović, Serbia
G. Poparić, Serbia
P. Roncin, France
I. Savić, Serbia
Y. Serruys, France
N. Simonović, Serbia
M. Škorić, Japan
M. Trtica, Serbia
S. Tošić, Serbia
R. White, Australia

ADVISORY COMMITTEE

D. Belić
N. Bibić
M. S. Dimitrijević
S. Đurović
N. Konjević
M. M. Kuraica
J. Labat
G. Malović
B. P. Marinković
Z. Mijatović
M. Milosavljević
Z. Lj. Petrović
L. Č. Popović
J. Purić
B. Stanić

ORGANIZING COMMITTEE

J. Cvetić (Co-chair)
B. Obradović (Co-chair)

M. Ignjatović (Co-secretary)
L. Gavanski (Co-secretary)

N. Konjević
N. Cvetanović
T. Gajo
I. Krstić
N. Sakan

CONTENTS

Progress Reports

Contributed Papers

Contributed Papers

Section 3. LOW TEMPERATURE PLASMAS

Invited Lectures

Topical Invited Lectures

Progress Reports

Contributed Papers

Contributed Papers

The Workshop on X-ray and VUV Interaction with Biomolecules in Gas Phase (XiBiGP)

PREFACE

This special issue of the Publication of Astronomical Observatory in Belgrade (PubAOB) contains the contributed papers and abstracts of Plenary Lectures, Topical Invited Lectures and Progress Reports that will be presented at the **31st International Symposium on the Physics of Ionized Gases (SPIG 2022)** which will be held from 5th to 9th September 2022, in Belgrade, Serbia. The SPIG 2022 is organized by the University of Belgrade – Faculty of Physics, University of Belgrade – School of Electrical Engineering and Serbian Academy of Sciences and Arts, with the support of the Ministry of Education, Science and Technological Development of the Republic of Serbia. The 4th workshop on X-ray and VUV Interaction with Biomolecules in Gas Phase (4th XiBiGP), organized in collaboration with the SOLEIL synchrotron (France) will be attached to the SPIG 2022 conference.

Due to the ongoing COVID 19 pandemic, which is still affecting all our activities, and especially causing additional challenges for travels and meetings, the Organizing Committees of the SPIG 2022 conference have decided that the conference will be organized in a blended format, which allows participants to choose between virtual and regular (on-site) attendance. We expect to have virtual and regular participants, who will present 8 plenary invited talks, 18 topical invited, 21 progress reports, and 53 contributed papers (posters) within the main SPIG 2022 conference, and 17 invited talks within the XiBiGP workshop, from mainly four disciplines connected with physics of ionized gasses which have strong interactions in numerous applications: Atomic Collision Processes, Particle and Laser Beam Interactions with Solids, Low Temperature Plasmas and General Plasmas.

The SPIG reflects the progress in plasma physics and related fields. The conference has a long tradition, with the first meeting that was organized in Belgrade in 1962 under the title: ”1st Yugoslav Symposium on the Physics of Ionized Gases” (SPIG). This issue of

PubAOB presents new results in the fundamental and frontier theories and technology in the area of general plasma physics (including astrophysical and fusion plasmas), atomic collision processes and particle and laser beam interactions with solids.

Editors would like to thank the members of the Scientific and Advisory Committees of SPIG 2022 for their efforts in proposing the invited lectures and reviewing the contributed papers, as well as to thank the authors for their contribution and support to this Publication, and to wish all participants a pleasant and productive stay in Belgrade. We are grateful to the Serbian Academy of Sciences and Arts for their long term commitment to support this event as well as the Serbian Ministry of Education, Science and Technological Development for their continuing support.

Editors:
Dragana Ilić, Vladimir Srećković,
Bratislav Obradović and Jovan Cvetić,

Belgrade, August 2022

Section 1.

ATOMIC COLLISION PROCESSES

ULTRAFAST DYNAMICS OF IONIZED MOLECULES AND MOLECULAR CLUSTERS IN THE GAS PHASE

SERGIO DIAZ-TENDERO[1,2,3]

[1]*Departamento de Química, Universidad Autónoma de Madrid (UAM), Spain*

[2]*Condensed Matter Physics Center (IFIMAC), UAM, Spain*

[3]*Institute for Advanced Research in Chemistry (IAdChem), UAM, Spain*
E-mail sergio.diaztendero@uam.es

Abstract. Molecules and molecular clusters exposed to ionizing radiation can undergo numerous complex processes, leading to changes in their molecular and electronic structure. In the last years, we have studied the fragmentation dynamics of amino-acids and amino-acids derivatives induced by collisions with highly-charged ions, as well as the time-resolved photo-induced fragmentation dynamics of hydrocarbon derivatives. When these molecules are ionized and excited, they follow the so-called Coulomb explosion, where the charge splits in different fragments that repeal each other after cleavage of bonds in the molecular backbone. However, other non-expected processes appear in competition, such as hydrogen migration [1,2], intramolecular charge transfer [3], isomerization [4], methyl roaming [5], etc. They occur in the cation and dication molecules, and take place within a few tens of femtoseconds to picoseconds. We have also determined the distribution of the energy deposited in the ionized molecule as a result of a collision with a highly-charged ion [6,7], which is the responsible for triggering the atomic reorganization. In the case of molecular clusters, in addition to the Coulomb explosion, ionizing radiation also induces intracluster reactions, producing molecular growth and leading to new ionized stable structures. In this context, we have shown the formation of peptide bonds in clusters of amino acids induced by collisions with alpha particles [8] and intermolecular reactivity in clusters of CO_2 [9] and in mixed clusters of NH_3 and H_2O [10] induced with soft X-ray radiation. A complete picture of the mechanisms underlying the dynamics was obtained using both experimental and theoretical state-of-the-art techniques. In this communication, comparison of the different processes, induced in the ionizing radiation and observed in the above-mentioned systems, will be presented and discussed. I will detail the joint theoretical and experimental strategy implemented in the last decade, which has allowed us to understand fundamental chemical processes of ionized molecules and clusters in the gas phase.

References

[1] S. Maclot et al. 2013, *J. Phys. Chem. Lett.* **5**, 3903.
[2] N. Kling et al. 2019, *Nat. Commun.* **10**, 2813.
[3] P. Rousseau et al. 2021, *Sci. Adv.* **7**, eabg9080.
[4] M. McDonnell et al. 2020, *J. Phys. Chem. Lett.* **11**, 6724.
[5] D. Mishra et al. 2022, *Phys. Chem. Chem. Phys.* **24**, 433.
[6] S. Maclot et al. 2016, *Phys. Rev. Lett.* **117**, 073201.
[7] E. Erdmann et al. 2020, *Phys. Chem. Chem. Phys.* **23**, 1859.
[8] P. Rousseau et al. 2020, *Nat. Commun.* **11**, 3818.
[9] S. Ganguly et al. 2022, *Commun. Chem.* **5**, 16.
[10] B. Oostenrijk et al. 2019, *Phys. Chem. Chem. Phys.* **21**, 25749.

ELECTRON SPECTROSCOPIES FOR PROBING ELECTRONIC STRUCTURE AND COLLISION DYNAMICS

DARRYL B. JONES

College of Science and Engineering, Flinders University
E-mail darryl.jones@flinders.edu.au

Abstract. Electrons-impact spectroscopies provide mechanisms for investigating the dynamics of collisions and the electronic structure of materials. An accurate depiction of collision processes is essential in understanding charged-particle transport, and the creation of excited and reactive species in plasma-like environments. They are therefore essential for describing and developing radiation-based therapies and plasma chemical processing technologies. At Flinders we have been employing a range of experimental techniques and theoretical methodologies to improve our understanding of collision phenomena. We also work with the modelling community to apply this knowledge in simulations aimed at describing and predicting properties in plasma-like environments.

In this presentation I will review some of our work on the dynamics of low-energy electron-impact ionization. Here we have employed an (e,2e) technique in an asymmetric coplanar geometry to investigate the ionization of the outermost molecular orbitals of R-carvone (Jones et al. 2019) and pyrazine (Jones et al. 2021). This work uses experiments to benchmark and assess developments in the theoretical descriptions of the ionization process. We will also discuss the role of molecular structure in ionization dynamics by considering the ionized orbital's momentum profile. By studying a range of molecular systems, we have investigated how the shape of the triple differential cross sections in the binary and recoil scattering regions relates to the properties of the ionized orbital.

I will also discuss current research efforts into how we can use electron and momentum-based spectroscopies to probe electronic excitation processes and the dynamics of electronically-excited molecules and materials.

Dr Darryl Jones is currently the recipient of an Australian Research Council (ARC) Future Fellowship (FT210100264) funded by the Australian Government.

References

Jones, D. B., Ali, E., Chakraborty, H. S., Ning, C. G., García, G., Madison, D. H., & Brunger, M. J. : 2021, *Chem. Phys. Lett.*, **781**, 139000.

Jones, D. B., Ali, E., Ning, C. G., Silva, F. F. d., Ingólfsson, O., Lopes, M. C. A., Chakraborty, H. S., Madison, D. H., & Brunger, M. J.: 2019, *J. Chem. Phys.,* **151**, 124306.

EXPERIMENTS WITH POSITRONS - FROM FUNDAMENTAL TO APPLIED SCIENCE

JAMES SULLIVAN

Positron Research Group, Research School of Physics, Austra;ian National University, 60 Mills Rd, Acton ACT, AUSTRALIA
E-mail james.sullivan@anu.edu.au

Abstract. Since their prediction by Dirac in 1928 and subsequent discovery by Anderson in 1932, positrons have been used in a range of experiments to probe both fundamental and applied science. This has led to the discovery of exotic compounds such as positronium and the positronium ion, as well as leading to the first production, trapping and then spectroscopy of antihydrogen. Positrons have also found use in materials science, probing the nanostructure of solids, and in medical science, through the development of Positron Emission Tomography (PET).

At the Australian National University, we have two positron beamlines, based on Surko trap technology. These provide pulsed positron beams with tunable energy, up to 20 keV, in the case of materials studies. Beams can be conditioned for optimal energy or temporal resolution, to probe a wide range of different physical processes. Since 2008, we have been conducting a range of experiments covering atomic and molecular, materials and medical physics. This covers highly accurate measurements of low energy scattering cross sections to provide benchmarks for theoretical calculations, such as in Sullivan et al. 2008, tracking of material degradation, see Kluth et al. 2014, and measurements of positron scattering from biomolecules, as shown in Edwards et al. 2021.

This talk will provide an overview of the beamlines and their operation, as well as a sample of experimental results covering all three of the previously mentioned areas of study. Plans for future experimental programs will also be outlined, including measurements of positron transport in liquid water.

References

Dirac, P. A. M.; 1928 *Proc. Roy. Soc. A* **117** 610
Anderson, C. D. ; 1932 *Science* **76**, 238
Sullivan, J. P. *et al.*; 2008 *J. Phys. B* **41** 081001
Kluth, P. *et al.*; 2014 *App. Phys. Lett.* **104** 023105
Edwards, D. *et al.*; 2021 Phys. Rev. A **104** 042807

THERMALISATION TIME OF ELECTRON SWARMS IN NOBLE GASES FOR UNIFORM ELECTRIC FIELDS

G. J. BOYLE[1], M. J. E. CASEY[1], D. G. COCKS[1], R. D. WHITE[1] and R. J. CARMAN[2]

[1]*Jame Cook University, Townsville, Australia*
E-mail gregory.boyle@jcu.edu.au

[2]*Macquarie University, Sydney, Australia*
E-mail robert.carman@mq.edu.au

The time taken for an electron swarm to reach its equilibrium with an instantaneously applied electric field (E/N) is typically less than 10^{-9} s for most medium and high-pressure plasmas (p=0.01-5bar). Thus, a steady-state Boltzmann code is usually sufficient to deduce the electron energy distribution function (EEDF) and the requisite electron swarm parameters as a function of E/N for plasmas driven by relatively slow time-varying voltage waveforms ($\tau >> 10^{-9}$ s). In the last few years, however, plasmas driven by fast transient voltage pulses (e.g. risetimes >100V.ns^{-1}, 1-10ns duration) are being rapidly developed, as reviewed in the Special issue on Fast Pulse Discharges 2017. It is not yet clear whether the EEDFs in these fast transient plasmas deviate significantly from "thermalised". To investigate this issue, we have calculated the time taken for electrons to become thermalised for a given E/N, over a range of fields applicable to most medium-high pressure plasma discharges (Boyle et al. 2019). We have numerically solved the multi-term, spatially-homogenous Boltzmann equation (BE), subject to a constant electric field, to follow the EEDF as it evolves from an initial room-temperature Maxwellian distribution toward the steady-state. Transport quantities such as the mean energy ε, the drift velocity W, and the ionisation coefficient α_i, were calculated as a function of time. The time taken for the slowest swarm parameter (α_i) to converge to an acceptable level (e.g. to within 90% of its steady-state value) has been used universally as the benchmark for evaluating the thermalisation time. In this work, we report results for thermalisation times in noble gases from helium to xenon, and discuss the presence of short-lived (transient) discrepancies that occur in the EEDF from low-term BE calculations.

References

Boyle, G. J., Casey, M. J. E., Cocks, D. G., White, R D., Carman, R. J. : 2019*, Plasma Sources Sci. Tech.,* **28**, 035009.

Special issue on Fast Pulse Discharges, (20 papers): 2017, *Plasma Sources Sci. Tech.*, **26,** 020201

ELECTRON TRANSPORT, TRANSIENT PLASMAS AND HIGH-ENERGY PHENOMENA IN PLANETARY ATMOSPHERES

SAŠA DUJKO[1], DANKO BOŠNJAKOVIĆ[1], ILIJA SIMONOVIĆ[1] and CHRISTOPH KÖHN[2]

[1]*Institute of Physics Belgrade, University of Belgrade, Pregrevica 118, 11080 Belgrade, Serbia*
E-mail sasa.dujko@ipb.ac.rs

[2]*Technical University of Denmark, National Space Institute (DTU Space), Elektrovej 328, Kgs Lyngby 2800, Denmark*

Abstract. Lightning on Earth is a complex natural phenomenon bridging several lengths, time, and energy scales ranging from the scattering and motion of the lower-energy electrons in streamer discharges to the emission of MeV leptons, hadrons, and photons by kilometer long lightning leaders. Lightning, and other types of transient plasmas in our atmosphere are responsible for the production of nitrogen oxides, ozone, and other greenhouse gases. Likewise, the Miller-Urey experiment has shown that the electrical discharges in the atmosphere of Primordial Earth may have catalyzed the production of amino acids as a precursor of life on our planet (Köhn et al. 2019, 2022).

In this work, we study the properties of electron transport in gas mixtures that reflect diverse planetary atmospheres, keeping in mind that lightning is not limited to our planet only. Using a numerical multi term solution of the Boltzmann equation and a Monte Carlo simulation approach (Dujko et al. 2010), calculations were carried out over a range of planetary atmospheric conditions relevant for the modeling of electrical discharges and transient plasmas such as sprites and elves. Thermalization of high-energy electrons produced by cosmic rays in Earth's atmosphere and the impact of a planetary magnetic field on the transport properties of the electrons in atmospheres of the gas and ice giants are also examined. We also discuss electron avalanches and avalanche-to-streamer transitions in the atmospheres of Primordial Earth and Titan (the largest satellite of Saturn), by modeling the electron dynamics with the fluid and particle models.

References

Köhn, C., Dujko, S., Chanrion, O., Neubert, T.: 2019, *Icarus*, **333**, 29.
Köhn, C., Chanrion, O., Bodker Enghoff M., Dujko, S.: 2022, *Geophys. Res. Lett.*, **49**, e2021GL097504.
Dujko, S., White R.D., Petrović, Z.Lj., and Robson, R.E.: 2010, *Phys. Rev. E*, **81**, 046403.

NUMERICAL INVESTIGATIONS OF THE IMPACT OF THE MAGNETIC FIELD OF RADIATION ON AMINO ACIDS

TEODORA KIROVA[1] and JELENA TAMULIENĖ[2]

[1]*Institute of Atomic Physics and Spectroscopy, University of Latvia, Riga, LV-1004, Latvia*
E-mail teo@lu.lv

[2]*Institute of Theoretical Physics and Astronomy, Vilnius University, Vilnius, LT-10257, Lithuania*
E-mail Jelena.Tamuliene@tfai.vu.lt

Abstract Amino acids are the structural units of proteins and have important roles as metabolic intermediates in biosynthesis or synthesis of other molecules. Tryptophan is a precursor of the neurotransmitter serotonin, see Savelieva et al. 2008, tyrosine is essential in producing norepinephrine and dopamine, valine and isoleucine are associated with insulin resistance in mammals, see Lynch et al. 2014. After deposition of high-energy ionizing quanta, electrons with different energies are formed and destroy biological molecules, such as DNA and proteins, causing chromosome aberrations, cancer mutations, genetic transformations etc. Structural changes of amino acids are investigated using electron ionization mass spectrometry, while mass spectra are typically interpreted by theoretical calculations, see Tamulienė et al. 2020. We investigate theoretically and numerically the effects of magnetic field of radiation on the fragmentation of different amino acids. The effects are accounted for by using the anisotropic Gaussian type orbitals method, see Schmelcher, et al. 1988, where anisotropy in the wavefunction is used in order to describe the elongation of electron orbitals/densities along the magnetic field direction. As a testing ground for our model we have used light molecules (e.g. H_2), following the procedure outlined by Zhu et al. 2017. Currently, various amino acids are being analyzed, including geometrical parameters of the initial molecule rearrangement. In the case of fragmentation, additional analysis will be performed be in order to determine whether it is due to simple bond cleavage or to more complex reactions involving molecular rearrangements.

References.

Savelieva, K.V. et al.: 2008, *PLoS One*, **3(10)**, e3301.
Lynch, C. J. and Adams, S. H.: 2014, *Nature Reviews. Endocrinology,* **10(12)**, 723.
Tamulienė, J. et al.: 2020, *EPJD*, **74**, 13.
Schmelcher, P. and Cederbaum, L. S.: 1988, *Phys. Rev. A*, **37(3)**, 672.
Zhu, W. and Trickey, S. B.: 2017, *J. Chem. Phys.,* **147**, 244108.

ELECTRON-ION COINCIDENCE EXPERIMENTS WITH ELECTRON AND PHOTON IONIZATION

MINNA PATANEN

Nano and molecular systems research unit, Faculty of Science, P.O. Box 3000, 90014 university of Oulu, Finland
E–mail minna.patanen@oulu.fi

Abstract. Chemical reactions take place at the atomic level where electrons, following the laws of quantum mechanics, move from one atom to another, forming and breaking molecular bonds. Thus complex processes such as catalysis, protein folding, and photosynthesis are triggered at the atomic level when a part of the complicated system changes its quantum state. A complete understanding of for example radiation damage of living matter thus requires an atomic scale description of radiation induced process. These initial steps determine what kind of particles are released, e.g. energetic electrons, low kinetic energy electrons, and free radicals, which further interact with surroundings leading to final radiation damage. Electron - ion coincidence experiments provide a tool for capturing simultaneously charged reactants resulting from radiation - matter interaction event, and are thus a key forward for complete understanding of the process. In this talk I will concentrate on recent examples of electron - ion coincidence experiments performed at a synchrotron radiation facility MAX IV for a large organic molecule (Abid et al. 2020) and using a laboratory electron source ionising for mixed argon - water clusters (Pelimanni et al. 2022). In these gas-phase experiments, the electron detection using a hemisperical electron analyser allows selection of a specific site of ionisation while correlation between detected ions can give hints for the specific mechanisms of the fragmentation.

References

Abid, A. R., Pelimanni, E., Reinhardt, M., Boudjemia, N., Kivimäki, A., Huttula, M., Björneholm, O., Patanen, M. : 2020, *J. Phys. B* **53**, 244001.

Pelimanni, E., Hans, A., Heikura, E., Huttula, M. Patanen, M. : 2022, *Phys. Chem. Chem. Phys.* **24**, 11646-11653.

X-RAY ACTION SPECTROSCOPY OF GAS-PHASE BIOMOLECULAR IONS

L. SCHWOB[1], J. LEROUX[1], A. KOTOBI[1], S. DÖRNER[1], K. SCHUBERT[1], I. UNGER[2], K. ATAK[1], V. ZAMUDIO-BAYER[3], J. T. LAU[3] and S. BARI[1]

[1]*Deutsche Elektronen-Synchrotron DESY, Hamburg, Germany.*

[2]*Department of Physics and Astronomy, Uppsala University, SE-751 20 Uppsala, Sweden*

[3]*Abteilung Hochempfindliche Röntgenspektroskopie, Helmoltz-Zentrum Berlin für Materialien und Energie, Berlin, Germany*

E-mail lucas.schwob@desy.de

Abstract. Over the past decades, peptides and proteins have been investigated in the gas phase using state-of-art mass spectrometric techniques combined to electrospray ionization sources. In order to obtain new insights into the electronic and structural properties of such biomolecules, X-ray action spectroscopy experiments, which are based on the resonant photoexcitation of core electrons, have been carried out at synchrotron facilities, which offer a broad photon energy range and a high photon flux. It has been used successfully to unravel different aspects of the photodissociation of peptides and to probe conformational features of proteins. It is a current question to which extent the resonant photoabsorptions are sensitive toward effects of conformational isomerism, tautomerism, and intramolecular interactions in gas-phase peptides. Additionally, in the soft X-ray regime, the high degree of localization of the deposited energy allows getting a deeper understanding on the dissociation processes. However, identifying products of site-selective dissociation in large biomolecules is challenging at the carbon, nitrogen, and oxygen edges because of the high number of these atoms and related chemical groups. Probing the inner shells of a single sulfur atom within a biomolecule as the one and only excitation site is a promising way to overcome this obstacle.I will present here am overview of recent synchrotron-based experimental studies on the X-ray action spectroscopy of model peptides, carried across at the carbon, nitrogen, and oxygen K-edges[1] as well as sulfur L-edge[2].

References

[1] Dörner S. *et al*.: 2021, *J. Am. Soc. Mass Spectrom.,* **32**, 3, 670-684

[2] L. Schwob L. *et al*.: 2020, *J. Phys. Chem. Lett.*, **11**, 1215‑1221.

RELATIVE IMPORTANCE OF THE ELECTRON CONTINUUM INTERMEDIATE STATE IN SINGLE-ELECTRON CAPTURE INTO ANY STATE OF FAST PROTONS FROM HELIUM-LIKE ATOMIC SYSTEMS

DANILO DELIBAŠIĆ

Department of Physics, Faculty of Sciences and Mathematics, University of Niš, Serbia
E-mail danilo.delibasic@pmf.edu.rs

Abstract. Single-electron capture by fast protons from helium-like atomic targets is investigated at intermediate and high impact energies. The main purpose of the present study is a comprehensive analysis of the relative importance of the electron continuum intermediate state (ionization continua), with respect to direct transfer. To achieve this goal, first- and second-order theories are employed, and their results are thoroughly compared. The prior form of the boundary-corrected continuum intermediate state method (BCIS) is utilized, in both its three-body (Milojević et al. 2020) and four-body (Mančev et al. 2015) formulation, in addition to the four-body boundary-corrected first-Born approximation (CB1-4B), in both its prior (Mančev et al. 2012) and post form (Mančev et al. 2013, Milojević 2014). BCIS methods belong to the class of second-order theories, while CB1 methods belong to the class of first-order theories. Relative importance of ionization continua will be examined in the example of single-electron capture in $p + \mathrm{He}(1s^2)$ collisions. Both differential and total cross sections will be analysed, for single-electron capture into any final state of the projectile. The presented cross sections, aside from their fundamental importance, are relevant in various interdisciplinary applications, such as in astrophysics (Cravens 2002), thermonuclear fusion and plasma physics (Isler 1994) and medical physics (Belkić 2021).

References

Belkić, Dž. : 2021, *Z. Med. Phys*., **31**, 122.
Cravens, T. E. : 2002, *Science,* **296**, 1042.
Isler, R. C. : 1994, *Plasma Phys. Control. Fusion,* **36**, 171.
Mančev, I., Milojević, N., Belkić, Dž. : 2012, *Phys. Rev. A*, **86**, 022704.
Mančev, I., Milojević, N., Belkić, Dž. : 2013, *Phys. Rev. A,* **88**, 052706.
Mančev, I., Milojević, N., Belkić, Dž. : 2015, *Phys. Rev. A*, **91**, 062705.
Milojević, N., Mančev, I., Delibašić, D., Belkić, Dž. : 2020, *Phys. Rev. A*, **102**, 012816.
Milojević, N. : 2014*, J. Phys.: Conf. Ser.,* **565**, 012004.

FRAGMENTATION OF CORE-IONIZED ADAMANTANE MOLECULE

S. GANGULY[1] and S. MACLOT[2]

[1]*Department of Physics, Lund University, 22100 Lund, Sweden*
E-mail smita.ganguly@sljus.lu.se

[2]*Institut Lumiere Matiere, CNRS, Univ Lyon, F-69100 Villeurbanne, France*
E-mail sylvain.maclot@univ-lyon1.fr

Abstract. Adamantane is the smallest diamondoid molecule with a highly stable cage structure. In this project, we study the fragmentation of the adamantane molecule following C-1s ionization using soft X-rays. We measured NEXAFS, XPS and Auger electron-Photoion coincidence data at the PLEIADES beamline in SOLEIL, France. Experimental data and theoretical calculations show site-selective Auger decay, followed by hydrogen evaporation and dissociation. We present a complete study of all the ion pairs formed after fragmentation and the total kinetic energy released. We also compared our results to the dissociation dynamic of valence ionized adamantane reported by Maclot et al. 2020.

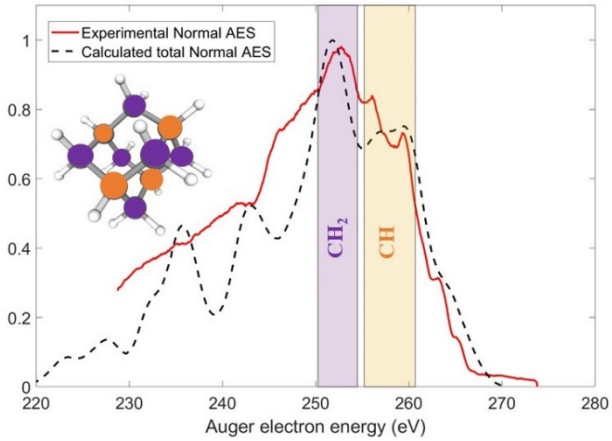

Figure 1: Auger electron spectrum of adamantane recorded at 350 eV photon energy, showing the contribution of CH and CH_2 type carbons.

References

Maclot, Sylvain, et al. : *Scientific reports* 10.1 (2020): 1-12

VUV PHOTOIONIZATION AND FRAGMENTATION OF CYANO-PAHs

M. Roy Chowdhury[1], G. A. Garcia[1], E. Rouquet[1], H. Hrodmarsson[2], J.C. Loison[3] and L. Nahon[1]

[1]*Synchrotron SOLEIL, L'Orme des Merisiers, 91192 Gif Sur Yvette, France*
E-mail : madhusree.roy-chowdhury@synchrotron-soleil.fr

[2]*Laboratory for Astrophysics, Leiden Observatory, Leiden University, NL-2300 RA Leiden, The Netherlands*

[3]*ISM, Universite Bordeaux 1, CNRS, 351 cours de la Libération, 33405 Talence Cedex, France*

Abstract. Polycyclic aromatic hydrocarbons (PAHs) are postulated to be present abundantly in the interstellar medium (ISM) and they constitute a major reservoir of carbon. Although their presence is widely acknowledged through the observation of the aromatic infrared emission bands (AIBs), the individual identification of the PAHs is hindered due to their highly symmetric molecular structures. The attention is shifted to detect less symmetric ones like the substituted PAHs. Recently, the two nitrile group functionalized PAHs, i.e., 1- and 2-cyanonaphthalenes and cyanobenzene have been detected in the TMC-1 molecular cloud, (McGuire et al. 2021 and 2018).

The detection of these molecular species has driven further interest in studying the photoionization and fragmentation of these molecules in the laboratory in the VUV spectral region. We have performed experimental investigations at the VUV DESIRS beamline at Synchrotron SOLEIL to study the photoelectron spectroscopy of 1- and 2-cyanonaphthalene and cyanobenzene using the double imaging electron/ion coincidence spectrometer, DELICIOUS 3. We have obtained the high resolution threshold photoelectron spectrum (TPES) over an extended binding energy range which will be compared with *ab initio* calculations. The state-selected fragmentation over a wide photon energy range have been obtained which when compared with the case of unsubstituted PAHs unravels the effect of cyano-substitution in terms of photostability. Theoretical investigations predict that PAHs contribute abundantly to the photoelectric heating of the ISM by thermalization of the emitted electrons, (Bakes et. al. 1994). The present measurements provide the KE distributions of the photoelectrons which can be employed to model the photoelectric heating for any incoming photon spectral distribution.

References

Bakes, E. L. O., Tielens, A. G. G. M. : 1994, *Astrophys. J.* **427**, 822.
McGuire, B. A. et al. : 2018, *Science* **359**, 202.
McGuire, B. A. et al. : 2021, *Science* **371**, 1265.

Publ. Astron. Obs. Belgrade No. 102 (2022), 33 - 36 *Contributed Paper*

FORMATION AND PROPAGATION OF STREAMERS IN CF_3I-SF_6 GAS MIXTURES

J. ATIĆ[1], D. BOŠNJAKOVIĆ[1], I. SIMONOVIĆ[1],
Z. Lj. PETROVIĆ[2] and S. DUJKO[1]

[1]*Institute of Physics Belgrade, University of Belgrade, Pregrevica 118, 11080 Belgrade, Serbia*
E-mail sasa.dujko@ipb.ac.rs

[2]*Serbian Academy of Science and Arts, Knez Mihailova 35, 11000 Belgrade, Serbia*

Abstract. The formation and propagation of streamers in CF_3I-SF_6 mixtures are studied by the classical fluid model in 1D and 1.5D configurations. We calculate the electron density, electric field, and velocity of streamers as a function of the applied reduced electric fields for various CF_3I-SF_6 mixtures. We found that the transition of an electron avalanche into a negative streamer occurs more slowly with an increasing fraction of CF_3I in the mixture.

1. INTRODUCTION

In high voltage technology, strong electronegative gases are used to prevent the electrical breakdown in power transmission and distribution systems. SF_6 is widely used in these applications because of its extraordinary dielectric characteristics (primarily, high critical electric field and low boiling point). However, SF_6 is a very powerful greenhouse gas with an extremely high global warming potential (22800 on a 100-year horizon) and a very long atmospheric lifetime (3200 years). Research on alternative gases is therefore one of the main activities of researchers worldwide.

The first step in this effort involves reducing the SF_6 concentration using gas mixtures. CF_3I, one of the most promising candidates for replacement of SF_6, is also a strong electronegative gas. Its critical electric field is higher than that of SF_6 and it has a very short atmospheric lifetime (shorter than 2 days), as well as negligible global warming potential (lower than the referent gas CO_2). However, in comparison with SF_6, its boiling point is not sufficiently low. Using these CF_3I characteristics as motivation factors, we investigated the formation and propagation of negative streamers in CF_3I-SF_6 mixtures.

2. METHODS OF CALCULATIONS

The transition from an avalanche to a streamer, and the propagation of streamers were considered by a numerical model based on fluid equations. We use the classical fluid model where the equation of continuity is combined with the drift-diffusion approximation. The resulting equation is coupled to the Poisson equation for space charge electric field calculations. The corresponding system of partial differential equations is solved numerically assuming the local field approximation (Bošnjaković et al. 2016). The calculations are carried out in the 1D and 1.5D configurations where the fixed value of the streamer radius is incorporated into the axial symmetrical model. The streamer velocities are calculated from the modeling performed in 1D and by using the analytical expression (Li et al. 2007) which requires knowledge of electron mobility, longitudinal diffusion coefficient and ionization coefficient as a function of the reduced electric field. The cross-section sets for electron scattering in CF_3I and SF_6 were developed in our laboratory (Mirić et al. 2016), and by Itoh and co-workers (Itoh et al. 1993) respectively.

3. RESULTS AND DISCUSSION

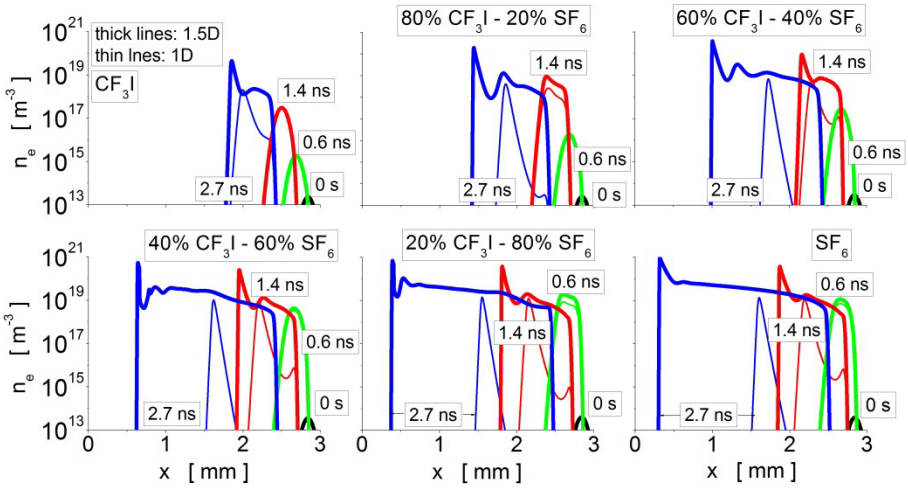

Figure 1: Electron density during streamer formation and propagation in CF_3I-SF_6 mixtures for E_0/n_0 = 480 Td.

Figure 1 shows the electron density during streamer formation and propagation in CF_3I-SF_6 mixtures. The results are obtained from the classical 1D and 1.5D fluid models in which the input data are electron bulk transport coefficients calculated by Monte Carlo simulations. The external electric field is 480 Td, which is larger than the critical electrical fields of the two gases. This requirement permits the development of streamers. Comparing the results in two different configurations

for the fixed mixture shows that the electron density is higher in the 1.5D model. The results in the same configuration show that the development of streamers is slower with the decrease of SF_6 in mixture. This behavior is expected based on a greater critical electric field of CF_3I (437 Td) than SF_6 (361 Td). This is one of the indicators that CF_3I is better dielectric than SF_6 because of its capacity to prevent the development of streamers at higher electric fields.

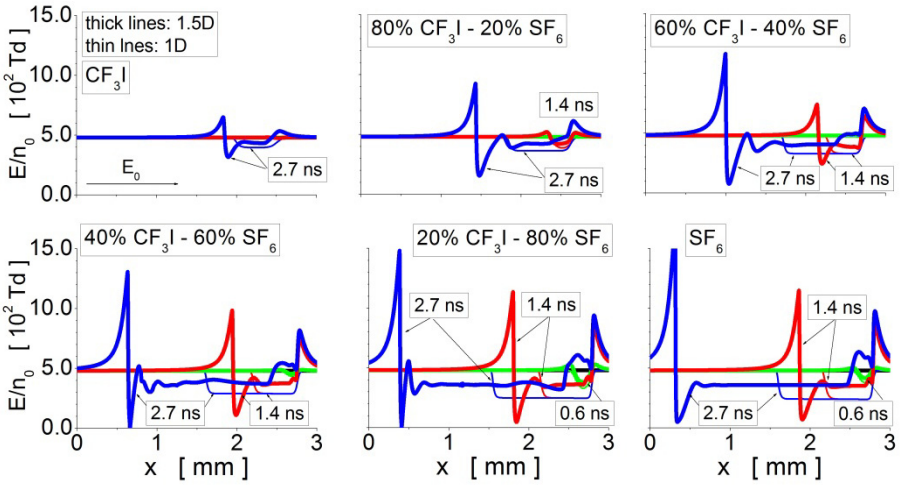

Figure 2: Electric field during streamer formation and propagation in CF_3I-SF_6 mixtures for E_0/n_0 = 480 Td. The calculation is performed using the 1.5D and 1D setups and balk transport coefficients as input to the classical fluid model.

Figure 2 shows the temporal development of the electrical field of the streamers in the CF_3I-SF_6 mixtures according to the same conditions as in Figure 1. The results of the 1.5D configuration show that the electric field in the streamer channel is equal to the critical electric field of the studied gas mixture. Field amplification in the region ahead of the streamer front starts from 40 % (pure CF_3I) up to 200 % (pure SF_6). By comparing the 1D and 1.5D configurations, we observe that the electrical field in the streamer channel descends to the lower level in the 1.5D configuration. In the 1D configuration, the electrical field in the region ahead of the streamer front is equal to the external field, independently of the gas mixture.

Figure 3 shows the streamer velocity and drift velocity of the electrons for various CF_3I-SF_6 mixtures. As the development of streamers is possible in electrical fields above the critical electrical field, the streamer velocity of gas mixtures can be calculated by the fluid model (left panel) starting from different electrical fields. The increase in streamer velocity with increasing concentration of SF_6 is a consequence of the evolution of streamers (Figures 1 and 2). Although it seems unexpected, the streamer velocity in the pure SF_6 is lower than that in the mixture 20% CF_3I - 80% SF_6 because of the behavior of the drift velocity of

electrons (right panel). The comparison of these two sets of results shows that the streamer velocity is higher than the drift velocity of electrons regardless of the gas mixture and the electric field. This follows from the fact that the streamer velocity is a combination of the electron drift velocity, the velocity induced by the strong diffusive flux at the streamer front and the creation of the electrons by electron-impact ionization. A comparison of the streamer velocities computed from the fluid model (left panel) and the analytical expression (middle panel) shows that these two sets of results differ from each other. This figure clearly illustrates the limits of the analytical formula that is often used for calculating streamer velocity.

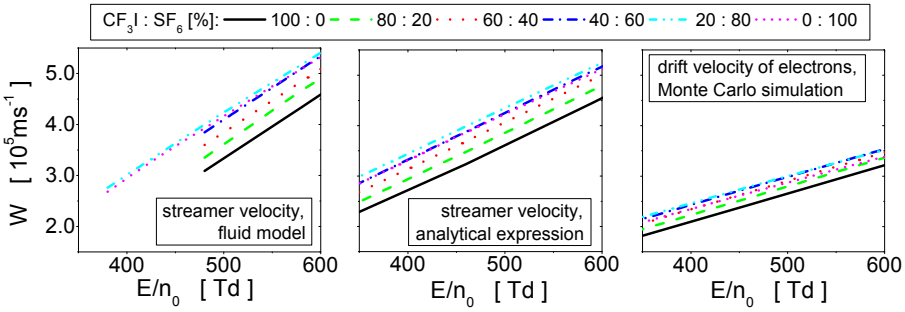

Figure 3: Streamer velocity calculated by the fluid model (left panel) and analytical expression (middle panel) and the drift velocity of electrons (right panel). Results in the CF_3I-SF_6 mixtures are given as a function of the reduced electric field.

Acknowledgment

This research was supported by the Institute of Physics Belgrade, and the Science Fund of the Republic of Serbia [Grant No. 7749560, EGWIn].

References

Bošnjaković, D., Petrović, Z.Lj., Dujko, S.: 2016, *J. Phys. D: Appl. Phys*. **49**, 405201.

Li, C., Brok, W.J.M., Ebert, U., van der Mullen, J.J.A.M.J.: 2007, *Appl. Phys*. **101**, 123305.

Mirić, J., Bošnjaković, D., Simonović, I., Petrović Z.Lj., Dujko, S.: 2016, *Plasma Source Sci. Technol*. **25**, 065010.

Itoh, H., Matsumura, T., Satoh, K., Date, H., Nakano, Y., Tagashira, H.: 1993, *J. Phys. D: Appl. Phys*. **26**, 1975.

Publ. Astron. Obs. Belgrade No. 102 (2022), 37 - 40 *Contributed Paper*

ELECTRON TRANSPORT COEFFICIENTS IN CO: SCANNING DRIFT TUBE MEASUREMENTS AND KINETIC COMPUTATIONS

S. DUJKO[1], D. BOŠNJAKOVIĆ[1], M. VASS[2,3], I. KOROLOV[3], P. HARTMANN[2], N. PINHAO[4], D. LOFFHAGEN[5] and Z. DONKO[2]

[1]*Institute of Physics Belgrade, University of Belgrade, Pregrevica 118, 11080 Belgrade, Serbia*
E-mail sasa.dujko@ipb.ac.rs

[2]*Institute for Solid State Physics and Optics, Wigner Research Centre for Physics, Konkoly-Thege Miklos str. 29-33, 1121 Budapest, Hungary*

[3]*Department of Electrical Engineering and Information Science, Ruhr-University Bochum, 44780 Bochum, Germany*

[4]*Instituto de Plasmas e Fusao Nuclear, Instituto Superior Tecnico, Universidade de Lisboa, Av. Rovisco Pais, 1049-001 Lisboa, Portugal*

[5]*Leibniz Institute for Plasma Science and Technology, Felix-Hausdorff-Str. 2, 17489 Greifswald, Germany*

Abstract. In this work, we present scanning drift tube measurements and kinetic computations of electron swarm transport coefficients in CO, including drift velocity, longitudinal diffusion coefficient and ionization rate coefficient, as a function of the reduced electric field at room temperature. Kinetic computations are carried out based on a Monte Carlo (MC) simulation approach and by solving the electron Boltzmann equation. Using an MC technique, the ionization coefficient is computed from the spatial profile of the number of electrons in an idealized steady-state Townsend (SST) experiment. It is found that the measured and calculated transport coefficients agree generally very well.

1. INTRODUCTION

The knowledge of electron collisions and transport processes in CO is essential for understanding the fundamental electron-CO interactions in planetary atmospheres and interstellar media (Cambell et al. 2011). CO also offers a broad range of plasma-based technology applications, ranging from plasma etching (Omori et al. 1996) and plasma medicine (Carbone and Douat 2018) to gas lasers (Grigorian and Kochetov 2008) and syngas production (Cimerman et al. 2018). Experimental and

modelling studies on the activation of the CO_2 molecule (Pietanza et al. 2017), where the CO molecule is one of the most important resultant species, can also benefit from the related swarm-based studies.

In this work, as a part of our on-going investigations of electron transport in CO, we present scanning drift tube measurements of electron swarm transport coefficients and make comparisons with previous measurements. In addition, we test the completeness and consistency of Biagi's most recent cross-section set for electron scattering in CO (Biagi 2021) by comparing the measured electron swarm transport coefficients with those obtained by kinetic calculations and MC simulations. Finally, we investigate the spatial relaxation of electrons in an idealized SST setup in CO with the particular emphasis upon the calculation of the density-reduced effective Townsend ionization coefficient.

2. EXPERIMENTAL SYSTEM AND METHODS OF CALCULATIONS

Our measurements of the electron transport coefficients are performed with a ‘scanning' drift tube apparatus. Similar measurements with this system have already been carried out for several gases (Vass et al. 2017, Pinhão et al. 2021). The system operates under time-of-flight (TOF) conditions, where the evolution of the initiated electron cloud is monitored through the detection of particles beyond a zone of variable drift length. The experimental system is unique because it allows the recording of ‘swarm maps' which show the spatial and temporal development of electron clouds under TOF conditions. The derivation of the swarm transport coefficients of the electrons is based on fitting the swarm maps using the solution of the diffusion equation under hydrodynamic conditions. We observed a certain sensitivity of the detector system with respect to the pressure and the energy distribution of the electrons. A correction procedure was developed, which is based on the simulation of the electrons’ motion in the experimental system, under the same conditions at which experimental recordings for the transport coefficients are made.

We apply two different methods to solve the electron Boltzmann equation. The first method includes a multi-term approach for the solution of this kinetic equation under spatially homogeneous (BE MT) and SST (BE SST) conditions. The second method is based on an expansion of the electron velocity distribution function with respect to spatial gradients of the electron density (BE DG). These two methods and the associated mathematical machinery are by now standard and for details the reader is referred to previous works (Vass et al. 2017, Pinhão et al. 2021).

In addition, we also employ an MC simulation technique. In our Monte Carlo simulations, we track many electrons (typically 10^6-10^7) simultaneously under TOF and SST conditions, respectively. The movement of a single electron is monitored until it collides with the background molecules of CO. The equation of the collision

probability is solved numerically by using the appropriate set of random numbers. The type of collision determines the scattering parameters after the collision, including the electron speed and direction of motion. Electron transport coefficients are determined after relaxation in the stationary state using formulae given in our earlier publications (Dujko et al. 2021).

3. RESULTS AND DISCUSSION

In figure 1 we show the variation of the drift velocity (a) and longitudinal characteristic energy (b) with the reduced electric field E/N. Panel (a) shows both families of the transport coefficients, the flux and the bulk ones, and panel (b) displays the bulk values of D_L/μ.

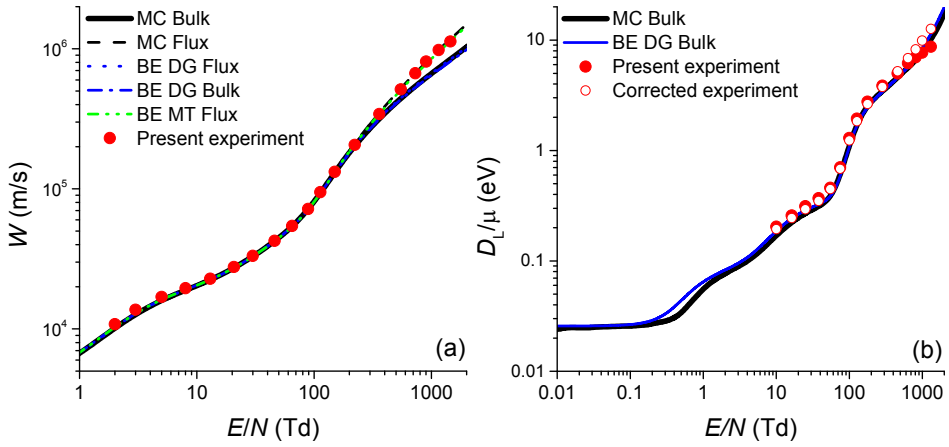

Figure 1: Comparison of the calculated flux and bulk drift velocities and the present experimental data (a), and comparison between the calculated bulk values of the longitudinal characteristic energy and the corrected and uncorrected experimental data (b).

The present experimental and calculated data for the bulk drift velocity (a) and D_L/μ (b) agree very well over the entire range of E/N considered in this work. This indicates that the experimental data in the scanning drift tube apparatus are the bulk transport coefficients. For $E/N \geq 130$ Td the bulk values are greater than the corresponding flux values for both the drift velocity and D_L/μ, which is a clear indication of the explicit effects of ionization processes on the transport coefficients.

In figure 2, we show the variation of the density-reduced effective Townsend ionization coefficient α_{eff}/N with E/N. The present experimental data for α_{eff}/N, are derived from the set of measured data $\{\nu_{eff}/N, W, ND_L\}$ where ν_{eff}/N is the density-

reduced effective ionization frequency, W is the bulk drift velocity and ND_L is the bulk longitudinal diffusion coefficient. The present modelling results include the MC and BE SST calculations under SST conditions (BE SST), while the MC and the BE DG results under hydrodynamic conditions (e.g., the MC Hydro and the BE DG Hydro) are derived from the set of the calculated coefficients $\{\nu_{eff}/N, W, ND_L\}$. For E/N < 300 Td, the agreement between experimental and modelling results is very good and lies within 5 %. For higher values of E/N the present experimental data agree very well with the modelling results (within 10 %), particularly with the MC SST results.

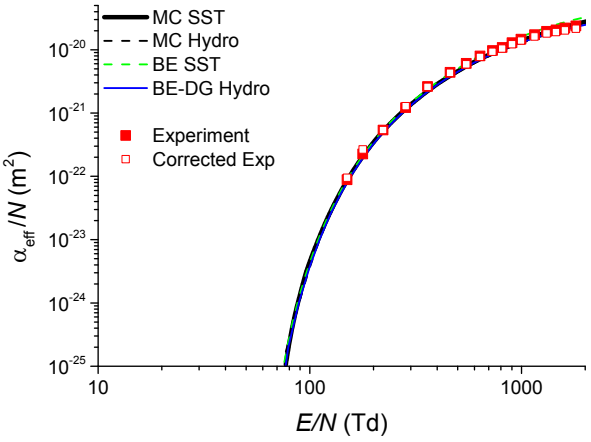

Figure 2: Variation of the density-reduced effective Townsend ionization coefficient with E/N.

References

Biagi, S.: 2021, https://magboltz.web.cern.ch/magboltz/ (v11.11).
Cambell, L., Allan, M., Brunger, M.: 2011, *J. Geophys. Res.*, **116**, A09321.
Carbone, E., Douat, C.: 2018 *Plasma Med.*, **8**, 93.
Cimerman, R., Račkova, D., Hensel, K.: 2018, *J. Phys. D: Appl. Phys.*, **51**, 274003.
Dujko et al.: 2021, *Plasma Sources Sci. Technol.*, **30**, 115019.
Grigorian, G.M., Kochetov, I.V.: 2008, *Quantum. Electron.*, **38**, 222.
Omori, N., Matsuo, H., Watanabe, S., Puschmann, M.: 1996, *Surf. Sci.*, **352-354**, 988.
Pietanza, L.D., Colonna, G., Capitelli, M.: 2017 *Plasma Sources Sci. Technol.* **26** 125007.
Pinhão, N.R., Loffhagen, D., Vass, M., Hartmann, P., Korolov, I., Dujko, S., Bošnjaković, D., Donkó Z.: 2021, *Plasma Sources Sci. Technol.*, **29**, 045009.
Vass, M., Korolov, I., Loffhagen, D., Pinhão, N.R., D., Donkó Z.: 2017, *Plasma Sources Sci. Technol.*, **26**, 065007

Publ. Astron. Obs. Belgrade No. 102 (2022), 41 - 44 *Contributed Paper*

SINGLE-ELECTRON CAPTURE FROM He BY FAST ALPHA PARTICLES

NENAD MILOJEVIĆ, DANILO DELIBAŠIĆ and IVAN MANČEV

Department of Physics, Faculty of Sciences and Mathematics, University of Niš, P.O. Box 224, 18000 Niš, Serbia
E–mail nenad.milojevic@pmf.edu.rs

Abstract. Single-electron capture cross sections in collisions between fast alpha particles and helium atoms are investigated by means of the prior form of the three- and the prior and post form of the four-body boundary-corrected first Born approximation (CB1-3B and CB1-4B, respectively). The dielectronic interaction $1/r_{12} \equiv 1/|\mathbf{r}_1 - \mathbf{r}_2|$ explicitly appears in the complete perturbation potential V^+ of the post four-body transition probability amplitude T_{nlm}^{4B+}. An illustrative computation is performed involving state-selective and state-summed total cross sections at intermediate and high impact energies. The obtained theoretical state-summed total cross sections are in excellent agreement with the available experimental data.

1. INTRODUCTION

Single-electron capture from one- and multielectron targets, as one of the charge-exchange processes, is very important in a number of applications in astrophysics (Heng et al. 2008), plasma physics (Thomas 2012), thermonuclear fusion research (Marchuk 2014) and medical ion therapy of tumors (Belkić 2021a, Belkić 2021b). Electron capture from He by ionized impurities in plasma gives a unique method for measuring the concentration of impurity nuclei (Joachain et al. 1981).

The present work is a theoretical investigation of single-electron capture from helium atoms in the ground state $\mathrm{He}(1s^2)$ colliding with alpha particles He^{2+}. We studied this pure four-body problem by using three high energy first order theories, the prior form of the three-body boundary-corrected first Born (CB1-3B) approximation and the prior and the post form of the four-body boundary-corrected first Born (CB1-4B) approximation. These methods preserve the correct boundary conditions in both entrance and exit collisional channels according to the principles of quantum scattering theory, where it is known that the boundary conditions (Dollard 1964, Belkić 2004, Belkić 2009) are of essential importance for atomic collisions whenever the aggregates are charged in the asymptotic channels. The CB1-3B method in both forms was first developed in the work (Belkić et al. 1979), while the CB1-4B, also in both forms, was formulated and applied in the works (Mančev et al. 2012, Mančev et al. 2013) Atomic units will be used throughout unless otherwise stated.

2. THEORY

We are considering the following symmetric collisions:

$$Z_{\rm P} + (Z_{\rm T}, e_1, e_2)_{1s^2} \rightarrow (Z_{\rm P}, e_1)_{nlm} + (Z_{\rm T}, e_2)_{1s}\,, \tag{1}$$

$$Z_{\rm P} + (Z_{\rm T}, e_1, e_2)_{1s^2} \rightarrow (Z_{\rm P}, e_1)_{\Sigma} + (Z_{\rm T}, e_2)_{1s}, \tag{2}$$

where $Z_{\rm P}=2$ and $Z_{\rm T}=2$ are the charges of the bare projectile P and target nucleus T, nlm is the usual set of three quantum numbers of hydrogenlike atomic systems while the symbol Σ denotes the capture into all final states of the projectile. The parentheses symbolize the bound states. Let $\vec{s}_1$ and $\vec{s}_2$ ($\vec{x}_1$ and $\vec{x}_2$) be the position vectors of the first and second electron (e_1 and e_2) relative to the nuclear charge of the projectile $Z_{\rm P}$ (target $Z_{\rm T}$), respectively. Further, let $\vec{R}$ be the position vector of $Z_{\rm P}$ with respect to $Z_{\rm T}$. The CB1-3B method, as a purely three-body theory, is not instantly usable for the four-particle process (1). For this reason we used the frozen-core approximation in which the non-captured, passive electron (e_2) is assumed to occupy the same orbital before and after capture of the active electron (e_1). We also applied independent particles model in which the passive electron e_2 is turned on only through a shielding the original nuclear charge $Z_{\rm T}$. Based on these assumptions we can write $Z_{\rm T}^{\rm eff}=Z_{\rm T}-5/16$ instead $Z_{\rm T}$, where 5/16 is the Slater screening constant charge. Now, in three-body formalism, the original processes (1) and (2) are reduced to one-electron counterpart:

$$Z_{\rm P} + (Z_{\rm T}^{\rm eff}, e)_{1s} \rightarrow (Z_{\rm P}, e)_{nlm} + Z_{\rm T}^{\rm eff},\; Z_{\rm P} + (Z_{\rm T}^{\rm eff}, e)_{1s} \rightarrow (Z_{\rm P}, e)_{\Sigma} + Z_{\rm T}^{\rm eff}. \tag{3}$$

The prior and post form of the state-selective transition amplitude for process (1) in the CB1-4B approximation read as (Mančev et al. 2012, Mančev et al. 2013):

$$T_{nlm}^{4B\pm}(\vec{\eta}) = \iiint {\rm d}\vec{x}_1 {\rm d}\vec{x}_2 {\rm d}\vec{R} \varphi_{nlm}^{*}(\vec{s}_1)\varphi_{100}^{*}(\vec{x}_2) V^{\pm} \varphi_i(\vec{x}_1,\vec{x}_2) {\rm e}^{-i\vec{\alpha}\cdot\vec{R}-i\vec{v}\cdot\vec{x}_1} (vR+\vec{v}\cdot\vec{R})^{i\xi}\,, \tag{4}$$

$$V^{-} = Z_{\rm P}\left(\frac{2}{R}-\frac{1}{s_1}-\frac{1}{s_2}\right),\; V^{+} = Z_{\rm P}\left(\frac{1}{R}-\frac{1}{s_2}\right)+(Z_{\rm T}-1)\left(\frac{1}{R}-\frac{1}{x_1}\right)+\frac{1}{r_{12}}-\frac{1}{x_1}. \tag{5}$$

On the other hand, the prior form of the state-selective transition amplitude for process (3) in the CB1-3B approximation can be written as (Belkić et al. 1987):

$$T_{nlm}^{3B-}(\vec{\eta}) = Z_{\rm P}\iint {\rm d}\vec{s}{\rm d}\vec{R} \varphi_{nlm}^{*}(\vec{s})\left(\frac{1}{R}-\frac{1}{s}\right)\varphi_{100}(\vec{x}) {\rm e}^{i\vec{\beta}\cdot\vec{R}-i\vec{v}\cdot\vec{s}} (vR+\vec{v}\cdot\vec{R})^{i\frac{Z_{\rm P}-Z_{\rm T}^{\rm eff}}{v}}\,, \tag{6}$$

where $\xi=(Z_{\rm P}-Z_{\rm T}+1)/v$ and v is the velocity of the projectile along the $z-$ axis. The vector of the distance between the two electrons e_1 and e_2 is denoted by $\vec{r}_{12}=\vec{x}_1-\vec{x}_2=\vec{s}_1-\vec{s}_2$, and we have $r_{12}=|\vec{r}_{12}|$. Here the $\vec{\alpha}=\vec{\eta}-(v/2-(E_i+Z_{\rm P}^2/[2n^2]+Z_{\rm T}^2/2)/v)\hat{\vec{v}}$ and $\vec{\beta}=-\vec{\eta}-(v/2+(Z_{\rm P}^2/[2n^2]-(Z_{\rm T}^{\rm eff})^2/2)/v)\hat{\vec{v}}$ are the momentum transfers, while transferse momentum transfer is given by $\vec{\eta}=(\eta\cos\phi_\eta,\eta\sin\phi_\eta,0)$ with the property $\vec{\eta}\cdot\vec{v}=0$. The position vectors of the electron relative to the $Z_{\rm T}^{\rm eff}$ and $Z_{\rm P}$ are denoted by $\vec{x}$ and $\vec{s}$, respectively. The functions $\varphi_{nlm}(\vec{s}_1)$, $\varphi_{100}(\vec{x}_2)$, $\varphi_{nlm}(\vec{s})$ and $\varphi_{100}(\vec{x})$ represent the bound state wave functions of the hydrogen-like atomic systems $(Z_{\rm P},e_1)_{nlm}$, $(Z_{\rm T},e_2)_{1s}$, $(Z_{\rm P},e)_{nlm}$ and $(Z_{\rm T}^{\rm eff},e)_{1s}$, respectively. The superscripts $-$ and $+$ denote the prior and the post form, respectively. We shall use the two-parameter wave function of Silverman et al. (Silverman et al. 1960) for the ground state of the He($1s^2$):

$\varphi_{\rm i}(\vec{x}_1,\vec{x}_2) = N(\mathrm{e}^{-\alpha_1 x_1-\alpha_2 x_2}+\mathrm{e}^{-\alpha_2 x_1-\alpha_1 x_2})$, with $\alpha_1 = 2.183171$ and $\alpha_2 = 1.18853$ and $E_i = -2.8756614$, where N is the normalization constant.

The nine-dimensional integral for transition amplitude (4) can be analytically reduced to a two- and four-dimensional integral over real variables in prior and post form, respectively. In the three-body case, six-dimensional integral (6) is reduced to a two dimensional over real variables. Finally, the state-selective total cross sections in the CB1-4B and CB1-3B methods are given by:

$$Q_{nlm}^{4B\pm,3B-}(\pi a_0^2)=\frac{1}{2\pi^2 v^2}\int_0^\infty d\eta\eta|T_{nlm}^{4B\pm,3B-}(\vec{\eta})|^2,\;\; Q_n^{4B\pm,3B-}=\sum_{l=0}^{n-1}\sum_{m=-l}^{+l} Q_{nlm}^{4B\pm,3B-}. \quad (7)$$

Numerical calculations of the integral (7) are performed by means of the Gauss-Legendre (GL) and Gauss-Mehler (GM) quadratures. The numbers N_{GL} and N_{GM} of integration points were $N_{GL} \leq 112$ and $N_{GM} \leq 20$. State-summed total cross sections for electron capture into all the final states are obtained by applying the Oppenheimer (n^{-3}) scaling law (Oppenheimer 1928) via:

$$Q_\Sigma^{4B-,3B-} = Q_1^{4B-,3B-} + Q_2^{4B-,3B-} + Q_3^{4B-,3B-} + 2.561 Q_4^{4B-,3B-}, \quad (8)$$

$$Q_\Sigma^{4B+} = Q_1^{4B+} + Q_2^{4B+} + 2.081 Q_3^{4B+}. \quad (9)$$

3. RESULTS AND DISCUSSION

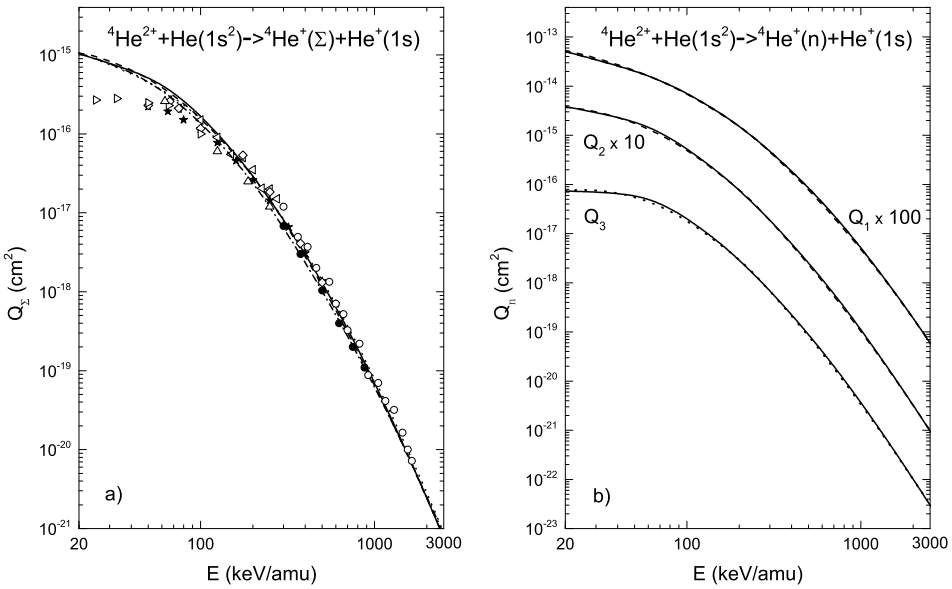

Figure 1: Panel a): State-summed total cross sections as a function of the laboratory incident energy. Present results: the full curve - CB1-4B prior, the dashed curve - CB1-4B post and the dotted curve - CB1-3B prior approximations. The dash-dotted curve represents theoretical results in the CB1 model within the RHF model (Belkić 1989). Experimental data: ○ (Hvelplund et al. 1976), △ (Mergel et al. 1995), ◇ (DuBois 1987), ▷ (Alessi et al. 2011), ◁ (Pivovar et al. 1962), ⋆ (Shah et al. 1985), • (de Castro Faria et al. 1988). Panel b): State-selective total cross sections as a function of the laboratory incident energy. Present results: the full curve - CB1-4B prior and the dashed curve - CB1-4B post approximations.

Total cross sections for the $^4He^{2+} + He(1s^2) \rightarrow {}^4He^+ + He^+(1s)$ reaction in the energy range 20 to 3000 keV/amu are plotted in Figure 1. It can be seen from panel a) that the all theoretical results (four curves) for capture into all the final states systematically exhibit excellent agreement with experimental results and each other, except that the theoretical curve (Belkić 1989) slightly underestimates presented curves, at all energies above 100 keV/amu. At energies below that value our results overestimate experimental data, which is not unexpected because these are high-energy approximations. Post-prior discrepancy is very small and only noticeable at energies below 35 keV/amu, which can be seen in panel b), where the results of the capture into $n = 1\,(Q_1 \equiv Q_1^{4B\pm})$, $n = 2\,(Q_2 \equiv Q_2^{4B\pm})$ and $n = 3\,(Q_3 \equiv Q_3^{4B\pm})$ states are shown.

4. CONCLUSIONS

We have investigated the process of single-electron capture in collisions of alpha particles with helium atoms by means the prior and the post form of the CB1-4B approximations as well as the prior form of the CB1-3B method. It is found that the methods are in excellent agreement with the available measurements at energies above 100 keV/amu. The difference between the results for the prior and post cross sections is very small. This is an excellent property of the CB1-4B approximation, since the same physical assumptions are involved in the prior and post forms of this theory.

Acknowledgements Authors thank the Ministry of Education, Science and Technological Development of the Republic of Serbia for support under Contract No. 451-03-68/2022-14/200124.

References

Alessi, M., Otranto, S., Focke, P. : 2011, *Phys. Rev. A* **83**, 014701.
Belkić, Dž. : 2004, *Principles of Quantum Scattering Theory*, Institute of Physics, Bristol.
Belkić, Dž. : 2008, *Quantum theory of High-Energy Ion-Atom Collisions*, London: Taylor & Francis.
Belkić, Dž. : 2021a, *Z. Med. Phys.*, **31**, 122.
Belkić, Dž. : 2021b, *Adv. Quantum Chem.*, **84**, 267.
Belkić, Dž., Gayet, R., Salin, A. : 1979 *Phys. Rep.* **56**, 279.
Belkić, Dž., Taylor, H. S. : 1987 *Phys. Rev. A* **35**, 1991.
Belkić, Dž. : 1989, *Phys. Scr.* **40**, 610.
Dollard, D. : 1964, *J. Math. Phys.*, **5**, 729.
DuBois, R. D. : 1987, *Phys. Rev. A* **36**, 2585.
de Castro Faria, N. V., Freire, Jr. F. L., de Pinho, A. G. : 1988, *Phys. Rev. A* **37**, 280.
Heng, K., Sunyaev, R. A. : 2008, *Astronomy & Astrophysics*, **481**, 117.
Hvelplund, P., Heinemeier, J., Horsdal-Pedersen, E., Simpson., F. R. : 1976, *J. Phys.B* **9**, 491.
Joachain, C. J., Post, D. E. : 1981, *Atomic and Molecular Processes in Controlled Thermonuclear Fusion*, New York: Plenum.
Marchuk, O. : 2014, *Phys. Scr.*, **89**, 114010.
Mančev I., Milojević N., Belkić Dž. : 2012, *Phys. Rev. A* **86**, 022704.
Mančev I., Milojević N., Belkić Dž. : 2013, *Phys. Rev. A* **88**, 052706.
Mergel, V., et al. : 1995, *Phys. Rev. Lett.* **74**, 2200.
Oppenheimer, J. R. : 1928, *Phys. Rev.* **31**, 349.
Pivovar, L. I., Tabuev, V. M., Novikov, M. T. : 1962, *JETP* **14**, 20.
Silverman, J. N., Platas, O., Matsen, F. A. : 1960, *J. Chem. Phys.* **32**, 1402.
Shah, M. B., Gilbody, H. B. : 1985, *J. Phys. B* **18**, 899.
Thomas, D. M., : 2012, *Phys. Plasmas* **19**, 056118.

Publ. Astron. Obs. Belgrade No. 102 (2022), 45 - 48 *Contributed Paper*

REDUCED MOBILITY OF H^+ IONS IN n-BUTANOL GAS

Ž. NIKITOVIĆ and Z. RASPOPOVIĆ

Institute of Physics, University of Belgrade, Pregrevica 118, 11080 Belgrade, Serbia

E-mail zeljka@ipb.ac.rs
E-mail zr@ipb.ac.rs

Abstract. In this paper we show predictions for the low energy cross sections and transport properties for the H^+ ions in n-Butanol gas. These data are needed for modelling in numerous applications of technologically importance. Appropriate gas phase enthalpies of formation for the products were used to calculate scattering cross section as a function of kinetic energy. Calculated cross sections can be used to obtain reduced mobility as a function of *E/N* (*E* -electric field strength; *N*-gas density) for H^+ in n-Butanol gas.

1. INTRODUCTION

n-Butanol occurs naturally as a minor product of the fermentation of sugars and other carbohydrates and is present in many foods and beverages as well as in a wide range of consumer products. Although most volatile organic compounds can be detected by fast methods such as ion mobility spectroscopy, precise determination is possible only if reaction of specific ions with targeted compound is well known.

The goal of this work is to calculate transport parameters of fragment ions of n-Butanol. We employ Denpoh-Nanbu's theory (DNT) see Denpoh et al. 1998 to calculate transport cross section sets for H^+ ions scattering on n-Butanol appropriate for low energies of H^+ ions. By using Monte Carlo technique that properly takes into account thermal collisions see Ristivojević et al. 2012 we calculated transport parameters as a function of *E/N*.

2. CROSS SECTION SETS

The scattering cross sections of H^+ on n-Butanol are calculated by using the DNT see Denpoh et al. 1998. separating elastic from reactive collisions. The induced dipole polarizability of 8.9×10^{-24} cm^3 see Ababneh et al. 2003 is used for the n-Butanol target. In resemblance with our recent work see Stojanović et al. 2013 DNT method is used to separate elastic from reactive endothermic collisions by accounting for the thermodynamic threshold energy and branching ratio according to the Rice-Rampsperger- Kassel (RRK) theory see Rice et al. 1928. Within the RRK theory the internal energy is being distributed among an empirical number of ***s*** equivalent effective modes of the complex selected from the total number of atoms involved in the complex.

Appropriate gas phase enthalpies of formation for the products see Lias et al. 1988 were used to calculate thermodynamic thresholds.

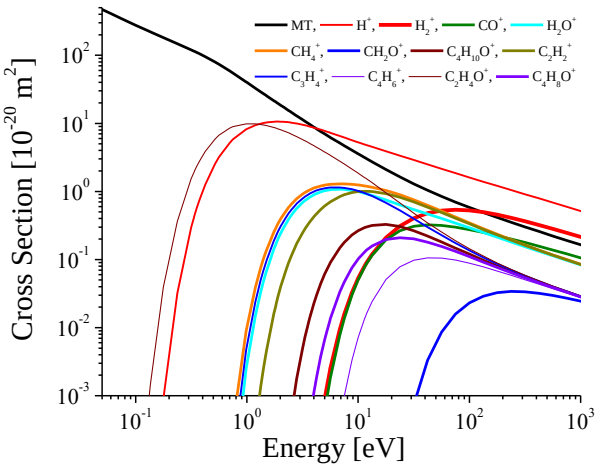

Figure 1: Cross section sets for H^+in n-Butanol gas.

The cross section sets for endothermic and exothermic reactions of H^+ with n-Butanol is presented in Figure 1.

2. RESULTS AND DISCUSSION

The transport properties of species in gas plasma are of great importance for understanding the nature of molecular and ionic interactions in gas mixtures see Todd et al. 2002, Mason et al. 1957. These properties include mean energy, drift velocity, diffusion coefficients, ionization and chemical reaction coefficients, ion chemical reaction coefficients and rarely excitation coefficients, and are very useful in the chemical industry for the design of many types of transport and process equipment. Swarm parameters, which are functions of the reduced electric field *E/N* (E-electric field strength, N-gas density) in direct electric fields are usually used for plasma modeling and simulation.

The flux and bulk drift velocities for H^+ in n-Butanol gas as a function of *E/N* are given in Figure 2. The drift velocities obtained by the Monte Carlo simulation are calculated in real space (bulk) and in velocity space (flux) values which are obtained as $\langle v \rangle$ and $d\langle x \rangle/dt$, respectively. As *E/N* increases, the high-energy ions from the distribution function increasingly have non-conservative collisions in which the H^+ ions disappear, shifting the center of mass of the swarm backward, resulting in a bulk velocity less than the flux.

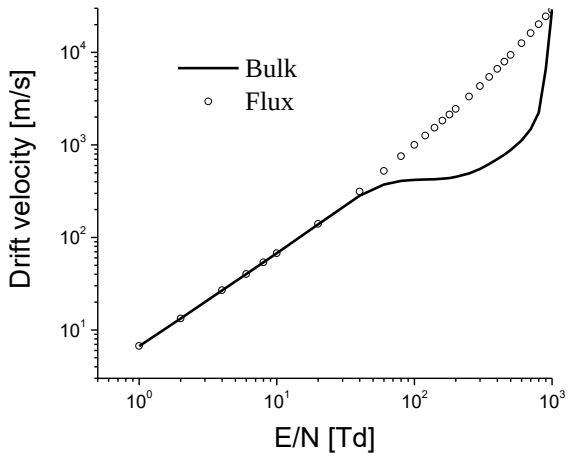

Figure 2: Drift velocity of H^+ ions in n-Butanol gas as a function of *E/N* at $T = 300$ K.

In Figure 3. we show the results of Monte Carlo simulation for reduced mobility as a function of *E/N*. Due to reactive collisions bulk and flux values of reduced mobility are separated.

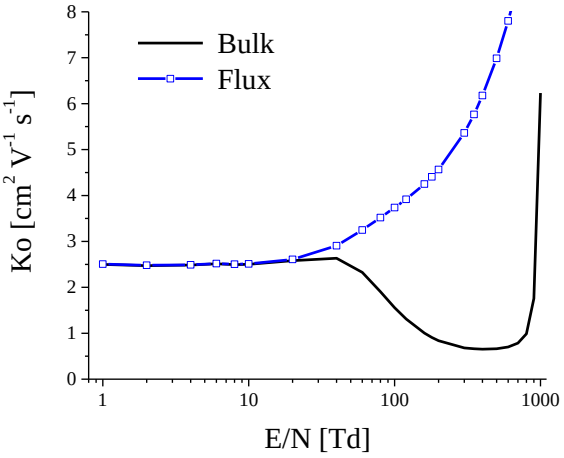

Figure 3: Reduced mobility of H^+ ions in n-Butanol gas as a function of *E/N* at *T*=300 K.

The mobility *K* of an ion is the quantity defined as the velocity attained by an ion moving through a gas under the unit electric field. One often exploits the reduced or standard mobility defined as:

$$K_0 = \frac{v_d}{N_0 E} N \,, \tag{1}$$

where v_d is the drift velocity of the ion, *N* is the gas density at elevated temperature *T* and *E* is the electric field.

Acknowledgements

The authors acknowledge funding provided by the Institute of Physics University Belgrade, through the grant by the Ministry of Education, Science and Technological Development of the Republic of Serbia.

References

A. M. Ababneh, C. C. Large and S. Georghiou: 2003, *Biophysical Journal* **85** 1111.
K. Denpoh and K. Nanbu : 1998, *J. Vac. Sci. Technol.* **A 16 (3)** 1201.
S. Lias, J. Bartmess, J. Liebman, J. Holmes, R. Levin, W. Mallard: 1988, *J Phys Chem Ref Data* **17** 1.
E. Mason: 1957, *J. Chem. Phys.* **27** 782.
O. K. Rice, H. C. Ramsperger: 1928, *J. Am. Chem. Soc.* **50 (3)** 617.
Z. Ristivojević and Z. Lj. Petrović : 2012, *Plasma Sources Sci. Technol.* **21** 035001.
V. Stojanović, Z. Raspopović, J. Jovanović, Ž. Nikitović and Z. Lj. Petrović: 2013, EPL **101** 45003.
B. Todd, J. B. Young: 2002, *J. Power Sources* **110** 186.

Publ. Astron. Obs. Belgrade No. 102 (2022), 49 - 52 *Contributed Paper*

THIRD-ORDER TRANSPORT COEFFICIENTS FOR ELECTRONS IN C_3F_8

I. SIMONOVIĆ[1], D. BOŠNJAKOVIĆ[1], Z. LJ. PETROVIĆ[2], and S. DUJKO[1]
[1] *Institute of Physics Belgrade, Pregrevica 118, 11080 Belgrade, Serbia*

[2] *Serbian Academy of Sciences and Arts, Knez Mihailova 35, 11000 Belgrade, Serbia*

Abstract. Monte Carlo simulations and multi term method for solving the Boltzmann equation are used to calculate the third-order transport coefficients for electrons in C_3F_8. The influence of elastic, inelastic and non-conservative collisions of electrons with molecules of the background gas on the individual components of the third-order transport tensor is investigated. The differences between flux and bulk values of the third-order transport coefficients are analyzed. The concurrence of the third-order transport tensor with diffusion is observed and studied.

1. INTRODUCTION

The investigation of electron transport in gases under the influence of an electric field is important for many technological applications. These applications are often modelled assuming hydrodynamic conditions in which the flux of electrons is represented in terms of drift velocity and the diffusion tensor, as higher-order transport coefficients have been systematically ignored in the traditional interpretation of swarm experiments. However, the longitudinal third-order transport coefficient has been recently measured from the arrival-time spectra of an electron swarm by Kawaguchi et al. (see Kawaguchi et al. 2021). It has been shown by Kawaguchi and coworkers that third-order and higher-order transport coefficients should be considered to obtain the longitudinal diffusion coefficient properly in the arrival-time spectra experiment at moderate and high reduced electric fields. Third-order transport coefficients are also necessary for the conversion of the hydrodynamic transport coefficients into transport data that is measured in the steady-state Townsend experiment (see Dujko et al. 2008.). If third-order transport coefficients were both calculated and measured with a sufficient precision, they would be very useful in the swarm procedure for determining the complete sets of cross sections, due to the high sensitivity of these transport coefficients to the energy dependence of cross sections for individual scattering processes (Vrhovac et al. 1999). In this work we investigate the third-order transport coefficients for electrons in C_3F_8 by employing Monte Carlo simulations and the multi term method for solving the Boltzmann equation. In section 2 we give a brief description of the methodology that is used in this work. Results and discussion are presented in section 3.

2. THEORETICAL METHODS

In our Monte Carlo simulations, we follow a swarm of electrons moving in a homogeneous background gas. The interactions between electrons are neglected due to their small number density, and the dynamics of an individual electron is determined by the electric field and by collisions with the molecules of the background gas. In these simulations random numbers are extensively employed in order to determine the time and the type of the next collision as well as postcollisional velocity of an electron. Transport coefficients are calculated from polynomials of the components of the position and velocity vectors of individual electrons, which are averaged over the entire swarm. The details of our Monte Carlo code are given in previous papers (see Dujko et al. 2010.). The bulk values of the third-order transport coefficients are determined from

$$\mathbf{Q}^{(b)} = \frac{1}{3!}\frac{\mathrm{d}}{\mathrm{d}t}\langle \mathbf{r}^{\star}\mathbf{r}^{\star}\mathbf{r}^{\star}\rangle, \tag{1}$$

while the flux third-order transport coefficients are calculated as:

$$\mathbf{Q}^{(f)} = \frac{1}{3!}\left\langle \frac{\mathrm{d}}{\mathrm{d}t}\left(\mathbf{r}^{\star}\mathbf{r}^{\star}\mathbf{r}^{\star}\right)\right\rangle, \tag{2}$$

where $\mathbf{r}^{\star} = \mathbf{r} - \langle \mathbf{r}\rangle$, and the brackets $\langle\rangle$ represent ensamble averages. As these expressions have pronounced statistical fluctuations, a large number of electrons (at least 10^7) are followed in our Monte Carlo simulations in order to determine the third-order transport coefficients.

In the second method that is used in this work we employ numerical solutions of the Boltzmann equation. The Boltzmann equation represents the equation of continuity in the phase space, and it can be written as:

$$\frac{\partial f(\mathbf{r},\mathbf{c},t)}{\partial t} + \mathbf{c}\cdot\frac{\partial f(\mathbf{r},\mathbf{c},t)}{\partial \mathbf{r}} + \frac{q}{m}\mathbf{E}\cdot\frac{\partial f(\mathbf{r},\mathbf{c},t)}{\partial \mathbf{c}} = -J(f,f_0), \tag{3}$$

where q and m are electron charge and electron mass respectively, $\mathbf{E}$ is electric field and J is collision operator. In the multi term method the phase space distribution function is expanded in terms of the spherical harmonics and Sonine polynomials in angular and radial parts of the velocity space, respectively. Under hydrodynamic conditions, the dependence of the phase space distribution function on the coordinates from the configuration space is expressed in terms of the density gradient series expansion. Then the Boltzmann equation is decomposed into a hierarchy of equations in terms of the coefficients in this expansion (the moments of the distribution function). Transport coefficients are then expressed in terms of these moments and this hierarchy of equations is truncated when the convergence of the transport coefficients is reached. The details of the multi term method, which is employed in this work, are given in previous papers (see Dujko et al. 2010.). Expressions for those components of the flux third-order transport tensor, which are independent in the electric field only configuration, are given by the following equations:

$$Q^{(f)}_{xxz} = \frac{1}{\sqrt{2}\alpha}\left[\mathrm{Im}(F(011|221;\alpha)) - \mathrm{Im}(F(01-1|221;\alpha))\right], \tag{4}$$

$$Q^{(f)}_{zxx} = -\frac{1}{\alpha}\left[\frac{1}{\sqrt{3}}\mathrm{Im}(F(010|200;\alpha)) + \frac{1}{\sqrt{6}}\mathrm{Im}(F(010|220;\alpha))\right] + \frac{1}{\alpha}\mathrm{Im}\left[F(010|222;\alpha)\right], \quad (5)$$

$$Q^{(f)}_{zzz} = \frac{1}{\alpha}\left[\sqrt{\frac{2}{3}}\mathrm{Im}(F(010|220;\alpha)) - \frac{1}{\sqrt{3}}\mathrm{Im}(F(010|200;\alpha))\right], \quad (6)$$

where Im denotes imaginary parts of the moments of the phase space distribution function, and the z-axis is directed along the electric field.

3. RESULTS AND DISCUSSIONS

In this section we show the calculated values of the third-order transport coefficients, which are obtained by employing the methods described in the previous section. The calculation of the third-order transport coefficients by employing these two methods is described more thoroughly in our previous paper (see Simonović et al. 2022.). The cross section set for electron scattering on C_3F_8 molecules, that is used in these calculations, has been developed by Biagi (see Biagi).

In figure 1.a we show all three components of the skewness tensor for electrons in C_3F_8 that are independent in the electric field only configuration. These results are obtained by using the multi term method for solving the Boltzmann equation. The $n_0^2 Q_{zzz}$ component has two local maximums and one local minimum, $n_0^2 Q_{xxz}$ component has three local maximums and two local minimums, while the $n_0^2 Q_{zxx}$ component has two local maximums and two local minimums.

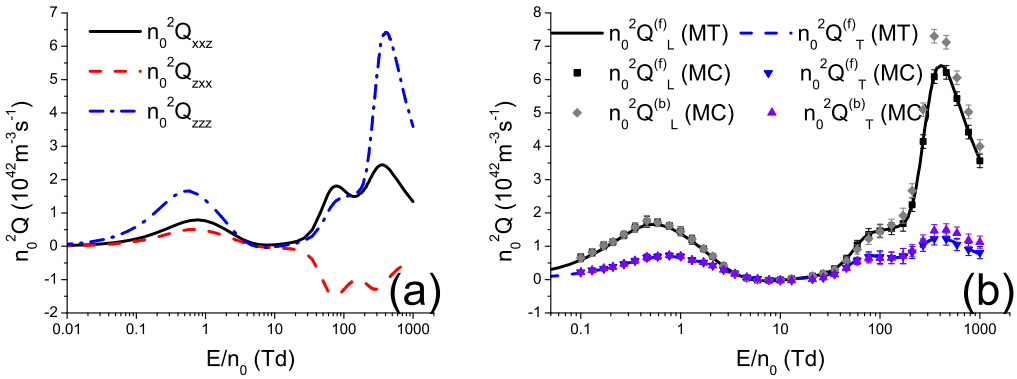

Figure 1: Independent components of the third-order transport tensor (a) and comparison of bulk and flux values of $n_0^2 Q_L$ and $n_0^2 Q_T$ (b) for electrons in C_3F_8.

In figure 1.b we show the comparison between bulk and flux values of $n_0^2 Q_L$ and $n_0^2 Q_T$. Bulk values are obtained by using Monte Carlo simulations, while flux values are determined by employing Monte Carlo simulations and the multi term method for solving the Boltzmann equation. Flux values that are obtained by using these two independent methods are generally in a good agreement, which verifies the validity of these two methods. At high electric fields bulk values are higher than the corresponding flux values, due to explicit effects of electron impact ionization.

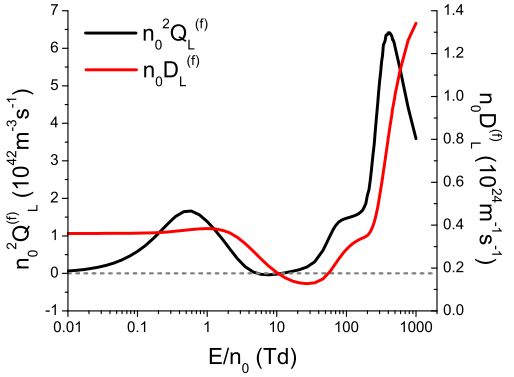

Figure 2: Concurrence between $n_0^2 Q_L^{(f)}$ and $n_0 D_L^{(f)}$ for electrons in C_3F_8.

In figure 2 we show the concurrence between $n_0^2 Q_L^{(f)}$ and $n_0 D_L^{(f)}$. This concurrence implies that $n_0^2 Q_L^{(f)}$ is being reduced with increasing E/n_0 when $n_0 D_L^{(f)}$ is being reduced, or when it increases as a concave function of E/n_0 (see Simonović et al. 2022.). The observed concurrence can be attributed to the high sensitivity of the third-order transport coefficients to the elementary scattering processes, which quench diffusive motion. It can be seen in figure 2 that $n_0^2 Q_L^{(f)}$ has a local maximum and it starts to decrease at about 0.59 Td where $n_0 D_L^{(f)}$ becomes a concave function of E/n_0. It can also be seen that $n_0^2 Q_L^{(f)}$ has a local minimum at about 8 Td, and it starts increasing at higher fields, although $n_0 D_L^{(f)}$ continues to decrease up to about 27 Td. However, $n_0^2 Q_L^{(f)}$ has negative values between approximately 5 Td, and 11 Td, and the concurrence with diffusion is violated in the vicinity of the field region where $n_0^2 Q_L^{(f)}$ is negative, as in the case of CF_4 (see Simonović et al. 2022.). Between approximately 70 Td and 170 Td, the rise of both functions slows down, while this rise becomes rapid again at higher fields. In the field region between approximately 400 Td and 1000 Td $n_0 D_L^{(f)}$ becomes a concave function of E/n_0, while $n_0^2 Q_L^{(f)}$ is being reduced with increasing field.

Acknowledgment

This research was supported by the Institute of Physics Belgrade, and the Science Fund of the Republic of Serbia [Grant No. 7749560, EGWIn].

References

Biagi, S.F., Magboltz code v11.11, https://magboltz.web.cern.ch/magboltz/

Dujko, S., White, R.D., and Petrović, Z.Lj.: 2008, *J. Phys. D: Appl. Phys.*, **41**, 245205.

Dujko, S., White, R.D., Petrović, Z.Lj., and Robson, R.E.: 2010, *Phys. Rev. E*, **81**, 046403.

Kawaguchi, S., Nakata, N., Satoh, K., Takahashi, K., and Satoh, K.: 2021 *Plasma Sources Sci. Technol.* **30**, 035006.

Simonović I., Bošnjaković D., Petrović Z. Lj., and Dujko S.: 2022 *Plasma Sources Sci. Technol.* **31**, 015003

Vrhovac, S.B., Petrović, Z.Lj., Viehland, L.A., Santhanam, T.S.: 1999 *J. Chem. Phys.* **110**, 2423

Publ. Astron. Obs. Belgrade No. 102 (2022), 53 - 56 *Contributed Paper*

PHOTOELECTRON ENERGY SPECTRA IN SEQUENTIAL TWO-PHOTON IONIZATION OF HYDROGEN BY GAUSSIAN AND HALF-GAUSSIAN LASER PULSES

N. S. SIMONOVIĆ, D. B. POPOVIĆ and A. BUNJAC
Institute of Physics, University of Belgrade, Pregrevica 118, 11080 Belgrade, Serbia
E–mail simonovic@ipb.ac.rs

Abstract. Energy spectra of photoelectrons produced in sequential two-photon ionization of hydrogen by gaussian and half-gaussian laser pulses are studied using a three-level model (1s, 2p, continuum). The spectra show an intensity dependent splitting of the resonant peak and associated modulations. The splitting can be attributed to the existence of two dressed states whose quasi-energies repel each other by the field-induced coupling. The modulations can be explained by the interference of electron waves emitted at different times during the pulse duration.

1. INTRODUCTION

We study the sequential two-photon ionization of the hydrogen atom by an intense short laser pulse and analyze interference effects in the photoelectron energy spectrum (PES). The atom, which was initially in its ground state (1s), is resonantly excited into the intermediate 2p state by the absorption of a single photon of energy $\omega = E_2 - E_1 = 3/8$ a.u. and subsequently ionized by a second photon (see Fig. 1).

In order to determine the populations of atomic states during the action of the laser pulse and after, and to obtain the PES, we calculate the evolution of atomic state $|\psi(t)\rangle$ by solving the time-dependent Schrödinger equation (in atomic units)

$$i\frac{\mathrm{d}}{\mathrm{d}t}|\psi(t)\rangle = H|\psi(t)\rangle \tag{1}$$

with the initial condition $|\psi(t_0)\rangle = |1\mathrm{s}\rangle$. The total Hamiltonian has the form $H = H_0 + W$, where H_0 is the Hamiltonian of the field-free (bare) atom, while the term $W(t)$ describes the atom-field interaction. We consider a linearly polarized laser pulse whose electric component, directed along the z-axis, reads

$$\mathcal{E}(t) = \mathcal{E}_0\, g(t) \cos\omega t. \tag{2}$$

$\mathcal{E}_0 g(t)$ is the time-dependent amplitude of the electric field strength, where $g(t)$ is the pulse envelope and ω is the carrier frequency of the pulse. Then the interaction term in the dipole approximation has the form $W(t) = z\mathcal{E}(t)$, where z is the projection of the electron-nucleus distance in the field direction.

2. THE THREE-LEVEL MODEL

2. 1. EQUATIONS FOR THE AMPLITUDES FOR POPULATION OF STATES

In the case of resonant excitation of an intermediate state (here 2p), the other excited states are nonessential and at weak fields their role in the ionization process may be neglected, i.e. the process may be adequately described within the three-level

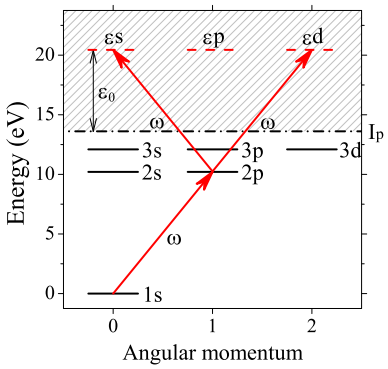

Figure 1: Energy level scheme of the hydrogen atom and the two-photon absorption paths for transitions from the ground (1s) state to the final continuum states (εs and εd) via one-photon resonant excitation of 2p state.

model (1s, 2p, continuum). Then, the atomic state at time t reads (Demekhin and Cederbaum 2012)

$$|\psi(t)\rangle = a_I(t)|I\rangle + a_R(t)e^{-i\omega t}|R\rangle + \int a_\varepsilon(t)e^{-2i\omega t}|F\varepsilon\rangle \mathrm{d}\varepsilon, \tag{3}$$

where $a_I(t)$, $a_R(t)$ and $a_\varepsilon(t)$ are the time-dependent amplitudes for the population of states $|I\rangle \equiv |1s\rangle$ (initial), $|R\rangle \equiv |2p\rangle$ (resonant) and $|F\varepsilon\rangle$ (final), respectively. The states $|R\rangle$ and $|F\varepsilon\rangle$ have been multiplied with the phase factors $e^{-i\omega t}$ and $e^{-2i\omega t}$ in order to simplify the set of equations for the amplitudes.

By inserting Eq. (3) in the Schrödinger equation (1) and applying the rotating wave approximation (Steck 2020) and the local approximation (Demekhin and Cederbaum 2011), one obtains the following set of equations for the amplitudes (Demekhin and Cederbaum 2012)

$$\begin{aligned} i\dot{a}_I &= \frac{1}{2} D^* \mathcal{E}_0\, g(t)\, a_R(t), \\ i\dot{a}_R &= \frac{1}{2} D \mathcal{E}_0\, g(t)\, a_I(t) + \Big(E_R - \frac{i}{2}\Gamma g^2(t) - \omega\Big) a_R(t), \\ i\dot{a}_\varepsilon &= \frac{1}{2} d_\varepsilon\, \mathcal{E}_0\, g(t)\, a_R(t) + (I_p + \varepsilon - 2\omega) a_\varepsilon(t), \end{aligned} \tag{4}$$

where $D = \langle R|z|I\rangle$ and $d_\varepsilon = \langle F\varepsilon|z|R\rangle$ are the dipole transition matrix elements for the excitation of the intermediate state and for its subsequent ionization, respectively. Here we set the ground state energy to zero ($E_I = 0$, as in Fig. 1). Then the energies of the resonant and final (continuum) states are $E_R = I_p + E_2 = 3/8$ a.u. and $E_F = I_p + \varepsilon$, where $I_p = 1/2$ a.u. is the ionization potential of the hydrogen atom and ε is the kinetic energy of photoelectrons. The resonant value of ε is $\varepsilon_0 = 2\omega - I_p$ (see Fig. 1). Finally, $\Gamma = 2\pi\,|d_{\varepsilon_0}/\mathcal{E}_0 2|^2$ is the ionization rate of the intermediate resonant state $|R\rangle$. The imaginary term $-\frac{i}{2}\Gamma g^2(t)$ describes the losses of the population of the intermediate state by the ionization into all final electron continuum states $|F\varepsilon\rangle$.

2. 2. DRESSED STATES AND THE ENERGY SPLITTING

The resonantly coupled dynamics of states $|I\rangle$ and $|R\rangle$ in the first two of Eqs. (4) is governed by the 2×2 Hamiltonian

$$\mathcal{H} = \begin{pmatrix} 0 & \frac{1}{2}\Omega_0^* g(t) \\ \frac{1}{2}\Omega_0 g(t) & -\frac{i}{2}\Gamma g^2(t) \end{pmatrix}, \tag{5}$$

where $\Omega_0 = D\mathcal{E}_0$ is the frequency of Rabi flopping between populations of the coupled states at the peak value of laser intensity. By solving the eigenvalue problem of Hamiltonian (5) we obtain two dressed states as superpositions $|\pm\rangle \approx (|I\rangle \pm |R\rangle)/\sqrt{2}$ and the corresponding complex eigenenergies $E_\pm(t) \approx \pm\frac{1}{2}\Omega_0 g(t) - \frac{i}{4}\Gamma g^2(t)$. Due to the imaginary parts of $E_\pm$, dressed states $|\pm\rangle$ are decaying, i.e. they are two decoupled resonances. The real parts of E_- and E_+ move apart as the pulse arrives, and towards each other as the pulse expires, estimating the splitting of the resonant peak in the PES $\Delta\varepsilon \sim \Omega_0 g_0$, where g_0 is the maximum value of envelope $g(t)$ (usually $g_0 = 1$).

3. RESULTS

The evolution of the ground state of the hydrogen atom exposed to the laser pulse of carrier frequency $\omega = E_R = 3/8$ a.u. $= 10.2$ eV has been calculated for two pulse shapes: (a) the gaussian shape $g(t) = e^{-t^2/\tau^2}$ with $\tau = 30$ fs and (b) the half-gaussian shape $g(t) = e^{-t^2/\tau^2}\mathrm{H}(t)$ with $\tau = 60$ fs ($\mathrm{H}(t)$ is the Heaviside step function). The computed dipole transition matrix elements for the excitation and ionization, used in Eqs. (4), are $D = 0.744936$ a.u. and $d_{\varepsilon_0} = 0.407759$ a.u. Figure 2 shows the evolution of populations of the ground (1s) and excited 2p state for the pulses of these two shapes and peak intensity $I_0 = 1\,\mathrm{TW/cm^2}$ ($I_0 = \mathcal{E}_0^2/(8\pi\alpha)$, $\alpha = 1/137$), while figure 3 shows the populations of these states as functions of I_0 in the domain of 10^9-10^{13} $\mathrm{W/cm^2}$ after the pulses have expired. One can see that the latest populations for the two pulses practically coincide.

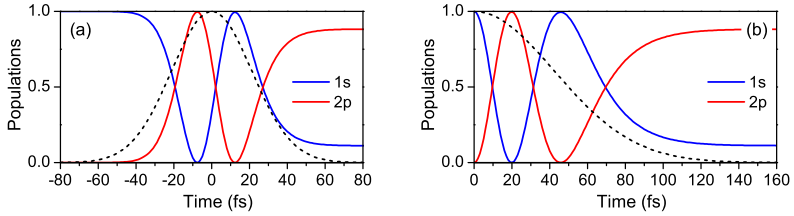

Figure 2: (a) Populations of the ground (1s) and the excited 2p state, calculated as $|a_I(t)|^2$ and $|a_R(t)|^2$, respectively, at the sequential two-photon ionization of hydrogen by a gaussian laser pulse of $1\,\mathrm{TW/cm^2}$ peak intensity, $\tau = 30$ fs and the carrier frequency $\omega = 10.2$ eV which fits to the energy of $1\mathrm{s} \to 2\mathrm{p}$ transition. (b) The populations obtained using the half-gaussian pulse with $\tau = 60$ fs and the same frequency and intensity. The dashed lines represent the envelopes of the laser pulses.

Figure 4 shows the photoelectron energy spectra calculated for the two shapes of the laser pulse and the peak intensities I_0 marked in figure 3 by vertical lines. For each value of I_0 the spectra consist of the resonant peak whose splitting, according to relation $\Delta\varepsilon \sim \Omega_0 g_0$, increases with the peak value of field strength $\mathcal{E}_0$ ($\sim \sqrt{I_0}$).

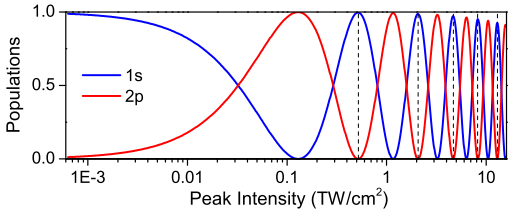

Figure 3: Populations of the ground (1s) and excited 2p state of hydrogen as functions of the laser peak intensity after the laser pulse has expired. The results obtained for the gaussian and half-gaussian pulses of the same carrier frequency $\omega = 10.2\,\mathrm{eV}$ with $\tau = 30\,\mathrm{fs}$ and $\tau = 60\,\mathrm{fs}$, respectively, which practically coincide, are presented. The vertical dashed lines indicate the peak intensities at which the atom manages to complete an integer number of Rabi cycles during the pulse.

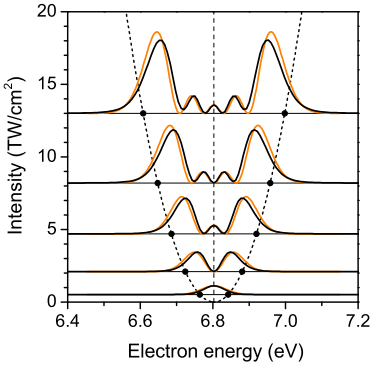

Figure 4: Photoelectron energy spectra represented by distributions $w(\varepsilon) = |a_\varepsilon(3\tau)|^2$ calculated for the gaussian and half-gaussian laser pulses (orange/black lines) with the peak intensities marked in Fig. 3 by vertical lines. Black dots mark the real parts of $E_\pm(0)$, whose separation ($\approx \Omega_0$) estimates the splitting of the resonant peak.

Demekhin and Cederbaum (2012) analyzed the modulations in the PES obtained for the photoionization with the gaussian pulse. They explained the occurrence of modulations between the positions of $E_\pm$ resonances by the interference of two photoelectron waves emitted with the same kinetic energy at two different times – at time when the pulse is growing and at time when it decreases. Our calculations, however, show that similar modulations exist also in the case of photoionization with the half-gaussian pulse, that has no growing part. Based on this, we conclude that the modulations are due to the interference of electron waves emitted all the time during the pulse duration, rather than at two specific times.

References

Demekhin, P. V., Cederbaum, L. S. : 2011, *Phys. Rev. A*, **83**, 023422.
Demekhin, P. V., Cederbaum, L. S. : 2012, *Phys. Rev. A*, **86**, 063412.
Steck, D. A., *Quantum and Atom Optics*, available online at http://steck.us/teaching (revision 0.13.4, 24 September 2020).

Publ. Astron. Obs. Belgrade No. 102 (2022), 57 - 60 *Contributed Paper*

DISSOCIATION OF N_2 BY ELECTRON IMPACT IN RF ELECTRIC FIELD

V. STANKOVIĆ[1], M. RISTIĆ[2], R. RANKOVIĆ[2], M. AONEAS[3], M. VOJNOVIĆ[1] and G. B. POPARIĆ[1]

[1]*University of Belgrade, Faculty of Physics, Studentski Trg 12, P.O.Box 44, 11000 Belgrade, Serbia*

[2]*University of Belgrade, Faculty of Physical Chemistry, Studentski Trg 12, P.O.Box 47, 11000 Belgrade, Serbia*

[3]*University of Zawia, P.O. Box 16418, Zawia, Libya*

E-mail ristic@ffh.bg.ac.rs

Abstract. Rate coefficients for electron impact dissociation of the N_2 molecule to neutral fragments under the presence of radio-frequency (RF) electric field are calculated for field frequencies of 13.56, 100 and 200 MHz and for root mean square values of the reduced electric field strength of 300 and 500 Td.

1. INTRODUCTION

Dissociation of excited nitrogen molecules is important from many aspects of environmental and industrial chemistry as well as in many technological processes such are RF plasma nitriding, sterilization of medical instruments by nitrogen atoms and many others (see Guiberteau et al. 1997, Villeger et al. 2003).

Dissociation of N_2 to neutral fragments is taking place via electronically excited states of N_2 that subsequently dissociates into atoms:

$$e + N_2 \rightarrow N_2^* \rightarrow N + N + e \qquad (1)$$

Threshold energy for reaction (1) is 9.75 eV and most of nitrogen molecules' electronic states lie above this energy. Excess energy during dissociation is transferred to atoms.

Zipf and McLaughlin 1978 were first to recognize the importance of dissociation of the excited N_2 molecules over radiative relaxation across manifold of singlet valence and Rydberg states. They have shown that nitrogen molecules that were excited to various $^1\Pi_u$ and $^1\Sigma_u^+$ states, whether by electron impact or UV photon absorption, mostly follow the predissociation path, although photon relaxations via dipole-allowed transitions to the singlet ground state were expected

to be dominant (see Green and Barth 1967). Dissociation to neutrals occurs in a time interval of 10^{-13} s, while radiative decay lasts 10^{-8} s (Itagaki et al. 2003). Main contribution to N_2 dissociation below 100 eV electron energies originates from family of $^1\Pi_u$ states, which predissociate with almost 100% efficiency. Contributions of $^1\Sigma_u^+$ states to dissociation vary depending on the states' vibrational level. Above 100 eV, the states contributing to dissociative ionization become dominant contributors to dissociation. The cross sections for reaction (1) are measured and reported by several groups (see Itikawa et al. 1986, Itikawa 2006). In the present work, we shall calculate the rate coefficients for dissociation to neutral fragments only, under the presence of RF electric field for frequencies of 13.56, 100 and 200 MHz and for E_R/N values of 300 and 500 Td. For this purpose we will use the cross sections that were measured and recommended by Cosby 1993 and electron energy distribution functions (EEDF) that are obtained by using our Monte Carlo simulation.

2. METHOD

Monte Carlo simulation code has been developed previously to track the electron transport trough the nitrogen atmosphere in the presence of RF electric field (see Popović et al. 2014, Ristić et al. 2017). Electrons are exposed to the action of a time-varying electric field that periodically oscillates at a fixed frequency f as a function of time t:

$$\boldsymbol{E}(t) = \sqrt{2}E_R\boldsymbol{k}cos(2\pi ft) \tag{2}$$

where E_R denotes the root mean square value of the electric field strength and $\boldsymbol{k}$ is the unit vector set in the direction of the electric field. After certain time that electrons have passed in the simulation, quasi-steady state is reached and EEDF is sampled over a period of the field oscillation. Electron's coordinates and velocity components are determined in each small time step of the simulation, dt by solving the differential equation of motion:

$$m\frac{d^2\boldsymbol{r}}{dt^2} = e\boldsymbol{E}(t) \tag{3}$$

where $\boldsymbol{r}$ is the electron radius vector, m is the electron mass and e is its charge. All scattering processes that can happen in interaction of electron and N_2 molecules (elastic, inelastic and ionization) were included in the model by carefully choosing the cross sections for all relevant processes. Dissociation is involved implicitly through the inclusion of all available electronic states that contribute to the dissociation process. For more details of the Monte Carlo code we refer the reader to reference Ristić et al. 2017.

The EEDFs obtained by simulation at a given point in time within one period of field oscillation and for the mean electron energy $\bar{\varepsilon}_t$, were used to calculate the rate

coefficients $K(\bar{\varepsilon}_t, t)$ for the dissociation with the corresponding effective cross section $\sigma(\varepsilon)$, having a threshold energy ε_{th}, using the formula:

$$K(\bar{\varepsilon}_t, t) = \sqrt{\frac{2}{m}} \int_{\varepsilon_{th}}^{\infty} \sigma(\varepsilon) \sqrt{\varepsilon}\, f_\varepsilon(\bar{\varepsilon}_t, \varepsilon, t) d\varepsilon \quad (4)$$

where ε represents the actual kinetic energy of the electron and $f_\varepsilon(\bar{\varepsilon}_t, \varepsilon, t)$ is the EEDF at specific time *t*.

3. RESULTS AND DISSCUSION

The rate coefficients for dissociation of N_2 to neutral fragments vs. phase of the RF electric field for frequencies of 13.56, 100 and 200 MHz are presented in Fig. 1 for E_R/N values of 300 (Fig. 1 a) and 500 Td (Fig. 1 b).

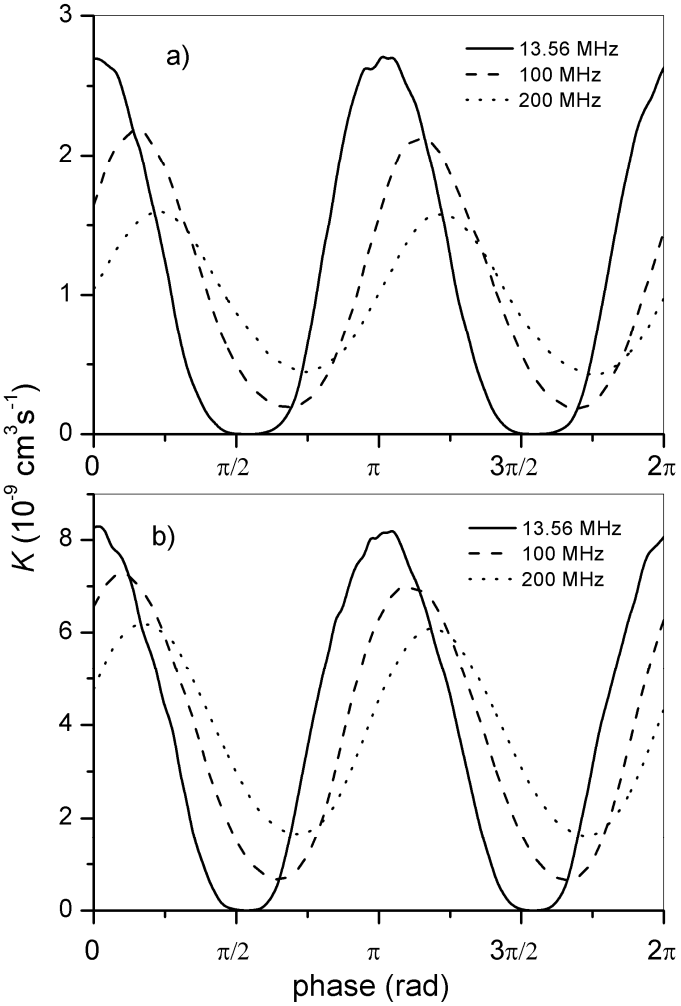

Figure 1: Rate coefficients for dissociation of N_2 to neutral fragments vs. phase of the RF electric field for indicated frequencies and at a) E_R/N=300 Td and b) E_R/N=500 Td.

One can see that the dissociation rates are higher at 500 Td than at 300 Td. This is because the cross section for dissociation is rising steeply from its threshold and at higher E_R/N electrons will have higher energies and overlapping integral between $\sigma(\varepsilon)$ and $f_\varepsilon(\bar{\varepsilon}_t, \varepsilon, t)$ shall have greater value.

At 13.56 MHz, the rates are in phase with the electric field, but with rising the frequency of the field, a phase lag of the dissociation rates is becoming more pronounced. This is caused by electrons' inertia while moving through the nitrogen gas.

Table 1: Period averaged rate coefficients (in 10^{-9} cm^3s^{-1}) for dissociation of N_2 to neutral fragments under considered conditions

	f = 13.56 MHz	f = 100 MHz	f = 200 MHz
E_R/N = 300 Td	1.1590	1.0640	0.9709
E_R/N = 500 Td	3.9337	3.7783	3.7960

For the sake of practical purposes, we have calculated period-averaged dissociation rates to neutral fragments. These values are presented in Table 1. When frequency is raised at E_R/N=300 Td, the period-averaged rate is decreasing. At E_R/N=500 Td, relative changes of the period-averaged dissociation rates are lower and no constant decreasing with rising the f is present. We believe that presented dissociation rates can be useful in many processes that involve capacitively-coupled RF nitrogen plasma.

Acknowledgments

This work was supported in part by the Ministry of Education, Science and Technological Development of the Republic of Serbia under contracts No. 451-03-9/2022-14/200162 and 451-03-68/2022-14/200146.

References

Cosby P. C: 1993, *The Journal of Chemical Physics* **98,** 9544

Green A. E. S. and Barth C. A: 1967, *J. geophys. Res.* **72,** 3975

Guiberteau E, Bonhomme G, Hugon R, and Henrion G: 1997, *Surf. Coat. Technol.* **97**, 552.

Itagaki N, Iwata S, Muta K, Yonesu A, Kawakami S, Ishii N, and Kawai Y: 2003, *Thin Solid Films* **435,** 259

Itikawa Y, Hayashi M, Ichimura A, Onda K, Sakimoto D, Takayanagi K, Nakamura M, Nishimura H. and Takayanagi T: 1986, *J. Phys. Chem. Ref. Data* **15,** 985

Itikawa Y: 2006, *J. Phys. Chem. Ref. Data* **35,** 31

Popović M. P, Vojnović M. M, Aoneas M. M, Ristić M. M, Vićić M. D, and Poparić G. B 2014: *Phys. Plasmas* **21**, 063504

Ristić M. M, Aoneas M. M, Vojnović M. M, and Poparić G. B: 2017, *Plasma Chem. Plasma Process*. **37**, 1431

Villeger S, Cousty S, Ricard A, Sixou M: 2003, *J. Phys. D: Appl. Phys.* **36**, L6.

Zipf E. C. and McLaughlin R. W: 1978, *Planet. Space Sci.* **26,** 449

Publ. Astron. Obs. Belgrade No. 102 (2022), 61 - 64 *Contributed Paper*

EXCITATION OF $^1\Sigma^+_u$ and $^1\Pi_u$ STATES AND IONIZATION OF CO_2 IN DC ELECTRIC FIELD

VIOLETA V. STANKOVIĆ[1], MIRJANA M. VOJNOVIĆ[1], MIROSLAV M. RISTIĆ[2], SAVA M. D. GALIJAŠ[1] and GORAN B. POPARIĆ[1]

[1]*University of Belgrade, Faculty of Physics, Studentski Trg 12, P.O.Box 44, 11000 Belgrade, Serbia*

[2]*University of Belgrade, Faculty of Physical Chemistry, Studentski Trg 12, P.O.Box 47, 11000 Belgrade, Serbia*

Email violeta.stankovic@ff.bg.ac.rs

Abstract. The topic of this research are the rate coefficients for formation of CO_2 molecules ions formed as a result of collisions between electrons and CO_2 gas molecules. For rates calculation we used non-equilibrium electron energy distribution function obtained by a Monte Carlo simulation in the homogenous external electric field. The calculations are performed for reduced electric field values, E/N, in the range from 20 Td to 1000 Td.

1. INTRODUCTION

CO_2 molecules are currently the research topic by many research communities since the electron interaction with CO_2 molecules is very important in terms of natural phenomena as well as in plasma devices and laser technology. Today the most common natural phenomenon is the greenhouse effects, for which the CO_2 molecule is largely responsible, since it is an essential part of the Earth's atmosphere composition. Also knowledge of energy transfer in the atmosphere of Mars and Venus is increased by the fact that electrons are cooling in process of collision with CO_2 molecules. In order to model all mentioned phenomena, it is necessary to know the probabilities for the involved processes as well as the rate coefficients of them. Electron ionization is a crucial process for maintaining plasma in discharge devices and is also one of the process by which CO_2 is activated. Ionization of CO_2 molecules provides a multitude of ionic species where positive and negative ions are important for plasma maintenance.

CO_2 molecule has already been the subject of research by our group in terms of non- equilibrium rate coefficients. The calculations of them had done by using a

Monte Carlo simulation of electron transport trough CO_2 gas in the presence of DC electric field. Calculations of the rate coefficients for vibrational excitation of CO_2 vs. E/N values, ranging only up to 150 Td, had been performed (see Poparić et al. 2010). The aim of this paper is to provide database of rate coefficients for many ways of obtaining CO_2 ions caused by the movement of electrons under the influence of an external electric field. Such a data set enables the application of modeled plasmas.

2. MONTE CARLO METHOD

The results presented in this paper were obtained using the Monte Carlo simulation. Simulation involves monitoring the transport of an ensemble of electrons (10^7). Electrons are moving under the influence of the external homogenous DC electric field in the infinite space filled with neutral CO_2 gas (pressure 5 Torr). Each electron is observed and monitored individually for a given set of input parameters. At the initial moment electrons are characterized by the nonzero kinetic energy which is seated around the expected mean electron energy as input parameter. The following differential equation describes the motion of each electron in mentioned ensemble:

$$m\frac{d^2\boldsymbol{r}}{dt^2} = e(\boldsymbol{E}) \tag{1}$$

In this equation $\boldsymbol{r}$ is the radius vector of the electron, m and e are the electron`s mass and charge and $\boldsymbol{E}$ is the electric field. The CO_2 molecules are assumed to be at zero temperature at their vibrational, rotational and electronic ground states. The possible collision event is determined by the random number which is weighted by probability of the certain event. Probability of possible elastic or inelastic event is calculated by using the integral cross section which the program contains as input data folder and interpolated for the corresponding kinetic energy. When equilibrium is established between the energy transmitted by the electrons to the neutrals and the energy which electron is receive by the electric field, the electron energy distribution function is sampled in equidistant time steps.

Our cross section (CS) database contains CSs for elastic and nonelastic collision processes, mostly originating from measurements, while some are determined by theoretical models.

To validate the simulation code, we performed tests by comparing the electron transport parameters obtained by the simulation with benchmark calculations found in literature for different model gases. These are the Reid model gas (see White et al. 1999) for conservative collision processes and the modified Ness-Robson model gas (see Nolan et al. 1997) for nonconservative collision processes (ionization and electron attachment). For more details about Monte Carlo simulation code and our cross section database we refer to reference Vojnović at al. 2019.

3. RESULTS

After the EEDF is sampled for certain parameters (E_r/N), it is used to calculate the value of the electronic excitation rate at a certain moment of the external electric DC field influence. The calculation is performed by the following equation:

$$K(\bar{\varepsilon}_t) = \sqrt{\frac{2}{m}} \int_{\varepsilon_{th}}^{\infty} \sigma(\varepsilon) \sqrt{\varepsilon}\, f_\varepsilon(\bar{\varepsilon}_t, \varepsilon) d\varepsilon \qquad (2)$$

where $\sigma(\varepsilon)$ is the cross section for the certain process and ε_{th} is the treshold energy for that process.

In Figure 1 the partial ionization rate coefficients of the formed several ionic species of CO_2 gas are represented, depending on the reduced electric field, E_r/N, in the range form 20 Td to 1000 Td.

Also, in Figure 2, one can see the rate coefficients for excitation of the $^1\Sigma^+_u$ and rate $^1\Pi_u$ electronic states of CO_2 gas calculated in the condition of zero magnetic field and reduced electric field, E_r/N, in the range from 20 Td to 1000 Td.

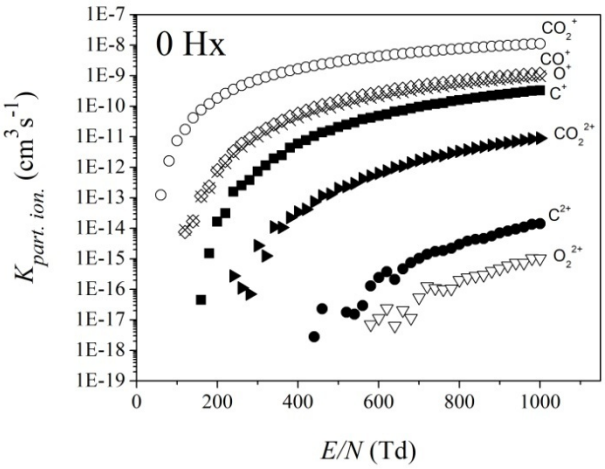

Figure 1: Partial ionization rate coefficients of the CO_2 gas vs. reduced electric field, E/N, in the range from 20 Td to 1000 Td and for zero magnetic field.

In addition to the fact that the pure CO_2 gas after ionization by electrons becomes a complex mixture of the shown ionic species and neutrals, we can see that the highest rate coefficient is for formation of CO_2^+ ion almost in the whole applied range of reduced electric field. It is expected because formation of the CO_2^+ ion is the most probable formation by electron impact ionization, in relation to formation of other ionization channels. The formation of other ionic species requires the application of a more intense electric field, but the rate coefficient of electron impact ionization for these species is certainly lower.

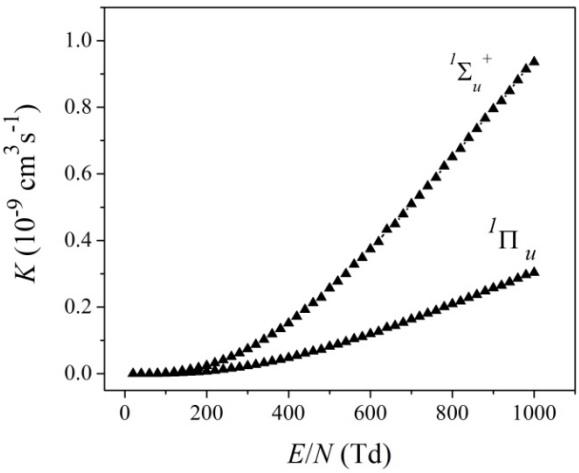

Figure 2: Rate coefficients of the $^1\Sigma^+_u$ and $^1\Pi_u$ state excitations of CO_2 gas vs. reduced electric field, E/N, in the range from 20 Td to 1000 Td and for zero magnetic field.

In the figure 2 one can see the rate coefficients values of the $^1\Sigma^+_u$ and $^1\Pi_u$ electronic state follow the growth of the applied electric field strength. The rate coefficient of $^1\Sigma^+_u$ electronic state increases almost exponentially with increasing strength of the applied electric field, where it can be noticed that the value of the its rate coefficient is the highest at the maximum applied field strength (1000 Td). Both electronic states can be said to have a uniform value of the ionization rate coefficient in the initial part of the curve in figure 2, approximately in the range from 0 Td to 200 Td, after which a slightly weaker increase of excitation rate coefficient of $^1\Pi_u$ electronic state is observed.

The presented dataset is expected to be helpful for understanding the processes of DC CO_2 plasma which also directly affects the quality modeling of this plasma type.

Acknowledgments

This work was supported in part by the Ministry of Education, Science and Technological Development of the Republic of Serbia under contracts No. 451-03-9/2022-14/200162 and 451-03-68/2022-14/200146.

References

Poparić G. B, Ristić M. M. and Belić D. S.: 2010, *J. Phys. Chem. A,* **114**, 1610

Vojnović M. M., Ristić M. M., Stanković V. V.: 2019, *Phys. Rev. E,* **99,** 063211

White R. D, Ness K. F, Robson R. E. and Li B.: 1999, *Phys. Rev. E*, **60**, 2231

Nolan A. M, Brennan M. J, Ness K. F. and Wedding A. B.: 1997, *J. Phys. D: Appl. Phys*., **30**, 2865

Publ. Astron. Obs. Belgrade No. 102 (2022), 65 - 68 *Contributed Paper*

TOTAL CROSS SECTION MEASUREMENTS FOR ELECTRON SCATTERING ON METHYL FORMATE ($HCOOCH_3$) MOLECULE: METHYLATION EFFECT

NATALIA TAŃSKA, KUBA WÓJCIK, SYLWIA DYLNICKA, ELŻBIETA PTASIŃSKA-DENGA, CZESŁAW SZMYTKOWSKI and PAWEŁ MOŻEJKO

Division of Electron Collisions Physics, *Institute of Physics and Applied Computer Science, Faculty of Applied Physics and Mathematics, Gdańsk University of Technology, ul. Gabriela Narutowicza 11/12, 80-233 Gdańsk, Poland*
E-mail natalia.tanska@pg.edu.pl

Abstract. We present the absolute total cross section (TCS) for electron scattering from the methyl formate ($HCOOCH_3$) molecule measured in the 10-300 eV energy range, with electrostatic electron spectrometer working in the linear transmission mode. Comparison of TCS for the $HCOOCH_3$ molecule with that measured earlier for the formic acid (HCOOH) compound manifests the methylation effect i.e. the response of the electron scattering dynamics on replacing of the hydrogen atom in the hydroxy group in HCOOH with the methyl group ($-CH_3$). It is also shown that the TCS for methyl formate can be estimated with simple additivity rule, using TCSs for the formic acid, ethane and hydrogen molecules. The energy dependence of determined this way TCS for $HCOOCH_3$ and the measured values are in very good agreement above 20 eV.

1. INTRODUCTION

Small organic molecules trapped in icy grains in the interstellar space, see e.g. Herbst and Dishoeck 2009, can interact with free electrons, coming from ionization events inside bulk or from other sources. Such interactions can significantly contribute to processes resulting in synthesis of complex organic molecules in space, see Boamah et al. 2013. Methyl formate ($HCOOCH_3$) has been detected towards many extraterrestrial sources, e.g. hot molecular cores, see e.g. Cazaux et al. 2003, or on Hale-Bopp comet, see Despois et al. 2005. Therefore, accurate and comprehensive electron scattering data for the methyl formate and its isomers, glycolaldehyde and acetic acid, as precursors to larger compounds are of great astrobiological importance. Interest in methylation increased when it has been recently revealed that DNA methylation plays an important role in the formation of many common human diseases, see in Jin and Liu 2018.

Total cross section (TCS) for electron scattering is the sum of the partial cross sections for all possible processes occurring during the electron-target molecule collisions. It can be measured in an absolute scale, yielding useful information over wide electron impact energy range, see e.g. Szmytkowski and Możejko 2020. However, not all compounds can be easily investigated experimentally, e.g. due to chemical instability, high toxicity or environmental risk. It is therefore desirable to employ theoretical and/or semiempirical methods for determining scattering cross sections. One of such methods is the additivity rule, see e.g. Domaracka et al. 2008, which allows to estimate cross section at the medium and high collisional energies by adding contributions from functional groups constituting the target molecule.

In this work we present preliminary results of experimentally obtained total cross sections for electron scattering on methyl formate ($HCOOCH_3$) in 10-300 eV energy range. Effects of the formic acid methylation is illustrated by the comparison of TCS data for HCOOH and $HCOOCH_3$ molecules.

2. EXPERIMENT

Presented experimental total cross section data have been obtained using electrostatic electron spectrometer working in the linear-transmission mode. The electron beam with given energy E, within the limits from 0.3 up to 300 eV and resolution of about 80 meV (FWHM), is directed into scattering chamber filled with studied molecules. Electrons leaving the collision volume by exit orifice, are energy discriminated by retarding-field analyzer and collected in Faraday cup. TCS, σ(E), at given energy E, is determined using the Bouguer-de Beer-Lambert attenuation formula, in which thermal transpiration effect was included:

$$\sigma(E) = \frac{k\sqrt{T_t T_m}}{pL} \ln \frac{I(E,0)}{I(E,t)}, \tag{1}$$

where $I(E,0)$ and $I(E,t)$ are transmitted electron currents taken in the absence and presence of target in the scattering chamber of the length L, p is the vapour pressure of studied target, T_t is the scattering cell temperature, T_m is the temperature of manometer head and k is the Boltzmann constant. Statistical uncertainties (about 1%) were estimated as standard deviation of the weighted mean of the results obtained in the successive measurement series. Potential systematic uncertainties are less than 10% at low collision energies and decrease to 5% at intermediate energies. For detailed description of the experimental equipment and measurement procedure see e.g. Szmytkowski and Możejko 2001.

3. RESULTS AND DISCUSSION

Figure 1 shows the TCS we recently measured for methyl formate in 10-300 eV energy range. Change in the TCS slope around 100 eV is most probably due to the maximum of ionization cross section, see e.g. Możejko 2007. For comparison, in Fig. 1, we also show experimental TCS for formic acid, see Możejko et al. 2017.

With respect to the shape, both TCS curves are very similar. However, over whole presented energy range TCS values for the $HCOOCH_3$ are distinctly higher than those for the HCOOH. Larger TCS for $HCOOCH_3$ is mainly related to the increase in the geometrical size of the molecule due to presence of the methyl group.

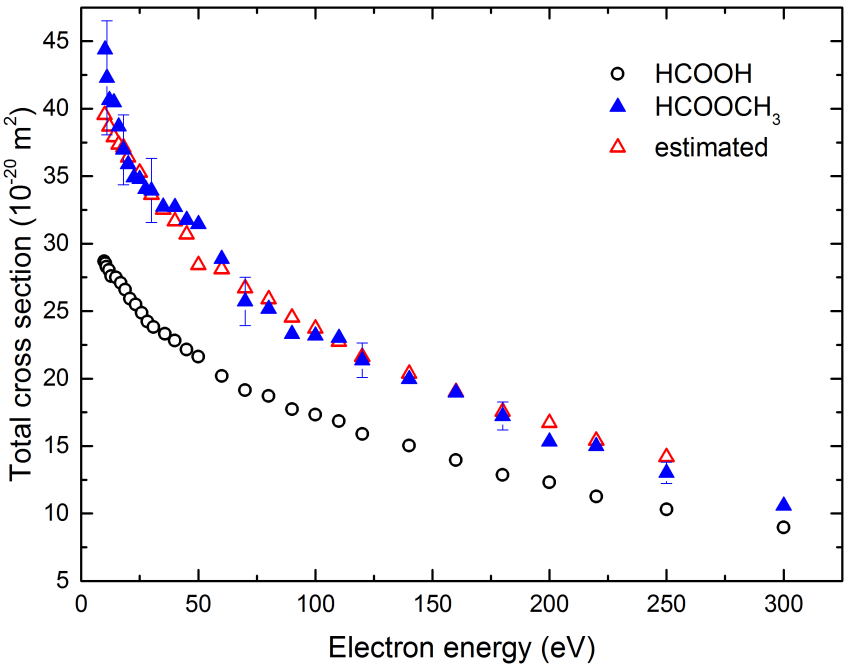

Figure 1: Comparison of preliminary TCS for electron scattering from methyl formate ($HCOOCH_3$), full blue triangles, with TCS for formic acid (HCOOH), Możejko et al. 2017, open circles. The error bars, at selected energies, correspond to overall estimated experimental uncertainties. The TCS for $HCOOCH_3$, estimated with additivity rule, is also shown, red open triangles.

Because above 20 eV no efficient resonant-like processes are expected, we can assume that beyond this energy scattering process can be approximately seen as independent electron scattering from each atom (or group of atoms), so the additivity rule can be applied, see Domaracka et al. 2008. That is why the cross section for $HCOOCH_3$ can be expressed with the formula:

$$\sigma_{HCOOCH_3} = \sigma_{HCOOH} - \sigma_H + \sigma_{CH_3}, \quad (2)$$

where σ_{HCOOH}, can be directly used as the TCS for the formic acid molecule, see Możejko et al. 2017, while σ_H and σ_{CH_3} can be estimated as one half of TCS for the

hydrogen and ethane molecules, respectively. It is worth noting, that TCS values for H_2 and C_2H_6 come from measurements performed earlier with the same experimental system, see Szmytkowski et al. 1996 and Szmytkowski and Krzysztofowicz 1995. Above around 20 eV, TCS for methyl formate estimated according to the formula (2) is in excellent agreement with the experimental data, except for the small jump near 50 eV. Below 20 eV the curves diverge, as at low electron impact energies the geometry and structure of the target molecule grow in importance.

4. CONCLUSIONS

Total cross section for electron scattering on methyl formate is presented for the 10-300 eV energy range. The additivity rule was applied to estimate the TCS for this molecule based on TCSs for formic acid, molecular hydrogen and ethane. Above 20 eV, the estimated TCS values for $HCOOCH_3$ are in excellent agreement with the TCS obtained experimentally, showing that the reasonable accuracy can be obtained with the use of such simple approach.

Acknowledgments

This work is partially supported by the Polish Ministry of Education and Science (MEiN).

References

Boamah, M.D., Sullivan, K.K., Shulenberger, K.E., Soe, C., Jacob, L.M., Yhee, F.C., Atkinson, K.E., Boyer, M.C., Haines, D.R., Arumainayagam, Ch.R. : 2014, *Faraday Discuss.*, **168**, 249.

Cazaux, S., Tielens, A., Ceccarelli, C., Castets, A., Wakelam, V., Caux, E., Parise, B., Teyssier, D. : 2003, *Astrophys. J.*, **593**, L51.

Despois, D., Biver, N., Bockelee-Morvan, D., Croviser, J. : 2005, *Proc. Int. Astronom. Union*, **1**, 469.

Domaracka, A., Możejko, P., Ptasińska-Denga, E., Szmytkowski, Cz. : 2008, *Publ. Astrom. Obs. Belgrade*, **84**, 35.

Herbst, E., van Dishoeck, E.F. : 2009, *Ann. Rev. Astron. Astrophys.,* **47**, 427.

Jin, Z., Liu, Y. : 2018, *Genes Dis.*, **5**, 1.

Możejko, P. : 2007, *Eur. Phys. J. Special Topics*, **144**, 233.

Możejko, P., Domaracka, A., Zawadzki, M., Ptasińska-Denga, Szmytkowski, Cz. : 2017, *J. Phys.: Conf. Series*, **875,** 62047.

Szmytkowski, Cz., Krzysztofowicz, A.M. : 1995, *J. Phys. B*, **30,** 4363.

Szmytkowski, Cz., Maciąg, K., Karwasz, G. : 1996, *Phys. Scr.*, **54**, 271.

Szmytkowski, Cz., Możejko, P. : 2001, *Vacuum*, **63**, 549.

Szmytkowski, Cz., Możejko, P. : 2020, *Eur. Phys. J. D*, **74**, 1.

Publ. Astron. Obs. Belgrade No. 102 (2022), 69 - 72 *Contributed Paper*

RATE COEFFICIENTS FOR O_3^+ DISSOCIATION TO O^+ AND O_2^+ BY ELECTRON IMPACT

M. M. VOJNOVIĆ[1], M. M. RISTIĆ[2] and D. S. BELIĆ[1]

[1]*University of Belgrade, Faculty of Physics, Studentski Trg 12, P.O.Box 44, 11000 Belgrade, Serbia*

[2]*University of Belgrade, Faculty of Physical Chemistry, Studentski Trg 12, P.O.Box 47, 11000 Belgrade, Serbia*

Abstract. In the present study we make comparison of rate coefficients for electron impact dissociation of ozone cation to singly charged oxygen ions, calculated for two sets of the cross section data. The two cross section datasets were measured by different research teams. We performed calculations of the non-equilibrium rate coefficients, using the adopted electron distribution functions from the WIND spacecraft observations in the interplanetary medium. The mean electron energies of these non-thermal distributions cover the range from 4,53 eV to 72 eV. The corresponding rates were interpolated from 4 eV to 80 eV to allow comparison with the equilibrium rates, obtained with Maxwell-Boltzmann distribution in a wide range of the mean electron energies up to 2000 eV. The contribution of the electron impact dissociation of O_3^+ to the ozone layer depletion is analyzed.

1. INTRODUCTION

Although the ozone hole in the Earth's upper atmosphere has been shrinking since the adoption of the Montreal Protocol in 1987, the environmental crisis caused by ozone depletion is likely to lasts for a long time. The most harmful ozone depleting substances are air pollutants, such as nitric oxides and chlorine and bromine compounds (Vaida and Simon 1995). But ozone layer is also vulnerable to interaction with UV radiation, and to some extent to collision with atoms, ions and electrons (Davies et al. 1993, Allan et al. 1996, Sweeney and Shin 1996). The latter one is in the focus of the present work, more precisely, the interactions of electrons originating from the solar wind with ozone. The solar-wind electrons can reach the upper atmosphere of the Earth trough the polar cusp and harm the ozone molecules. The following processes of electron impact dissociation of O_3^+ to O^+ and O_2^+ fragments are considered:

$$e^- + O_3^+ \rightarrow O^+ + O_2 + e^- \quad (1)$$

$$e^- + O_3^+ \rightarrow O + O_2^+ + e^- \quad (2)$$

$$e^- + {O_3}^+ \rightarrow {O_2}^+ + O^+ + e^- \quad (3)$$

The dissociative excitation processes (1) and (2) are characterized by energy thresholds of 0.64 eV and 2.19 eV, respectively. The dissociative ionization process (3) has energy threshold of 14.26 eV.

The absolute cross sections for the production of the given fragments were measured by Deng et al. (Deng et al. 2010) at Oak Ridge National Laboratory (ORNL). Five years later, Belić and coworkers (Belić et al. 2015) performed measurements at Louvain-la-Neuve (LLN) which produced absolute cross sections for electron impact dissociation of ozone cation to O^+. In their publication, Belić et al. 2015 found that their cross sections for the production of O^+ are up to a factor of three larger than those obtained by ORNL group in the region of high energies. The authors from the LLN group demonstrated that their apparent cross sections needed to be corrected by including the possible loss of signal in the experiment. The same conclusion refers to the ORNL results, as well. In their following publication (Belić et al. 2022), they have renormalized the data from ORNL group for the production of ${O_2}^+$ ions to produce the recommended absolute cross sections for the formation of this fragment ion.

In the present work we will compare the rate coefficient data published in the aforementioned paper (Belić et al. 2022) with rate coefficients that we calculated using the ORNL data for the same processes. Results obtained for equilibrium and non-equilibrium electron distribution functions are shown. The aim of making these comparisons was to evaluate the significance of the given processes to the ozone layer depletion.

2. METHOD

Rate coefficients were calculated by using the formula:

$$K(\bar{\varepsilon}) = \sqrt{2/m}\int_{\varepsilon_{th}}^{\infty} \sigma(\varepsilon)\sqrt{\varepsilon} f_e(\bar{\varepsilon},\varepsilon)d\varepsilon \quad (4),$$

where $\bar{\varepsilon}$ is the mean electron energy, ε is the electron energy, $\sigma(\varepsilon)$ is the cross section for the corresponding process, ε_{th} is the threshold energy and $f_e(\bar{\varepsilon},\varepsilon)$ is the normalized electron energy distribution function. Rate coefficients were calculated by numerical integration, with the cross sections previously numerically interpolated.

In the case of the equilibrium conditions, $f_e(\bar{\varepsilon},\varepsilon)$ in Equation (4) is the Maxwell-Boltzmann distribution:

$$f_e(\bar{\varepsilon},\varepsilon) = \frac{2}{\sqrt{\pi}}\left(\frac{3}{2\bar{\varepsilon}}\right)^{\frac{3}{2}}\sqrt{\varepsilon}\exp\left(-\frac{3\varepsilon}{2\bar{\varepsilon}}\right) \quad (5).$$

Non-equilibrium rates were calculated by using electron energy distributions obtained at mean energy values of 4.53 eV, 6.4 eV, 46.2 eV and 71.7 eV, taken from measurements performed on the WIND spacecraft (Lin 1997).

As it was already stated, the cross sections we used in calculations are from the publication Deng et al. 2010. We extrapolated those cross sections in the range of high energies, since the non-thermal distributions possess a wide bulk, reaching 500 eV. The obtained rate coefficient results were interpolated in energy interval from 4 to 80 eV.

3. RESULTS

In Figure 1 we present rate coefficient results for O^+ and O_2^+ production, as well as the total rate coefficients for the production of singly charged fragments. Figure 1(a) shows equilibrium rate coefficients, while Figure 1 (b) presents non-equilibrium rate coefficients. Data herein calculated for the ORNL cross sections are presented with dashed lines and data presented in the publication Belić et al. 2022 are shown with full lines. A mutual comparison of the rates obtained for different cross section datasets reveals that using ORNL cross sections leads to much lower values of the corresponding rates than it is the case when cross sections from Belić et al. 2015 and Belić et al. 2022 are used. The difference between rate coefficient values for the two cross section sets is up to 3 times higher in the case of non-equilibrium conditions and up to 6 times higher in the case of equilibrium conditions.

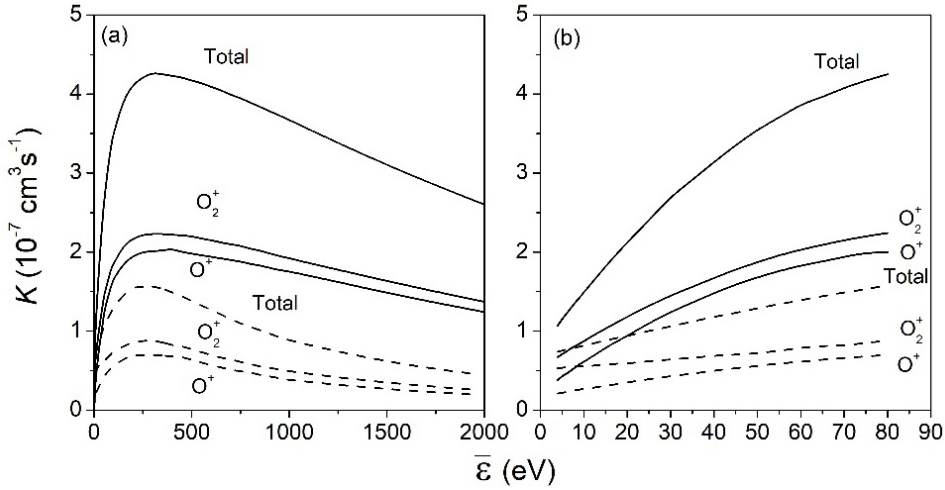

Figure 1: Equilibrium rate coefficients (a) and non-equilibrium rate coefficients (b); full lines – Belić et al 2022, dashed lines – results obtained for ORNL cross sections.

4. CONCLUSION

The comparison of the results show that cross section data from Belić et al. 2015 and Belić et al. 2022 give rise to much greater rate coefficients for both fragment ions than those from ORNL, which underestimate the contribution of the O^+ and O_2^+ production due to a loss of signal. It was also found that the non-equilibrium rates exceed the equilibrium ones. All this indicates a much greater importance of the contribution of the O_3^+ dissociation by the solar-wind electrons to the ozone layer depletion than it is expected.

Acknowledgments

This work was supported in part by the Ministry of Education, Science and Technological Development of the Republic of Serbia under contracts No. 451-03-9/2022-14/200162 and No. 451-03-68/2022-14/200146.

References

Vaida, V., Simon, J. D. : 1995, *Science*, **268**, 1443.

Davies, J. A., Johnstone, W. M., Mason, N. J., Biggs, P., Wayne, R. P. : 1993, *J. Phys. B: At. Mol. Opt. Phys.*, **26**, L767.

Allan, M., Asmis, K. R., Popović, D. B., Stepanović, M., Mason, N. J., Davies, J. A. : 1996, *J. Phys. B: At. Mol. Opt. Phys.*, **29**, 3487.

Sweeney, C. J., Shyn, T. W. : 1996, *Phys. Rev. A*, **53**, 1576.

Deng, S. H. M., Vane, C. R., Bannister, M. E., Fogle, M. : 2010, *Phys. Rev A.*, **82**, 062715.

Belić, D. S., Urbain, X., Defrance, P.: 2015, *Phys. Rev. A.*, **91**, 012703.

Belić, D. S., Vojnović, M. M., Ristić, M. M., Urbain, X., Defrance, P.: 2022, *J. Serb. Chem. Soc.*, **87**, 479.

Lin, R. P. :1997, *Coronal Physics from Radio and Space Observations Lecture notes in Physics*, **483**, 93.

Section 2.

PARTICLE AND LASER BEAM INTERACTION WITH SOLIDS

LASER-INDUCED PERIODIC SURFACE STUCTURES, MECHANISMS, APPLICATIONS, AND UNSOLVED PROBLEMS

J. BONSE[1], K. WASMUTH[1], H. VOSS[1], J. KRÜGER[1] and S. GRÄF[2]

[1]*Bundesanstalt für Materialforschung und -prüfung (BAM), Berlin, Germany*
E-mail joern.bonse@bam.de

[2]*Otto-Schott-Institut für Materialforschung (OSIM), Jena, Germany*

Abstract. *Laser-induced Periodic Surface Structures* (LIPSS, ripples) are a universal phenomenon and can be generated in a contactless, single-step process on almost any type of solid upon irradiation with intense laser pulses (Bonse et al. 2012). They represent a (quasi-)periodic modulation of the surface topography in the form of a linear grating and are typically formed in a "self-ordered" way in the focus of a laser beam. Thus, they are often accompanying laser material processing applications. The structural sizes of LIPSS typically range from several micrometers down to less than 100 nanometers – far beyond the optical diffraction limit – while their orientations exhibit a clear correlation with the local polarization direction of the laser radiation.

From a theoretical point of view, a controversial debate has emerged during the last decades, whether LIPSS originate from electromagnetic effects (seeded already during the laser irradiation) – or whether they emerge from matter-reorganization processes (distinctly after the laser irradiation) (Bonse et al. 2017). From a practical point of view, however, LIPSS represent a simple and robust way for the nanostructuring of solids that allows creating a wide range of different surface functionalities featuring applications in optics, tribology, medicine, energy technologies, etc. (Florian et al. 2020 and Gräf 2020). While the currently available laser and scanner technology already allows surface processing rates at the m^2/min level, industrial applications of LIPSS are sometimes limited by the complex interplay between the nanoscale surface topography and the specific surface chemistry. This typically manifests in difficulties to control the processing of LIPSS and in limitations to ensure the long-term stability of the created surface functions.

This presentation reviews the currently existent theories of LIPSS (Bonse & Gräf 2020). A focus is laid on the historic development of the fundamental ideas behind the LIPSS, their corresponding mathematical descriptions and numerical implementations, along with a comparison and critical assessment of the different approaches. Moreover, some unsolved scientific problems related to LIPSS are identified and the pending technological limitations are discussed (Bonse & Gräf 2021). Hereby, it is intended to stimulate further research and developments in the field of LIPSS for overcoming these limitations and for supporting the transfer of the LIPSS technology into industry (Bonse 2020 and Bonse & Gräf 2021).

References

Bonse, J., Krüger, J., Höhm, S., Rosenfeld, A. : 2012, *J. Laser Appl.*, **24**, 042006.
Bonse, J., Höhm, S., Kirner, S. V., Rosenfeld, A., Krüger, J. : 2017, *IEEE J. Sel. Top. Quantum Electron.*, **23**, 9000615.
Bonse, J., Gräf, S. : 2020, *Laser Photonics Rev.*, **14**, 2000215.
Bonse, J. : 2020, *Nanomaterials*, **10**, 1950.
Bonse, J. Gräf, S. : 2021, *Nanomaterials*, **11**, 3326.
Florian, C., Kirner, S. V., Krüger, J., Bonse, J. : 2020, *J. Laser Appl.*, **32**, 022063.
Gräf, S. : 2020, *Adv. Opt. Technol.*, **9**, 11.

HIGH-POWER LASER INTERACTIONS WITH LOW DENSITY POROUS MATERIALS AND THEIR APPLICATIONS

J. LIMPOUCH

Czech Technical University in Prague, Faculty of Nuclear Sciences and Physcical Engineering, Břehová 7, 115 19 Prague 1, Czech Republic
E-mail jiri.limpouch@fjfi.cvut.cz

Abstract. First part of the lecture will be devoted to an overview of low density solid porous materials that are used in high power laser interaction experiments. Low density porous targets have been used for smoothing laser beam intensity modulations and for studies of laser-plasma instabilities in long hot corona relevant for shock ignition of inertial confinement fusion. They are also efficient sources of soft X-ray emission, potentially suitable for applications. They have been also used in studies of high energy density matter and in laboratory astrophysics. Electron and ion acceleration by intense femtosecond laser pulses in nearly critical plasmas formed from porous materials have also been investigated. Additionally, low density foams have been utilized as a mold of cryogenic targets.

Second part of the lecture will describe this year's experiment carried out in PALS laboratory in Prague. Three types of low-density porous targets were irradiated by intense sub-nanosecond laser pulses on the 3rd and 1st harmonics of iodine laser at laser intensities in the range 10^{14} – 10^{15} W/cm^2: a) plastic TMPTA targets of average density 10 mg/cc doped with 8 weight percent of chlorine, b) 3D graphene targets of average density about 7 mg/cc and c) 3D printed regular porous targets of average density 8 mg/cc composed of plastic wires of radius 2.2 μm. We measured the speed of ionization wave propagation into the low-density porous matter via X-ray streak. Laser energy transformation into fast electrons was detected via time-integrated spatially resolved absolutely K-α emission from the copper foil placed at the target rear side. Chlorine emission spectra from chlorine doped TMPTA foams were used for measurement of electron and ion temperatures. Experimental results are compared with the results of fluid simulations using our novel sub-grid model of laser interaction with low density porous matter incorporated into PALE and FLASH hydrodynamic codes.

Acknowledgements

I want to express enormous gratitude to my colleagues O. Renner, Sh. Agarwal, T. Burian, J. Dostál, R. Dudžák, D. Ettel, L. Juha, M. Krupka, S. K. Singh, S. Weber, W. Nazarov, M. Šilhavík, J. Červenka, T. Laštovička, O. Maliuk, T. Wiste, L. Hudec, R. Liska, A. Gintrand, S. Shekhanov and V.T. Tikhonchuk for their contributions to this year's experiment at PALS laboratory in Prague, to its preparation and interpretation.

ACTION OF PULSED LASERS ON TITANIUM TARGET: SURFACE EFFECTS

JOVAN CIGANOVIĆ, MILOŠ MOMČILOVIĆ, SANJA ŽIVKOVIĆ, JELENA STASIĆ and MILAN TRTICA

VINČA Institute of Nuclear Sciences
– National Institute of the Republic of Serbia
University of Belgrade, PO Box 522 11351 Belgrade, Serbia
E-mail jovanc@vinca.rs

Abstract. The interaction of lasers with metals has been studied for decades, and has been especially intensified lately, due to the development of new, efficient pulsed lasers. Titanium has a number of excellent properties, making it applicable in various modern technologies. Treatment and processing of titanium is possible with various techniques, and the application of lasers gives a special quality, such as high precision machining or obtaining specific structures on the surface which cannot be generated by other methods.

During our research, surface processing of titanium was conducted by various pulsed lasers: nanosecond CO_2 laser, picosecond Nd:YAG laser and femtosecond Ti: sapphire laser. In order to find the optimal conditions for surface modification of titanium, the influence of different laser parameters (wavelength, pulse duration, pulse energy, etc.), as well as the influence of the ambient, was examined. The titanium samples were irradiated in different environments, ie. in air, oxygen, nitrogen, carbon dioxide, helium and in vacuum, which affected the chemical composition and morphology of the target surface.

Acknowledgments

This research was supported by the Ministry of Education, Science and Technological Development of Republic of Serbia; Grant number 451-03-68/2022-14/200017.

References

Ciganovic, J., Stasic, J., et al.: 2012, Appl. Surf. Sci., **258**, 2741-2748.
Trtica, M., Batani, D., et al.: 2013, Laser Part. Beams, **31**, 29-36.
Ciganovic, J., Zivkovic, S., et al.: 2016, Opt. Quantum Electron. **48**, 133.
Ciganovic, J., Matavulj, P., et al.: 2017, Russ. J. Phys. Chem. A, **91**, 2696-2701.
Trtica, M., Stasic J., et al.: 2018, Appl. Surf. Sci., **428**, 669-675.

Publ. Astron. Obs. Belgrade No. 102 (2022), 78 - 79 *Progress Report*

STUDY OF TWO DIMENSIONAL CRYSTALS BY RAINBOW SCATTERING EFFECT

M. HADŽIJOJIĆ and M. ĆOSIĆ

Laboratory of Physics, "Vinča" Institute of Nuclear Sciences
National Institute of the Republic of Serbia, University of Belgrade,
P. O. Box 522, 11001 Belgrade, Serbia

Abstract. In this report we present results of our theoretical study of 5 keV proton transmission through graphene. For these proton energies and considered fluences energy losses, irradiation induced defects of graphene and diffraction effects are negligible in this process. Proton trajectories were obtained by numerical solving of Newton's equations of motion, and subsequently used for construction of the proton angular yield. In the scattering angle plane we identified lines, along which the angular yield is very large. These lines correspond to singularities of the function that maps proton initial positions to the respective scattering angles. In analogy with meteorological rainbow, these lines are named – rainbow lines. It was found that rainbow pattern can be partitioned into outer and inner rainbow lines. The former are generated by trajectories of protons which scatter in the close vicinity of individual atoms, while the latter are formed by protons scattering within the graphene hexagon. Dependence of the rainbow pattern on the interaction potential was carefully investigated, revealing that inner rainbows can be useful for studying proton-graphene interaction potential. Change in the interaction potential, caused either by variation of the model parameters or by reorientation, induces regular change in the rainbow pattern and corresponding angular yield. These changes, also called metamorphoses, follow strict rules of the catastrophe theory. We conducted a thorough study of these metamorphoses, which led to development of the morphological method, relying solely on the shape of the rainbow pattern and not on the exact position of the rainbow lines or the particle count. Firstly, the closed form of the scattering law was derived using the momentum approximation. Then we used elements of the catastrophe theory to provide a local model of the rainbow pattern and the index theory of algebraic topology to describe the evolution of the rainbow pattern via bifurcations of the critical points of the reduced potential. We demonstrated that pre-images of the rainbows in the impact parameter plane are attracted and repelled by the nearest saddles and maxima of the reduced proton−graphene interaction potential. The ridge maxima of the angular distributions were investigated and related to the spectrum of the Jacobian matrix of the map generated by the scattering law. Observed evolution was summarized into five simple principles were introduced, allowing an experimentalist to sketch a qualitatively correct pre-image of the rainbow pattern in the impact parameter plane, as well as the distribution of the reduced potential critical points. Benefit of the introduced method is that it is based on the study of shape, making it insensitive to noise.

Established morphological method was used for study of thermal vibrations and point defects of graphene. Thermal motion of atoms was incorporated by averaging the static proton-graphene interaction potential over the distribution of atom displacements. The covariance matrix of atom displacements was modeled by Debye theory, and calculated using Molecular Dynamics approach. It was shown that outer rainbow lines can be modeled by ellipses whose parameters are very sensitive to the structure of the covariance matrix. Numerical procedure was developed for extraction of the covariance matrix from the corresponding outer rainbow lines in the general case, when atoms perform fully anisotropic and correlated motion. We have studied transmission of protons through the graphene containing point defects. It was shown that each defect type produces its distinctive inner rainbow pattern. Finally, it was demonstrated how the acquired knowledge about inner rainbow patterns could be used to determine the unknown defect densities of the different defect types present in the same sample.The outer rainbow pattern caries information about the composition of the sample, while the inner rainbows informs about its structure. Therefore, these lines could be named compositional and structural rainbows, respectively. Moreover, we have shown that compositional and structural rainbows do not interact, making morphological analysis appropriate for characterization of the graphene-like materials.

References

M. Ćosić, S. Petrović, N. Nešković, The forward rainbow scattering of low energy protons by a graphene sheet, *Nucl. Instrum. Methods Phys. Res., Sect. B* **422**, 54 (2018)

M. Ćosić, M. Hadžijojić, S. Petrović, R. Rymzhanov, S. Bellucci, Investigation of the graphene thermal motion by rainbow Scattering, *Carbon* **145**, 161 (2019)

M. Ćosić, M. Hadžijojić, S. Petrović, R. Rymzhanov, The morphological analysis of rainbow scattering in graphene, *Chaos* **31,** 093115 (2021)

M. Hadžijojić, M. Ćosić, R. Rymzhanov, Morphological Analysis of the Rainbow Patterns Created by Point Defects of Graphene, *J. Phys. Chem. C*. 125, **38**, 21030–21043 (2021)

SPECTROSCOPIC INVESTIGATION OF THE INFLUENCE OF NO_3^- ANIONS ON THE CRYSTALLIZATION OF SiO_2 MATRIX

VIOLETA N. NIKOLIĆ

Department
of Theoretical Physics and Condensed Matter Physics (020), Vinča Institute of Nuclear Sciences - National Institute of the Republic of Serbia, University of Belgrade,
Belgrade, P.O. Box 522, 11001, Serbia
E-mail violeta@vin.bg.ac.rs

Abstract. In this study was performed Fourier-transform infrared spectroscopy (FTIR) analysis of the impact of nitrate (NO_3^-) anions on the dynamic of silica (SiO_2) matrix crystallization. Samples were prepared by acid-catalyzed sol-gel route (T_{ann} = 800 °C and 1000 °C). Origin of the partial crystallization of silica matrix at 1000 °C was commented.

PICOSECOND PULSED LASER ABLATION OF SILICON SINGLE CRYSTAL

D. M. POPOVIC[1], A. KUSHIMA[2], A. A. ZEKIC[1], B. KASALICA[1], J. STASIC[3], J. CIGANOVIC[3], M. BOGDANOVIC[1] and M. TRTICA[3]

[1]*University of Belgrade, Faculty of Physics, Studentski trg 12, 11001 Belgrade, Serbia*
E-mail dusan@ff.bg.ac.rs

[2]*Advanced Materials Processing and Analysis Center, Department of Materials Science and Engineering, University of Central Florida, Orlando, Florida 32816, USA*

[3]*Vinca Institute of Nuclear Science, University of Belgrade, P.O. Box 522, 11001 Belgrade, Serbia*

Abstract. Silicon-based nanoparticles (SiNPs) attract authors' attention due its application prospects in a mutual field, from energy storage to bio-imaging. One of the most prominent methods for synthesis of SiNPs is pulsed laser ablation in liquid media (LAL), because it is simple, and it provides the minimum of contamination of the sample produced. Employed pulsed lasers in LAL are ns- and ps-, and the usage of fs- lasers are reported recently, as well. The objects of the LAL analyses are ablated craters on the Si target surface and, predominantly, the ablated material.

Here, SiNPs are synthesized by ps- laser (150 ps, 1064 nm) ablation of Si single-crystal plates in de-ionized water. The focus of the work is the impact of the additional continuous wave (CW) laser (532nm) on the properties of the ablated material, i.e. SiNPs produced. The comprehensive analyses were performed, including the SiNPs' size distribution, agglomeration abilities, aging, chemical properties (amount of oxygen and its distribution within the particles), and photoluminescence (PL) properties of the solution produced. It is demonstrated that PL properties of obtained SiNPs solution are impacted by introducing the CW laser in the ablation process. The peculiarity lies in the fact that such impact depends on both the PL excitation wavelength and the power of the introduced CW laser, which might open the possibility of successful tailoring of SiNPs produced by LAL.

References

Petersen, S., Barcikowski, S. 2009, Adv. Funct. Mater. 19(8), 1167.

Intartaglia, R., Bagga, K., Brandi, F., 2014, Opt. Express 22(3), 3117.

Vaccaro, L., Sciortino, L., Messina, F., Buscarino, G., Agnello, S., Cannas, M., 2014, Appl. Surf. Sci. 302, 62.

Caltagirone, C., Bettoschi, A,. Garau, A., Montis, R., 2015, Chem. Soc. Rev. 44(14), 4645.

Popovic, D. M., Kushima, A., Bogdanovic, M. I., Chai, J. S., Kasalica, B., Trtica, M., Stasic, J., Zekic, A. A., 2017, Journal of Applied Physics, 122(11), 113107.

ION-CRYSTAL RAINBOW INTERACTION POTENTIAL IN CHANNELING

N. STARČEVIĆ

Institute for Nuclear Sciences "Vinča", Mike Petrovića Alasa 12-14, 11351 Belgrade, Serbia
E-mail nikolas@vinca.rs

Abstract. One of the most important effects in the movement of positive ions through oriented crystals relative to an ion beam is the rainbow effect. The problem of accurate ion - atom interaction potential is one of the fundamental problems in describing ion - crystal interaction. It is assumed that ion - atom interactions can be treated as an two - particle collision process and that the interaction potential is a screened Coulomb potential. Construction of an accurate interaction potential of the channeled ion in the crystal is the main goal of this work. The effect of the crystal rainbow is predicted in the theoretical analysis of the transmission of positive ions through axial channels of thin crystals using a so-called impulse approximation model, which is valid when the ion energy is large enough or the crystal thickness is small enough that the trajectories of transmitted ions can be described by straight lines. After that, the crystal rainbow theory was formulated including curved trajectories or thicker crystals. Experimental measurements have shown that the predictions of the crystal rainbow model and theory are correct. It was shown that the rainbow lines represent the „skeleton" of the angular distributions of the channeled ions. The crystal rainbow theory was used for the morphological method to construct ion - atom interaction potentials in the sequence analysis of experimentally obtained high - resolution angular distributions of protons with energy of 2 MeV and a Si^{14} crystal membrane in the (001) orientation. The construction of the rainbow interaction potential is obtained by modifying the Moliere interaction potential so that it becomes precise in the whole space of the crystal channel, i.e. near the channel axis and near the atomic strings defining the channel. This modification was performed by adjusting the shape of the rainbow lines in a way that the corresponding theoretical angular distributions of the transmitted protons were in excellent agreement with the corresponding experimental distributions for proton energies of 2 MeV, 1.5 MeV, 1 MeV and 0.7 MeV. In this way, the rainbow proton - silicon interaction potential for channeling was successfully obtained. After that, a universal axial (001) and (111) rainbow ion - atom interaction potential was constructed for the case of proton channeling in the following 28 cubic crystals: FCC crystal structure: aluminum, calcium, nickel, copper, strontium, rhodium, palladium, gold, lead and thorium; BCC crystal structures: vanadium, chromium, iron, niobium, molybdenum, barium, europium, tantalum and tungsten; and with diamond crystallographic structure: carbon, silicon, germanium and tin. Furthermore, the analysis of the proton channeling in the case of the above mentioned 28 cubic crystals was extended and improved by considering two orientations (001) and (111) simultaneously. As a result, the two axial channeling directions could be treated with the same physical arguments, leading to consistent values of the interaction potential fitting parameters.

References

N. Starčević, S. Petrović: 2021, *Nucl. Inst. Methods Phys. Res. B*, **499**, 39–45.
S. Petrović, N. Starčević, M. Ćosić: 2019, *Nucl. Inst. Methods Phys. Res. B*, **79**, 447.
S. Petrović, N. Starčević, M. Ćosić, N. Nešković: 2021, *Advanced Ceramics and Applications*, De Gruyter, Berlin, Boston.

Publ. Astron. Obs. Belgrade No. 102 (2022), 83 - 86 *Contributed Paper*

INVESTIGATION OF PROPERTIES OF YTTRIUM VANADATE YVO_4 FILMS

N. A. BOSAK[1], A. N. CHUMAKOV[1], L. V. BARAN[2], V. V. MALYUTINA-BRONSKAYA[3], T. F. RAICHENOK[1], A. A. IVANOV[1], V. V. KIRIS[1], E. M. DYATLOVA[4], A. A. SHEVCHENOK[5], A. V. BUKA[4] and A. S. KUZMITSKAYA[3]

[1]*B.I. Stepanov Institute of Physics, National Academy of Sciences of Belarus, 68-2 Nezavisimosti Ave., 220072, Minsk, Belarus*
E-mail n.bosak@ifanbel.bas-net.by

[2]*Belarusian State University, Minsk*

[3]*GNPO "Optics, optoelectronics and laser technology", Minsk*

[4]*Belarusian State Technological University, Minsk*

[5]*Belarusian State Agrarian Technical University*

Abstract. Films of yttrium vanadate oxide were obtained on a silicon substrate by way of high-frequency (13 kHz) multi-pulse laser evaporation of a ceramic target in vacuum. The morphology of the films was studied using an atomic force microscope. Transmission spectra in the visible, near and middle IR regions, photoluminescence spectra, as well as volt-ampere and volt-farad characteristics were studied.

1. INTRODUCTION

Yttrium vanadate is widely used in the manufacture of birefringent crystals in laser technology. Nanostructured films of yttrium vanadate can be useful in the development of new photoactive systems for photovoltaic devices [1]. High-frequency laser action on a ceramic sprayed target [2] is capable of providing effective film production. The aim of the work is to obtain and comprehensively study laser-deposited yttrium vanadate films.

2. EXPERIMENT AND RESULTS

The experimental installation based on a neodymium laser (λ = 1.06 microns) included an optical system for transporting laser radiation to a sprayed target, a vacuum chamber, and a measuring and diagnostic complex. To obtain a multi-pulse laser generation mode with a high pulse repetition rate, a passive optical shutter made of radiation-irradiated lithium fluoride, LiF, with $F2^-$ color centers was installed inside the resonator. The repetition frequency of laser pulses was varied by changing the level of laser pumping and the optical density of the shutter; the duration of the laser pulses at half-height was ~ 85 ns. Effective deposition of thin films was achieved at a laser radiation power density, q = 64 MW/cm2, and a pulse repetition rate f ~ 13 kHz. The films were deposited at a pressure of 3 Pa. Ceramic targets were obtained by molding and subsequent sintering at a temperature of T = 1500°C in air.

Morphology of the sample surface was studied using a Solver P47-Pro scanning probe microscope (NT-MDT, Russia) in a semi-contact mode. The volt-ampere characteristics (VAC) at room temperature were measured on an automated basic laser test complex with a multispectral laser radiation source (a set of laser diodes with wavelengths of 405, 450, 520, 660, 780, 808, 905, 980, and 1064 nm with a common fiber-optic output and calibrated radiation power). The transmission of optical radiation by thin films in the near infrared (IR) range of the spectrum was measured using a Carry 500 Scan spectrophotometer. Transmission spectra in the far infrared region were recorded using the NEXUS Infrared Fourier spectrometer (Thermo Nicolet) in the range of 400–4000 cm-1 with a resolution of 2 cm-1 after 128 scans.

The AFM images of the surface of the yttrium vanadate films on the KDB-12 (100) silicon substrate are shown in Fig.1, 2. Using the atomic force microscopy method, it is found that deposition of the films on the silicon substrate results in the formation of a developed surface with a droplet phase of various sizes. The lateral size of large droplets on the film surface ranges from 0.5 to 2.5 microns (Fig. 1a, b), whith the height of the droplets not exceeding 350 nm. The fraction of the large droplet phase is found to be 2% of the total surface area of the films. The YVO4 film consists of fine particles with a lateral size from 20 to 250 nm (Fig. 2), while the average height difference does not exceed 50 nm and the average arithmetic roughness is 17 nm.

The transmission (a) and reflection (b) spectra of the yttrium vanadate film on a silicon substrate in the visible and near-infrared regions are shown in Fig. 3. The transmission reaches 2.9% at a wavelength of λ = 1192 nm and decreases to T = 2.1% at λ = 2793 nm. In the reflection spectrum, two minima (R1min = 11.2% at 242 nm and R2min = 1.2 % at 603 nm) and one maximum R1max = 41% at 358 nm are observed.

The luminescence (1) and luminescence excitation (2) spectra of the YVO4 film on silicon are shown in Fig. 4, a. The wavelength of luminescence excitation is 350 nm, and the maxima in the luminescence spectrum are located in the region

between 413 and 438 nm, which is most likely due to the introduction of yttrium or its complex with oxygen.

The volt-ampere characteristics (VAC) of the studied films on the silicon substrate are shown in Fig. 4, b. The photoelectric effect of the YVO4/Si structures is observed at both the negative polarity of the voltage at the YVO4 and the action of laser radiation at 450 nm and 905 nm wavelengths (at the voltage offset of more than -15 V). At other wavelengths of laser radiation, the photoelectric effect is insignificant.

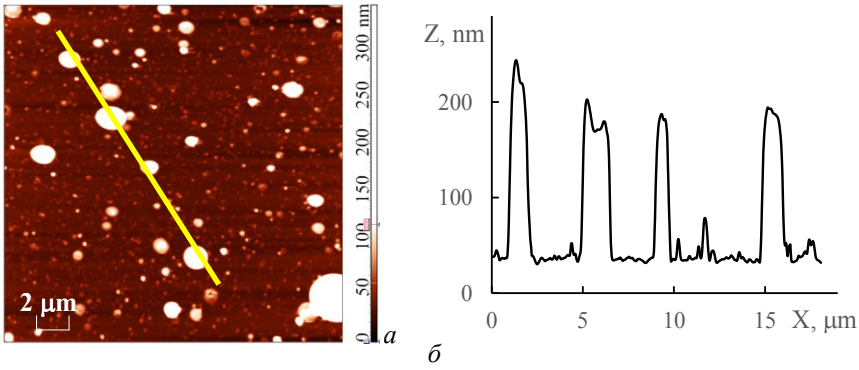

Figure 1: Surface morphology (a) and a cross-section profile along the selected line (b) of the laser-deposited thin film of yttrium vanadate on silicon.

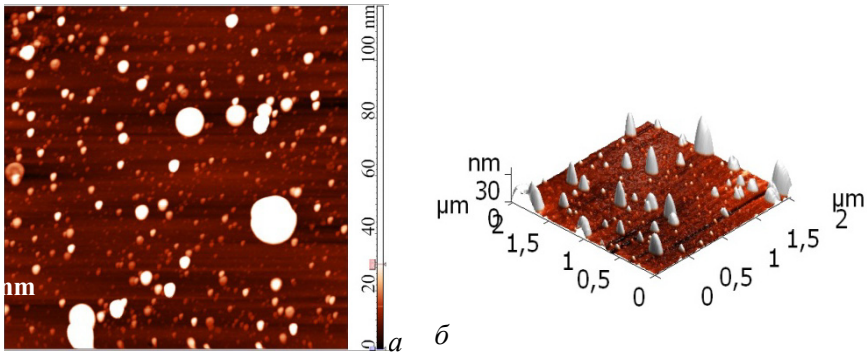

Figure 2: AFM images of the surface of yttrium vanadate thin film on silicon.

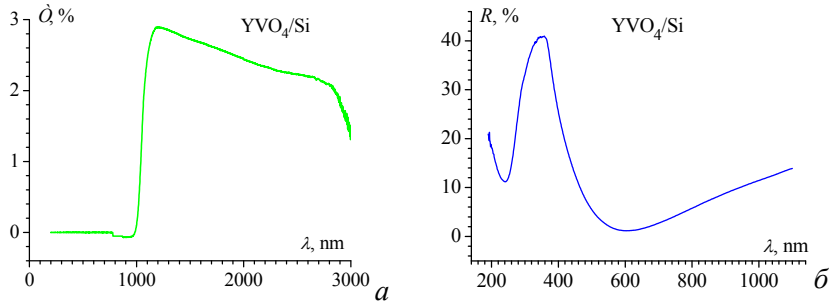

Figure 3: Transmission (a) and reflection (b) spectra of the yttrium vanadate film in the visible and near-infrared regions.

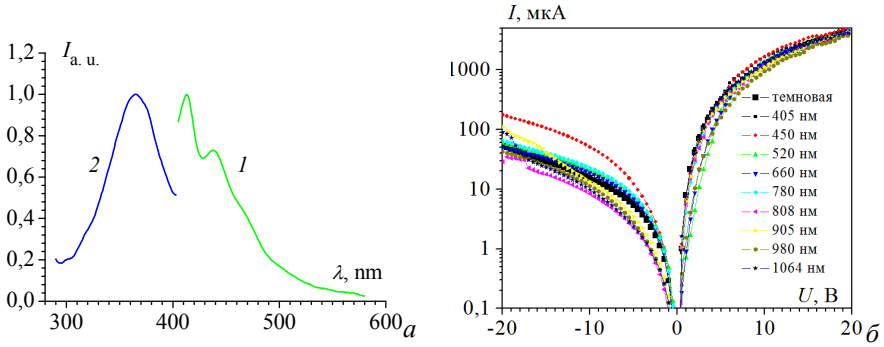

Figure 4: Spectra of luminescence (1) and luminescence excitation (2) of the YVO4 film on the silicon substrate (a). Volt-ampere characteristic of the yttrium vanadate thin film (b).

3. CONCLUSIONS

Films of yttrium vanadate oxide on a silicon substrate are obtained using high-frequency pulsed laser deposition and studied by different methods. The obtained films are characterized by both a finely dispersed structure with an average roughness of 50 nm and the presence of an insignificant number of large particles on the surface with a lateral size from 0.5 to 2.5 microns. Two minima are observed in the reflection spectrum (R1min = 11.2% at λ = 242 nm and R2min = 1.2 % at λ = 603 nm) and one maximum R1max = 41% at λ = 358 nm. At the wavelength of luminescence excitation, λ = 350 nm, the observed maxima in the luminescence spectrum are located in the region between 413 and 438 nm. The photoelectric effect and photoluminescence are caused by the introduction of yttrium or its complexes with oxygen into the film.

References

Nagovitsyn, I. A., Chudinova, G. K., Zubov, A. I., Zavedeev, E. V., Tairov, Yu. M., Moshnikov, V. A., Kononova, I. E., Kurilkin, V. V. : 2016, *Chemical Physics*, **35,** 55.
Minko, L. Ya., Chumakov, A. N., Bosak, N. A. : 1990, *Quantum Electronics*, **17,** 1480.

Publ. Astron. Obs. Belgrade No. 102 (2022), 87 - 90 *Contributed Paper*

FEATURES OF SILICON ABLATION IN AIR UNDER THE INFLUENCE OF ND:YAG LASER HARMONICS

A. N. CHUMAKOV, V. V. LYCHKOVSKY and I. S. NIKONCHUK

B.I. Stepanov Institute of Physics of the National Academy of Sciences of Belarus, 220072, Minsk, Independence ave., 68-2
E-mail a.chumakov@dragon.bas-net.by

Abstract. Ablation of silicon sample in air under irradiance of single and double laser pulses with wavelengths 355 and 532 nm was studied by means of optical and scanning electron microscopy, as well as video registration of plasma's plume radiation in time. Dependence of specific sample's material removal on laser fluence and time interval between coupled pulses of bichromatic laser irradiance was established.

1. INTRODUCTION

Since silicon is used widely in microelectronics, laser treatment of silicon wafers has been studied extensively in recent years to determine efficient treatment regimes. The absorption coefficient of silicon increases by three orders of magnitude as the irradiation wavelength decreases from 1064 to 266 nm. Therefore, laser treatment of silicon may be made more efficient if one uses the 2nd, 3rd, or 4^{th} harmonics of radiation of a Nd : YAG laser / see Liu H.C. et al. 1999, Yoo J.H. et al. 2000, Panzner M. et al. 2002 /. The aim of the work was to determine the features of laser ablation of silicon in atmospheric air when it was irradiated with nanosecond pulses of monochromatic and bichromatic radiation with wavelengths of 355 and 532 nm in a wide range of parameters and to identify the modes of effective specific mass removal and the formation of erosive plasma.

The use of coupled LR pulses (especially those that differ in wavelength) with an adjustable time interval and sequence order should provide an opportunity to enhance considerably the efficiency of ablation of materials, heating of ablation plasma, and generation of shock waves / see Min'ko L.Ya. et al.: 1990, Chumakov A.N. et al.: 2014, 2017 /. Double-pulse bichromatic laser treatment offers more degrees of freedom for control over the process of laser ablation of materials differing in their thermophysical and optical characteristics. However, it still remains understudied. The aim of the present study is to determine the specific features of laser ablation of silicon in atmospheric air irradiated with nanosecond

monochromatic and bichromatic (355 and 532 nm) LR pulses in a wide range of parameters and identify the regimes of efficient specific mass removal and production of near-surface plasma.

2. EXPERIMENTAL SETUP AND MEASUREMENT TECHNIQUES

The setup was constructed based on two Nd : YAG lasers LH−2132 and LH−2137 (OOO ”LOTIS TII“, Minsk) and a synchronization system for generation of paired nanosecond LR pulses with wavelengths of 355 and 532 nm and durations of 18 and 15 ns, respectively. The sequence order and the time interval between pulses could be adjusted. The shape of the laser pulses was measured with a 11HSP-V2 (Standa) photodetector and Wave Surfer 510R digital oscilloscope. The energy of laser pulses was monitored using an Ophir instrument with a PE25BF-DIF-V2 ROHS measurement head. A coaxial beam of radiation of both lasers was formed using a spectrum splitter and focused with an achromatic lens (f = 150 mm) on the surface of a silicon wafer into a spot with diameter of ~200 microns. The targets were (111) silicon wafers with a thickness of 180 μm.

The specific mass removal was determined experimentally based on the volume of a through hole in a silicon wafer with a thickness of 180 μm, which was made by a countable number of laser pulses, with the known density of silicon (2.33 g/cm^3) and the measured total energy of laser pulses taken into account. In the case of doublepulse bichromatic treatment, the specific mass removal was determined at different time intervals between laser pulses falling within the range from −40 to +40 μs (negative intervals correspond to pulse sequences in which the shortwave laser pulse came first). The surface of irradiated samples was examined with a TESCAN VEGA 3 (TESCAN, Czech Republic) scanning electron microscope. The ablation laser plume was recorded with a video camera / see Nikonchuk I.S. et al: 2016 / featuring an ICX415AL CCD sensor. Emission spectra of laser-induced plasma were recorded using the SL40-2 spectrometer (SOL instruments).

3. RESULTS AND DISCUSSION

It should be noted that silicon ablation was observed at the following threshold values of LR power density: $Q_{355} \sim 1.7$ J/cm^2 for 355 nm and $Q_{532} \sim 2.5$ J/cm^2 for 532 nm. The results of examination of the specific mass removal of silicon in different regimes of monochromatic LR treatment and irradiation with paired bichromatic radiation pulses with wavelengths of 532 and 355 nm are presented in Fig. 1. The obtained results revealed the nonlinear nature of dependences of the specific mass removal of silicon on the power density of the irradiating monochromatic LR with wavelengths of 532 and 355 nm within the interval from 0.1 to 5 GW/cm^2 (Fig. 1, *a*). The nonlinear nature of the experimental dependences of the specific mass removal on the radiation intensity q at both wavelengths indicates a change in the mechanism of silicon ablation. Thus, at $q_{355} \sim 1$ GW/cm^2 (curve 1, λ = 355 nm,), the decline in the efficiency of specific mass removal is

replaced by its sharp increase with subsequent saturation. At the same time, the formation of a through hole in a silicon wafer was characterized by the signs of brittle fracture with spallation of individual fragments on its back side.

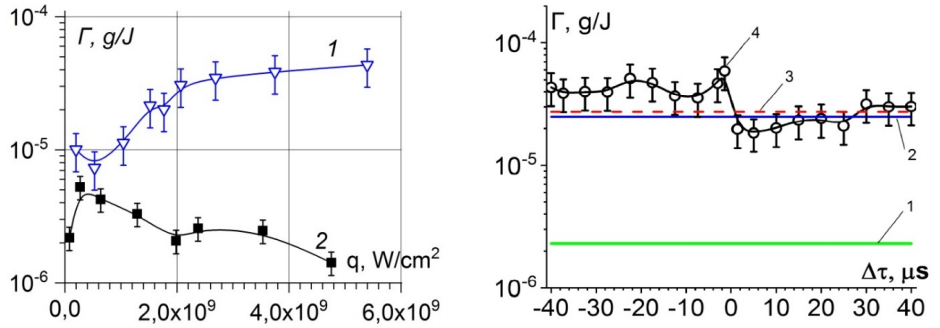

a b

Figure 1: Dependences of the specific mass removal of silicon: *a* – on the power density of LR with wavelengths of 355 (*1*) and 532 nm (*2*); *b* – on the time interval within bichromatic LR pulses with power density q_{355} = 1.9 and q_{532} = 3.5 GW/cm^2 (*1* – λ = 532, *2* – λ = 355, *3* – estimate of the overall effect of LR at both wavelengths; *4* – irradiation with bichromatic LR pulses (negative time intervals correspond to pulse sequences in which the 355-nm pulse came first))

A similar pattern was observed under the influence of LI 532 nm (curve 2), while the transition from a decline to a local increase in mass removal occurred at q_{532} = 2 GW/cm^2. Probably, in the first sections of the curves (up to the intensities of 1 and 2 GW/cm2 for λ = 355 and 532 nm, respectively), the melting-evaporation mode is implemented, and at q > 2 GW/cm^2, brittle fracture with spallation is added.

The specific mass removal was also examined under irradiation of silicon in air with paired bichromactic LR pulses with wavelengths of 355 and 532 nm. The dependence of mass removal on the time interval between paired pulses and their sequence order was studied for a number of regimes. A typical dependence of this kind is presented in Fig. 1, *b*. This dependence is also nonlinear. If the shortwave LR pulse came first (i.e, the time interval is negative), specific mass removal *4* is 2−3 times higher than overall removal *3* in the case of monochromatic irradiation at both wavelengths. The maximum values of specific mass removal are achieved at interpulse intervals $\Delta\tau$ = −20 and −1.3 μs. In the region of positive time intervals between laser pulses, specific mass removal *4* generally remains lower than overall removal *3* and exceeds it somewhat only at intervals from +30 to +40 μs.

The identified differences between the dependences of specific mass removal of silicon on the power density of incident radiation at the examined wavelengths correspond to the observed features of dynamics of the plasma plume (Figs. 2).

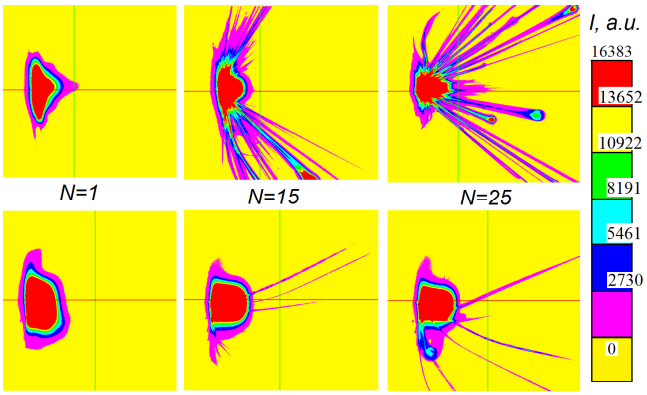

Figure 2**:** Individual still images of the plasma plume corresponding to the irradiation of silicon in air with the 1st, the 15th, and the 25th laser pulses in a series with a wavelength of 355 (*a*) and 532 nm (*b*)

Specifically, intense ejection of particles of the condensed phase, which continues well after the disintegration of the plasma plume, is observed on exposure of silicon to LR with λ = 355 nm, while LR with λ = 532 nm produces a glowing plasma plume with weakly pronounced ejection of particles of the condensed phase.

4. CONCLUSIONS

The nonlinear dependence of the specific mass removal of silicon on the power density of the acting laser radiation, the time interval and sequence order of bichromatic nanosecond laser pulses with wavelengths of 355 and 532 nm and a power density from 0.2 to 5 GW/cm2 has been revealed. An increase in the efficiency of silicon ablation under the influence of bichromatic laser pulses has been established.

Acknowledgments

This work was supported by the state scientific research program of the Republic of Belarus “Convergence — 2025” (subprogram “Microworld, Plasma and the Universe” 2.2.02.1).

References

Chumakov, A.N. et al.: 2014, *High Temp. Mater. Processes,* **18** (4), 269.
Chumakov, A.N. et al.: 2017, *J. Appl. Spectr.,* **84**, 620.
Liu, H.C. et al.: 1999, *Spectrochim. Acta, Part B*, **54** (11), 1607.
Min’ko, L.Ya. et al.: 1990, *Sov. J. Quantum Electron.,* **20** (11), 1389.
Nikonchuk, I.S. et al.: 2016, *J. Phys.: Conf. Ser.,* **666**, 012021.
Panzner M. et al.: 2002, *Proc. SPIE,* **4637**, 496.
Yoo J.H., et al.: 2000, J. Appl. Phys., **88** (3), 1638

Publ. Astron. Obs. Belgrade No. 102 (2022), 91 - 94 *Contributed Paper*

SILICON SPALLING DESTRUCTION AND ABLATION IN AIR UNDER BICHROMATIC LASER RADIATION

A. N. CHUMAKOV, V. V. LUCHKOUSKI and I. S. NIKONCHUK

B.I. Stepanov Institute of Physics of the NASB,
68-2 Nezavisimosti Ave., Minsk, 220072 Belarus,
E-mail i.nikanchuk@ifanbel.bas-net.by

Abstract. The ablation of silicon in air under one- and two-pulse nanosecond laser irradiation with wavelengths of 355 and 532 nm is studied experimentally. The specific mass removal, the spectra of the near-surface plasma, and the microstructure of the surface of irradiated targets are investigated depending on the power density of the laser radiation and the time interval between laser pulses. The features of ablation and spalling destruction of irradiated silicon planar targets, as well as the formation of near-surface plasma, have been established.

1. INTRODUCTION

The laser effect on silicon wafers is being actively investigated to identify effective modes of their modification and processing due to the widespread use of silicon in microelectronics /see Yoo J.H. et al. 2000, Bonse J. et al. 2002, Bovatsek J.M. et al. 2010, Galasso G. et al. 2015/. Researchers associate the mass removal from the silicon surface under nanosecond laser action with the process of explosive boiling /see Yoo J.H. et al. 2000, Bovatsek J.M. et al. 2010, Galasso G. et al. 2015/. Femtosecond laser exposure to silicon revealed amorphization, melting, crystallization, evaporation, ablation and the formation of periodic structures /see Bonse J. et al. 2002/. It is shown that laser pulses shorter than 500 fs do not provide advantages for silicon processing. The results of laser exposure to materials depend on many parameters, including the wavelength of laser radiation. Therefore, the use of bichromatic laser radiation makes it possible to influence the efficiency of laser ablation of materials and the formation of near-surface plasma /see Chumakov A.N. et al. 2014/.

The purpose of this work was to determine the features of nanosecond bichromatic laser action on silicon in atmospheric air in a wide range of parameters and to identify the modes of effective specific mass removal and the formation of laser erosion plasma.

2. EXPERIMENTAL DETAILS

Experimental setup was based on two Nd:YAG lasers LH−2132 and LH−2137 (LOTIS TII, Belarus) and a synchronization system for generation of paired nanosecond laser pulses with wavelengths of 355 and 532 nm and durations of 18 and 15 ns, respectively. The sequence order and the time interval between pulses could be adjusted. The time profile of laser pulses was measured with a 11HSP-V2 (Standa) photodetector and a Teledyne Lecroy Wave Surfer 510R oscilloscope with a bandwidth of 1 GHz. The energy of laser pulses was monitored using an Ophir instrument with a PE25BF-DIF-V2 ROHS measurement probe. Emission spectra of laser-induced plasma were recorded using the SL40-2 spectrometer (SOL instruments, Belarus). A coaxial beam of radiation of both lasers was formed using a spectrum splitter and focused with an achromatic lens (f = 150 mm) on the surface of a silicon wafer. The diameter of spots of laser irradiation on the target was 200 μm for λ = 355 nm and 250 μm for λ = 532 nm. The surface of irradiated samples was examined with a TESCAN VEGA 3 (TESCAN, Czech Republic) scanning electron microscope. The profiles of laser craters on the surface of silicon were measured with an ACCRETECH Surfcom Crest DX-T profilometer with a resolution of 1 μm.

3. RESULTS AND ANALYSIS

In the case of bichromatic laser exposure, the specific mass removal of silicon and the intensity of the spectral lines of the near-surface plasma depend on the time interval between the pulses and the order of their sequence (Figures 1-2, negative values of the interval correspond to the advancing effect of radiation with λ=355 nm).

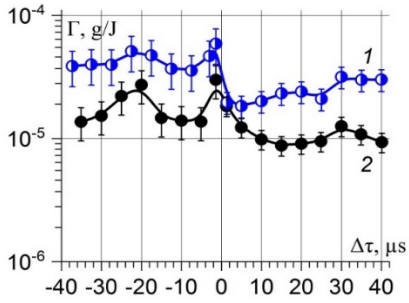

Figure 1: Dependences of the specific mass removal of silicon on the time interval within bichromatic laser pulses with power density q_{355} = 1.9 and q_{532} = 3.5 GW/cm^2 (1), q_{355} = 1.0 and q_{532} = 1.94 GW/cm^2 (2)

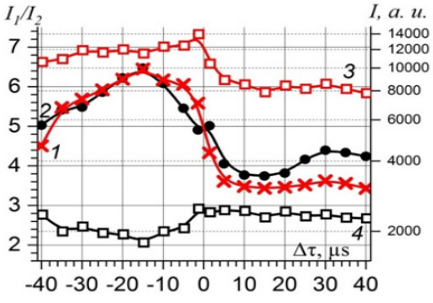

Figure 2: Ratio between the intensities of spectral lines Si II 412.9/N II 501.1 nm (1), Si II 412.9/Si I 288.2 nm (2), and dependences of the intensity of spectral line Si II 412.9 nm (3), N II 501.1 nm (4) on the time interval within bichromatic laser pulses with power density q_{355} = 1.9 and q_{532} = 3.5 GW/cm^2

Especially effective was the laser action with q_{355} = 1.9 GW/cm^2, q_{532} = 3.5 GW/cm^2 and q_{355} = 1 GW/cm^2, q_{532} = 1.94 GW/cm^2 (Figure 1). At the same time, the bichromatic laser effect was accompanied by a spalling destruction on the back side of the target /see Savenkov G.G. 2002/**.**

Local increasing of specific mass removal of silicon (Figure 1) at time intervals between laser pulses -20 μs, -3 μs and +30 μs correlated with an increase in the intensity ratio of the Si II spectral line (412.9 nm) to both the Si I atomic line (288.2 nm) and the nitrogen spectral line N II (501.1 nm). These data may indicate a significant heating of the destruction products from the first pulse by the second one, as well as an increase in the intensity of NII spectral lines in the region of positive intervals (Figure 2).

The experiments revealed that two pairs of bichromatic irradiating laser pulses did not induce spallation on the bottom side of the silicon wafer. Spallation in the indicated regime was observed only after irradiation with four or more pairs of bichromatic laser pulses.

Typical SEM images of ablation and spallation craters are shown in Fig. 3 for irradiation with four (Figs. 3, a and 3, b) and eight (Figs. 3, d and 3, e) pairs of pulses.

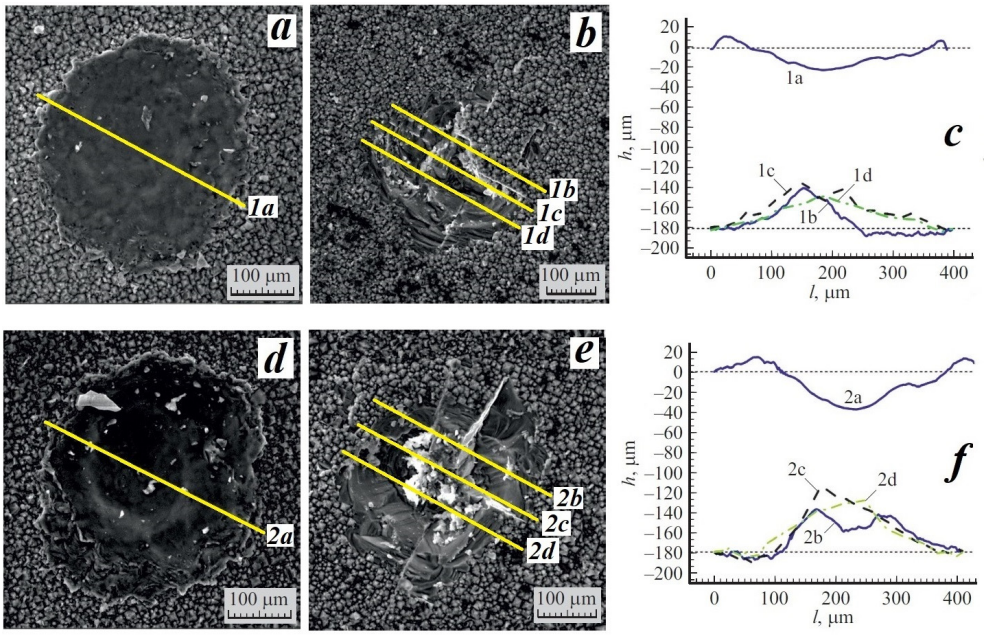

Figure 3: SEM images of ablation (a, d) and spallation (b, e) craters and the corresponding profiles (c, f), formed as a result of irradiation with four (a−c) and eight pairs (d−f) of laser pulses with wavelengths of 355 and 532 nm (treatment parameters: q_{355} = 1.9 GW/cm^2, q_{532} = 3.5 GW/cm^2, $\Delta\tau$ = −3 μs).

The results of measurement of their profiles are also presented (Figure 3, c, f). The difference in shape between ablation and spallation craters stands out. The typical shape of ablation craters is that of a sphere segment, while spallation craters have an irregular shape (formed by several partial spalls) with a roughly triangular profile.

It should be noted that the maximum depth of spallation craters is 1.5−2 times higher than the maximum depth of ablation ones. This suggests that spallation produces a significant contribution to the specific mass removal in the process of drilling of through holes in the indicated treatment regimes.

The analysis of the profiles of laser ablation and spallation craters on the surfaces of silicon wafers (Figure 3) showed that the phenomenon of spalling destruction under bichromatic laser exposure occurs before the formation of a through hole, and the depth of the ablation and spallation craters increases with the number of pairs of impacting pulses.

Such phenomenon was not observed with monochromatic exposure of laser radiation with wavelength of 532 nm, but when exposed to radiation of 355 nm, the spalling destruction was observed only with a large number of acting laser pulses (more than 20).

4. CONCLUSIONS

Laser spalling destruction and ablation of silicon in air has been experimentally investigated and the nonlinear dependence of the specific mass and intensity of spectral lines of near-surface plasma on the laser radiation power density, time interval and sequence order of bichromatic nanosecond laser pulses with wavelengths of 355 and 532 nm and radiation power density from 0.2 to 3.5 GW/cm^2 has been revealed.

The features of ablative and spalling destruction of irradiated flat silicon targets, which are amplified by the action of paired bichromatic laser pulses on silicon, are established.

Acknowledgments

This work was supported by the state scientific research program of the Republic of Belarus “Convergence — 2025” (subprogram “Microworld, Plasma and the Universe” 2.2.02.1).

References

Bonse J., Baudach S. et al.: 2002, *Applied Physics A*, **74**, 19–25.
Bovatsek James M. et al.:2010, *Proc. SPIE* **7585**, 75850K.
Chumakov A.N., et al.:2014, *High Temp. Material Proces*., **18**(4), 269-272.
Galasso G., et al.: 2015, *J. of Applied Physics*, **117**, 123101.
Savenkov G.G.: 2002, *Zh. Tekh. Fiz*., **72**, No. 12, 44–48 (in russian)
Yoo J.H., Jeong S.H., Greif R. et al.: 2000, *J. of Applied Physics*, **88**, 1638.

Publ. Astron. Obs. Belgrade No. 102 (2022), 95 - 99 *Contributed Paper*

BOHMIAN DYNAMICS OF POSITRONS CHANNELED THROUGH A CHIRAL CARBON NANOTUBES

M. ĆOSIĆ[1], M. HADŽIJOJIĆ[1] and N. NEŠKOVIĆ[2]

[1]*Laboratory of Physics, "Vinča" Institute of Nuclear Sciences, National Institute of the Republic of Serbia, University of Belgrade, P. O. Box 522, 11001 Belgrade, Serbia*

[2]*World Academy of Art and Science, Napa, California, USA*

E-mail mcosic@vinca.rs

Abstract. The framework of the dynamical system theory was used for studying the dynamics of the quantum positron trajectories channeling through a chiral carbon nanotube. Obtained insight was used to explain the pattern-forming ability of the quantum self-interference.

1. INTRODUCTION

We shall analyze a dynamic of the quasi-parallel positron beam, of energy $E_k = 2$ MeV, transmitting through a chiral single-wall-carbon-nanotube (SWCNT) of chiral indices (11, 9). The circumference of this SWCNT consists of 602 atomic string pairs Saito et al. 1998. Consequently, positron-nanotube interaction potential is axially symmetric. If the linear momentum of the incoming positron is parallel to the SWCNT axis it will undergo through a series of correlated small-angle scatterings. As a result, longitudinally averaged SWCNT potential gently steers trajectories of these so-called *channeled* particles, Gemmell 1974.

Let us introduce Descartes's coordinate axis whose z-axis coincides with the SWCNT's axis. The $y = 0$ cross-section of the SWCNT potential is given by the following expression, (see Artru et al. 2005)

$$V(x) = \frac{8e^2R}{\sqrt{3}\varepsilon_0 l^2}\sum_{s=1}^{3}\alpha_s \begin{cases} I_0\left(\beta_s\dfrac{|x|}{a_{TF}}\right)K_0\left(\beta_s\dfrac{R}{a_{TF}}\right), & \text{for } |x| \le R, \\ K_0\left(\beta_s\dfrac{|x|}{a_{TF}}\right)I_0\left(\beta_s\dfrac{R}{a_{TF}}\right), & \text{for } |x| > R, \end{cases} \tag{1}$$

here e and ε_0 are elementary charge and vacuum permittivity, $R = 0.69$ nm and $l = 0.144$ nm are SWCNT's radius and C-C bond length (see Saito et al. 1998), α_s, β_s, and $a_{TF} = 0.0258$ nm are Molière's universal fitting parameters and

Thomas-Fermi's screening radius of C atom (see Molière 1947), while I_0 and K_0 are modified Bessel's functions of zeroth (Oliver 1972). Since potential $V(x)$ does not depend on the z coordinate, positron dynamics is effectively one-dimensional. Thus, classical trajectories $x(z)$ are solutions to the following Newton's equation

$$m_{\mathrm{p}} \frac{d^2x}{dz^2} = -\frac{1}{v_z^2} \partial_x V(x), \tag{2}$$

where m_{p} is positron's relativistic mass, v_z is its conserved longitudinal velocity. The maximal deflection angle of positron trajectory is given by the following expression $\Theta_c = \sqrt{V(R)/E_k}$ =8.8 mrad called the critical angle [Gemmell]. The quantum trajectories $x_{\mathrm{qu}}(z)$ were obtained in a two-step procedure. In the first step the corresponding Schrödinger equation

$$i\partial_z \psi(x,z) = -\frac{\hbar}{2m_p v_z} \partial_x^2 \psi(x,z) + \frac{1}{\hbar v_z} V(x) \psi(x,z), \tag{3}$$

was solved assuming Gaussian initial state

$$\psi_0(x) = \frac{\sigma_\theta^{1/2}}{(2\pi)^{1/4} \left(\hbar m_{\mathrm{p}} v_z\right)^{1/2}} \exp\left[-\frac{\sigma_\theta^2}{\hbar^2 m_p^2 v_z^2} x^2\right] \tag{4}$$

of very small angular divergence $\sigma_\theta = 0.01\Theta_c$. In the second step, the polar form of the wave function $\psi = \sqrt{\rho(x,z)} \exp\left[\frac{i}{\hbar} S(x,z)\right]$ was used to solve Bohm's equations of motion

$$\frac{\mathrm{d}}{\mathrm{d}z} x_{\mathrm{qu}}(z) = \frac{1}{m_{\mathrm{p}} v_z} \partial_x S\big(x_{\mathrm{qu}}(z), z\big), \tag{5}$$

and to calculate the quantum potential

$$Q(x,z) = -\frac{\hbar^2}{2m_{\mathrm{p}}} \frac{\partial_x^2 \sqrt{\rho(x,z)}}{\sqrt{\rho(x,z)}}. \tag{6}$$

In the end, the quantum dynamics was characterized using finite-length local Lyapunov's exponent defined by the following integral, see Ott 2002

$$\lambda_z\left(x_{\mathrm{qu}}(z)\right) = \frac{1}{m_{\mathrm{p}} z} \int_0^z \partial_x^2 S\big(x_{\mathrm{qu}}(z'), z'\big)\, dz'. \tag{7}$$

2. RESULTS

Figure 1 (a) shows the evolution of classical trajectories obtained by the numerical integration of Eq. (2) using the Runge-Kutta method of the fourth-order elaborated in Press et al. 2007. The dynamics of shown trajectory family is regular since it is one-dimensional Ott 2002. Its nontrivial aspect is the appearance of the cusped caustic

lines labeled $c_1, \ldots c_4$. Caustics separate regions of the $y = 0$ plane whose positron multiplicity locally differs by two see Arnol'd 2004. Thus, positron density is infinite along caustics which dominantly determine the shape of the spatial positron yield.

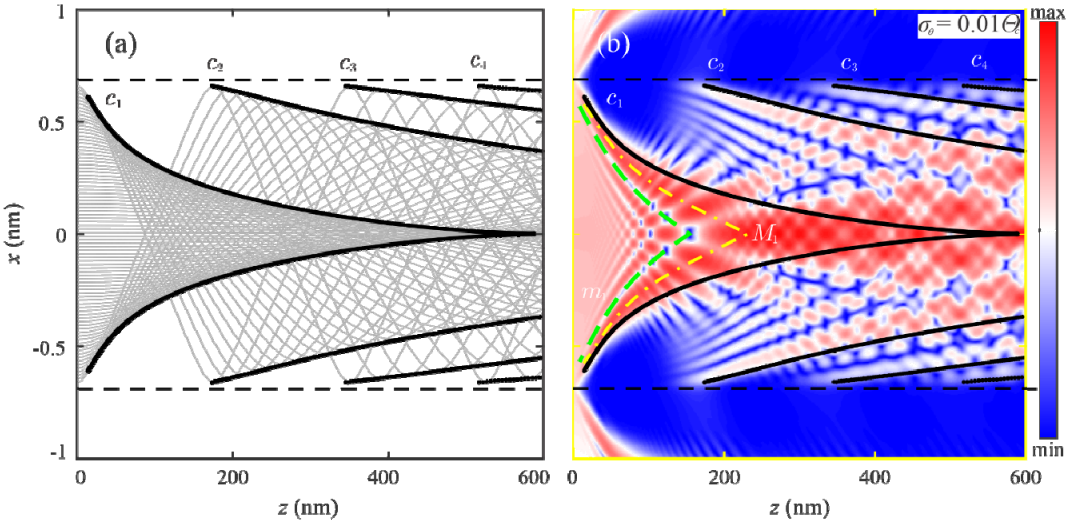

Figure 1: (a) Classical trajectories initially representing parallel beam. (b) Evolution of the quantum positron probability density initially representing quasi-parallel beam. Values of the probability density are color-coded according to the shown colormap. Dashed black lines indicate SWCNT walls. Thick black lines show the classical caustic lines $c_1, \ldots c_4$. The cusped dashed green line and dot-dash yellow lines show lines of dominant maxima and minima M_1 m_1 associated with the caustic c_1.

Figure 1 (b) shows the evolution of the corresponding quantum state obtained by numerical integration of Eq. (3) using Chebyshev's global propagation method, details are in Ćosić et al. 2014. Note accumulation of the probability density on the caustic's side of higher multiplicity see Ćosić et al. 2016. Since total probability is conserved, it cannot have singular maxima. Instead, quantum self-interference creates alternating lines composed of local extrema running "parallel" to the caustics. For simplicity, in Fig. 1(b) only dominant lines labeled $m_1$and M_1 associated with caustic c_1 are specially designated.

The obtained numerical solution enables the study of quantum dynamics in all of its details. However, using it alone, it is very difficult to understand the wave packet's pattern-forming ability. To gain additional insight scientists are often recoursing to the semiclassical approximation, which associates a primitive wave to each classical trajectory, thus reducing every physical effect to the interference of waves arriving at the same location (Berry 1972). Although simple, this approach has several drawbacks. It is difficult to understand pattern formation in regions with no classical trajectories or interference of real and evanescent waves

visible in the region between caustic lines c_1 and c_2 in Fig. 1(b). It cannot be applied in circumstances when positron's de Broglie's wavelength is not negligible, nor when dynamics of the underlying classical system is not regular (Berry 1972).

We shall demonstrate an alternative approach designed to transcend the limitations of the semiclassical approximation. It is known that Bohm's quantum trajectories are always defined and contain the same information as quantum state ψ. Therefore, it is natural to analyze quantum trajectories from the standpoint of the dynamical systems theory and connect it to the wave packet's local focusing generated by the self-interference.

For simplicity, Fig 2(a) shows a subfamily of quantum trajectories occupying the region close to the SWCNT axis, obtained by the numerical integration of Eq. (5) using the Runge-Kutta method of the fourth-order (Press et al. 2007). This Fig. shows that only a few trajectories run across the classical caustic c_1 which represents also a virtual barrier for the quantum trajectories. Note that lines m_1 and M_1 connect together regions repelling and attracting neighboring trajectories the most strongly. Inspection of the quantum potential (6) along the lines m_1 and M_1 reveled that it has very large negative values in the vicinity of the minima while it has moderate values in the vicinity of the maxima. Therefore, the quantum potential is respon-

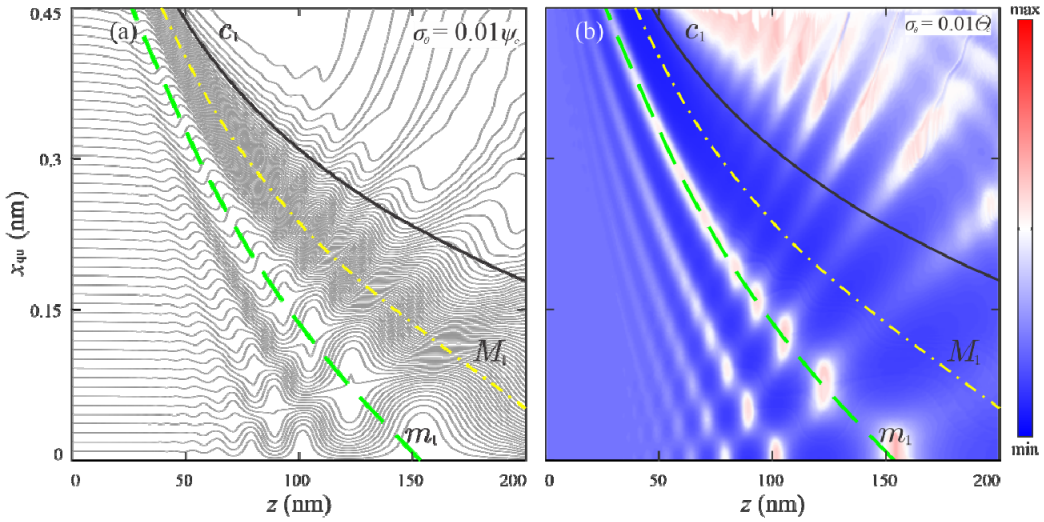

Figure 2: (a) Evolution of the representative subset of the quantum trajectories corresponding to the quantum state shown in Fig. 1 (b). (b) The corresponding distribution of the local finite length Lapunov's exponents. Negative values of the exponents are indicated by different tones of the blue color while positive values are indicated by different tones of the red color. Thich black line shows the classical caustic c_1, while dashed green and dot-dash yellow lines show dominant lines of minima and maxima, m_1 and M_1 respectively associated with caustic c_1.

sible for the creation of regions of strong local repletion of trajectories called repeltors, which explains the exitance of the local destructive self-interference. In this framework, local constructive self-interference is also generated by the action of local repeltors because of the conservation of the total probability.

To characterize the strength of introduced repeltors we have calculated the distribution of the finite-length local Lyapunov's exponents calculated using trapezoidal quadrature (see Press et al. 2007). Figure 2(b) reveals that only some minima are sufficiently low to generate positive islands of Lyapunov's exponents. Closer inspection has confirmed that only those minima have a noticeable influence on the neighboring trajectories. Their basins of repulsion are defined as a zero-level line of Lyapunov's exponent surrounding its positive local maxima.

Since local self-interference is a generic process it can be argued that local repeltors will always appear. Each quantum trajectory can be designated by a list of repeltors it encounters in its evolution. Since in this case evolution of the quantum state is aperiodic evolution of quantum trajectories cannot be periodic. This means that for most trajectories list of encountered repeltors is infinite and aperiodic which according to the information theory has a positive information gain (see Ott 2002) which makes dynamics of Bohmian trajectories in chiral SWCNT weakly complex.

References

Arnol'd, V. I.: 2004, *Catastrophe Theory*, second edition, Berlin: Springer-Verlag.

Artru, X., Fominb, S. P., Shul'ga, N. F., Ispirian, K. A., and Zhevago, N.K.: 2005, *Phys. Rep*. **412**, 89

Berry, M. V., Mount, K.E.: 1972, *Semiclassical approximations in wave mechanics*, Rep. Prog. Phys. **35**, 315.

Ćosić, M., Petrović, S., and Nešković, N.: 2014, *Computational method for the long time propagation of quantum channeled particles in crystals and carbon nanotubes*, Nucl. Instrum. Methods Phys. Res. B, **330**, 33.

Ćosić, M., Petrović, S., and Nešković, N.: 2016, *Quantum primary rainbows in transmission of positrons through very short carbon nanotubes*, Nucl. Instrum. Methods Phys. Res. B, **373**, 52.

Gemmell, D. S.: 1974, Rev. Mod. Phys., **46**, 1.

Molière, G.: 1947, *Z. Naturforschg.*, **2a,** 133

Olver F. W. J.: 1972, 9. *Bessel Functions of Integer Order*, Chap. 9, p. 355 in *Handbook of Mathematical Functions,* edited by Abramowitz, M., and Stegun, I. A., tenth edition, Washington, D.C: National Bureau of Standards.

Ott, E.: 2002, *Chaos in dynamical systems*, second edition, Cambridge: Cambridge University Press.

Press, W. H., Teukolsky, S. A., Vetterling, W. T., and Flannery, B. P.: 2007 *Numerical Recipes*, third edition, Cambridge: Cambridge University Press.

Saito R., Dresselhaus G., and Dresselhaus M. S.: 1998, *Physical Properties of Carbon Nanotubes*, Singapore: Imperial College Press.

Publ. Astron. Obs. Belgrade No. 102 (2022), 101 - 104 *Contributed Paper*

ANALYTICAL PREDICTION AND NUMERICAL ANALYSIS OF PLASMA MEDIATED ABLATION OF SKIN TISSUE SAMPLES WITH NANOSECOND-TO-FEMTOSECOND LASER PULSES

H. DELIBAŠIĆ MARKOVIĆ[1], V. PETROVIĆ[1] and I. PETROVIĆ[2]

[1]*Faculty of Science, Department of Physics, University of Kragujevac, Serbia*
E-mail hristina.delibasic@pmf.kg.ac.rs

[2]*Academy of Professional Studies Šumadija, Department in Kragujevac, Serbia*

Abstract. Based on the assumption initially developed by Jiao and Guo 2012, in this paper, we have introduced an analytical tool that performs analysis on the free-electron evolution (FEE) in plasma-mediated ablation of the skin tissue samples. Using the proposed calculations, the FEE can be determined in an excellent agreement with that resulting from (Jiao and Guo 2012) on the nanosecond time scale. However, the compatibility between the presented analytical approaches is not satisfactory for the ultrashort laser pulses. To eliminate such inconsistency, a simple modification to the rate equation for the free-electron density has been made when including the tunneling rate instead of the multiphoton rate. Our findings confirm that the results of the presented analytical models of both short and ultra-short laser ionization process in skin tissues may have direct biomedical applications based on the use of various pulses.

1. INTRODUCTION

Throughout the past few decades, lasers have found their way into many areas of medicine and biology, with a variety of applications ranging from basic research to clinical trials (Ilina and Sitnikov 2021). While keeping up with medical advancements in the field, a theoretical understanding of laser-tissue interaction mechanisms using short and ultrashort pulsed lasers became increasingly important. As a consequence, a few models have been proposed to explain distinct laser ablation mechanisms (Ravi–Kumar et al. 2019; Zheng and Shen 2022). Among different approaches, the plasma-mediated ablation approach presented by Noack and Vogel 1999 has been most commonly used to explain the laser-induced breakdown (LIB) phenomenon while considering the case when the plasma is induced by a strong electromagnetic field. However, a small percentage of investigators remain focused on determining the "breakdown threshold" in terms of finding an exact analytical solution to calculate a critical number of free electrons generated within the laser-tissue interaction region.

The difficulties in answering questions about the optical breakdown structure for the ablation of skin tissue have been attributed to the complex nature of the processes, which are dependent on both the laser properties, as well as the time-dependent plasma–particle interaction processes. In order to shed more light on the LIB phenomenon, a temporal model for examining the breakdown threshold and form of laser-induced plasma (LIP) in skin tissue samples is developed by revising the general form of the well-known rate equation (Noack and Vogel 1999) and simultaneously, accounting for the tunneling, multiphoton, cascade, thermal, and chromophore ionization influences on short and ultrashort laser pulse propagation. Besides, electron loss processes due to diffusion out of the focal volume and recombination were also investigated. In this study, plasma-mediated ablation is postulated as two distinct processes during different time stages: *(i)* multiphoton and cascade ionization operated in the short-range pulse regime and *(ii)* tunneling and cascade ionization while observing ultrashort events. The rate equation for each stage is solved analytically. The conditions under which different ionization mechanisms occur and prevail in the plasma-mediated laser ablation process are validated using developed analytical models in combination with available experimental findings and numerical modeling. The presented approach is further extended to investigate the temperature evolution in the focal volume and threshold intensity dependence on laser pulse duration.

2. MODEL DESCRIPTION

The skin tissue is composed of multiple layers containing distinct cellular populations, making it challenging to understand the processes that occur under the interaction of laser with skin. According to (Rogov et al. 2014), water (70%) is the predominant constituent of the skin, which is why, in a first approximation, the human skin tissue can be thought of as a water-like tissue media. This phenomenon has attracted wide attention for its significance in the fundamental research on laser-matter interaction and as a baseline model for studying the ablation of skin tissues. The primary mechanism of optical ablation in the present work is plasma-induced ablation during short and ultrashort pulses, hence describing the process demands taking into account a variety of ionization processes.

This paper is comprised of two major subsystems:

1. *The free-electron density*. Photoionization (PI) mechanisms (that are predominantly in the tunneling (TI) or in the multiphoton (MPI) regimes), cascade ionization (CI), thermal ionization (TI), chromophore ionization (ChI) and free-electron absorption (FEA) may all be triggered depending on the intensity of the incident radiation. Phenomena that generate free-electrons are namely MPI, TI and CI. The free electron density will be reduced by recombination effects as well as free carrier diffusion.
2. *The free-electron temperature.* The absorbed laser energy will first be stored in the free-electrons before it is transferred via electron-phonon scattering events. The density in the free electron subsystem can be denoted as the sum of the kinetic energy and bandgap energy per unit of volume. Energy

transfer is herewith described by the well-known two-temperature model (Uehlein et al. 2022), which is derived under the assumption that electron and phonon energy transport is described by the classical Fourier law.

3. RESULTS

The solution of the free-electron density rate equation could provide insight into the differences between the breakdown mechanisms at different pulse durations. To discuss these differences, Figure 1(a) displays the comparison of the free-electron density between the analytical and numerical predictions for ablation in the skin tissue sample, while Figure 1(b) shows the evolution of the free-electron density for laser pulses of different duration.

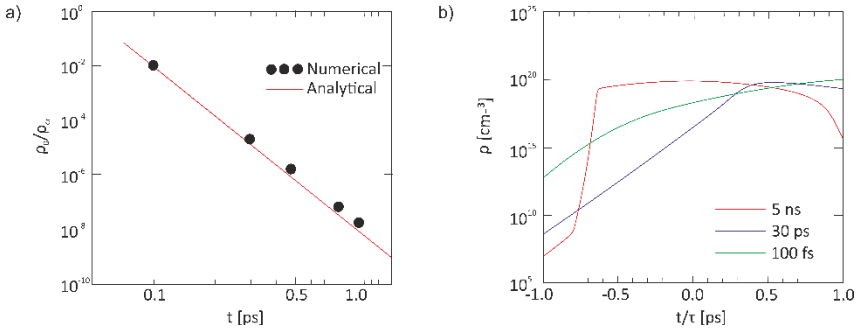

Figure 1: (a) Comparison of the free-electron density between the analytical and numerical predictions, (b) evolution of the free-electron density at threshold irradiance for laser pulses of different durations. All curves were calculated for $\lambda = 532$ nm.

Table 1 lists the irradiance thresholds for optical breakdown in skin tissue for wavelengths of 532 nm and 355 nm, and pulse durations of 5 ns, 30 ps and 100 fs.

Pulse duration	ρ_{cr} [cm^{-3}]	I_{th} [10^{11} Wcm^{-2}]	
		355 nm	532 nm
5 ns	10^{20}	1.2	0.5
30 ps	10^{21}	7.8	3.7
100 fs	10^{21}	68.5	80.5

Table 1: Calculated irradiance thresholds I_{th} for LIB in skin tissue. The values chosen for ρ_{cr} yielded the best agreement between calculated and experimental findings.

4. CONCLUSION

We derived analytical solutions for the free-electron evolution of skin tissue media based on the postulate developed in (Jiao and Guo 2012). The theoretical model is validated via comparisons with the available experimental findings of the ablation threshold in skin tissue samples. A complete numerical model with all the ionization and loss mechanisms is also employed in the comparison to verify the conditions when CI prevails in the plasma-mediated laser ablation process. The proposed model is useful for ablation with both short and ultrashort pulses.

Acknowledgements

This work was supported by the RS MESTD, Project No. OI 171020, and COST Action CA17126 “Towards understanding and modelling intense electronic excitation”.

References

Ilina, I. and Sitnikov, D., 2021: *Diagnostics,* **11**(10), 1897.
Jiao, J. and Guo, Z.: 2012, *Appl. Surf. Sci.*, **258**(17), 6266-6271.
Noack, J. and Vogel, A., 1999: *IEEE J Quantum Electron*, **35**(8), 1156-1167.
Ravi–Kumar, S., Lies, B., Zhang, X., Lyu, H. and Qin, H., 2019: *Polym Int*, **68**(8), 1391-1401.
Rogov, P. U., Smirnov, S. V., Semenova, V. A., Melnik, M. V. and Bespalov, V. G. : 2016, *J. Phys. Conf. Ser.*, **737**(1), 012047.
Uehlein, M., Weber, S.T. and Rethfeld, B., 2021: arXiv preprint arXiv:2112.01851.
Zheng, C. and Shen, H., 2022: *J Manuf Process*, **73**, 354-363.

Publ. Astron. Obs. Belgrade No. 74 (2022), 105 - 108 *Contributed Paper*

THE TIME-SYMMETRIC DESCRIPTION OF ELECTRON EXCHANGE IN ION-ION COLLISION

S. M. D. GALIJAŠ, V. M. MILOSAVLJEVIĆ and G. B. POPARIĆ
University of Belgrade, Faculty of Physics, P. O. Box 368, 11000 Belgrade, Serbia
E–mail galijas@ff.bg.ac.rs

Abstract. In this work we consider the process of one electron exchange between the Rydberg states of ions using two-wave-function (TWF) model. Investigation of atomic collision processes is very important for a detailed understanding of the elementary processes in plasma, especially in order to develop appropriate diagnostic methods of plasma fusion. The specific approach within the model imposes the use of two wave functions necessary for determining the transition probability and corresponding rates and finally estimating of the neutralization distances. We study the intermediate stages of the population of the Rydberg states of highly charged SiIV, PV and SVI ions escaping the targets ArVIII and KrVIII.

1. INTRODUCTION

We analyze one electron transfer into the Rydberg state of multiply charged projectile ion with core charge Z_A after collision with stationary multiply charged target ion with core charge Z_B (see Janev, R. K. 1986). A specific feature of the time-symmetric model under consideration is the description of representative electron transfer from ion B to ion A in two scenarios with two wave functions: $\Psi_B(\vec{r},t)$ and $\Psi_A(\vec{r},t)$.

For fixed initial $\Psi_{\nu_B=(n_B,l_B,m_B)}$ $(t = t_{in})$ and final states $\Psi_{\nu_A=(n_A,l_A,m_A)}$ $(t = t_{fin})$, by using the evolution operators $\hat{U}_B(t_1,t_2)$ and $\hat{U}_A(t_1,t_2)$, we are able to find evolution of the system, i.e. $\Psi_B(\vec{r},t) = \hat{U}_B(t_{in},t)\Psi_{\nu_B}$ and $\Psi_A(\vec{r},t) = \hat{U}_A(t_{fin},t)\Psi_{\nu_A}$, taking into account that the mentioned evolution operators are determined by Hamiltonians $\hat{H}_B$ and $\hat{H}_A$, respectively, which can be presented in the following form:

$$\hat{H}_B = -\frac{1}{2}\nabla^2 - \frac{Z_B}{r_B} + \sum_{l=0}^{\infty} \frac{c_{l_B}}{r_B^2}\hat{P}_l + \hat{U}_{B,A}, \tag{1}$$

$$\hat{H}_A = -\frac{1}{2}\nabla^2 - \frac{Z_A}{r_A} + \sum_{l=0}^{\infty} \frac{c_{l_A}}{r_A^2}\hat{P}_l + \hat{U}_{A,B}. \tag{2}$$

In both equations, the second and third terms are the potential energy of the electron in the field of polarized ionic core expressed over Simons-Bloch potential form in which the projection operator $\hat{P}_l$ onto the subspace of an orbital quantum number l are appears. On the other hand, by $\hat{U}_{B,A}$ and $\hat{U}_{A,B}$ we introduce the potential

energy of the electron due to the presence of ion A and B, respectively. At large distances between ions $R \gg 1$, it is justified to use approximations $\hat{U}_{B,A} = -Z_A/r_A$ and $\hat{U}_{A,B} = -Z_B/r_B$. Even more, in cases where the narrow cylindrical area around the ion trajectory is considered (the case of small values of angular momentum) which are the subject of this paper, a quite satisfactory approximation is given in the form $\hat{U}_{B(A)} \approx -Z_{A(B)}/R$.

Normalized transition probability $\tilde{T}_{\nu_B,\nu_A}(t) = T_{\nu_B,\nu_A}(t)/T_{\nu_B,\nu_A}^{t\to t_{fin}}$ and corresponding normalized rate $\tilde{\Gamma}_{\nu_B,\nu_A}(t) = d\tilde{T}_{\nu_B,\nu_A}(t)/dt$ can be obtained from mixed flux $I_{\nu_B,\nu_A}(t)$ (see Nedeljković et al. 2012.) by following expression:

$$T_{\nu_B,\nu_A}(t) = \left| \int_{t_{in}}^{t} I_{\nu_B,\nu_A}(t)dt \right|^2 , \tag{3}$$

whose analytical expression is given in the reference Galijaš et al. 2021, 2019. Finally, taking the position of the maximum of the normalized rate, it is possible to give an estimate of the partial neutralization distance under different conditions in which the appropriate system can be found.

2. RESULTS

In Fig. 1 we present normalized transition probability and corresponding rate for population of the high charged ion SVI ($n_A = 6, l_A = 0, m_A = 0$) escaping KrVIII ($n_B = 8, l_B = 0, m_B = 0$) for two different velocities a) $v = 3$ a.u. and b) $v = 7$ a.u. We point out that $\tilde{\gamma}_B$ and $\tilde{\gamma}_A$ are the most important parameters appearing in the mixed flux function $I_{\nu_B,\nu_A}(t)$ and are related to the values of the considered energy levels of ions and can be determined by spectroscopic measurements, see Ralchenko Yu. et al. 2007. Here we discussed only values corresponding to the ground state of the ionic cores. Comparing atomic collision processes under the same conditions but at different projectile ion velocities, it can be concluded that the significance of the value of the orbital angular momentum l_A decreases with increasing of the velocity in case of estimation of the most likely neutralization distances.

On the other hand, at a fixed value of the angular momentum $l_A = 0$, different ions with same paired electronic core configurations are considered: SiIV($n_A = 4$, solid curves), PV($n_A = 5$, dotted curves) and SVI($n_A = 6$, dashed curves) in a wider range of intermediate velocities v. It is obvious from Fig. 2a, that neutralization distances move towards higher values with increasing of core charge (with the same ratio Z/n) so that the difference is greater with increasing of relative ion-ion velocity. In order to compare, data for KrVIII($n_A = 8$, circles) and XeVIII($n_A = 8$, squares) taken from Ref. Galijaš et al. 2021., were entered on the graph.

Finally, Fig. 2b presents the normalized neutralization rates $\tilde{\Gamma}_{\nu_A}(t)$ (scaled by v) for PIII, PIV, PV ($n_A = 5, l_A = 0$) and for SIV, SV, SVI ($n_A = 6, l_A = 0$). As can be stated in both cases, ion-ion neutralization distance R_{ec} is significantly reduced in the case when in addition to the closed projectile ionic core $2p^6 3s^2$ we have electron capture in the far $^2S_{1/2}$ (Rydberg) empty shell. Moreover, at higher projectile velocities, this effect becomes even more pronounced.

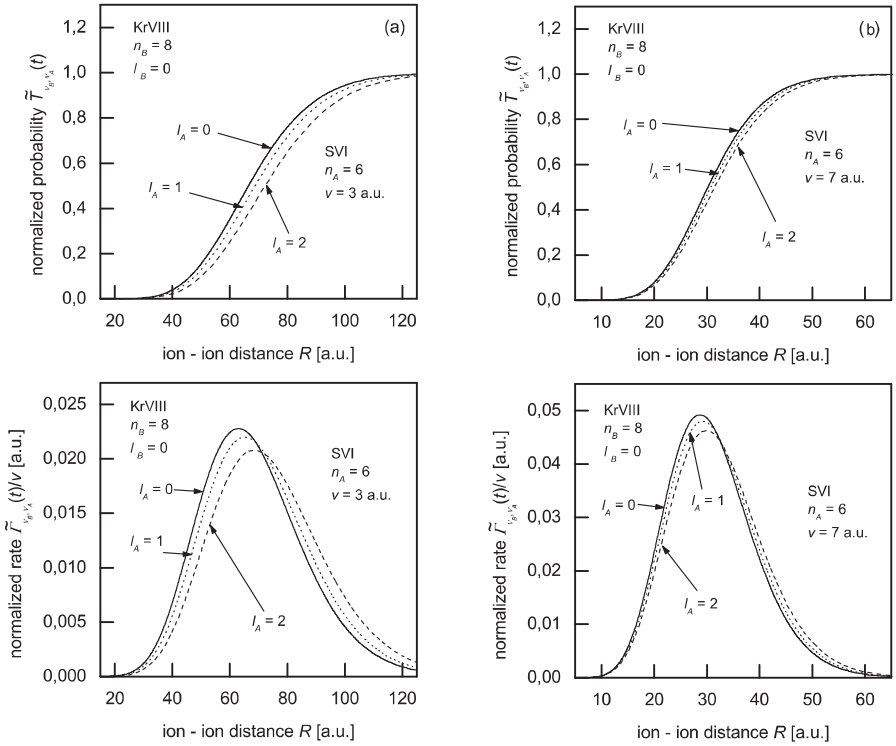

Figure 1: Population of the Rydberg levels of SVI ion for $n_A = 6$ and $l_A = 0, 1$ and 2. Normalized transition probabilities $\tilde{T}_{\nu_B,\nu_A}$ and corresponding normalized neutralization rates $\tilde{\Gamma}_{\nu_B,\nu_A}$ (scaled by v) are presented for two different ion-projectile (ion A) velocities a) $v = 3$ a.u. and b) $v = 7$ a.u.

3. DISCUSSION

All the results presented in this paper clearly indicate the conclusion that the application of the two-wave-function model is extremely useful in understanding the process of the electron capture in ion-ion collisions. We analyzed only atomic particles with ground state of the ionic cores, i.e.: PV($2p^6$), PIV($3s$), PIII($3s^2$), SVI($2p^6$), SV($3s$), SIV($3s^2$). The neutralization distances R_{ec} were estimated for electron capture in the state $n_A = 5$ in the case of P ions and in the state $n_A = 6$ in the case of S ions, with the lowest possible energies: PV($^2S_{1/2}$), PIV($^3S_1$), PIII($^2S_{1/2}$) and SVI($^2S_{1/2}$), SV($^3S_1$), SIV($^2S_{1/2}$). For PIII($3s^2 5s, {}^2S_{1/2}$) i SIV($3s^2 6s, {}^2S_{1/2}$) a significant reduction in the neutralization distance was observed.

Additionally, despite the fact that a pronounced velocity dependence of electron capture distance has been found, the model has not yet been tested outside the limits of intermediate velocities.

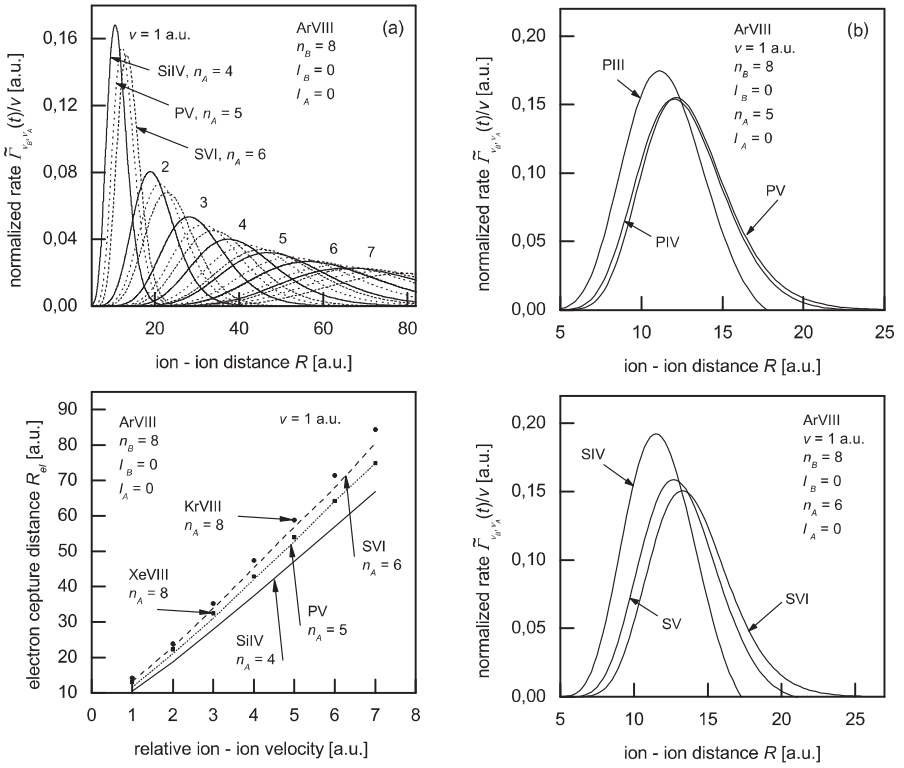

Figure 2: a) Normalized neutralization rates $\tilde{\Gamma}_{\nu_A}(t)$ scaled by v and appropriate velocity dependence of the electron capture distance R_{ec} in the velocity region $1 \leq v \leq 7$ a.u. Electron capture in the Rydberg state $(n_A, l_A) = (4, 0)$, $(5, 0)$ and $(6, 0)$ of the SiIV (solid curves), PV (dotted curves) and SVI (dashed curves) ions, respectively, escaping the ArVIII $(n_B = 8, l_B = 0)$ was considered. b) Normalized neutralization rates $\tilde{\Gamma}_{\nu_B,\nu_A}$ (scaled by v) are presented for P and S ions with a different core charge.

Acknowledgement. The authors would like to thank Professor N. N. Nedeljković for useful discussions. This work is supported by the Ministry of Education, Science and Technological Development of the Republic of Serbia through project No. 451-03-68/2022-14/200162.

References

Janev, R. K. : 1986, in *Atomic Processes in Electron-Ion and Ion-Ion Collisions, NATO ASI Series* (*Series B: Physics*, ed. by F. Brouillard Springer, Boston), **145**.

Galijaš, S. M. D., Poparić, G. B. : 2019, *Phys. Scr.*, **94**, 025401.

Galijaš, S. M. D., Poparić, G. B. : 2021, *Eur. Phys. J. D*, **75**.

Ralchenko, Yu., Yoy, F. C., Kelleher. D. E., Kramida, A. E., Musgrove, A., Reader, J., Wiese, W. L., Olsen, K. : 2007, NIST *Atomic Spectra Database,*htpp://physics.nist.gov. /PhysRefData/ASD/levels form.html, Gaithersburg.

Nedeljković, N. N., Majkić, M. D., Galijaš. S. M. D. : 2012, *J. Phys. B: At. Mol. Opt.*, **45**, 215202.

Publ. Astron. Obs. Belgrade No. 102 (2022), 109 - 112 *Contributed Paper*

INFLUENCE OF CARBON IONS OF DIFFERENT MULTIPLICITY ON REGIMES OF PROMISING LASER TECHNOLOGIES FOR THE DEPOSITION OF DIAMOND-LIKE CARBON NANOCOATINGS

V. K. GONCHAROV, G. A. GUSAKOV and M. V. PUZYREV

A.N.Sevchenko Institute of Applied Physics Problems, Belarusian State University
7 Kurchatov St., 220045, Minsk, Belarus
E-mail puzyrev@bsu.by

Abstract. The possibility of controlling physical processes in erosive laser plumes under the action of laser radiation on a graphite target using an electric field has been shown. It has been experimentally shown that it is possible to realize two regimes of the processing of the substrate surface. This is ion etching of the surface, as well as the deposition of diamond-like carbon films on various materials.

INTRODUCTION

The main advantage of laser-plasma deposition of nanocoatings is sterility, the ability to obtain plasma from any substance in any state of aggregation. However, this method has a significant drawback. To realize different regimes of nanocoating deposition, it is necessary to change the power density of laser radiation. We can make it if to change the energy in the laser pulse and change a focusing. Unfortunately, the dynamic range of laser pulse energy change in modern technological lasers is small (0.1 ÷ 0.5 J), and modern optomechanical systems for smooth focus adjustment are rather complicated, expensive and unreliable.

We have a aim to eliminate it. It was proposed to locate a grid between the laser target and the substrate in the laser-plasma source for applying nanocoatings. By applying a negative potential to the grid with respect to the target, after the grid we can obtain a flow of charged particles. This flow consists mainly of ions. By applying a negative potential to the substrate relative to the grid, it is possible to control the ion velocity in the grid–substrate interval [1]. In order for the sources of the electric field in the interval target - grid and grid - substrate to be independent, the grid must be grounded.

INSTRUMENTS AND TECHNIQUE OF EXPERIMENT

The LOTIS-TII pulsed YAG:Nd^{3+} laser with a wavelength λ = 1064 nm and a pulse duration $\tau \sim 20$ ns (as a full width at half maximum - FWHM) was used for experiments. Laser pulse was focused on a graphite target which is placed in a vacuum chamber under pressure of $2.6 \cdot 10^{-3}$ Pa. The target was mounted at angle of 45° with respect to the laser beam propagation and was constantly rotated to provide initial surface for ablation. The sample deposition was carried out at room temperature. The target was made from highly oriented pyrolytic graphite (HOPG).

The signal from the detector transferred to Tektronix TDS2022B oscilloscope.

RESULTS AND DISCUSSION

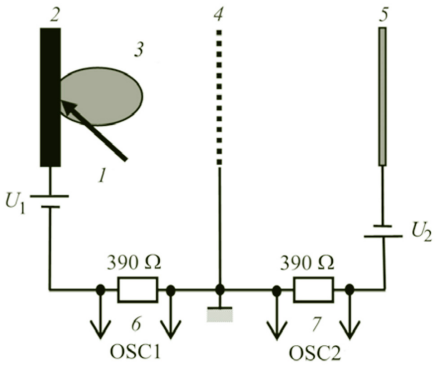

Figure 1: Scheme of the experiment: 1 - laser radiation; 2 - laser target; 3 - erosion plume; 4 - grid; 5 – substrate; 6 and 7 signals to the first and second beam of oscillograph from load resistances of 390 Ohm; U_1 and U_2 - independent power supplies

Experiments were carried out when the grid was located at a distance of 2.5 cm from the target surface. The target–substrate distance was 12 cm. A negative potential of 2.5 V with respect to the target was applied to the grid. The electrons to be decelerated by this field and return to the target, and after the grid a flow of charged particles was formed, consisting mainly of ions. In this case, a negative potential of 100 V was applied to the substrate with respect to the grid (Figure 1).

We can consider the processes occurring in the interval between the grid and the substrate. The results of the experiments are presented in Figure 2. The time curves of the ion current at different power densities have several humps. This is explained by the fact that, under these conditions, the erosive laser plume of carbon contains both singly ionized carbon atoms C II and multiplies ionized carbon atoms C III, C IV, and possibly C V [2]. Since an accelerating potential of 100 V is applied to the grid-substrate interval, ions of different multiplicity come to the target at different speeds. The main peak of the ion current pulse on the substrate is due to the arrival of the maximum number of single C II ions on the substrate.

It can be seen from Figure 2 that the speed of ions of different multiplicity increases with an increase in the power density of the acting laser radiation.

In addition to experiments at a constant potential (100V) in the grid-substrate interval, experiments were carried out at different potentials in this interval, but at a constant power density of the acting laser radiation. The results of these experiments are presented in Figure.3.

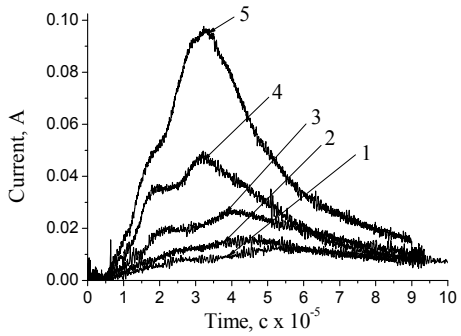

Figure 2: Dependence of the current on the substrate on time at different power densities of the laser radiation acting on the HOPG graphite target: 1 - $1.75 \cdot 10^8$ W/cm^2, 2 - $2.07 \cdot 10^8$ W/cm^2, 3 - $3.02 \cdot 10^8$W/cm^2, 4 - $3.82 \cdot 10^8$ W/cm^2, 5 - $4.93 \cdot 10^8$W/cm^2

This figure shows the leading edges of the substrate current pulses at a power density of $1.75 \cdot 10^8$ W/cm^2 laser radiation acting on the target at different potentials of the electric field in the grid-substrate interval. This figure show that, with an increase in the potential in the interval between the grid and the substrate, the time delay for the appearance of ions on the substrate decreases, The ion velocity increases.

However, this happens only until the electric field potential reaches~100V. A further increase in the potential does not lead to a decrease in the delay in the appearance of an ion flux on the substrate.

The slowdown in the growth of the ion flow rate at electric field potentials greater than ~ 100V. This can be estimated according to the Zygmund theory in the mode of primary direct knockout [3].

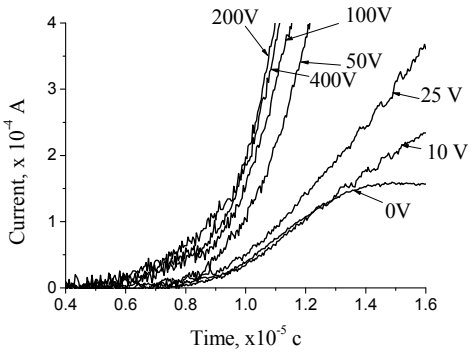

Figure 3: Dependence of the current on the substrate on time at a power density of the acting laser radiation of $1.75 \cdot 10^8$ W/cm^2, at different accelerating potentials between the grid and the substrate

Estimates of the secondary emission coefficient according to the Zygmund theory show that for a singly ionized carbon atom CII at an electric field potential in the grid-substrate interval 100 V at a power density of the acting laser radiation of 1.75·108 W/cm^2 is 0.56. Under the same conditions, for a doubly ionized CIII carbon atom, it is 1, that is, 100%, and for a triple ionized CIV, it is 1.6. The ion charge significantly affects the sputtering coefficient. The carbon charge influences on energy atoms at increase of the ionization. Energy atoms influence on the sputtering coefficient. It increases.

On the other hand, the sputtering coefficient is significantly depends on the potential of the electric field in the interval between the grid and the substrate. For a doubly ionized CIII carbon atom at an electric field potential 25V, the sputtering coefficient is 0.024. It is less than 2.5%, and at 400V it reaches 2.2. The incident one ion on the substrate knocks out two or more ions.

CONCLUSION

Thus, the current pulse of the ions is proportional to their velocity and concentration at low energies of ions reaching the surface of the substrate. The velocity of the ion flow also increases with an increasing the potential of the electric field in the interval between the grid and the substrate. Secondary ion emission appears when the ions energy has a value exceeding the surface potential. In this case the substrate surface is sputtered. A reverse current of secondary ions is formed from the substrate surface. It partially compensates the values of the direct ion current. The ions have the highest velocity due to ions of a higher ionization multiplicity on the leading edge of the direct ion current (see Figure 3). The influence on the value of the total ion current in the grid-substrate interval is especially significant at the beginning of the total ion current pulse. The results of these experiments determine two regimes of processing the substrate surface. It is possible to clean the substrate surface due to ion etching at significant values of the electric field in the interval between the grid-substrate. It is possible to deposit the highly adhesive diamond-like nanocoatings on the substrate surface of various materials at low values of the electric field.

References

[1]. Goncharov V.K., Pekhota A.A., Puzyrev M.V.: 2021, *Journal of Engineering Physics and Thermophysics,* **94**, No. 2, 503.

[2]. Goncharov V., Puzyrev M., Stupakevich V.: 2018: *29th Summer School and International Symposium on the Physics of Ionized Gases* , *eds G.Poparić, B.Obradović, D. Borka, V.Rajkobić.*. Belgrade, Serbia, pp.162.

[3]. Zigmund, P.:1984. *Spraying by ion bombardment: in Spraying of Solids by Ion Bombardment*, Mir, Moscow, pp. 55, 75.

Publ. Astron. Obs. Belgrade No. 102 (2022), 113 - 116 *Contributed Paper*

STUDY OF GRAPHENE BY RAINBOW SCATTERING EFFECT

M. HADŽIJOJIĆ[1] and M. ĆOSIĆ[2]

Laboratory of Physics, "Vinča" Institute of Nuclear Sciences
National Institute of the Republic of Serbia, University of Belgrade,
P. O. Box 522, 11001 Belgrade, Serbia
[1]*E-mail milivoje@vin.bg.ac.rs*
[2]*E-mail mcosic@vinca.rs*

Abstract. We have studied transformations of the rainbow pattern generated by the classical rainbow scattering of protons by graphene. Change in the interaction potential transforms rainbow pattern and corresponding angular proton yield. By studying morphological properties of the rainbow pattern it is possible to determine covariance matrix of atomic thermal displacements and characterize point defects present in graphene.

1. DYNAMICS OF PROTON RAINBOW SCATTERING

These are results of proton rainbow transmission through graphene. Selected proton energy is 5 keV. Associated proton de Broglie wavelength of 4.0476×10^{-4} nm is negligible compared to the distance of adjacent carbon atoms. Hence diffraction effects can be neglected and proton trajectories are well approximated by solutions of the classical equations of motion. According to the Ziegler-Biersack-Littmark theory of energy loss, the total proton energy loss and scattering angle dispersion due to interaction with electrons are small compared to the detector resolutions and can be neglected. Probability for neutralization of 5 keV proton is approximately 40%. In calculations we neglected neutralization. Hence calculated and measured angular yields are not comparable unless electrostatic analyzer is implemented to ensure detection of non-neutralized protons only. Let us define the coordinate system such that z-axis coincides with the direction of the proton beam. Direction of the proton beam relative to normal on the crystal surface is specified by polar and azimuthal angles Θ and Φ. Proton–atom interaction potential was constructed by averaging static Doyle–Turner's proton–atom interaction potential over the distribution of thermally induced atom displacements. The covariance matrix of atomic thermal displacements $\mathbf{\Sigma}$ was modeled by Debye theory, and calculated using Molecular Dynamics approach. More realistic model of graphene thermal motion was constructed using Molecular Dynamics. Let

(v_x, v_y, v_z) be the velocity of the transmitted proton. Proton scattering angles θ_x and θ_y are defined by expressions:

$$\tan\theta_x = \frac{v_x}{v_z}, \quad \tan\theta_y = \frac{v_y}{v_z}. \tag{1}$$

Angular yield of transmitted protons $Y(\theta_x, \theta_y)$ is the number of protons scattered in the element $d\theta_x d\theta_y$ centered at the (θ_x, θ_y). Proton impact parameter (b_x, b_y) is projection of the proton initial position to the (x, y) plane. Proton trajectories define mapping of the proton impact parameters to the set of proton scattering angles:

$$f_{(\Theta,\Phi)}: (b_x, b_y) \rightarrow (\theta_x, \theta_y), \tag{2}$$

where Θ and Φ are parameters. Differential cross section is given by the expression:

$$\sigma(b_x, b_y; \Theta, \Phi) \sim \left|\det \mathcal{J}_{(\theta_x,\theta_y)}(b_x, b_y)\right|^{-1}, \tag{3}$$

where $\mathcal{J}_{(\theta_x,\theta_y)}(b_x, b_y)$ is Jacobian matrix of the mapping (2). σ is infinite if Jacobian matrix is singular. Singularities of $\mathcal{J}_{(\theta_x,\theta_y)}(b_x, b_y)$ are curves in the impact parameter plane. Images of these curves obtained by mapping (2) are *rainbow lines*. As singularities of differential cross section, rainbow lines have significant influence on shape of the angular distribution of transmitted protons. Optical rainbow, nuclear, Coulomb and crystal rainbow effects are manifestations of the same rainbow scattering effect. Next will be shown how study of the rainbow pattern could be utilized for characterization of graphene.

2. CHARACTERIZATION OF GRAPHENE

We have investigated influence of covariance matrix **Σ** and graphene defects on the angular distributions and associated rainbow patterns of transmitted protons. Three different cases were analyzed: perfect graphene with atoms performing isotropic oscillations, perfect graphene with atoms performing anisotropic oscillations, and graphene with vacancies and isotropic thermal motion of atoms. Figures 1(a)-1(c) are illustrations of these three cases. In the case of isotropic atomic displacements, **Σ** is a scalar matrix and interaction potential near individual atoms has a spherical symmetry. This is not the case if atomic thermal vibrations are anisotropic. Blue surfaces represent equipotential surfaces in the vicinity of the individual carbon atoms. In figures 1(a')-1(c') are shown corresponding angular distributions of transmitted protons, calculated by solving equations of motion. Angular yields are presented in the scattering angle plane (θ_x, θ_y). Maximal scattering angles are approximately 150 mrad. Rectangular insets 1(a")-1(c") are enlarged views of the angular distributions in the regions of small scattering angles. Black curves are

calculated rainbow lines. Particle count is large along rainbow lines and they outline shapes of all angular distributions. The outer rainbows O_1, O_2 and O_3 are formed by protons which experienced close collisions with carbon atoms. Hence outer rainbows contain information about properties of the interaction potential in the vicinity of individual atoms. Consequently outer rainbow O_1 is circular regardless of direction of the incident proton beam. In figures 1(b') and 1(b") are shown angular yields and rainbow patterns of protons transmitted through graphene with anisotropic thermal vibrations of carbon atoms. In this case interaction potential near individual atoms does not have a spherical symmetry. Hence shape of the outer part of angular distribution is not necessarily circular. In general, corresponding outer rainbow O_2, and consequently the entire distribution, has shape of a tilted ellipse. Symmetry axes of rainbow O_2 are represented by cyan lines.

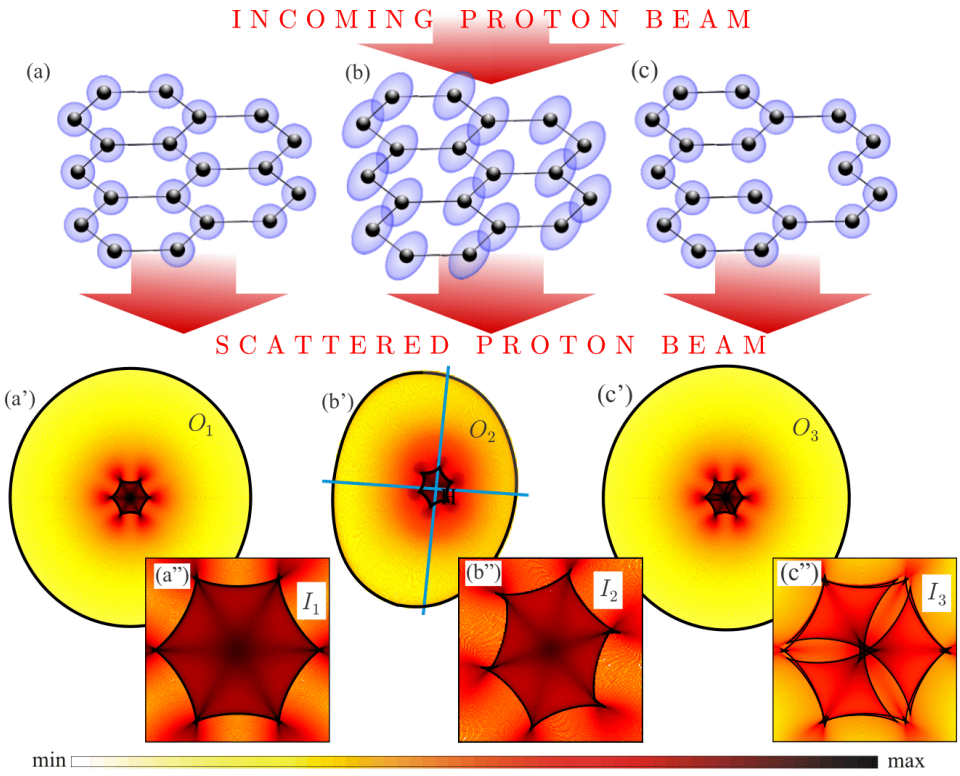

Figure 1: (a),(b) Illustrations of perfect graphene in the case of isotropic and anisotropic atomic thermal vibrations; (c) graphene with vacancies and isotropic thermal motion of atoms. Blue surfaces are sketches of equipotential surfaces near carbon atoms. (a')-(c') corresponding angular yields, color-coded according to the color bar. Rectangular insets (a")-(c") are enlarged views of angular distributions in the range of small scattering angles. Rainbows are shown by black lines. Cyan lines are symmetry axes of the rainbow O_2.

Outer rainbow line O_3 in figure 1(c') is indistinguishable from the rainbow O_1. This is consequence of the isotropic thermal vibrations of carbon atoms. We found that outer rainbow line behaves qualitatively equal as normal projection of the ellipsoid associated with the matrix $\mathbf{\Sigma}^{-1}$. We showed that parameters of the outer rainbow line could be used to solve the inverse problem, i.e. to determine the covariance matrix $\mathbf{\Sigma}$, even if atoms perform anisotropic and correlated motion. The inner rainbow lines, labeled by I_1, I_2 and I_3, are generated by synergetic action of carbon atoms forming graphene lattice. Therefore, inner rainbow pattern carries information about crystal structure. Symmetry of the inner rainbows I_1 and I_2 coincides with the symmetry of the graphene hexagon projected to the (x, y) plane. We showed that inner rainbows are not influenced by the thermal motion of carbon atoms. The inner rainbow pattern I_3 is generated by protons transmitted through graphene with vacancies. It is composed of four rainbow lines. It differs significantly from the inner rainbow pattern formed by proton scattering on a perfect graphene. We found that different defect types produce different inner rainbow patterns. Furthermore, we have shown that rainbow patterns and angular distributions of protons transmitted through graphene with point defects could be used to determine densities of the unknown defects even in the case of a sample containing a combination of the different defect types. Developed procedure could enable characterization of graphene defects.

References

Adams, A. : 2002, *Phys. Rep.* **356**, 229.
Connor, J. N. L., Farrelly, D. : 1981, *J. Chem. Phys.* **75**, 2831.
Ford K. W., Wheeler, J. A. : 2002 (reprinted), *Ann. Phys.* **281**, 608.
Gruber, E., et al, : 2016, *Nat. Commun.* 7, 1-7 (Supplementary material).
Nešković, N. : 1986, *Phys. Rev. B* **33**, 6030.
Zhao, S. et al, : 2016, *J. Phys. Condens. Matter* 27, 1-6.
Ćosić, M., Hadžijojić, M., Petrović, S., Rymzhanov, R., Bellucci, S. : 2019, *Carbon* **145**, 161.
Ćosić, M., Hadžijojić, M., Petrović, S., Rymzhanov, R. : 2021, *Chaos* **31**, 093115.
Hadžijojić, M., Ćosić, M., Rymzhanov, R. : 2021, *J. Phys. Chem. C*. **125**, 38, 21030–21043.

Publ. Astron. Obs. Belgrade No. 102 (2022), 117 - 120 *Contributed Paper*

ANALYTICAL EXPRESSION FOR STOPPING FORCE ACTING ON A SLOW CHARGED PARTICLE MOVING PARALLEL TO A THICK GRAPHENE-SAPPHIRE-GRAPHENE STRUCTURE

A. KALINIĆ[1,2], I. RADOVIĆ[2], L. KARBUNAR[3], V. DESPOJA[4] and Z. L. MIŠKOVIĆ[5]

[1]*School of Electrical Engineering, University of Belgrade, Bulevar Kralja Aleksandra 73, Belgrade 11120, Serbia*
E-mail ana.kalinic@vin.bg.ac.rs

[2]*Department of Atomic Physics, "VINČA" Institute of Nuclear Sciences - National Institute of the Republic of Serbia, University of Belgrade, P.O. Box 522, Belgrade 11001, Serbia*
E-mail iradovic@vin.bg.ac.rs

[3]*School of Computing, Union University, Knez Mihailova 6, Belgrade 11000, Serbia*
E-mail lkarbunar@raf.rs

[4]*Institute of Physics, Bijenička 46, Zagreb 10000, Croatia*
E-mail vito@phy.hr

[5]*Department of Applied Mathematics, and Waterloo Institute for Nanotechnology, University of Waterloo, Waterloo, Ontario N2L 3G1, Canada*
E-mail zmiskovi@uwaterloo.ca

Abstract. We derive an analytical expression for the stopping force acting on an external charged particle moving parallel to a sandwich-like structure consisting of two undoped graphene sheets separated by a layer of Al_2O_3 (sapphire).

1. INTRODUCTION

Experimental designs of nanoscale devices involving graphene require stacking of graphene layers with insulating spacer layers (Yan et al. 2012), which usually support strong Fuchs-Kliewer (FK) or optical surface phonon modes (Fischetti et al. 2001). In our previous publication (Despoja et al. 2017), as a prototype of layered heterostructures involving graphene sheets, we have studied a graphene-Al_2O_3-graphene (for short, denoted by gr-Al_2O_3-gr) composite system and derived

an expression for its effective dielectric function. In the following papers (Despoja et al. 2019 and Kalinić et al. 2021), the wake potential produced by an external charged particle that moves parallel to a sandwich-like gr-Al_2O_3-gr structure was investigated. We have found that in a low-velocity regime (below the threshold for excitations of the Dirac plasmon in graphene, given by its Fermi velocity v_F) only the transverse optical (TO) phonons in the Al_2O_3 layer contribute to the wake potential in the plane of the graphene layer closest to the incident particle. Finally, in our recent publication (Kalinić et al. 2020) we have derived general expressions for the stopping and image forces acting on the external charged particle moving parallel to the gr-Al_2O_3-gr composite. In this work, in order to provide an analytical estimate of the peak in the stopping force in the range of speeds below v_F, we analytically evaluate the stopping force on the external charged particle moving parallel to two undoped graphene layers with Al_2O_3 in between. Note that we use Gaussian electrostatic units, set $\hbar = 1$, and denote the charge of a proton by $e > 0$.

2. BASIC THEORY

We use a Cartesian coordinate system with coordinates $\{\vec{R}, z\}$, where $\vec{R} = \{x, y\}$ is a two-dimensional (2D) position vector in the xy-plane and z is the distance from it. Two graphene sheets are placed in the planes $z = \pm a/2$, with the space between them being a layer of Al_2O_3 (sapphire) of thickness a. Assuming that the layered structure is translationally invariant in the xy directions, we perform a 2D spatial ($\vec{R} \to \vec{q}$) and a temporal ($t \to \omega$) Fourier transform of all relevant quantities. The sapphire layer is approximated by a homogeneous dielectric slab described by local dielectric function $\varepsilon_s(\omega)$, whereas bottom and top graphene sheets are described by the 2D response functions $\chi_1(q, \omega)$ and $\chi_2(q, \omega)$, respectively. The entire system is assumed to be in vacuum or air.

The stopping force acting on the external point charge Ze moving parallel to a gr-Al_2O_3-gr composite at a fixed distance b above the top graphene layer with a constant velocity v may be expressed as (Preciado Rivas et al. 2021)

$$\mathrm{F}_s = -\frac{2(Ze)^2}{\pi v}\int_0^\infty e^{-2qb}dq\int_0^{qv}\frac{\omega}{\sqrt{(qv)^2-\omega^2}}Im\left[-\frac{1}{\varepsilon(q,\omega)}\right]d\omega \qquad (1)$$

where the effective 2D dielectric function $\varepsilon(q, \omega)$ is given by (Despoja et al. 2017)

$$\varepsilon(q,\omega) = \frac{1}{2}\left[1+\varepsilon_s(\omega)\coth(qa)+\frac{4\pi e^2}{q}\chi_2\right] - \frac{1}{2}\frac{\varepsilon_s^2(\omega)cosech^2(qa)}{1+\varepsilon_s(\omega)\coth(qa)+\frac{4\pi e^2}{q}\chi_1} \qquad (2)$$

It is shown (Kalinić et al. 2022) that, for the choice of the parameters $a \gg b$, the two surfaces of our sandwich-like structure are electrostatically decoupled. Mathematically, this occurs when $qa \gg 1$. Then, setting $\coth(qa) \approx 1$ and $cosech(qa) \approx 0$ in Eq. (2) one obtains an effective dielectric function for a single-

layer graphene with polarization χ_2 deposited on a semi-infinite substrate with the dielectric permittivity ε_s

$$\varepsilon(q,\omega) = \frac{1}{2}\left[1 + \varepsilon_s(\omega) + \frac{4\pi e^2}{q}\chi_2\right] \tag{3}$$

Since we are interested in low speeds, we may approximate the response function of the top graphene layer by its static limit. For an undoped graphene, this gives $\chi_2 \approx q/(4v_F)$. In that case, Eq. (3) may be approximated as

$$\varepsilon(\omega) \approx \frac{1}{2}\left[1 + \varepsilon_s(\omega) + \frac{\pi e^2}{v_F}\right] \tag{4}$$

As a result, the energy loss function (ELF) in Eq. (1), $Im[-1/\varepsilon(q,\omega)]$, becomes independent of q and it features sharp peaks at frequencies corresponding to the FK phonons in the Al_2O_3 substrate, modified by the static screening by graphene. By solving the equation $\varepsilon(\omega) = 0$, and taking the expression for $\varepsilon_s(\omega)$ (Fischetti et al. 2001) which includes two TO phonon modes at 48 meV and 71 meV with zero damping, one obtains the screened FK phonon frequencies in the Al_2O_3 substrate as $\omega_{FK1} \approx 54$ meV and $\omega_{FK2} \approx 86$ meV. Thus, we may approximate the ELF in Eq. (1) by (Preciado Rivas et al. 2021)

$$Im\left[-\frac{1}{\varepsilon(\omega)}\right] \approx \sum_{i=1}^{2} A_i \delta(\omega - \omega_{FKi}) \tag{5}$$

with the weight constants $A_i = \pi/|\varepsilon'(\omega_{FKi})|$, which take values $A_1 \approx 1.5$ meV and $A_2 \approx 8.8$ meV.

Substituting Eq. (5) into Eq. (1) one obtains an analytical approximation as

$$\mathrm{F}_s \approx -\frac{2(Ze)^2}{\pi v^2}\sum_{i=1}^{2} A_i \omega_{FKi} K_0\left(2\frac{b}{v}\omega_{FKi}\right) \tag{6}$$

where K_0 is a Bessel function.

3. RESULTS AND DISCUSSION

In Fig. 1 we show the four stopping forces in the range of speeds from 0 to $0.9v_F$ for two undoped graphene sheets [Fermi energy is $E_F = 0$, marked as gr(0)] a distance $a = 5$ nm apart with the Al_2O_3 layer in between, using the particle distance $b = 0.5$ nm: F_s is evaluated from Eq. (1) using Eq. (2) and the dynamic polarization function of graphene within the random phase approximation for its π bands; $F_s^{(1+2)}$, $F_s^{(1)}$, and $F_s^{(2)}$ are evaluated from Eq. (6) for both FK phonons, only for ω_{FK1}, and only for ω_{FK2}, respectively. It is evident that analytical expression for the stopping force well reproduces the peak at $v \approx 0.08v_F$, showing that its origin is dominantly in the phonon mode in the Al_2O_3 surface with ω_{FK2}.

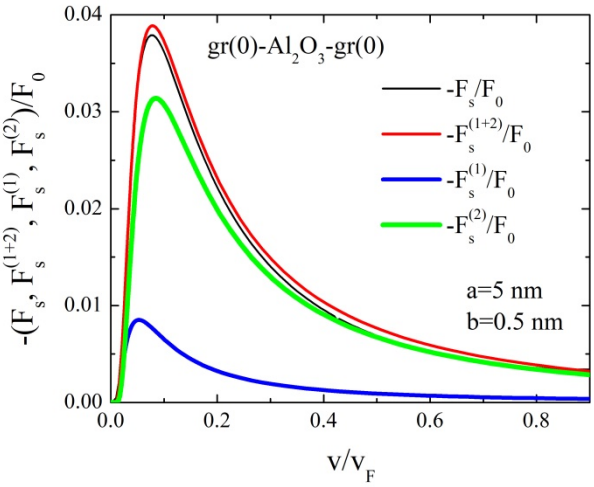

Figure 1: The stopping forces: F_s (thin black line), $F_s^{(1+2)}$ (medium red line), $F_s^{(1)}$ (thick blue line), and $F_s^{(2)}$ (extra thick green line), normalized by $F_0 = [Ze/(2b)]^2$, as functions of the speed v (normalized by v_F) of a proton ($Z = 1$) moving at a distance $b = 0.5$ nm above two undoped graphene sheets with Al_2O_3 in between. The separation between graphene layers (or the Al_2O_3 slab thickness) is $a = 5$ nm.

Acknowledgments

This research is funded by the Ministry of Education, Science and Technological Development of the Republic of Serbia, the Croatian Science Foundation (Grant No. IP-2020-02-5556), the European Regional Development Fund for the 'QuantiXLie Centre of Excellence' (Grant No. KK.01.1.1.01.0004), and the Natural Sciences and Engineering Research Council of Canada (Grant No. 2016-03689).

References

Despoja, V., Djordjević, T., Karbunar, L., Radović, I., Mišković, Z. L. : 2017, *Phys. Rev. B*, **96**, 075433.

Despoja, V., Radović, I., Karbunar, L., Kalinić, A., Mišković, Z. L. : 2019, *Phys. Rev. B*, **100**, 035443.

Fischetti, M. V., Neumayer, D. A., Cartier, E. A. : 2001, *J. Appl. Phys.*, **90**, 4587.

Kalinić, A., Radović, I., Karbunar, L., Despoja, V., Mišković, Z. L. : 2020, *Publ. Astron. Obs. Belgrade*, **99**, 97.

Kalinić, A., Radović, I., Karbunar, L., Despoja, V., Mišković, Z. L. : 2021, *Phys. E Low-dimens. Syst. Nanostruct.*, **126**, 114447.

Kalinić, A., Despoja, V., Radović, I., Karbunar, L., Mišković, Z. L. : 2022, *Phys. Rev. B*, submitted.

Preciado Rivas, M. R., Moshayedi, M., Mišković, Z. L. : 2021, *J. Appl. Phys.*, **130**, 173103.

Yan, H., Li, X., Chandra, B., Tulevski, G., Wu, Y., Freitag, M., Zhu, W., Avouris, P., Xia, F. : 2012, *Nat. Nanotechnol.*, **7**, 330.

Publ. Astron. Obs. Belgrade No. 102 (2022), 121 - 124 *Contributed Paper*

EFFECT OF THE IONIC TYPE ON THE SHAPE OF THE NANOSTRUCTURES CREATED BY AN IMPACT OF SLOW HIGHLY CHARGED IONS ON GOLD SURFACE

M. D. MAJKIĆ[1], N. N. NEDELJKOVIĆ [2] and M. A. MIRKOVIĆ[3]

[1] *University of Priština-Kosovska Mitrovica, Faculty of Technical Sciences, Knjaza Miloša 7 38220 Kosovska Mitrovica, Serbia*
E–mail milena.majkic@pr.ac.rs

[2] *University of Belgrade, Faculty of Physics, P.O. Box 368, 11001 Belgrade, Serbia*
E–mail hekata@bg.ac.rs

[3] *Academy of Technical and Art Applied Studies, College of Applied Studies of Civil Engineering and Geodesy, Hajduk Stankova 2, 11050, Belgrade, Serbia*
E–mail marko.a.mirkovic@gmail.com

Abstract. We study the interaction of slow highly charged Ar^{Z+}, Kr^{Z+} and Xe^{Z+} ions, (charge $Z \gg 1$) with gold surface and propose a theoretical model for determination of the shapes of the obtained surface nanostructures. Within the framework of the model we introduce the critical ionic velocity as a measure of the interplay of the neutralization energy and the deposited kinetic energy, both necessary for the surface nanostructure creation. The influence of the core polarization, i.e. the ionic type on the value of the critical ionic velocity is discussed. The value of the critical velocity we use to define a sufficiently accurate criterion whether the nanohillock or nanocraters are the result of the surface modification, i.e., we predict the shape of the created nanostructure for the particular ionic type.

1. INTRODUCTION

Irradiation of solid by swift heavy ions or slow highly charged ions (HCI) results in the nanometric surface modification such as hillock, crater, caldera, pit etc. The condition that has to be satisfied for the production of the particular surface structure is an important information of the surface modification, from the experimental as well as the theoretical point of view. The commonly used theoretical models which describe the surface modification are the molecular dynamics simulations, see Nordlund et al. 2014 and inelastic thermal spike model Toulemonde et al. 1992. Up to now, the theoretical model (energy dissipation model - EDM) confirmed by the experiment that predict the shape of the surface nanostructure has been proposed only for slow highly charged xenon ion impacting upon a gold surface (Majkić et al. 2021). The EDM is based on the quantum two-state vector model and micro staircase model for the neutralization energy calculation and charge dependent ion-atom potential model

for the kinetic energy loss calculation. The model enable us to define the critical velocity for various ion-surface combinations. We analyze the influence of the core polarization on the value of the critical ionic velocity as well as on the shape of the formed surface nanofeatures.

2. SHAPE OF THE NANOSTRUCTURE

We consider the highly charged Ar^{Z+}, Kr^{Z+} and Xe^{Z+} ions impinging upon a gold

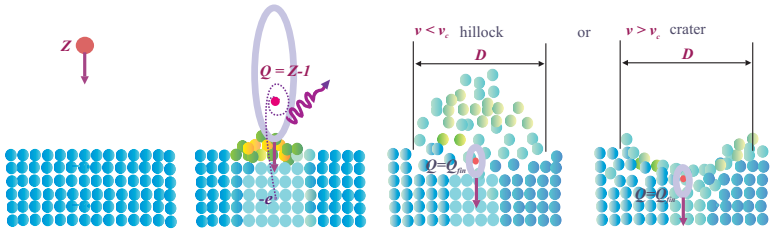

Figure 1: Schematic description of the nanohillock ($v < v_c$) and nanocrater ($v > v_c$) formation during the interaction of HCI with gold surface.

surface at low to moderate ionic velocity. For the same charge Z, the considered ions have different electronic core structures. The energy necessary for the surface nanofeatures creation within the EDM consists of the neutralization energy and the deposited kinetic energy, both dependent on the ionic electronic core structure.

Above the surface, the neutralization process is quantified by the population probability for the electron capture from the metal into the highly excited (Rydberg) state; the process we consider as an electron tunnelling through the potential barrier formed between the solid and the ion. We solve the time-dependent Schrödinger equations with in- and out- Hamiltonians $\hat{H}_1$ and $\hat{H}_2$, see Nedeljković et al. 2007. In the treatment of the intermediate stages of the neutralization process the polarization of the electronic cloud of the ionic core is taken into account via the appropriate interaction of the Simons-Bloch type of the active electron and the ionic core. This interaction governed the out Hamiltonian $\hat{H}_2$. Outside the solid, the in Hamiltonian $\hat{H}_1$ describes the electron interaction with polarized solid; inside the solid, the electron is in the mean field described by the potential well of the Somerfield model of the solid. The more accurate treatment is to solve the Schrödinger equation for a particle in the one-dimensional lattice with the periodic potential within the framework of the homotopy perturbation approach, see Kevkić et al. 2019. Within the framework of the micro staircase model (in which the fine structure of the neutralization cascade of the ions approaching the solid surface is taken into account) the initial ionic charge reduces in time: $Q = Z \rightarrow Q = Z - 1 \rightarrow ... \, Q(R) \rightarrow ... \rightarrow Q_{fin}$, see Fig. 1. The core polarization modifies the population probabilities and the corresponding neutralization distances, while the final ionic charges Q_{fin} are almost the same, see Majkić et al. 2019. The neutralization energy $W^{(Z,MV)} = W_{Z,pot} - W_{Q_{fin}^{MV},pot}$ defined as difference of the initial and final potential energies, depends on the ionic type via the initial potential energy.

Inside the solid, the deposited kinetic energy into the active interaction volume of depth Δx is given by $E_{k,dep} = (dE_n/dx)\Delta x$ (see Majkić et al. 2021). Nuclear

stopping power dE_n/dx we calculate using the charge dependent interaction between the HCI and target atoms. This interaction is significantly different for different ionic types, due to different nuclear charges of the considered ions.

The facts that both the neutralization energy and deposited kinetic energy are sensitive to the ionic type, directly influences on the nanosturcture shape. That is, the critical ionic velocity v_c:

$$W^{(Z,MV)}(v_c) = E_{k,dep}(v_c), \tag{1}$$

separates the velocity region into two subregions: for very low ionic velocities ($v < v_c$) the EDM predicts the hillocks as a dominant structures, while for the velocities larger than the critical one ($v > v_c$), expected structures are craters. In the first case (hillock formation), the neutralization energy has a dominant influence in the surface modification, while the main contribution in the surface nanocraters formation is given by the deposited kinetic energy.

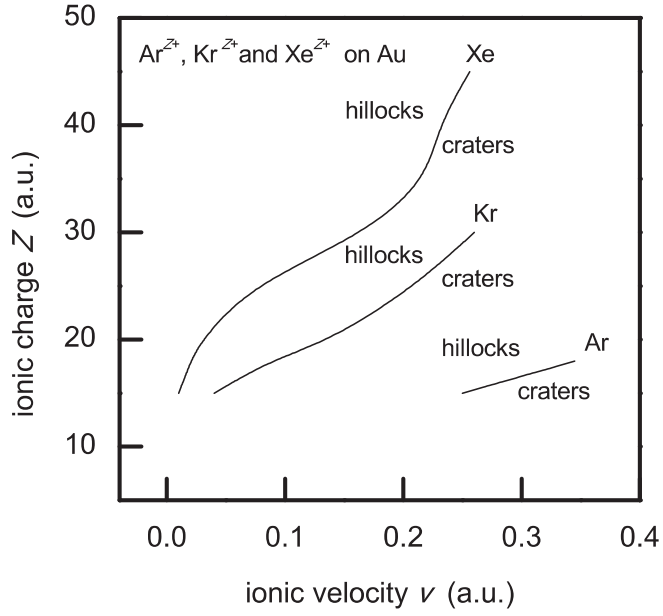

Figure 2: $\{Z-v\}$ diagram for Ar^{Z+}, Kr^{Z+} and Xe^{Z+} ions, $Z = 15, 18, 20, 25, 30, 35, 40$ and 45, interacting with gold surface. Solid curves are the kritical velocities.

3. RESULTS

The critical velocities enable us to analyze the effect of the ionic type on the shape of the nanofeatures created by the impact of slow HCI on the metal surface.

In Fig.2. we present the $\{Z - v\}$ diagram with critical ionic velocity v_c for Ar^{Z+}, Kr^{Z+} and Xe^{Z+} ions impacting upon the Au target. From figure one can see the decreasing character for the critical ionic velocities with increasing of the core polarization ($Ar^{Z+} \rightarrow Kr^{Z+} \rightarrow Xe^{Z+}$) for the same ionic charge Z. According to $\{Z - v\}$

diagram, for example, the interaction of the Kr^{30+} ions with gold surface at velocity lower than $v_c = 0.26$ a.u. results in a hillock formation, while Xe^{30+} ions at velocities $v = 0.26$ a.u forms the craters. The Ar^{18+} ions in the interaction with gold target will form craters for velocities larger than $v_c = 0.34$ a.u., while Kr^{18+} and Xe^{18+} ions create the same structure for velocities larger than $v_c = 0.09$ a.u. and $v_c = 0.02$ a.u., respectively.

The predicted types of the nanostructures are in accord with the experimental results for the interaction of the Xe^{Z+} ions with gold targets (Stabrawa et al. 2017, Stabrawa et al. 2022, Pomeroy et al. 2007). The critical velocities for other ion-target combinations can be also obtained from our model. The agreement is also obtained for Xe^{Z+} ions interacting with titanium targets (Stabrawa et al. 2017, Majkić et al. 2021). From the $\{Z - v\}$ diagrams one can tune the velocity needed for the particular surface structure formation by an impact of the ion of a given charge Z.

Acknowledgments

This work was supported in part by the Ministry of Education, Science and Technological Development of the Republic of Serbia (Project 171016, 171029).

References

Kevkic, T., Stojanovic, V., Petkovic, D.: 2019, *Romanian Reports in Physics*, **71**, 101.
Majkić, M. D., Nedeljković, N. N., Mirković, M. A. : 2019, *Vacuum*, **165**, 62-67.
Majkić, M. D., Nedeljković, N. N.: 2021, *Vacuum*, **190**, 110301.
Nedeljković, N. N, Majkić, M. D.: 2007, *Phys. Rev. A*, **76**, 042902
Nordlund, K., F. Djurabekova, F.: 2014, *J. Comput. Electron.*, **13**, 122141.
Pomeroy, J.M. Perrella, A.C., Grube, H., Gillaspy, J.D.: 2007, *Phys. Rev. B* , **75**, 241409(R).
Toulemonde, M., Dufour, C., Paumier, E.: 1992, *Phys. Rev. B*, **46**, 14362.
Stabrawa, I., Banaś, D., Kubala-Kukuś, A., Szary, K., Braziewicz, J., Czub, J., Jabłoński, Ł., Jagodziński, P., Sobota, D., Pajek, M., Skrzypiec, K., Mendyk, E., Teodorczyk, M.: 2017, *Nucl. Instrum. Methods Phys. Res. B* , **408**, 235-240
Stabrawa, I., Banaś, D., Kubala-Kukuś, A., Szary, K., Braziewicz, J., Czub, J., Jabłoński, Ł., Jagodziński, P., Sobota, D., Pajek, M., Skrzypiec, K., Mendyk, E., Teodorczyk, M., Majkić, M. D., Nedeljković, N. N.: 2022, to be published

Publ. Astron. Obs. Belgrade No. 102 (2022), 125 - 128 *Contributed Paper*

THE INFLUENCE OF THE ION-TARGET PARAMETERS ON THE SIZE OF THE SURFACE NANOHILLOCKS CREATED BY AN IMPACT OF HIGHLY CHARGED IONS

N. N. NEDELJKOVIĆ[1], M. D. MAJKIĆ[2], M. A. MIRKOVIĆ[3], I. STABRAWA[4(a)] and D. BANAŚ[4(b)]

[1] *University of Belgrade, Faculty of Physics, P.O. Box 368, 11001 Belgrade, Serbia*
E–mail hekata@bg.ac.rs

[2] *University of Priština-Kosovska Mitrovica, Faculty of Technical Sciences, Knjaza Miloša 7 38220 Kosovska Mitrovica, Serbia*
E–mail milena.majkic@pr.ac.rs

[3] *Academy of Technical and Art Applied Studies, College of Applied Studies of Civil Engineering and Geodesy, Hajduk Stankova 2, 11050, Belgrade, Serbia*
E–mail marko.a.mirkovic@gmail.com

[4] *Jan Kochanowski University, Institute of Physics, Uniwersytecka 7, 25-406 Kielce, Poland*
E–mail (a)i.stabrawa@ujk.edu.pl
E–mail (b)d.banas@ujk.edu.pl

Abstract. We study the interaction of slow highly charged Xe^{Z+}ions (charge $Z \gg 1$) with gold and titanium targets and propose the theoretical model of the surface nanohillock formation for low to moderate ionic velocities. We apply the quantum two-state vector model accompanied by the micro staircase model for the neutralization energy calculation; the nuclear stopping power we consider using the charge dependent ion-atom interaction potential. We propose the cohesive energy dissipation model for the calculation of the diameter of the considered nanohillocks. The effect of the ionic charge, velocity and target type on the size of the nanostructure is demonstrated.

1. INTRODUCTION

Theoretical and experimental studies of the surface nanostructure creation by an impact of the slow highly charged ions (HCI) have a diverse applications in a surface and material science. Theoretical studies that appears in the literature are mainly based on the molecular dynamics simulations (Nordlund et al. 2014) and the inelastic thermal spike model (Toulemonde et al. 1992). The theory concerning the metal-surface modification has been developed using the energy dissipation model (EDM); the model consists of the quantum two-state vector model accompanied by the micro-staircase model of the HCI neutralization, and the charge dependent model of the kinetic energy loss (Nedeljković et al. 2016, Majkić et al. 2021). The experimental

studies of the nanostructuring of the metal surface have been recently performed, see Stabrawa et al. 2017.

The aim of the present contribution is the calculation of the diameter of the surface nanohillocks that can be compared with experiment. The effect of the ion-target parameters (ionic charge, ionic velocity and the target type) on the size of the nanostructure we analyze within the framework of the EDM.

2. COHESIVE ENERGY DISSIPATION MODEL

We consider the highly charged Xe^{Z+}ions, (charge $Z \gg 1$) impinging upon a metal

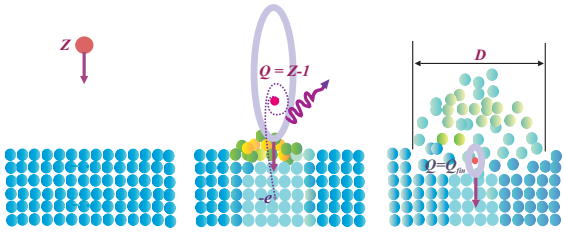

Figure 1: Schematic description of the nanohillock formation during the interaction of HCI with metal surface.

surface at a velocity in the range from very low to moderate. The interaction of the ions with the surface can be divided into two stages. In the first stage, the ions approach the surface and the cascade neutralization of the ions above it occurs, see intermediate stages of the ion neutralization presented in Fig. 1. This process is accompanied by the neutralization energy deposition. Below the surface the process of the elastic collisions of the projectile with target atoms is the main mechanism of the energy dissipation. The kinetic energy of the ions in the form of the kinetic energy loss is deposited into the surface. Both energies contribute to the surface modification. The shape of the nanostructure depends on the interplay of these two energy contribution, described by the critical ionic velocity v_c. The hillock-like structures appears for velocities $v < v_c$, for which the neutralization energy dissipation has a dominant role.

Within the EDM, the total deposited energy $E_{tot,dep}$ into the active volume V of the target consists of the neutralization energy and the deposited kinetic energy $E_{tot,dep} = W^{(Z,MV)} + E_{k,dep}$. Deposited energy during the surface modification is responsible for an increase of the target energy: $E_{tot,dep} = E_{fin} - E_{in}$, where E_{in} and E_{fin} describe the initial and the final state of the target. Within the framework of the cohesive energy dissipation model, the bounds between the target atoms change during the solid modification: $E_{in} = -E_{c0}$ and $E_{fin} = -E_c$, respectively, where E_{c0} and E_c are the absolute values of the cohesive energies of unperturbed (initial) and perturbed solid (final).

Therefore, $E_{tot,dep} = E_{c0} - E_c$, where $E_{c0} = n_0 U_0 V$, where n_0 and U_0 are the initial atomic density and (absolute value) of the corresponding cohesive energy per atom and $E_c = nU(V + V_h)$ where V_h is the hillock volume, n is the final atomic density and U is the (absolute value) of the corresponding cohesive energy per atom. The mass of the initial active volume V is distributed to the volume $V + V_h$, so that

$n_0V = n(V + V_h)$ and $E_c = n_0UV$. The total deposited energy in the considered model is given by $E_{tot,dep} = n_0(U_0 - U)V$ The energy $E_{tot,dep}$ can be expressed as a part of the (absolute value) of the initial cohesive energy E_{c0}:

$$E_{tot,dep} = \kappa_c E_{c0}, \kappa_c = \frac{U_0 - U}{U_0}, \tag{1}$$

where κ_c represents the degree of the surface modification. This parameter κ_c can not be directly obtained from our model (for each Z and v and particular target, one can estimate the parameter κ_c that exactly fits the experiment).

The active volume $V = (D^2/4)\pi\Delta x$ in which the energy is deposited we consider as a cylinder of diameter D with the high equal to the interaction depth Δx. For gold and titanium targets $\Delta x \approx 5\bar{c} \approx 38.5$ a.u. and $\Delta x \approx 5\bar{c} \approx 33.2$ a.u., respectively (see Majkić et al. 2021), where c is the mean lattice constant. In the first approximation diameter D coincides with the diameter of the formed nanohillock. According to the relation (1) for the nanohillock diameter we get a simple expression

$$D = 2\sqrt{\frac{E_{tot,dep}}{\pi\epsilon_{c0}\kappa_c\Delta x}}, \tag{2}$$

where $\epsilon_{c0} = n_0U_0$ is the (absolute value) of the initial cohesive energy density.

The cohesive energy per atom and the atomic density of the unperturbed gold and titanium are $U_0 = 3.93$ eV$= 0.144$ a.u., $n_0 = 8.7 \cdot 10^{-3}$ a.u., and $U_0 = 4.85$ eV$= 0.1783$ a.u., $n_0 = 8.4 \cdot 10^{-3}$ a.u., respectively.

3. RESULTS

We analyze the size of the nanohillocks created on the titanium and the gold nanolayers by an impact of slow Xe^{Z+} ions, $Z = 20, 25, 30, 35, 40$ and 45. The nanolayers are strongly perturbed during the ionic motion and the process of the nanostructure formation, what is described by the degree of the target modification κ_c. The values fitting the available experiments (see Stabrawa et al. 2017) are $\kappa_c = 0.05$ for titanium and $\kappa_c = 0.043$ for gold targets.

In Fig. 2 we present the nanohillock diameters calculating according to (2) for Ti and Au targets. From Fig. 2 we can recognize the decreasing behaviour of the nanohillock diameter D with increasing of the ionic velocities v, similar to the behaviour of the neutralization energy. This can be explained by the dominant influence of the neutralization energy on the creation of the nanohillocks for low ionic velocities $v < v_c$. Also, for both types of targets, the nanohillock diameters increase with increasing the ionic charge. According to the relation (2) the type of the target has the significant influence on the nanostructure size. For the same Z, hillock diameters obtained on Au target are systematically larger than those obtained on Ti surfaces. Namely, the energy density $\epsilon_c = \kappa_c\epsilon_{c0}$ of the gold target $\epsilon_c = 5.4 \cdot 10^{-5}$ a.u. is smaller than the energy density of titanium $\epsilon_c = 7.5 \cdot 10^{-5}$ a.u, so that, according to the relation (2) the nanohillock diameter is larger.

Acknowledgments

This work was supported in part by the Ministry of Education, Science and Technological Development of the Republic of Serbia (Project 171016, 171029). D. Banaś

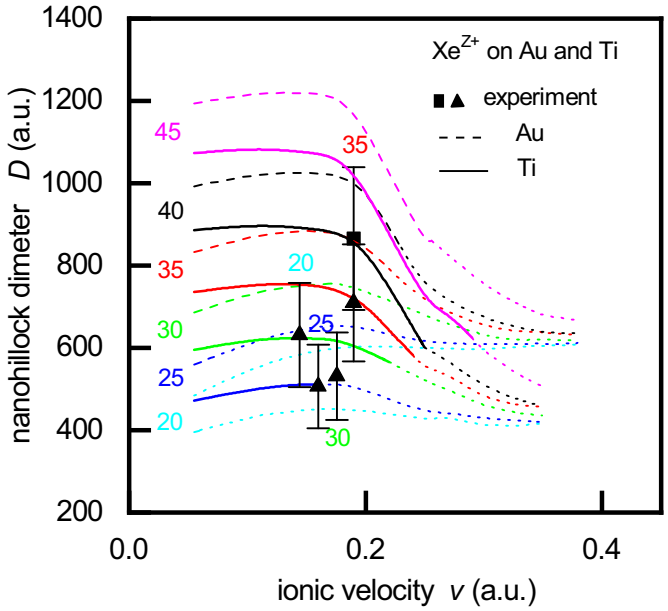

Figure 2: Diameter of the nanohillocks formed on the titanium and the gold targets by an impact of the Xe^{Z+} ions, $Z = [20, 45]$, versus ionic velocity. Solid and dashed curves are for $v < v_c$ and Ti ($\kappa_c = 0.05$) and Au ($\kappa_c = 0.043$) targets, respectively, and dotted curves are for $v > v_c$. Full triangles (Ti) and square (Au) are the experimental values, see Stabrawa et al. 2017.

and I. Stabrawa are grateful for the financial support of the European Regional Development Fund in the framework of the Polish Innovative Economy Operational Program (contract no. WNP-POIG.02.02.00-26-023/08) and the Development of Eastern Poland Program (contract no. POPW.01.01.00-26-013/09-04) for the purchase of the equipment.

References

Majkić, M. D., Nedeljković, N. N. : 2021, *Vacuum*, **190**, 110301. Nedeljković

Nedeljković, N. N, Majkić, M. D., Božanić, D. K., Dojčilović, R. J.: 2016, *J. Phys. B: At. Mol. Opt. Phys.*, **9**, 125201.

Nordlund, K., Djurabekova, F.:2014, *J. Comput. Electron.*, **13**, 122141.

Stabrawa, I., Banaś, D., Kubala-Kukuś, A., Szary, K., Braziewicz, J., Czub, J., Jabłoński, Ł., Jagodziński, P., Sobota, D., Pajek, M., Skrzypiec, K., Mendyk, E., Teodorczyk, M.: 2017, *Nucl. Instrum. Methods Phys. Res. B* , **408**, 235-240

Toulemonde, M., Dufour, C., Paumier, E.: 1992, *Phys. Rev. B*, **46**, 14362.

Publ. Astron. Obs. Belgrade No. 102 (2022), 129 - 132 *Contributed Paper*

COMBINING PLASMA-ASSISTED SYNTHESIS OF METAL OXIDE NANOPARTICLES WITH THIN FILMS DEPOSITION

NATALIE TARASENKA, VLADISLAV KORNEV, ALENA NEVAR, MIKHAIL NEDEL'KO, ANTON RADOMTSEV and NIKOLAI TARASENKO

B.I. Stepanov Institute of Physics, National Academy of Sciences of Belarus, Minsk, 220072, Belarus
E-mail natalie.tarasenka@dragon.bas-net.by

Abstract. Two approaches were developed for the simultaneous synthesis and deposition of metal oxide nanostructured thin films based on atmospheric pressure electrical discharge in contact with liquid and laser ablation in the applied electric field. Both techniques allowed formation of uniform thin films of zinc oxide promising for photovoltaic and photodetector applications. Laser-assisted approach demonstrated the possibility of non-spherical flower-like nanomaterials deposition that may find application in fabrication of supercapacitors electrodes.

1. INTRODUCTION

Nanosized materials offer a row of improved characteristics that can result in expanding the application range and overcoming the limitations and drawbacks of many current devices. Among the fields that are intensively developing due to the application of novel nanostructured materials is energy generation and storage. Recent advances in this field are associated with the development of new composite nanostructured materials, such as nanomaterials based on carbon, nanostructured inorganic materials, coordination polymers, perovskites, nanostructures of transition metal oxides, etc (Wang et al. 2020). Typically, nanoparticles (NPs) properties are determined by their size, composition and structure. In addition, a number of applications often require NPs deposition into thin films and ordered structures that imply that apart from the development of novel NPs synthesis methods, the new efficient techniques for NPs deposition are required. In this work we report on new approaches based on laser- and plasma-assisted synthesis of NPs in liquids with their simultaneous electrodeposition from a colloidal solution onto the substrate for thin films formation. These approaches allow gaining the main benefits of the plasma-assisted NPs synthesis in liquids: a versatility, simplicity, possibility of control over the particles formation processes along with the deposition of homogeneous nanostructured layers. Plasma-assisted

synthesis based on pulsed laser ablation in liquid (LAL) and on gaseous discharge in contact with liquid are known as the 'green synthesis' techniques as they provide non-inhalable colloidal NPs with no residues or chemical by-products, while often no further purification is required.

The developed approaches have been verified for the production of ZnO and CuO thin films on the conductive substrates such as a transparent conductive oxide or any other metal plate. In recent years, much attention has been paid to the production and study of semiconductor oxide thin films, which is associated with the wide possibilities of their practical application, in particular, for the creation of various types of detectors, photo- and optoelectronic devices (Velusamy et al. 2017). Among them, CuO and ZnO form an important pair for making heterojunctions for photodetectors and solar cells (Prabhu et al. 2017, Yang et al. 2014).

2. EXPERIMENTAL

For the synthesis of NPs and their deposition two methods were used, the schemes of the experimental setups used in the experiments are shown in Fig. 1. First, the method of electrodeposition from a colloidal solution formed in the process of an electrical discharge over the surface of the solution was used (Fig. 1a). In this setup, metal oxide NPs are produced by the method of electrical discharge with a liquid electrode. The discharge was powered by a stabilized source with a maximum voltage of 3.6 kV and a current of 5 mA. As a cathode, a thin hollow metal capillary was used with argon flowing through it, the argon flow rate was about 20 mL/min. The cathode was made of stainless steel with outer and inner diameters 800 μm and 500 μm, respectively, and was located at a distance of 3 mm from the liquid surface. As an anode, zinc or copper plates were used, immersed in a cuvette with a liquid. The advantage of this approach is that it operates under normal atmospheric conditions and does not require a sealed chamber. As the power source voltage increased, a breakdown of the discharge gap between the liquid surface and the end of the opposite electrode occurred, and a glow discharge of atmospheric pressure was ignited. The magnitude and stability of the discharge current characteristics depended on the source voltage and the argon pumping rate. To deposit the resulting NPs on the substrate and form thin-film structures, an additional substrate was placed in the cuvette, which was a glass plate with a sputtered ITO (indium tin oxide) layer. This substrate was connected to the power source through an additional ballast resistance (6.8 MΩ). The composition, morphology, and optical properties of the resulting nanoparticles and films have been studied by means of UV-Vis, Raman and FTIR spectroscopy, scanning and transmission electron microscopy.

The second approach uses laser ablation for the NPs synthesis. The scheme of the setup is presented in Fig. 1b. In the proposed scheme, the target is included in the electrical circuit as an anode, while as a counter electrode the conducting substrate can be used (metal foil, ITO, carbon fiber). In such a configuration NPs morphology and composition can be varied by changing not only laser parameters (wavelength, pulse duration, laser fluence), liquid and target composition, but also

upon the variation of the applied electric field. The production of particles in the presence of an external field leads to the deposition of the forming nanostructures on the cathode, which can serve as a tool for assembling the resulting particles into ordered structures.

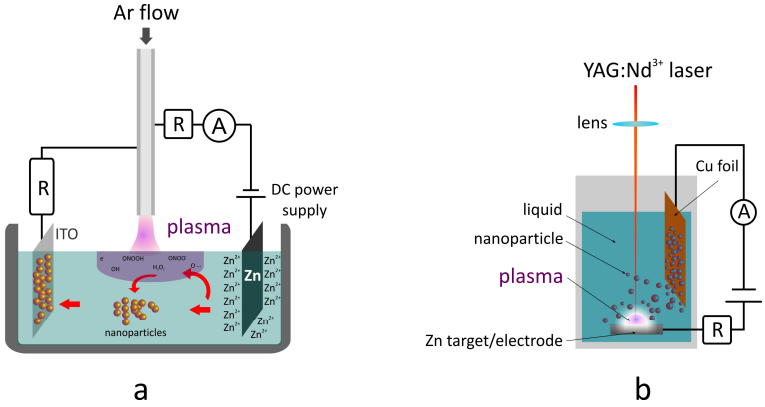

Figure 1: The experimental setups for simultaneous synthesis and deposition of NPs based on electrical discharge in contact with liquid (a) and laser ablation in liquid (b).

3. RESULTS AND DISCUSSION

Both techniques demonstrated a possibility of metal oxides thin-film layers formation on conductive substrates immersed in a solution during the plasma-assisted synthesis. In a discharge with a liquid electrode, plasma is formed between an electrode in the gas phase and a solution surface with a metal electrode immersed in the solution. The presence of electrons and ions in the gas discharge leads to the flow of current through the solution and to the initiation of electrochemical reactions, including dissolution of metal at the anode and reduction of metal cations from the solution at the cathode. Charged particles from the solution further migrate towards the conductive ITO plate at the cathode forming the thin film. As can be seen from its typical SEM image (Fig. 2a), the deposited films are composed of evenly distributed densely packed clusters of particles. Upon closer examination of the samples, it can be found that the shape of the particles is close to spherical, the average particle size is 50-80 nm, while the particles have a rather narrow size distribution. The particles had a hexagonal wurtzite-type ZnO structure that can be concluded from the Raman spectra analysis, shown in Fig. 2b. The major peaks found at 99 cm^{-1} and 437 cm^{-1} correspond well to the E_2^{low} and E_2^{high} vibrational modes in hexagonal ZnO crystal. The high intensity of these modes compared to the defect-induced LO band typically observed at around 580 cm^{-1} indicates of a high crystal quality of the formed nanocrystals (Mediouni et al. 2022). The deposited ZnO film was further used for preparation of multilayered thin film structures. As an example, a heterostructure has been formed by deposition of CuO over the ZnO layer. The resulting thin film heterostructure shows a photosensitive nature demonstrating a nonlinear diode-like behavior as

shown in Fig. 2c. From the i-V characteristics, it is found that the forward threshold or turn-on voltage (V_{on}) of the fabricated n-ZnO/p-CuO heterojunction is 2.0 V. Thus, the fabricated from ZnO/CuO heterojunctions can be used for production of low-cost photodiodes, photodetectors, solar cells and gas sensors.

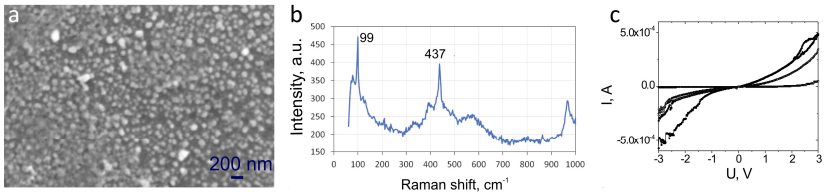

Figure 2: Thin films formed by electrodeposition from a colloidal solution prepared by atmospheric pressure plasma in contact with the solution: a - SEM image of the ZnO film, b - Raman spectra of ZnO, c – current-voltage characteristics of the bilayer ZnO/CuO heterostructure in the dark and under illumination (100 mW/cm^2).

The second approach based on laser ablation of a target in a liquid in the applied electric field also showed the applicability towards thin films formation. The results showed that application of the external electric field may serve as a tool to control the morphology of the prepared NPs. For example, nanostructures having a complex lamellar structure that are combined into layered flower-like structures with a size of several μm can be formed. Such structures, consisting of several interconnected layers, may have great prospects for use as a material for supercapacitor electrodes, since they can significantly increase the surface area while maintaining a small volume.

The analysis of the plasma evolution allowed drawing the conclusion on much shorter plasma lifetime if the external electric field is applied to a Zn target. Formation of non-spherical nanostructures can be attributed to the difference of NPs formation mechanism in electrical-field assisted laser ablation. By variation of the liquid composition it is possible to extend the possibilities of the developed approach that has been demonstrated by the formation of composite metal-carbon nanoparticles promising for supercapacitor applications. In general, the method introduces new possibilities for the control of morphology and composition of nanostructures obtained by laser ablation in a liquid.

The work was partially financed by the National Academy of Sciences of Belarus under project Convergence 2.2.05 and by the Belarusian Foundation for Fundamental Researches under Grants No. F 21KOR-006 and F21RM-104.

References

Mediouni, N., Guillard, C., Dappozze, F., Khrouz, L., Parola, S., et al. : 2022, *J. Hazard. Mater. Adv.*, **6**, 100081.
Prabhu, R.R. et al. : 2017, *Mater. Sci. Eng. B*, **220**, 82.
Velusamy, T., Liguori, A. et.al. : 2017, *Plasma Process. Polym.*, **14**, 1.
Wang, H., Liang, X., Wang, J., Jiao, S., Xue, D. : 2020, *Nanoscale*, **12**, 14.
Yang, C., Xiao, F.,Wang, J., Su, X. : 2014, *J. Colloid Interf. Sci.* **435**, 34.

Publ. Astron. Obs. Belgrade No. 102 (2022), 133 - 136 *Contributed Paper*

PULSED LASER ASSISTED FABRICATION OF Co-DOPED ZnO NANOCRYSTALLINE LAYERS ON A GLASS SUBSTRATE

NATALIE TARASENKA[1], VLADISLAV KORNEV[1], SVETLANA PASHAYAN[2] and NIKOLAI TARASENKO[1]

[1]*B.I. Stepanov Institute of Physics, National Academy of Sciences of Belarus, Minsk 220072, Belarus*

[2]*Institute for Physical Research, National Academy of Sciences of Armenia, 0203, Ashtarak-2, Republic of Armenia*

E-mail n.tarasenko@ifanbel.bas-net.by

Abstract. In this work, we present a new approach for fabrication of Co-doped ZnO nanocrystalline films based on the pulsed laser treatment of Co/ZnO layers on a glass substrate. The purpose is to achieve the incorporation of Co^{2+} ions on the Zn site inside ZnO nanoclusters through the fast laser induced heating, subsequent melting, and re-solidification processes at high cooling rates.

1. INTRODUCTION

Doped semiconductors nanostructures are of special interest in recent years due to the fact that their electronic, optical and magnetic properties can be tuned by varying their composition and size thus finding exceeding applications in electronics, engineering, plasmonics, biomedicine and catalysis (Yoo, Hocheon, et al. 2021, Wang, C. et al. 2012). The dependence of the doped NPs properties on size and composition explains the importance of control over their preparation procedure. Among the different techniques for NPs synthesis, plasma and laser assisted processes have received much attention last years due to the combination of such advantages, as high production rate, versatility and possibility of control over the NPs formation process (Tarasenka, N. et al. 2017, Kulinich, S. et al. 2013). However, although a number of successful applications of these processes for NPs production have been demonstrated, a task of the targeted fabrication of alloyed and doped NPs with controlled properties is still not completely solved.

This paper is focused on the pulsed laser assisted fabrication of Co-doped ZnO nanocrystalline layers on a glass substrate. Among the different doped ZnO structures, cobalt-doped ZnO films have attracted much attention because of their

potential applications in magneto-electrical and magneto-optical devices, spintronics, and as laser passive Q-switchers. Zinc oxide is a wide band gap semiconductor which is promising for these applications because of its chemical stability, low toxity and low cost. The composition, morphology, and optical properties of the resulting nanoparticles and films have been studied.

2. EXPERIMENTAL

The developed method of doped ZnO nanoparticles preparation is based on laser irradiation of the bi-layer structure consisting of the ZnO and Co films. The scheme of the experimental procedure is presented in Figure 1. First, 100 nm ZnO layer was deposited onto a glass substrate by magnetron sputtering technique. For the Co layer, Co NPs colloid was prepared by laser ablation of Co target in acetone. For this, Nd:YAG laser, operating on the fundamental harmonic (1064 nm) with a pulse duration of 8 ns, energy 80 mJ/pulse, repetition rate 10 Hz was used. After that Co NPs deposition was carried out by spin-coating over the preliminarily formed ZnO layer. Finally, laser treatment of the Co/ZnO bilayer film was performed using the 4th harmonic of a ns Nd:YAG laser (wavelength 266 nm, pulse repetition 10 Hz, energy 0.5-5.5 mJ/pulse, laser beam diameter 2 mm). In order to establish the optimal conditions for the doping, the dependence of Co incorporation on the laser parameters was studied. After adjusting the laser fluence to provide several hundreds nanometer penetration depth for the incident laser radiation it was possible to deliver very rapid melt/solidification cycles.

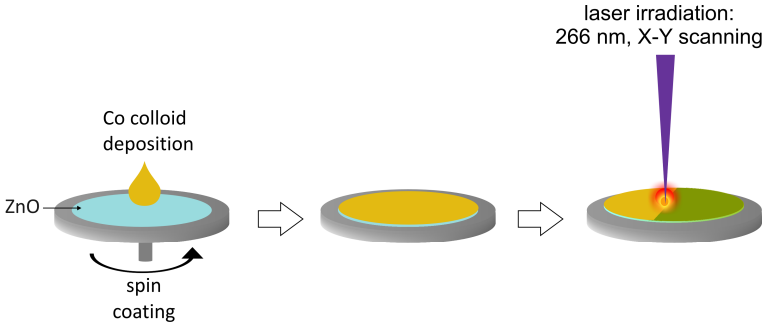

Figure 1: Scheme of the experiment on laser processing of the bilayer Co-ZnO structure

The morphology, structure and optical characteristics of the fabricated films depending on the experimental conditions were analyzed. To quantify the Co content in the sample after laser treatment, LIBS analysis of the samples composition was performed. The results showed the formation of the films with a rather homogenous distribution of cobalt ions inside the ZnO matrix with a dopant concentration of about 5%. The incorporation of Co ions into the ZnO structure could be also elucidated from the Raman spectra and XRD analysis.

3. RESULTS AND DISCUSSION

Incorporation of dopants has substantial effect on the optical properties of ZnO that were studied by measuring UV-Vis absorption spectra of the prepared films. The analysis of the absorption spectra was used to determine the changes in the energy band structure of ZnO in result of Co doping. The absorption spectrum of the ZnO film has a typical form for the zinc oxide structures, and, as can be seen in Figure 2, it consists of a wide band in the ultraviolet region of the spectrum with a rapid increase in the absorption near the band gap (at a wavelength of ~ 370 nm). The absorption spectrum of ZnO-Co sample after laser irradiation shows the absorption (Figure 2a) around 370–395 nm, and the absorption edge is slightly shifted upon cobalt doping in ZnO, which confirms the presence of Co in the crystal lattice of ZnO. In addition, in the irradiated sample several additional absorption bands at around 565 nm, 603 nm and 644 nm were observed that are typical to the Co-doped ZnO samples and correspond to the d–d transition of Co^{2+} ions in the tetrahedral field of ZnO (Ji, H. et al. 2018).

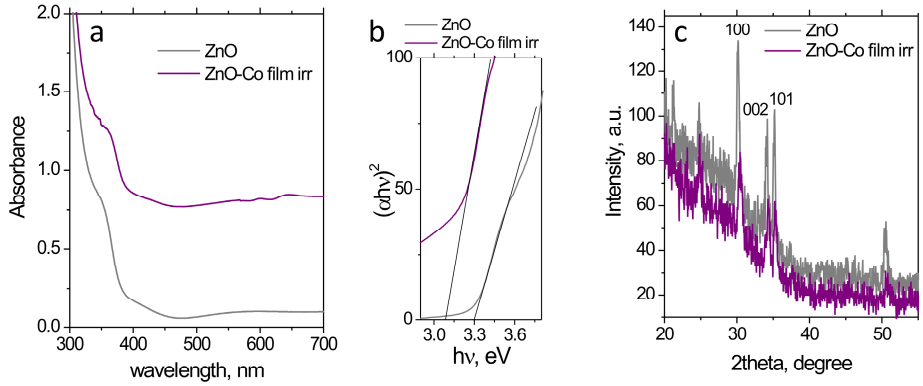

Figure 2: Properties of the ZnO and Co/ZnO films on the glass substrate after laser treatment (5.5 mJ/pulse): a – optical absorption spectra; b – Tauc plots: c – XRD patterns

The band gaps of the prepared ZnO samples were estimated using the Tauc`s model, being 3.13 eV and 3.3 eV for the Co-doped ZnO and pure ZnO films, respectively (Figure 2b). As can be seen the band gap values for both films were slightly lower than the tabulated value for the bulk material (Eg = 3.37 eV). This can be caused by the formation of defective energy levels near the bottom of the conduction band, for example, due to the partial non-stoichiometry of the film composition.

XRD of the fabricated thin films presented in Figure 2c, revealed the wurtzite-type structure of the formed samples. Cobalt ions introduced as dopants shifted the diffraction peaks to higher angles, suggesting the unit cell contracting. Variation of

the ZnO XRD peaks relative intensity additionally supports the conclusion on Co^{2+} substitution of Zn^{2+} in the ZnO lattice with the Co-doped ZnO formation.

Thus, the performed studies have shown the possibility of Co-doped zinc oxide thin films formation in the process of laser treatment of zinc and cobalt films. The results obtained are of interest for further development of laser ablation methods for solving practical problems of the doped nanostructures synthesis with controlled size and composition.

Acknowledgments

The work was partially financed by the National Academy of Sciences of Belarus under project Convergence 2.2.05.

References

Ji, H., Cai, C. et al.: 2018, *J. Mater. Sci.*, **29**, 12917.
Kulinich, S. et al.: 2013, *J. Appl. Phys.*, **113,** 033509.
Tarasenka, N., et al.: 2017, *Nano-Struct. Nano-Objects,* **12,** 210.
Wang, C. et al.: 2012, *AIP Advances,* **2**, 012182.
Yoo, H. et al.: 2021, *Nanomaterials* **11**, 832**.**

Publ. Astron. Obs. Belgrade No. 102 (2022), 137 - 140 *Contributed Paper*

ELEMENTAL ANALYSIS OF AUSTENITIC STEEL BY CALIBRATION-FREE LASER-INDUCED BREAKDOWN SPECTROSCOPY (CF-LIBS)

I. TRAPARIĆ[1], M. JOVANOVIĆ[1], M. KUZMANOVIĆ[2] and M. IVKOVIĆ[1]

[1]*Institute of Physics, University of Belgrade, PO Box 68, 11080 Belgrade, Serbia*

[2]*Faculty of Physical Chemistry, University of Belgrade, Studentski trg 12 - 16, 11158 Belgrade, Serbia.*

E-mail ivke@ipb.ac.rs

Abstract. Diagnostics of the plasma-facing components (PFC) of a fusion reactor is vital for the safe operation of the device. In this paper, the calibration-free (CF) LIBS procedure was used to assess the chemical composition of an ITER-relevant material, an austenitic steel sample. The self-absorption correction of the intensities of the chosen spectral lines was done for each element, using the estimated plasma temperature and the internal reference line. Obtained results suggest that this method could be suitable for the chemical analysis of austenitic steels, but further investigation is needed to quantify its analytical performance fully.

1. INTRODUCTION

The structural materials of fusion reactors are subjected to thermal, mechanical, chemical, and radiation loads. Due to their excellent manufacturability, good mechanical properties, welding ability, and corrosion resistance, austenitic stainless steels were chosen as structural reference material for ITER (P.J. Maziasz and J.T. Busby, 2012). In addition, to diagnose the composition of the deposits on the fusion reactor's first wall, test targets made of austenitic steel (AISI 316 L) were settled at ten positions on the LHD at NIFS in Japan (V. Kh. Alimov et al., 2019). A CF-LIBS analysis of the LIBS 316L(N)-IG (ITER Grade) was conducted to evaluate the applicability of LIBS for the determination of the composition of test targets and deposits at reactor walls.

2. EXPERIMENTAL SETUP

The experimental setup is shown in Figure 1. Target AISI 316L (YUS = Č.45703, DIN = X2CrNiMo17-12-2, EN 1.4404) plates were placed on the PC controllable x-y table. The impulse from Nd:YAG Q-switch laser (Quantel, λ = 532 nm, energy 55 mJ, pulse duration 6 ns) was focused on a target with a lens whose focal length

is 15 cm. Light emitted from a plasma was collected using fiber optic cable (Ø = 400 μm) and detected using Andor Tech. Mechelle 5000 spectrograph equipped with Andor iStar DH734 camera. The camera was triggered using an external photodiode, and the gating of the camera was done with the help of the external Stanford Research System Digital Delay Generator DG535.

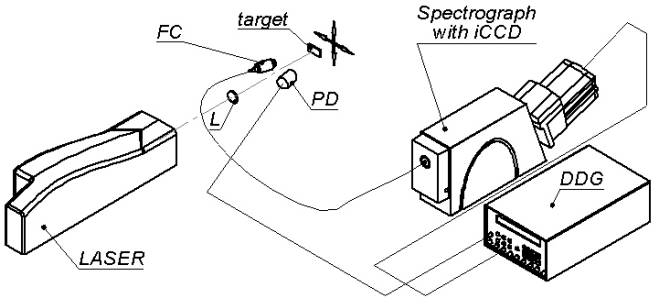

Figure 1: LIBS experimental setup

Delay was set to 0.6 μs, and 3 μs and 30 μs gates were used. LIBS experiments were performed in air at atmospheric pressure.

3. RESULTS

A part of the spectrum, in the range 350 nm to 370 nm, recorded for two different delay times is shown in Figure 2.

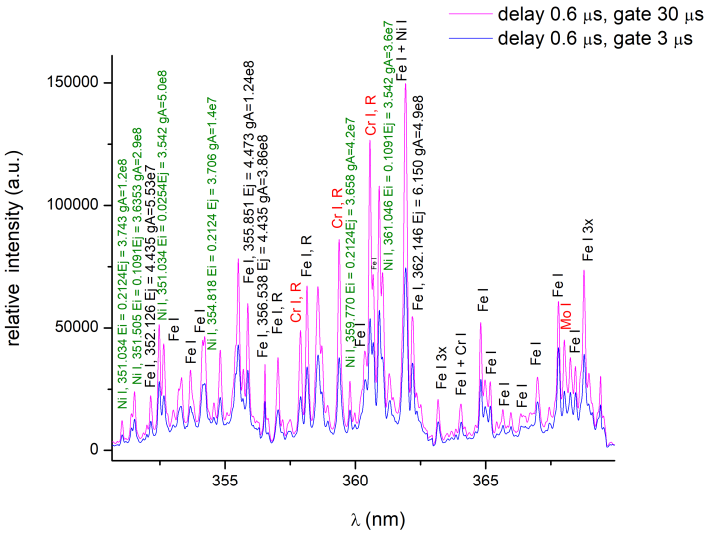

Figure 2: Part of the recorded spectrum with identified lines of Fe I, Ni I, Mo I, and Cr I.

For both delay times, 30 spectra were averaged to obtain the final one, and the gain of 100 was set to amplify the signal further and improve the signal-to-noise ratio.

Quantitative analysis was done using a calibration-free algorithm proposed by Yang et al. (Yang et al., 2018). As a first step, internal reference lines were selected manually for each plasma species. In the next step, self-absorption (SA) correction of the internal reference line was done using the following formula (Yang et al., 2018):

$$f_\lambda^s = f_{\lambda_R}^s \left(I_\lambda^{ki} / I_{\lambda_R}^{mn}\right)\left(A_{mn} g_m / A_{ki} g_k\right) e^{E_k - E_m / k_B T} \quad (1)$$

where f_λ and $f_{\lambda R}$ are the SA coefficients of the analytical and internal reference line; I_{mn}, A_{mn}, g_m, and I_{ki}, A_{ki}, g_k, are the intensity, coefficient of spontaneous emission, and statistical weight of the upper level for reference and analytical line, respectively.

In the third step, Boltzmann plots, constructed using uncorrected intensities of spectral lines for each analyte, were used to determine excitation temperatures. After this, the optimal temperature was searched in the interval ($T_{\min}$, $T_{\max}$) using Particle Swarm Optimization (PSO) algorithm. The selection of temperature interval was based on the minimal and maximal estimated temperatures from Boltzmann plots ($T_{\min}$ = 7477 K, and $T_{\max}$ = 18567 K). Number of particles was set to 20, inertia coefficient was w = 0.6, and cognitive and social coefficients were c_1 = c_2 = 0.5. The optimal temperature was found to be 7920 K (0.68 eV).

Finally, using equation (2) (Yang et al., 2018) and the optimal temperature found by PSO, we were able to correct the analytical lines for self–absorption:

$$I_\lambda^s = \left(I_{\lambda_R}^{mn} / f_{\lambda_R}\right)\left(A_{ki} g_k / A_{mn} g_m\right) e^{E_m - E_k / k_B T_{opt}} \quad (2)$$

Results of the optimization process are shown in figure 3.

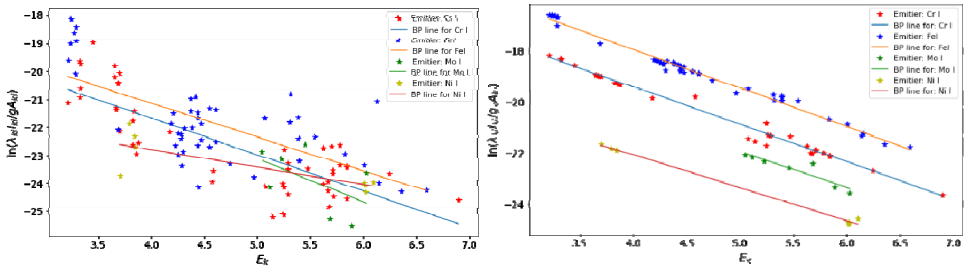

Figure 3. Boltzmann plots before any correction (left) and after all corrections (right).

After all corrections, concentrations of all species were calculated using standard calibration–free procedure (Yang et al., 2018):

$$c_s = \frac{1}{F} U_s(T) e^{q_s} \quad (3)$$

Here, F is the experimental parameter that includes the optical efficiency of the collecting system, $U_s(T)$ is the partition function of given species for temperature T, and q_s is the intercept of the Boltzmann plot.

Parameter F was determined from the following condition:

$$\sum_{s=1}^{n} c_s = \frac{1}{F}\sum_{s=1}^{n} U_s(T)e^{q_s} = 1 \quad (4)$$

By applying the described CF model to the experimentally determined intensities of spectral lines, the following elemental composition of the analyzed sample was calculated: Fe - 89.5%, Cr - 8.3 %, Mo - 1.7 %, and Ni - 0.50 %.

4. CONCLUSION

The applied CF model successfully corrected Boltzmann plots for self-absorption, but the obtained concentrations deviate significantly from the expected chemical composition of this type of steel. Careful analysis of the relative spectral intensities of the Fe, Mo, Cr, and Ni lines, considering the measured temperature value, indicates that the declared composition most likely does not correspond to the tested sample. In the next step, an independent chemical analysis of the same sample is planned to confirm the validity of the applied model for the analysis of this type of steels.

Acknowledgements

The research was funded by the Ministry of Education, Science and Technological Development of the Republic of Serbia, Contract numbers: 451-03-68/2022-14/200024 and 451-03-68/2022-14/200146, and supported by the Science Fund of the Republic Serbia, Grant no. 3108/2021.

References

Maziasz P.J., Busby J.T.: 2012, *Comprehensive Nuclear Materials*, Editor(s): Rudy J.M. Konings, Elsevier.

Cuicci A., Corsi M., Palleschi V., Rasteli S.: 1999, *Applied Spectroscop*y **53**, 960.

Alimov V. Kh., Yajima M., Masuzaki S., Tokitani M.; 2019, *Fusion Engineering and Design* **147,** 111228.

Yang J., Li X., Xu J., and Ma X.: 2018, *Applied Spectroscopy* **72**, 129.

Publ. Astron. Obs. Belgrade No. 102 (2022), 141 - 144 *Contributed Paper*

TREATMENT OF STEEL 16MnCr5 AND STEEL 42CrMo4 BY PLASMA FLOW GENERATED IN MAGNETOPLASMA COMPRESSOR

NORA TRKLJA BOCA[1], ŽARKO Z. MIŠKOVIĆ[2], RADIVOJE M. MITROVIĆ[2], BRATISLAV M. OBRADOVIĆ[1] and MILORAD M. KURAICA[1]

[1]*University of Belgrade, Faculty of Physics, P. O. Box 44, 11000 Belgrade, Serbia*
E-mail nora@ff.bg.ac.rs

[2]*University of Belgrade, Faculty of Mechanical Engineering, Kraljice Marije 16, 11000 Belgrade, Serbia*

Abstract. Two types of steel samples (16MnCr5, 42CrMo4) have been treated with plasma pulses created in magnetoplasma compressor, using helium - hydrogen mixture as a working gas. The energy flux density of the plasma flow in the region of plasma-sample interaction area is 9 J/cm2. Plasma melts the near-surface layer. During the rapid cooling process, a thin layer with structure different from initial is created. Changes in the physical composition of the substrate are monitored depending on the number of plasma treatments. After treatment with a plasma produced within MPC, a significant improvement of hardness has been achieved.

1. INTRODUCTION

Magnetoplasma compressor (MPC) is a plasma accelerator with operation based on the common theory of dense plasma flow and acceleration developed by Morozov, see Morozov 1968. High thermal loads, produced by plasma formed, accelerated and compressed within MPC device, are used for modification of steel samples. Steel 16MnCr5 has very good machinability, mechanical properties and weldability. Steel 42CrMo4 is a steel for tempering, with a good combination of strength and toughness in the quenched and tempered condition. The treatment with a plasma can further enhances the favorable characteristics of these materials.

2. EXPERIMENTAL SET-UP AND METHODS

The experimental setup is described in detail in Puric et al. 2003. The lifetime of the compressed plasma flow within analyzed experimental condition is around 150 μs, plasma velocity is up to 50 km/s, electron density and temperature are of the order of 10^{22} m^{-3} and 1 eV, respectively.

Four types of analysis have been used to characterize the modifications on steel surfaces after treatments with plasma: optical microscopy, hardness measurement (Zwick Mic 10 Hand Hardness Instrument), roughness measurement (MarSurf XR1 Surface Roughness Tester) and X-ray diagnostics (Rigaku Smartlab X-ray Diffractometer). Spectral investigation of the plasma-surface interaction area is realized using one meter spectrometer and PIMAX1 ICCD camera.

3. RESULTS AND DISCUSION

The experimental setup enables spectra recording at the position where plasma – material interaction is realized. Radiation is collected using the optic fiber. Collected data includes radiation from different spatial coordinated along the one analyzed optical path, with different electron densities contribute simultaneously to the overall profile. Hβ line has been fitted with two Voigt functions whose widths have been used for electron density calculation (Fig. 1). The wide Voigt function represents the influence of the radiation from the central region of the plasma flow, while the narrow function represents the influence of the outer region of the plasma flow. The average electron temperature value in the region close to the target surface is 1 eV and it was estimated using the Saha equation and relative intensity ratio of Fe I and Fe II lines.

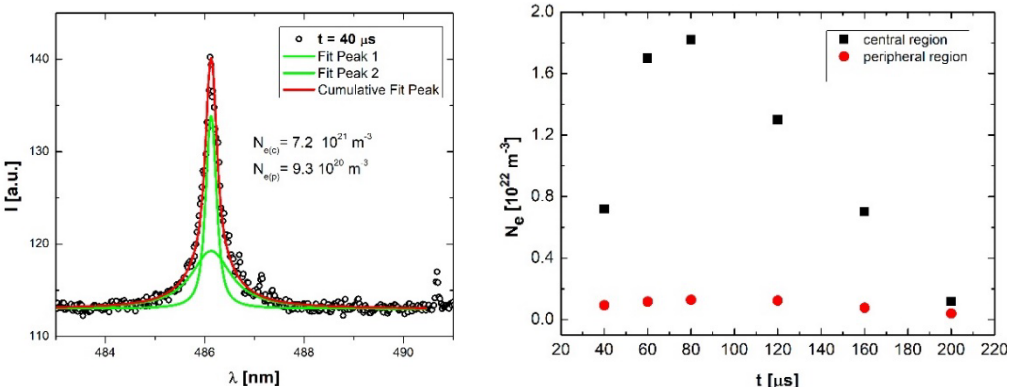

Figure 1: Fitting of H_β line and calculation of electron density.

Steel samples (1 cm x 1 cm) were divided into five groups: untreated, exposed to one plasma shot, to three, to five and to ten plasma shots. Position of the steel samples is fixed at z = 4.5 cm. Every plasma shot deposits 9 J/cm^2 of energy to the surface of the treated material, based on the results of calorimetric measurements, see Trklja et al. 2019.

After one plasma pulse, structures in the shape of the vortex are formed during fast cooling process (quenching effect). After the next pulses, new vortex structures are formed and the morphology of the surface is changing, see Trklja Boca et al. 2021.

When 16MnCr5 steel samples are treated with plasma, the initial hardness value is increased, independent of the number of plasma shots. From the initial 160 HV, the hardness goes up to 270 HV (Fig. 2). When samples are made from steel with the addition of chromium and molybdenum (42CrMo4), the hardness is increased after each treatment with plasma, indicating that it may continue to increase, no saturation was reached. After ten plasma shots, the hardness is 375 HV (Fig. 2).

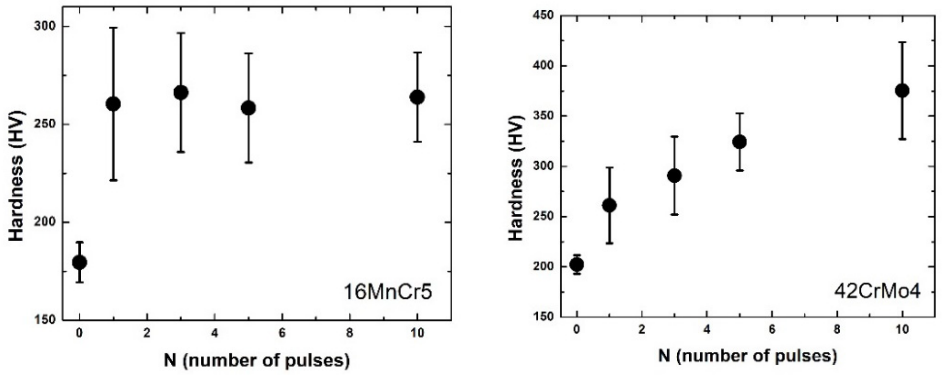

Figure 2: Hardness of the steel samples before and after 1, 3, 5 and 10 plasma treatments.

The roughness was measured in a fraction of the radius along the surface relative to the center of incidence of the plasma flow. Ten plasma pulses make a peripheral region of every treated sample smoother then the central region, see Fig. 3. The molten material of the sample is blown away by the plasma flow and forms a smooth layer on the periphery.

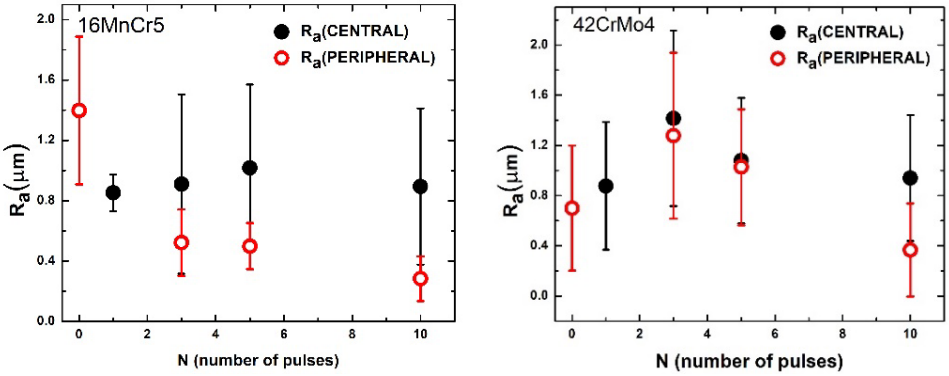

Figure 3: Roughness of the steel samples before and after 1, 3, 5 and 10 plasma treatments

Untreated thin surface layer of all analyzed steel samples contains only α-Fe. Small phase changes of only several weight percent of γ-Fe in the treated 16MnCr5 and 42CrMo4 steel samples were diagnosed.

4. CONCLUSIONS

Modification of steel 16MnCr5 and steel 42CrMo4 samples treated by an accelerated and compressed plasma flow formed within MPC have been monitored depending on the number of plasma treatments. Significant change of several characteristics of steel materials treated by a plasma produced within MPC, such as surface hardness and roughness, without compromising the properties within the depth of the sample, has been achieved.

References

Morozov, A. I.: 1968, *Soviet physics – technical physics*, **12**, 1580

Purić, J., Dojcinovic, I. P, Astashynski, V. M., Kuraica, M. M., Obradovic, B. M.: 2003, *Plasma Sources* Sci. Technol., **13**, 74.

Trklja, N., Iskrenovic, P. S., Miskovic, Ž. Z., Krstić, I. B., Obradovic, B. M., Mitrović, R, M., Kuraica, M. M.: 2019*, JINST*, **14**, C09041.

Trklja Boca, N., Mišković, Z.Ž., Mitrović, M. R. Obradović, M.B., Kuraica, M.M.: 2021, *Surf.and Surf.Coat*., **416**, 127157.

Publ. Astron. Obs. Belgrade No. 102 (2022), 145 - 148 *Contributed Paper*

ODS+Hf and AISI 316L STEEL SURFACE VARIATIONS at HIGH LASER INTENSITY, 10^{13} W/cm^2, in AIR and VACUUM: COMPARATIVE STUDY

M. TRTICA[1], J. STASIC[1], X. CHEN[2] and J. LIMPOUCH[3]

[1]*Vinca Institute of Nuclear Sciences - National Institute of the Republic of Serbia, University of Belgrade, P.O. BOX 522, 11001 Belgrade, Serbia*
E-mail etrtica@vinca.rs; jelsta@vinca.rs

[2]*School for Mechanical and Electrical Engineering, Wenzhou University, Wenzhou City, PC325035, People's Republic of China*
E- mail 30046766@qq.com

[3]*Faculty of Nuclear Sciences and Physical Engineering, Czech Technical University in Prague, CZ-115 19 Prague, Czech Republic*
E-mail jiri.limpouch@fjfi.cvut.cz

Abstract. The behavior of Oxide Dispersion Strengthened (ODS) steel with addition of hafnium, as well as AISI 316L steel, at high laser intensity of ~10^{13} W/cm^2 in ambiences of air and vacuum, was studied. Irradiation source was Ti:Sapphire laser operating at 804 nm and pulse length of ~65 fs. Morphological and chemical studies were considered, thus that: (i) given laser intensity induced damages on both steels with the damage being more prominent on AISI 316L steel; (ii) various surface features were present, such as coral-like structure and Laser Induced Periodic Surface Structures (LIPSS), with LIPSS being dominant on the surface; (iii) the interaction was accompanied by generation of plasma above the target, and (iv) chemical analysis has shown that surface elemental content also depends on the ambience used.

1. INTRODUCTION

The development of materials with extraordinary characteristics for applications in engineering (aerospace) and especially in nuclear complex is of constant interest nowadays, Trtica et al. 2020[a]; Suri et al. 2010. In this context, ODS+Hf as well as AISI 316L steel have desirable properties making them potential candidates for use in fusion technology. Among other, both steels have relatively high melting temperature (T_m) (higher by ~100 °C in case of ODS steel) and very good resistance to thermal loading. Both steels are serious candidates for structural fusion reactor materials, and their behavior under strong heat and radiation fluxes, in one approximation, can be simulated using high intensity laser radiation, see

Farid et al.: 2014; Montanari et al.: 2017. The goal of this work was to obtain data on the state of the material/steel under high laser intensity of the order of 10^{13} W/cm^2 in air and vacuum ambience – these researches are still insufficient thus they have applicative as well as fundamental significance.

2. EXPERIMENTAL

ODS steel employed in this work is 16Cr3Al+Hf ODS steel with the following constituents: Fe-16Cr-3Al-1.5W-0.35Y2O3+0.5Hf (wt%; Fe balance), see Dong et al.: 2017. Hafnium was added in the form of powder with purity 99.9% and average size 10 μm before the synthesis process. AISI 316L steel was standard commercial product. The samples were in the shape of plates, 10 × 10 mm, 500 microns thick, with the average roughness 0.8 μm. Experimental setup is explained in details in works, see Trtica et al. 2020[a,b]. Characteristic parameters of the Ti:sapphire laser are as follows: wavelength 804 nm, pulse duration around 65 fs, maximum output energy 12 mJ, operated in TEM_{00} mode. Laser beam was focused with 150 mm lens to 20 μm diameter (irradiated surface was positioned in front of the focus therefore spot sizes on the samples were larger). Irradiation effects were studied in air and vacuum. Microstructural characterization of the samples was conducted using scanning electron microscope (SEM), equipped with energy dispersive X-ray analyzer (EDX) for chemical analysis of the surface. Morphology of the laser-induced damages was investigated using optical profilometer.

3. RESULTS and DISCUSSION

In the main, laser surface variations are affected by numerous parameters of irradiation process – laser parameters (wavelength, pulse duration, pulse count, intensity, etc.), as well as material (absorptivity) and ambience parameters. The effects of fs-laser at 10^{13} W/cm^2 intensity acting on ODS+Hf steel in ambiences of air and vacuum are given in Fig. 1. Registered surface alterations after 100 accumulated pulses are the following: (i) the damage spot has a diffuse character in air unlike the one obtained in vacuum ambience; (ii) central irradiated zone shows sporadic coral-like structure without the appearance of cracking. Also, the initial development of Laser Induced Periodic Surface Structures (LIPSS) was recorded in this region, larger LIPSS with period ~2.4 microns and smaller LIPSS (~0.6 microns) perpendicular to the larger ones; (iii) in the peripheral zone only LIPSS were noted and, (iv) the interaction was accompanied by generation of plasma above the target. Profilometric analysis, Fig. 1, showed the damage was on a superficial level, deeper in vacuum (~2.0 μm) than in air (~1.75 μm), implying that coupling between laser radiation and the surface in vacuum is more efficient. Fs-laser – metal target interaction, see Trtica et al. 2020[a,b], is a complex process which in one approximation comprises the absorption of laser radiation by free electrons, thermalization of electron sub-system (ESS), transfer of energy from ESS to the lattice subsystem, its thermalization, etc.

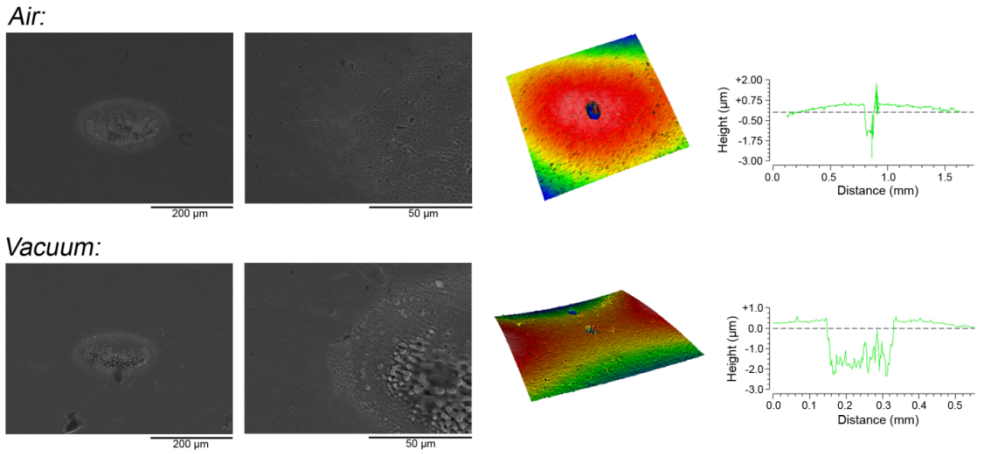

Figure 1: Analysis of the laser damage on ODS+Hf steel: SEM – entire spot and peripheral region; profilometry – 3D and 2D analysis. Laser intensity ≈10^{13} W/cm^2.

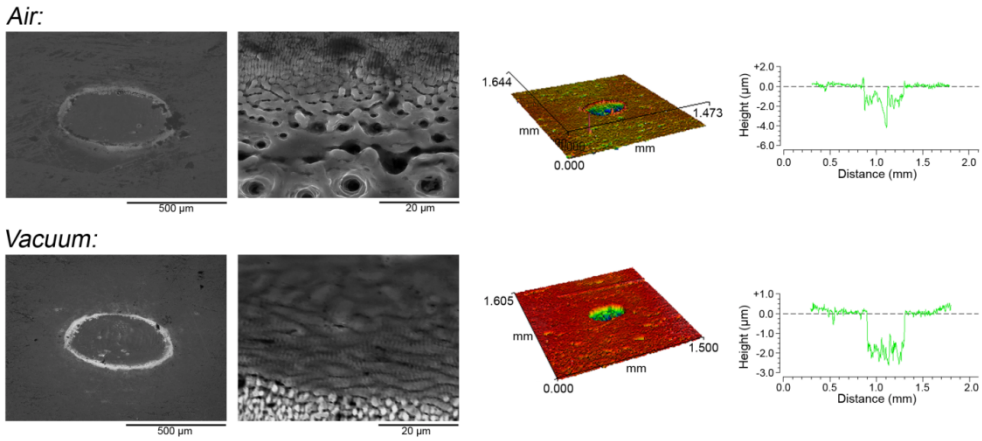

Figure 2: Analysis of the laser damage on AISI 316L steel: SEM – entire spot and peripheral region; profilometry – 3D and 2D analysis. Laser intensity ≈10^{13} W/cm^2.

The effects of fs-laser at 10^{13} W/cm^2 intensity acting on AISI 316L steel in ambiences of air and vacuum is shown in Fig. 2. The noticed surface variations after 100 accumulated pulses can be summarized in the following: (i) the damage spot has a diffuse character in air unlike in vacuum ambience; (ii) generally, the features induced have a more drastic/violent character then in the case of ODS steel. Central as well as peripheral zone are dominantly covered with LIPSS, similar to those on ODS steel; (iii) the transition from coral-like structure to LIPPS is present in the peripheral region; (iv) although the damages are shallow (profilometric analysis, Fig. 2), they showed higher level in vacuum than in air; (v) creation of plasma accompanied this interaction.

It should be pointed out that chemical surface alterations on both steels strongly depend on the ambience used. Also, changes differed depending on the damage area – oxides cleaning in the central zone, oxidation on the periphery in air ambience, local oxidation on ODS steel in vacuum due to oxides contained in the material.

4. CONCLUSIONS

Laser intensity of 10^{13} W/cm^2 induced damages on the surface of ODS+Hf as well as AISI 316L steel. Morphological as well as chemical changes strongly depend on the ambience used. As a rule, more prominent alterations were recorded in vacuum ambience. At this laser intensity used, dominant surface features are LIPSS. The damages are on a superficial level with a tendency to be more prominent on AISI 316L steel, which is probably related to lower melting temperature compared to ODS steel. These investigations have shown that, although laser intensity was high, surface changes are not so significant thus both steels can probably be considered as potential candidates for the use in fusion technology.

Acknowledgements

This research was sponsored by: (i) IAEA through CRP F13020, Contract no. 24076; (ii) Bilateral Project Serbia-China no. 451-02-818/2021-09/17 “Advanced Technologies Based on Pulsed Lasers for Modification/Processing and Synthesis of Selected Metal Materials”; (iii) The Ministry of Education, Science and Technological Development of the Republic of Serbia, contract no. 451-03-68/2022-14/200017; (iv) European Structural and Investment Funds and the Czech Republic-Project Centre of Adv. Appl. Sci. [CZ.02.1.01/0.0/0.0/16_019/0000778] in the frame of the Operational Programme Research, Development and Education; (v) Czech Ministry of Education, Youth and Sports [Project LTT17015].

References

Dong, H., et al.: 2017, *J. Alloys Comp*. **702**, 538.
Farid, N., et al.: 2014, *Nucl. Fusion,* **54**, 012002 (7pp).
Montanari, R., et al.: 2017, *Metals*, **7,** 454.
Suri, A.K., et al.: 2010, *J. of Phys.: Conference Ser.*, **208**, 012001 (16pp).
(a) Trtica, M., Stasic, J., et al.: 2020, *Fusion Engin. and Design*, **150**, 111360 (10pp).
(b) Trtica, M., et al.: 2019, *Appl. Surf. Sciences,* **464**, 99.

Publ. Astron. Obs. Belgrade No. 102 (2022), 149 - 152 *Contributed Paper*

PERSPECTIVE ON THE USE OF NANOPARTICLES TO IMPROVE THE TEA CO_2 BASED LIBS ANALYTICAL PERFORMANCES: COPPER NANOPARTICLES FOR NELIBS ANALYSIS OF POLYPROPYLENE

S. ŽIVKOVIĆ[1], J. PETROVIĆ[1], M. MOMČILOVIĆ[1], M. RADENKOVIĆ[1], N. KRSTULOVIĆ[2], J. CAR[2], D. PALASTI[3], F. CASIAN PLAZA[3] and G. GALBÁCS[3]

[1] *"VINČA" Institute of Nuclear Sciences - National Institute of the Republic of Serbia, University of Belgrade, PO Box 522 11351 Belgrade, Serbia*
E-mail sanjaz@vin.bg.ac.rs

[2]*Institute of Physics, Bijenička cesta 46, 10000 Zagreb, Croatia*

[3]*Department of Inorganic and Analytical Chemistry, University of Szeged, Dóm sq. 7, 6720 Szeged, Hungary*
E-mail galbx@chem.u-szeged.hu

Abstract. In this work, signal enhancement of the original TEA CO_2 LIBS setup was studied. Two different methods for copper nanoparticle synthesis were applied. Obtained nanoparticles were characterized and then used for Nanoparticle-Enhanced Laser-Induced Breakdown Spectroscopy (NELIBS) of plastic polypropylene. Preliminary results have shown that improvement in the analytical sensitivity for the detection of Cr in plastic materials was achieved.

1. INTRODUCTION

Laser-Induced Breakdown Spectroscopy (LIBS) is a modern method of analytical chemistry that uses an optical signal from laser-induced plasma to study the elemental composition of materials. Thanks to its unique features, LIBS has found numerous and diverse applications, from control of industrial processes, through diagnostics of cultural heritage objects and biomedicine to space research. On the other hand, application of LIBS is limited with respect to other standard spectrochemical techniques (ICP-OES, AAS) by a strong matrix effect, poor repeatability, and relatively weak sensitivity and therefore much effort has been put into improving the capabilities of LIBS in recent years. Recently, a new method of signal enhancement has emerged as a possible solution. This promising variant of the LIBS technique, namely Nanoparticle-Enhanced LIBS (NELIBS) is based on the use of nanoparticles (NPs), which can be used to control the laser-matter interaction by directly affecting better coupling of incoming laser electromagnetic

field with the irradiated material. In this work, Cu nanoparticles, synthesized by chemical method and by laser ablation in liquids, were applied to the analysis of Cr in polypropylene sample.

2. EXPERIMENTAL

2.1. Copper nanoparticles synthesis

Chemical method: For the synthesis of copper nanoparticles, 50 mL of 0.2 M $CuSO_4x5H_2O$ and 0.4 M $NaBH_4$ were prepared. Using NaOH, the pH was adjusted to 12 for these two solutions. PVP was used as a stabilizer, which helps prevent direct contact of particles and their aggregation when the conditions of the solution change or when the particles dry on the substrate. Therefore, 1% PVP (40 kDa) was made and added to the previously prepared $CuSO_4$ solution. The $NaBH_4$ solution was then added dropwise to the $CuSO_4$ solution in a beaker on a magnetic stirrer at 40 °C. The stirring continued for the next hour. The color of the mixture changed from blue to brown during heating and stirring, indicating that Cu nanoparticles precipitated.

Laser ablation in liquids: A pure copper target was immersed into the 25 ml of Milliq water and placed about 2.5 cm under the water surface. The surface of approximately 1 cm^2 in size was continually scanned by a pulsed laser beam in order to achieve homogenous ablation of a sample. The total number of pulses for irradiation of each sample was 5000 using the Nd:YAG laser (300 mJ, 5 Hz, 5 ns pulse duration, wavelength of 1064 nm, Quantel, Brilliant). The laser beam was focused by 10 cm lens in order to enhance ablation.
Characterization of formed nanocolloids were performed with the measurement of SPR band using a UV-VIS spectrophotometer (*LLG-uniSPEC 4 UV/VIS-Spectrophotometer*). Also, NP concentration as an important parameter for signal enhancement was determined by ICP-OES spectrometer (*Thermo Scientific iCap 7400 duo*).

2.2. LIBS setup and NELIBS experiments

LIBS measurements were conducted using a unique developed LIBS system based on pulsed gas TEA CO_2 laser and time-integrated spatially resolved spectroscopy (TISR). The polypropylene sample was prepared in duplicate. With a micropipette, the same amount of nanoparticles was added in a thin layer to each sample and then dried. The plasma was generated by focusing a pulsed TEA CO_2 laser that emits at 10.6 μm on the sample with copper NPs on the surface at atmospheric pressure. Applied laser energy was 170 mJ with a repetition rate of 1 Hz and the shot-to-shot fluctuation of its pulse energy was about 5%. Optical emission from the induced plasma was collected on the entrance slit of a Carl Zeiss PGS2 monochromator by using an achromat objective with a magnification of 1:1. LIBS analysis was conducted in time-integrated mode during 3s using CCD Apogee Alta F1007 camera as a detector. The TISR measurements were performed, and all measurements were carried out in triplicate. The obtained spectra present average values of line intensities from 3 different parts of the sample surface.

3. RESULTS AND DISCUSSION

The LIBS spectra segments of the analyzed sample with a focus on the chromium line are shown in Figure 1. The reason for the monitored chromium in the polypropylene sample is that it appears as one of the elements in the Ziegler-Natta catalyst for the synthesis of polypropylene for a variety of applications. Considering that TISR method utilizes the fact that intense continuum emission is mostly emitted from a region close to the sample surface, the best signal to background (SBR) value was achieved by changing the viewing position of plasma along its expanding direction toward the laser beam. Distance between the focusing lens and a target was constant and optimal SBR ratios were obtained at 0.5 mm in front of the target.

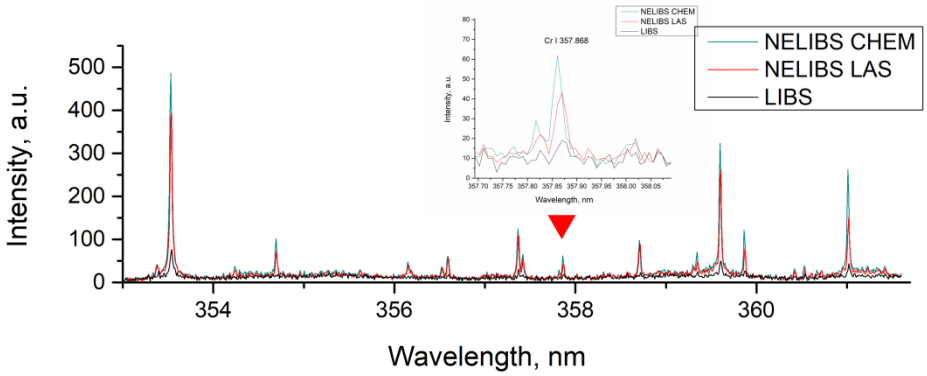

Figure 1: LIBS spectra of analyzed polypropylene sample

The limit of detection (LOD) was calculated using the formula LOD = (3 × c) / SNR, where c is a known analyte concentration of Cr obtained by the ICP-OES method, and signal-to-noise ratio (SNR) is the absolute intensity of the integrated peak area A, divided by the width of the peak area w, times the absolute value of the rms noise, SNR = A / (w × rms). Based on the results, we estimated that NELIBS based on chemical NPs can produce enhancement of the analyte emission signal up to 4.6 times, while laser NPs can produce up to 3.2 times. Furthermore, based on the calculated LODs, this method can lower the limits of the detection up 5 or 3 times, respectively. In our future publications, we will study in detail the improvement of analytical possibilities for multielement analysis by optimization of size and concentrations of NP and as well as deposition of NP on the plastic surface.

Acknowledgments

Authors thank the Ministry of Education, Science and Technological Development of the Republic of Serbia for the financial support to the research through institutional funding (Contract numbers 451-03-68/2022-14/200017); bilateral

project between Serbia and Croatia (337-00-205/2019-09/15) and by Serbian-Hungary bilateral project; Croatian Science Foundation under project HrZZ-PZS-2019-02-5276 and by Croatian-Serbian bilateral project; from the National Research, Development and Innovation Office (NKFIH, within projects No. K 129063 and TKP2021-NVA-19, 019-2.1.11-TÉT-2020-00236) of Hungary.

References

Galbács, G., Kéri, A., Kohut, A., Veres, M. and Geretovszky, Z. : 2021, *J. Anal. At. Spectrom*., **36**, 1826-1872.

Savovic, J., Stoiljkovic, M., Kuzmanovic, M., Momcilovic, M., Ciganovic, J., Rankovic, D., Zivkovic, S. and Trtica, M. : 2016, *Spectrochim. Acta B: At. Spectrosc.*, **118**, 127-136.

Section 3.

LOW TEMPERATURE PLASMAS

MEASUREMENT AND SIMULATION OF ATMOSPHERIC-PRESSURE STREAMER DISCHARGE

RYO ONO

Department of Advanced Energy, The University of Tokyo,
5-1-5 Kashiwanoha, Kashiwa, Chiba 227-8568, Japan
E-mail ryo-ono@k.u-tokyo.ac.jp

Abstract. Electric field, electron density, electron energy distribution, density of reactive species, and gas temperature are measured in an atmospheric-pressure positive streamer discharge in air. Spatiotemporal resolved laser spectroscopies, including femtosecond E-FISH, Thomson scattering, Talbot interferometer, and laser-induced fluorescence (LIF), are used (Inada et al. 2022, Tomita et al. 2020, Inada et al. 2019, Ono 2016). To avoid difficulties due to the lack of spatial reproducibility caused by streamer branching for measurements that require accumulation of many discharge pulses, a high reproducible, pseudo-2D single filament streamer is used. For example, the Thomson scattering required accumulation of 20,000 discharge pulses. Some of the results are compared with the results of 2D streamer simulation developed by our group (Komuro et al. 2013, Komuro et al. 2018). The shape, propagation, optical emission, and discharge current are also measured and compared with the simulation results to validate the simulation model (Ono and Komuro 2020). The simulation, measurements of electric field and electron density, and measurement of electron energy distribution were performed by Dr. Atsushi Komuro, Dr. Yuki Inada, and Dr. Kentaro Tomita, respectively.

References

Inada, Y., et al. : 2022, *J. Phys. D: Appl. Phys.*, accepted.
Inada, Y., et al. : 2019, *J. Phys. D: Appl. Phys.*, **52**, 185204.
Komuro, A. et al. : 2018, *J. Phys. D: Appl. Phys.*, **51**, 445204.
Komuro, A. et al.: 2013, *J. Phys. D: Appl. Phys.*, **46**, 175206.
Ono, R., Komuro, A. : 2020, *J. Phys. D: Appl. Phys.*, **53**, 035202.
Ono, R. : 2016, *J. Phys. D: Appl. Phys.*, **49**, 083001.
Tomita, K., et al. : 2020, *J. Phys. D: Appl. Phys.*, **53**, 08LT01.

Publ. Astron. Obs. Belgrade No. 102 (2022), 156 *Invited Lecture*

MEASUREMENTS OF RF PLASMA RE-IGNITION: RF-IV AND PROES

L. J. OVERZET[1], A. PRESS[2], K. HERNANDEZ[3], J. POULOSE[4] and M. J. GOECKNER[5]

[1]*UT Dallas, 800 W. Campbell Road, RL10, Richardson, TX 75080-3021*
E-mail overzet@utdallas.edu

[2]*Los Alamos National Lab., PO Box 1663, Los Alamos, NM, 87545 Mail stop P912*
E-mail alexpress@lanl.gov

[3]*Applied Materials, Santa Clara CA, 94085*
E-mail keith_hernandez@amat.com

[4]*Applied Materials, Sunnyvale, CA 94085*
E-mail John_Poulose@amat.com

[5]*UT Dallas, 800 W. Campbell Road, RL10, Richardson, TX 75080-3021*
E-mail goeckner@utdallas.edu

Abstract. The re-ignition of a capacitively coupled RF plasma (CCP) is complicated and difficult to measure. Changes in the plasma state occur on times scales from less than the rf-period (~75 ns) to several hundreds of microseconds. The manner in which energy is deposited into the electrons can change over just a few rf periods while the DC bias voltage can take a few hundreds of microseconds to establish. The electron density build up is accompanied by a peaking in the electron temperature and subsequent build down. The numbers of electrons capable of producing optical emission by impact with neutrals varies substantially within each RF period as well. Plasma "left over" from a prior pulse can dramatically affect each of these! We have made measurements of the RF voltage and current to a pulsed CCP with single RF period time resolution. We compared these measurements with Phase Resolved Optical Emission Spectroscopy (PROES) measurements during the re-ignition. Combining the two enables us to propose why Ar CCPs can exhibit a bright flash of light during turn-on even though the electron density is smaller and the RF power is still rising. The lower electron density at turn-on allows the electron heating mechanism to change from primarily stochastic heating at the sheath edge and primarily during local sheath expansion to a mixed stochastic and ohmic heating mechanism throughout the plasma volume and throughout the RF period. I intend to present the details of the measurement techniques as well as the results we have obtained.

INVESTIGATION OF THE RO-VIBRATIONAL LEVELS OF H_2/D_2 MOLECULES BY VUV-ABSORPTION SPECTROSCOPY FOR THE PRODUCTION OF H^-/D^- NEGATIVE IONS FOR FUSION APPLICATION

S. BÉCHU[1] , J. L. LEMAIRE[2] , M. MITROU[1,3] , N. DE OLIVEIRA[4] P. SVARNAS[3]
[1]*LPSC, Université Grenoble-Alpes, CNRS/IN2P3, F-38026 Grenoble, France*

[2]*Institut des Sciences Moléculaires d'Orsay (ISMO), CNRS - Université Paris-Sud (UMR 8214) , 91405 Orsay, France*

[3]*High Voltage laboratory, Electrical and Computer Engineering Department, University of Patras, Rion-Patras 26504, Greece*

[4]*DESIRS beam line, Synchrotron SOLEIL, Saint Aubin 91192 Gif sur Yvette, France*
E–mail bechu@lpsc.in2p3.fr

Abstract. Neutral beam injectors (NBI) will be employed to heat-up the plasma of future pre-industrial fusion reactors. Negative ions, created in the the ion source on ceasiated surfaces, will then be accelerated to 1 MeV and neutralised prior to their entrance in the fusion plasma. The caesium (Cs) layer reduces the work function of the tungsten surface but its use in NBI could be problematic as it potentially escapes the surfaces on which it is deposited and might promote aberration. Hence, a 'Cs-free' ion source is a conceivable solution to produce a uniform beam of H_0/D_0 neutral atoms for the DEMO reactor.
An alternative, omitting the need of Cs could be the creation of H^-/D^- ions by dissociative attachment (DA) between H_2/D_2 highly ro-vibrationally excited molecules ($v"$>5) in their electronic ground state X $^1\sum_g^+(v", J")$ and cold electron (<1eV). Ro-vibrationally excited molecules are created via plasma-volume reactions and enhanced by surface recombinative desorption (RD). RD mechanisms produce excited molecules—involved in the DA reaction—via different reaction pathways when an atom produced in the plasma volume reacts with an adsorbed atom present on the surface. The direct measurement of molecules in these ro-vibrationally excited v'' and J'' levels is essential to evaluate the effectiveness of RD mechanisms vs. volume production. The DESIRS beam line at the SOLEIL synchrotron offers a unique solution to diagnose these states thanks to an unparalleled VUV Fourier Transform spectrometer (FTS). In this study the VUV-FTS is applied to directly scrutinize the ro-vibrationally excited levels of the D_2 ground state in an electron cyclotron resonance plasma. Different plasma-facing materials are employed—to compare their relative impact in RD mechanisms—and various positions of the plasma source in the reactor are set to measure the distribution of these levels in the plasma volume.
A significant effect of these materials on the absolute distribution of the vibrationally states has been found above $v'' = 3$. Tantalum appears to be, at $v'' = 7$, ∼4.8 times more efficient than a quartz surface at populating high v'' levels which leads to an increase by a factor of 3, compared to quartz, of the negative ion production. The distribution of $v'' = 6$ shows an unexpected homogeneity, ∼10%, up to 75 mm from the plasma source.

References

de Oliveira, N., Roudjane, M., Joyeux, D., Phalippou, D., Rodier, J.-C., Nahon, L. : 2011, *Nature Photonics*, **5**, 149.

Bechu, S., Lemaire, J. L., Gavilan, L., Aleiferis, S., Shakhatov, V., Lebedev, Y. A., Fombaron, D., Bonny, L., Menu, J., Bes, A., Svarnas, P., de Oliveira, N. : 2020, *Journal of Quantitative Spectroscopy & Radiative Transfer*, **257**, 107325.

Taccogna, F., Bechu, et al., P. : 2021, *The European Physical Journal D* **75**, 1.

WHAT CAN PLASMA SPECTROSCOPY DO FOR ASTRONOMERS? MEASURING ATOMIC PARAMETERS OF ASTROPHYSICAL IMPORTANCE

M. T. BELMONTE[1], P. R. SEN SARMA[1], C. P. CLEAR[2], F. CONCEPCION[2], M. DING[2], J. C. PICKERING[2] and S. MAR[1]

[1]*Universidad de Valladolid, Departamento de Física Teórica, Atómica y Óptica. Paseo de Belén 7, 47011 Valladolid, Spain*
E-mail mariateresa.belmonte@uva.es

[2]*Blackett Laboratory, Physics Department, Imperial College London SW72AZ, UK*

Abstract. Plasma spectroscopy is a powerful tool that allows us to measure atomic parameters needed by astronomers such as transition probabilities, wavelengths, energy levels, hyperfine structure constants or Stark parameters. Access to high-quality atomic data allows astronomers to analyse astrophysical spectra and extract information from the shapes, widths and shifts of the spectral lines emitted by atoms and ions. Knowledge, not only of chemical composition but also of temperatures and electron densities of the astrophysical plasmas, can thus be obtained. However, a great quantity of the atomic data needed for spectra interpretation is yet to be measured.

The Atomic Spectroscopy Laboratory at the University of Valladolid (Spain) has a long history working in the generation, diagnostics and measurement of plasma spectra in the ultraviolet and visible spectral ranges. We collaborate with the Fourier Transform Spectroscopy Laboratory at Imperial College London (United Kingdom), the spectroscopy laboratory at NIST (USA) and the University of Lund (Sweden) to extend our measurements to the vacuum ultraviolet and the infrared regions with resolving powers of up to 2 000 000 at 200 nm.

In this talk, I will discuss in a comprehensive manner the different methods used by the aforementioned laboratories in the accurate measurement of atomic parameters of neutral and ionised species, providing examples of the latest results. The aim of this contribution is to explain the current capabilities of these laboratories to the plasma community with the intention of fostering interaction and new collaborations with those fields of research and industry in need of high-quality atomic data.

Acknowledgements

M. T. Belmonte acknowledges the funding provided by the University of Valladolid under the grant "Research projects UVa 2021" and by the Spanish government through a Beatriz Galindo Fellowship.

SURFACE PROCESSES IN LOW-PRESSURE CAPACITIVELY COUPLED PLASMAS

A. DERZSI

Wigner Research Centre for Physics, 1121 Budapest, Konkoly-Thege Miklós. street 29-33, Hungary
E-mail derzsi.aranka@wigner.hu

Abstract. Low-pressure radio frequency capacitively coupled plasmas (RF CCPs) are used for several applications, e.g. etching and deposition processes. Despite their high technological relevance, some details of their operation, e.g. plasma-surface interactions, are not understood in many cases. Kinetic simulations based on the Particle-in-Cell method combined with Monte Carlo type treatment of the collision processes (PIC/MCC approach) are widely used to study various phenomena in RF CCPs. Such simulations typically require a number of input parameters, including surface coefficients. Such coefficients are often unknown or suffer from large uncertainties, therefore, several assumptions related to the description of the interaction of plasma particles with the boundary surfaces are implemented in the simulations. Recently, the importance of the realistic description of the various surface processes in kinetic simulations of RF CCPs has attracted increasing attention (see e.g. Derzsi et al. 2020). The simple models used to describe e.g. the secondary electron emission induced by heavy-particles and electrons have been replaced by complex, more realistic models, which take into account the dependence of the secondary electron yield on various factors, such as the energy of the incident particles, the electrode material and its surface conditions. In this talk, the recent efforts to describe the interaction of plasma particles with the boundary surfaces realistically in particle based simulations of RF CCPs are presented, as well as an overview of how the realistic surface models implemented in the simulations have provided an improved understanding of the effects of elementary surface processes on the plasma parameters in low-pressure RF CCPs.

References

Derzsi, A., Horváth, B., Donkó, Z., Schulze, J. : 2020, *Plasma Sources Sci. Technol*, **29**, 074001.

HIGHER HARMONIC FREQUENCIES OF DISCHARGE VOLTAGE AND CURRENT IN CAPACITIVELY COUPLED DISCHARGES

P. DVOŘÁK[1], R. ŽEMLIČKA, R. PŘIBYL, M. TKÁČIK, J. PÁLENIK, P. VAŠINA, P. SKOPAL, Z. NAVRÁTIL and V. BURŠÍKOVÁ

Department of Physical Electronics, Faculty of Science, Masaryk University
Kotlářská 2, Brno, Czech Republic
[1]*E-mail pdvorak@physics.muni.cz*

Abstract. The current-voltage characteristics of capacitively coupled discharges has nonlinear character, which is caused by sheaths and which leads to generation of higher harmonic frequencies of discharge current and voltage. Higher harmonics are strong especially at low pressure, as demonstrated by an example of plasma potential waveform shown in the figure 1. Higher harmonics influence the behaviour of the plasma and, at the same time, they sensitively react on number of discharge parameters, which enables to use them for monitoring of various deposition and etching processes. The presentation summarizes several topics related to higher harmonic frequencies, namely the problematics of probe measurement of the high-frequency components of plasma potential, presence of higher harmonics at atmospheric-pressure discharges, modeling of generation of higher harmonics and analysis why higher harmonics react so sensitively on the presence of a thin film during deposition/etching processes.

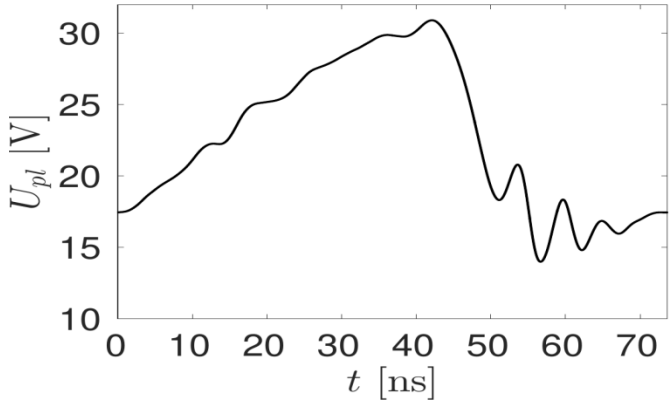

Figure 1: Plasma potential of an asymmetric low-pressure (6 Pa) capacitively coupled discharge ignited in Ar.

COUPLED KINETICS IN CO_2-N_2 PLASMAS

C. FROMENTIN[1] and T. C. DIAS[1] and T. SILVA[1] and V. GUERRA[1] and E. BARATTE[2] and O. GUAITELLA[2]

[1] *Instituto de Plasmas e Fusão Nuclear, Instituto Superior Técnico, Universidade de Lisboa, 1049-001 Lisboa, Portugal*

[2] *Laboratoire de Physique des Plasmas, Ecole Polytechnique-CNRS 91128 Palaiseau, France*

Abstract. CO_2 plasmas are interesting for a wide variety of applications, including CO_2 reforming for the production of solar fuels and added-value chemicals, polymer deposition, spacecraft reentry and in-situ resource utilization on Mars (Pietanza et al 2021). Control and optimization of the different applications requires a deep understanding of the energy transfer pathways and of the coupling of the different kinetics at play, such as the electron, vibrational, chemical and surface kinetics. Of major interest are the processes of conversion of CO_2 into CO and back reactions reconverting CO back into CO_2.

Experiments are performed in DC glow discharges operating at pressures around 1 Torr and discharge currents of the order of tenths of mA, measuring by Fourier Transform Infra-Red spectroscopy (FTIR) the vibrational temperatures of CO and of the three vibration modes of CO_2, as well as the dissociation fraction, [CO]/([CO_2]+[CO]). To interpret and analyze the experiments, a self-consistent kinetic model is developed, that solves the electron Boltzmann equation in the usual 2-term expansion in Legendre polynomials (Tejero-del-Caz et al 2019), coupled with a system of rate-balance equations describing the creation and loss of the most important neutral and charged heavy-particles.

It is verified that the dissociation fraction increases upon addition of N_2 into a CO_2 discharge, in line with previous measurements by Grofulović et al 2019 and Terraz et al 2019. The enhanced dissociation fraction is the outcome of a combination of different effects, such as the modifications in the Electron Energy Distribution Function (EEDF) induced by a different mixture of gases, with associated modifications in the electron impact dissociation rate coefficients, both from ground-state and from vibrationally excited CO_2, and the dilution of CO_2 in N_2, associated with a smaller influence of back reaction mechanisms.

Acknowledgments. This work was partially supported by the European Union's Horizon 2020 research and innovation programme under grant agreement MSCA ITN 813393, and by the Portuguese FCT - Fundação para a Ciência e a Tecnologia, under projects UIDB/50010/2020, UIDP/50010/2020 and PTDC/FIS-PLA/1616/2021 (PARADiSE).

References

Pietanza, L. D. et al: 2021, *Eur. Phys. J. D*, **75**, 237.
Tejero-del-Caz, A. et al: 2019, *Plasma Sources Sci. Technol.*, **28**, 043001.
https://nprime.tecnico.ulisboa.pt/loki/
Grofulović, M. et al: 2019, *Plasma Sources Sci. Technol.* **28**, 045014.
Terraz, L. et al: 2020, *J. Phys. D: Appl. Phys.*, **53**, 094002.

APPLICATION OF MACHINE-LEARNING TO SPECTROSCOPIC LINE EMISSION BY HYDROGEN ISOTOPES IN FUSION DEVICES FOR ISOTOPIC DETERMINATION AND PREDICTION

MOHAMMED KOUBITI

PIIM Laboratory, AIX-MARSEILLE UNIV, CNRS, Marseille, France
E-mail mohammed.koubiti@univ-amu.fr

Abstract. In magnetic fusion devices such as tokamaks and stellarators operated with a mixture of deuterium and tritium D-T, the knowledge of the isotopic ratio, i.e the ratio of the tritium density n_T to the total neutral density ($n_D + n_T$) is crucial for both operational control and safety reasons. Because of safety reasons, the quantity of tritium in the vacuum vessel of ITER is limited to 700g according to Roth 2008. Therefore, any method allowing a real-time determination of such a parameter is strongly welcomed. Usually in H-D or D-D plasmas, the isotopic ratio (n_D /$n_H + n_D$) is determined by fitting the experimental spectra of the Balmer-α line, i.e., Hα /Dα using an optimization algorithm based on a physical model. In this paper, I propose to apply Artificial Intelligence to Hα/Dα line spectra to identify the major spectral features, e.g., the positions and amplitudes of the peaks, the position of the dips and their y-values. These features with then be used by a Machine-Learning algorithm to determine the isotopic ratio in a faster way than a complete modelling or fitting of the entire profile of the line. By doing this, one can provide in real-time the values of the isotopic ratios along each spectral line of sight. The following step consists in the application of this method to the available spectroscopic data of several devices under H-D or D-D operation in order to extrapolate to D-T plasmas as expected for ITER in a later phase. We will make use here of a deep-learning tool (Tensorflow) based on neuronal networks. Some illustrations will also be shown using a supervised ML tool known as Sickit-Learn or SK-Learn see Pedregosa et al. 2011, this package was previously applied to the analysis of neutral helium ratios to determine the electron density and temperature in a linear simulator of a tokamak divertor, see Kajita et al 2021. Before tackling experimental data, I will consider synthetic spectra generated with given parameters using a python code, see Koubiti and Sheeba 2019. Finally, I will discuss the role that can be played by Artificial Intelligence in plasma physics.

References

Kajita, S. et al: 2021, *Plasma Phys. Control. Fusion*, **63**, 055018.
Koubiti, M., Sheeba, R.: 2019, *atoms* **7**, 23.
Roth, J. : 2008, *Plasma Phys Control. Fusion*, **50**, 103001.
Pedregosa, F. et al*:* 2011, *the Journal of machine learning research*, **12**, 2825.

CONTROL OF GUIDED STREAMER PROPAGATION AND INTERACTION WITH SUBSTRATE IN HELIUM ATMOSPHERIC PRESSURE PLASMA JET

MIKHAIL PINCHUK[1], OLGA STEPANOVA[1], MIKHAIL GROMOV[2], and ANTON NIKIFOROV[2]

[1]*Institute for Electrophysics and Electrical Power of the Russian Academy of Sciences, Dvortsovaya Naberezhnaya 18, Saint-Petersburg 191186, Russia*
E–mail pinchme@mail.ru

[2]*Department of Applied Physics, Ghent University, Sint-Pietersnieuwstraat 41, Gent 9000, Belgium*
E–mail anton.nikiforov@ugent.be

A control dynamics of the streamer development in atmospheric pressure plasma jets could be a basis in the design of adaptive plasma jets. In the report, the control dynamics of the guided streamer development in helium atmospheric pressure plasma jets near the surface is demonstrated.

The discharge system was as in (Pinchuk et al. 2021 i). A high-voltage tailoring signal was applied to the inner electrode, also as in (Pinchuk et al. 2021 i). Helium flow rates were chosen at 7 l/min. Accordingly (Pinchuk et al. 2021 ii), the flow rate corresponds to the stepwise propagation of the guided streamer.

The jet photo and development process of the guided streamer are shown in Fig. 1.

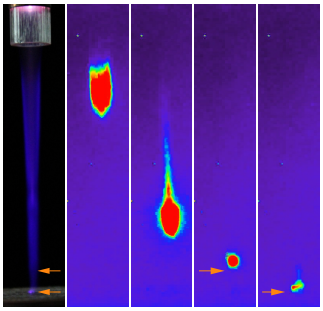

Figure 1: A soft touch of guided streamer to artificial skin steeping by physiologic saline: intermediate stop position and surface are marked by arrows.

It was demonstrated that by varying the voltage amplitude, duty cycle, and voltage waveform, the dynamics of the streamer can be controlled, stopping for a certain time the propagation of the streamer near the target.

The study was financially supported by the Russian Science Foundation (project 22-29-01215, https://rscf.ru/en/project/22-29-01215/).

References

Pinchuk M., et al. : 2021, (i) *Scientific Reports*, **11**, doi 10.1038/s41598-021-96468-4.
Pinchuk M., et al. : 2021, (ii) *Applied Physics Letters* **119**, 054103, doi 10.1063/5.0053672.

ON THE APPLICATION OF ITERATIVE KINETIC MODEL FOR DIAGNOSTICS OF ABNORMAL GLOW DISCHARGES IN NOBLE GASES

DJORDJE SPASOJEVIĆ[1], NIKOLA V. IVANOVIĆ[2], NIKODIN V. NEDIĆ[1], LUKA RAJAČIĆ[1], NIKOLA M. ŠIŠOVIĆ[1] and NIKOLA KONJEVIĆ[1]

[1]*Faculty of Physics, University of Belgrade, 11001 Belgrade, P.O. Box 44, Serbia*
E-mail djordjes@ff.bg.ac.rs

[2]*Faculty of Agriculture, University of Belgrade, 11080 Belgrade, Nemanjina 6, Serbia*

Abstract. We report the results of application of iterative kinetic model to the experimental profiles and electric field distributions recorded in the cathode sheath (CS) of abnormal glow discharges in noble gases and show the model enables determination of the most important CS parameters.

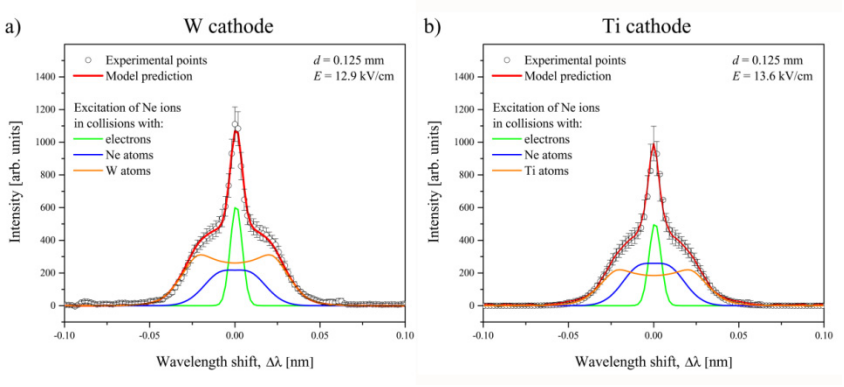

Figure 1: Intensity vs wavelength shift, Δλ , for the Ne II 371.308 nm line profile recorded side-on 0.125 mm from the W (a) and Ti (b) cathode. Experimental points are shown by symbols, and the model profiles by the full lines.

References

Dj. Spasojević *et al*: 2020, *Plasma Sources Sci. Technol.*, **29** 085008.

Dj. Spasojević *et al*: 2022, *Advances in Space Research*, Available online 19.11.2021 https://doi.org/10.1016/j.asr.2021.11.014

MEASUREMENTS OF CONTINUOUS OPTICAL SPECTRUM DURING NANOSECOND LASER PULSE INTERACTION WITH METALLIC TARGET

DEJAN DOJIĆ[1], MILOŠ SKOČIĆ[2] and SRDJAN BUKVIĆ[3]

[1] *University of Belgrade Faculty of physics*
E–mail dejan.dojic@ff.bg.ac.rs.

[2] *University of Belgrade Faculty of physics*
E–mail skocic@ff.bg.ac.rs.

[3] *University of Belgrade Faculty of physics*
E–mail ebukvic@ff.bg.ac.rs.

Abstract. Relying on classical time-resolved optical emission spectroscopy, experimental study of the evolution of the plasma plume created in nanosecond laser ablation of a copper sample at reduced atmospheric pressure (5 Pa) is done. The laser pulses of 5.6 ns duration had the carrier wavelength of 1064 nm and the intensity in the range from 10^9 W/cm^2 to 10^{12} W/cm^2. The measurement data were collected in the spectral range from 200 nm to 850 nm with temporal resolution of 1 ns. The spectral emission was observed simultaneously looking directly at the illuminated spot on the copper surface, and side-on, along the sample surface. The temperature of the copper surface and the plasma was deduced by fitting the emission spectrum to the theoretical Plancks law. Temperatures of the copper surface are in the 7 400-11 200 K range. These values are close to the most common estimated values for the critical temperature of the copper. After the plasma creation, it was found that its temperature overcome 50 000 K.

References

Skočić, M., Dojić, D., Bukvić, S. : 2022, *Physical Review E*, **105**, 045211.
Martynyuk, M.M. : 1977, *Combust. Explos. Shock Waves*, **13**, 178
Ionin, A.A., Kudryashov, S. I., Seleznev, L.V. : 2010, *Physical Review E*, **82**, 016404

THE INFLUENCE OF CORONA DISCHARGE ON THE LIGHTNING SURGE PROPAGATION ALONG THE TRANSMISSION LINES

MILAN IGNJATOVIC

School of electrical engineering, Bulevar kralja Aleksandra 73, Belgrade, Serbia
E-mail ignjatovic@etf.bg.ac.rs

Abstract. Atmospheric discharges are one of the most significant cause of failures of the energy distribution system (see Hileman 1999). Overvoltages caused by lightning strokes travel along transmission lines and they can reach substations where installed equipment is particularly sensitive to pulse amplitude and steepness. When the lightning overvoltage is generated on the transmission line, surge wave starts to travel along the overhead wires. Corona discharge around the wire is the main effect that has influence on the change of surge pulse during propagation and must be taken into account when designing surge protection. For corona discharge simulations drift-diffusion model is used for describing the particle dynamics by four continuity equations for electrons, positive ions and O_2^- and O^- negative ions (see Ignjatovic and Cvetic 2021). This model enables a detailed analysis of the temporal evolution and spatial dependence of the concentration of particles during the discharge. Result for the total generated corona charge is used to simulate the propagation of the surge wave along the overhead wire. Validity of the model is checked by the comparison with the results of experiments performed by Cooray and Noda. The corona model should be simple and without need for complex mathematical calculations in order to be applicable in wider engineering practice. On the other hand to achieve an accurate estimate of the electrical charge generated during the corona discharge, it is necessary to take account a variety of physical processes. Using more computationally demanding models is justified in order to discover new conclusions about corona discharge process that can be used to formulate simpler models.

References

Cooray, V. : 2000, *IEEE Trans. on Dielectrics and Electrical Insulation*, **7**, 734

Hileman, A. R. : 1999, *Insulation Coordination for Power Systems*, Boca Raton, USA

Ignjatovic, M., Cvetic, J., : 2021, International Journal of Electrical Power and Energy Systems, **129**, 106815

Noda T., Ono, T., Matsubara, H., Motoyama, H., Sekioka, S., Ametani, A. : 2003, *IEEE Transactions on Power Delivery*, **18**, 307

DESIGN, DEVELOPMENT, AND CHARACTERIZATION OF ATMOSPHERIC PLASMA SYSTEM FOR WASTEWATER TREATMENT

AMIT KUMAR[1,2], NIKOLA ŠKORO[1], WOLFGANG GERNJAK[3,4], SUZANA ŽIVKOVIĆ[5] and NEVENA PUAČ[1]

[1]*Institute of Physics, University of Belgrade, Pregrevica 118, 11080, Belgrade, Serbia*
E-mail amit@ipb.ac.rs, nevena@ipb.ac.rs, nskoro@ipb.ac.rs

[2]*Universitat de Girona, 17003, Girona, Spain*

[3]*Catalan Institute for Water Research (ICRA), 17003, Girona, Spain*

[4]*Catalan Institution for Research and Advanced Studies (ICREA),08010 Barcelona, Spain*
E-mail wgernjak@icra.cat

[5]*Institute for Biological Research "Siniša Stanković", University of Belgrade, Bulevar despota Stefana 142, 11060 Belgrade, Serbia*
E-mail suzy@ibiss.bg.ac.rs

Abstract. In recent years, cold atmospheric plasmas (CAPs) are gaining attention in the field of water decontamination. CAP is a new and emerging chemical free advanced oxidation process (AOP) for the removal of various organic micropollutants (OMPs) from water. In this study, 1-needle and 3-needle electrode atmospheric pressure plasma jet was used as a plasma source. Plasma was governed by using high voltage RF power supply with sine signal at 350 kHz, whereas argon was used a working gas. Three different OMPs (acid blue 25 dye, diclofenac and para-chlorobenzoic acid) were selected as model pollutants and treated with plasma. Electrical circuit in the experiment enabled electrical characterization at the jet and in the grounded line. This provided information about power deposition at two points in the plasma system: at the jet, i.e. the input power, and power from the plasma delivered to the sample. Optical measurements were obtained by using optical emission spectroscopy (OES) and imaging - an iCCD camera coupled with band pass filters for spectrally resolved imaging. The emission spectra provided the evidence of reactive and excited species within the plasma discharge while imaging gave time integrated information on spatial profiles of certain reactive species in the plasma ($HO^{\cdot}$, $O^{\cdot}$, ...). After plasma treatment the samples were analysed by using a HPLC and showed that faster degradation of OMPs was observed in the following order: diclofenac> acid blue 25 dye> para-chlorobenzoic acid. The highest degradation efficiency was achieved with diclofenac while para chlorobenzoic acid demonstrated the lowest decomposition. Nevertheless, the CAP based AOPs can be used for the efficient elimination of various OMPs from water.

This work was carried out under NOWELTIES project. NOWELTIES received funding from the European Union's Horizon 2020 research and innovation programme under the Marie Skłodowska-Curie grant agreement No. 812880. NS and NP are funded by the Ministry of Education, Science and Technological Development, grant number 451-03-68/2020- 14/200024.

References

Kumar, A., Škoro, N., Gernjak, W., & Puač, N.: 2021, *The European Physical Journal D*, *75*(11), 1-26.

MODELING OF RADIO-FREQUENCY BREAKDOWN BY MONTE CARLO TECHNIQUE

MARIJA PUAČ[1] and ZORAN LJ. PETROVIĆ[2]

[1]*Institute of Physics, University of Balgrade, Pregrevica 118 Belgrade*
E-mail smarija@ipb.ac.rs

[2]*Serbian Academy Of Science And Arts, Knez Mihailova 35, Belgrade*

Abstract. Plasmas ignited by radio-frequency (RF) electric fields are widely used in many applications. Accordingly, scientific research is ranges, from experimental setups through mathematical models, relevant data and applications. Defining information for any application of RF plasmas are its breakdown voltage and related gas pressure. Monte Carlo proved to be a reliable technique for modeling voltage breakdown curves of RF plasmas. Recent research explained double valued nature of RF breakdown voltage curves and scaling law of those curves (Savić et al 2011), gave an insight of the physical nature of the RF breakdown (Puač et al 2018) and the role of attachment in presence of oxygen (Puač et al 2020). In this paper we review our findings on the underlying physics of RF breakdown and we present a versatile numerical tool for simulation that has no inherent limitations.

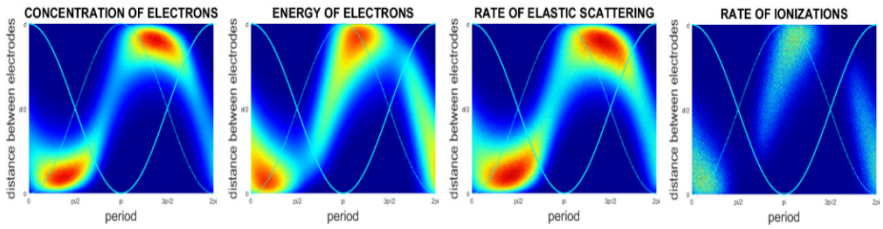

Figure 1: Spatial profiles of electron concentration, energy, and rates of elastic scattering and ionization. Background gas is helium, pressure and voltage are 1.13Torr and 330V, gap between electrodes is 23mm and frequency is 13.56MHz.

References

Savić, M., Radmilović-Radjenović, M., Šuvakov, M., Marjanović, S., Marić, D., Petrović, Z. Lj: 2011, *IEEE Trans. Plasma Sci.*, **39**, 2556.

Puač, M, Marić, D., Radmilović-Radjenović, M., Šuvakov, M., Petrović, Z. Lj: 2018, *Plasma Sources Science and Technologies*, **27**, 075013.

Puač, M., Đorđević, A., Petrović, Z. Lj: 2020, *The European Physical Journal D*, **74**, 72.

INTERACTION OF IONIZING RADIATION WITH DNA NANOSTRUCTURES

LEO SALA and JAROSLAV KOČIŠEK

J. Heyrovsky Institute of Physical Chemistry, The Czech Academy of Sciences, Dolejškova 3, 18223 Prague, Czech Republic
E-mail leo.sala@jh-inst.cas.cz

Abstract. Understanding the mechanisms of DNA damage by ionizing radiation is crucial in optimizing current radiotherapeutic modalities against cancer. Investigations span a broad scale from gas phase studies on electron-induced damage to DNA subunits, to irradiation studies of cell cultures and organisms. Damage to irradiated DNA subunits often cannot fully explain observed damages on the biological scale prompting studies at various levels of complexity in between. Here, we use DNA origami nanostructures as a platform to explore processes in the intermediate (nanoscale) dimensions. These self-assembling nanostructures are formed from folding single-stranded DNA scaffolds using short complementary oligomers (staples). The staples provide functionalizable ends so DNA sequences of interest or probes can be attached. They can then be closely studied by conventional microscopy techniques like atomic force microscopy (AFM). To explore the potential of such nanostructures as stable platforms for irradiation studies in solution, we subject them to various types of ionizing radiation from gamma rays (~1.2 MeV) to proton beams (30 MeV) to high-energy electrons (16 MeV). We observe structural stability even up to kGy doses. We also irradiate DNA origami nanoframes anchoring different types of sequences to study radiosensitization by halogenated nucleosides. Eventually, we plan to expose these systems to ion beams which could lead to some insights into mechanisms of DNA damage and radiosensitization for the improvement of ion beam radiotherapy.

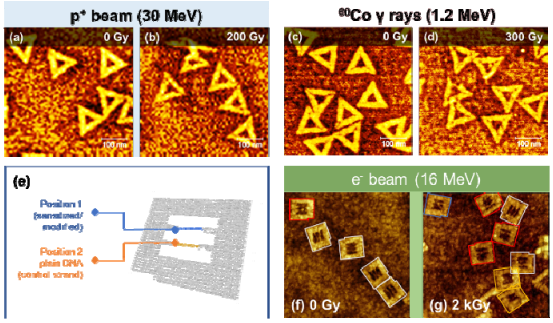

Figure 1: AFM images of control samples (a, c, f); proton irradiated (b) and gamma irradiated DNA origami nanotriangles (d); and electron irradiated DNA origami nanoframes (g). A scheme of the nanoframes is also shown (e).

References

Schürmann, R.,Vogel, S., Ebel, K., Bald, I., : 2018, *Chem. Eur. J.*, **24**, 10271.

Sala, L., Zerolová, A., Rodriguez, A., Reimitz, D., Davídková, M., Ebel, K., Bald, I., and Kočišek, J., : 2021, *Nanoscale*, **13**, 11197.

Sala, L., Lyshchuk, H., Šáchová, J., Chvátil, D., Kočišek, J., : 2022, *J. Phys. Chem. Lett.*, **13**, 3922.

MASS SPECTROMETRY OF PLASMA JET AND APPLICATION OF ELECTRICAL DISCHARGES OPERATING AT ATMOSPHERIC PRESSURE IN BIOMEDICINE

N. SELAKOVIĆ[1], D. MALETIĆ[1], N. PUAČ[1], G. MALOVIĆ[1] and Z. LJ. PETROVIĆ[2]

[1]*Institute of Physics, University of Belgrade, Pregrevica 118, 11080 Belgrade, Serbia*
E-mail nele@ipb.ac.rs

[2]*Serbian Academy of Sciences and Arts, Kneza Mihaila 35, 11000 Belgrade, Serbia*

Abstract. In the last few decades, the study of plasma jets has been the focus of interest for a large number of scientists especially because of its potential application in biomedicine. The physical phenomenon that characterizes plasma jets is the appearance of a "pulsed atmospheric pressure streamer" (PAPS), a fast ionization front that cannot be detected by a human eye, but its observation is enabled by the use of high-speed ICCD cameras. In order to integrate this type of plasma into biomedical applications it is necessary to perform analysis of the electrical discharge's behavior and its composition. In this work, we present mass spectrometry of three different atmospheric pressure plasma sources (plasma jet, multijet plasma device and dielectric coplanar surface barrier discharge). The results show different mass spectra of neutral, positive and negative ions whose composition and concentration significantly depend on the geometry of the source and the applied parameters: the power delivered to the plasma, the type of working gas and flow rate, humidity, etc. This diagnostic method gave us an insight into the dominant reactive species of oxygen and nitrogen, the so-called RONS, which play a crucial role in biomedical applications. In addition, we have used plasma needle, the atmospheric pressure plasma source, in treatments of bacteria, plant stem cells and cancer cells. and discussed numerous effects obtained by treatment.

References

Stancampiano, A., Selaković, N., Gherardi, M., Puač, N., Petrović, Z. L., and Colombo, V. 2018, *Journal of Physics D: Applied Physics*, *51*(48), 484004.

Puač, N., Živković, S., Selaković, N., Milutinović, M., Boljević, J., Malović, G., and Petrović, Z. Lj. 2014, *Applied Physics Letters*, *104*(21), 214106.

Čech, J., Brablec, A., Černák, M., Puač, N., Selaković, N., and Petrović: Z. Lj. 2017, *The European Physical Journal D*, *71*(2), 1-8.

DETERMINATION OF THE ELECTRIC FIELD STRENGTH IN GLOW DISCHARGES USING ARGON SPECTRAL LINES

M. M. VASILJEVIĆ and Dj. SPASOJEVIĆ

University of Belgrade, Faculty of Physics, 11001 Belgrade, P.O. Box 44, Serbia
E-mail milica.vasiljevic@ff.bg.ac.rs

Abstract. The cathode sheath (CS) region is the most important part of ~~an~~ abnormal glow discharge (GD) where various processes relevant for the operation and application of GD occur. This is the region where heavy charged particles accelerate and collide with other discharge constituents generating charged and neutral particles in the ground or excited state before bombarding cathode surface. The electrons and their collision products in the CS and negative glow (NG) region are the most important discharge constituents for sustaining the GD operation. One of the most important parameters of the CS region is the electric field strength distribution, which depends on current density, pressure, cathode material, geometry of the discharge etc. This distribution determines the acceleration of the charged particles, influencing their path and kinetic energy and consequently all processes relevant for the operation of GD and numerous GD applications in the field of spectroscopic analysis, plasma etching, thin film deposition and depth profiling of cathode material. In order to establish new methods for the electric field strength determination the profiles of seven argon lines and two Balmer hydrogen lines were studied. All profiles were experimentally observed side-on to the axis of our Grimm GD source operating at low pressure in argon, argon-hydrogen and neon-argon mixtures, with three different cathode materials. The side-on spectra show simultaneous Stark shifting and splitting of two Ar I lines (Ar I 518.75 nm i Ar I 522,17 nm), as well as ~~an~~ excessively broadened profiles of five Ar II lines (Ar II 434,81 nm; 458,99 nm; 460,96 nm; 484,78 nm; 487,98 nm) ~~of~~ in the cathode sheath region of the glow discharge. A study of argon glow discharge shows that the measured wavenumber DC Stark shifts $\Delta\nu$ of two neutral argon lines can be used for reliable determination of the electric field strength F distribution in the CS. In order to experimentally determine the coefficient c in quadratic correlation $\Delta\nu = cF^2$, manifested in a low field range (up to 15 kV/cm), the values of F are measured via Stark polarization spectroscopy of hydrogen Balmer beta line. Measurements in low electric field strength range showed that the Stark shifts, although rather small, can be determined with the aid of a suitable numerical procedure. Consequently, the simple and inexpensive tool for determination of the CS electric field strength distribution of ~~an~~ argon glow discharges has been developed. During the spectroscopic observation of CS region, the excessively broadened profiles of singly ionized argon spectral lines have been detected. It has been shown that at least two groups of excited ions of argon with significantly different energies participate in the formation of the overall profile of singly ionized argon lines. The influence that cathode material has on the Ar II line shape has been demonstrated, and a simple formula for determination of the electric field strength from the width of broadened wings of the side-on recorded Ar II spectral lines has been presented.

Publ. Astron. Obs. Belgrade No. 102 (2022), 173 - 174 *Contributed Paper*

HIGH-RESOLUTION SPECTROSCOPY OF ASTROPHYSICALLY RELEVANT MOLECULAR IONS

O. ASVANY[1], S. THORWIRTH[1], P. C. SCHMID[1], T. SALOMON[1] and S. SCHLEMMER[1]

[1] *I. Physikalisches Institut, Universität zu Köln, Zülpicher Str. 77, 50937 Köln, Germany*
E–mail asvany@ph1.uni-koeln.de

Abstract. High-resolution rovibrational and pure rotational spectra for molecular ions of astrophysical interest have been recorded in the Cologne laboratories. Recent examples include CN^+, $CH_2NH_2^+$, $CH_3NH_3^+$, c-$C_3H_2^+$, l-$CCCH^+$, and $HCCCO^+$ (see references below for the first four molecular ions). These have been investigated using ion trap instruments which feature mass selection via quadrupole mass analyzers, long storage times in cryogenic 22-pole ion traps, and cooling of the ions via He buffer gas to temperatures as low as 4 K. Due to the low number of stored ions (typically less than 10^5), so-called action spectroscopic techniques have to be applied, in which the ion count is used as the spectroscopic signal. As the ion counting efficiency is close to unity, action spectroscopy can be very sensitive. Several such action spectroscopic schemes have been developed in-house during the last couple of years. Recent technical advances along this direction are demonstrated for the ions l-$CCCH^+$ and $HCCCO^+$ in this contribution. The advantage of using mass-selected, cryogenically cooled ions is that very clear spectroscopic information is obtained, with only a handful of lines, but which can be intense and have very narrow linewidth. This allows to obtain accurate frequency information and to resolve overlapping lines. An example of such an approach is the first rotational spectrum of protonated methylamine, $CH_3NH_3^+$, shown in the Figure below. For this prolate symmetric top molecule thirteen transitions between 80 and 240 GHz were detected in the ground vibrational state, covering $J_K = 2_K - 1_K$ up to $J_K = 6_K - 5_K$ with $K = 0, 1, 2$. A comparison with spectroscopic simulations reveals that this symmetric top molecule is not rigid, but exhibits torsional motion between the CH_3 and NH_3 subunits. This result and the other laboratory rotational data presented here will further support and guide radio-astronomical searches of these species in space. A first search of $CH_3NH_3^+$ in the Sagittarius B2(N) and (M) regions was performed but unfortunately without a clear detection.

References

Thorwirth, S., Schreier, P., Salomon, T., et al.: 2019, *Astrophys. J. Lett.* **882**, L6
Markus, C.R., Thorwirth, S., Asvany, O., and Schlemmer, S.: 2019, *PCCP* **21**, 26406
Schmid, P. C., Thorwirth, S., Endres, C. P., et al.: 2022, *Frontiers in Astronomy* **8**, 805162
Markus, C.R., Asvany, O., Salomon, S., et al.: 2020, *Phys. Rev. Lett.* **124**, 233401

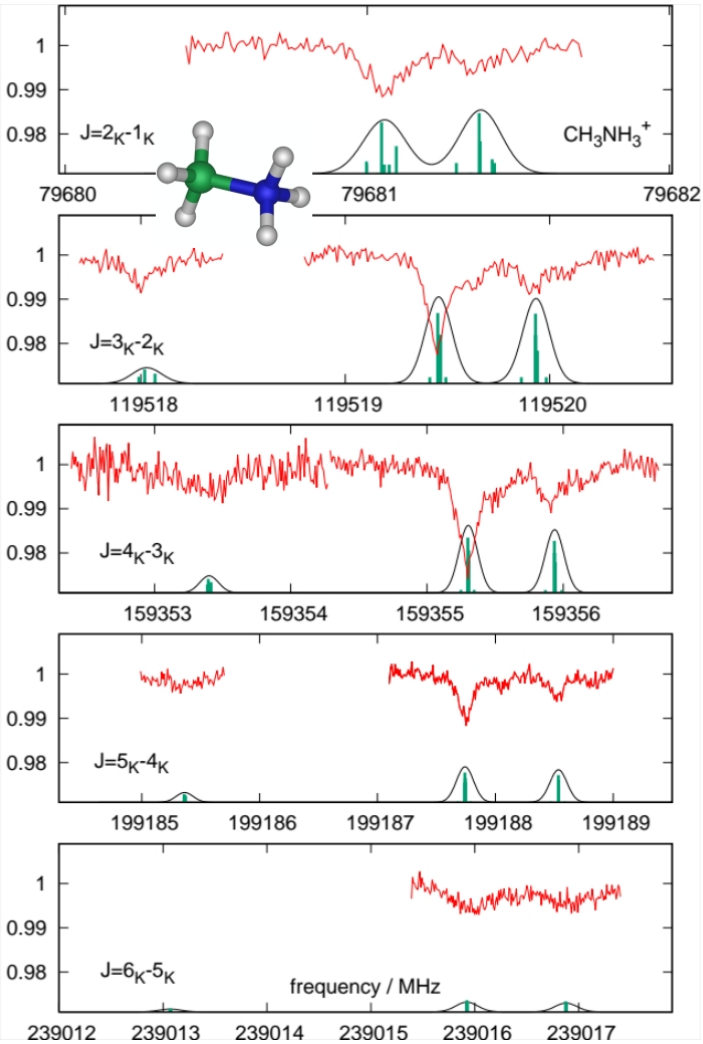

Figure 1: Measured rotational transitions $J'_K \leftarrow J''_K$ ($K = 0, 1, 2$) of $CH_3NH_3^+$ (red trace). The simulations (green sticks indicate nitrogen quadrupole hyperfine structure and their convolution is givens as black traces) are based on a simple rigid symmetric rotor model. Discrepancies between the simulated and measured spectra, in particular the blue-shifted shoulders for $K = 0$ and 1 (red trace), are due to the neglect of torsional motion between the CH_3 and NH_3 subunits in the simulation. Figure taken from Schmid et al 2022.

Publ. Astron. Obs. Belgrade No. 102 (2022), 175 - 178 *Contributed Paper*

THE EFFECT OF PLASMA SEED TREATMENT ON GERMINATION AND EARLY GROWTH OF *THUJA KORAIENSIS* NAKAI PLANTS

I. I. FILATOVA[1], V. A. LYUSHKEVICH[1], S. V. GONCHARIK[1], U. I. TORCHYK[2], Y. V. KANDRATAU[2] and M. O. SLESARENKA[2]

[1]*B.I. Stepanov Institute of Physics of the National Academy of Sciences of Belarus, 220072, Minsk, Nezavisimosti Ave., 68-2, Belarus*
E-mail filatova@presidium.bas-net.by

[2]*Central Botanical Garden of the National Academy of Sciences of Belarus, 220012, Minsk, Surganov Str. 2v*
E-mail kondratov.20144@mail.ru

Abstract. Seeds of *Thuja koraiensis* Nakai widely used in decorative gardening and landscaping were treated with radio frequency (RF) and dielectric barrier discharge (DBD) plasmas to enhance germination, improving the morphometric parameters and to obtain possible selective samples for subsequent breeding of ornamental species. Plasma seed treatment reduced the period of seed germination, significantly increased the average root length - by 75% for RF plasma treatment and by 175% when exposed to DBD plasma and induced morphological changes in seedlings.

1. INTRODUCTION

At present, the non-thermal plasma surface activation of seeds is increasingly being explored in the agricultural field as an effective pre-sowing treatment enhancing seed germination and plant growth, providing a certain degree of seed decontamination, see reviews Sera et al. 2018, Waskov et al. 2021. The authors mainly report on the short-term effects of plasma seed treatment at the juvenile stage of annual plants in laboratory conditions. However, only a few papers are known on the response of perennial species to plasma seed treatment [Puac et al. 2005, Mildaziene et al. 2016, Pauzaite et al. 2017, Ling Li et al. 2021]. Nevertheless the role of perennial ornamental plants, landscaping techniques in optimizing the living environment of the urban population is increasing, which requires new approaches to landscaping, taking into account the increasing anthropogenic pressure on plants.

Modern breeding of ornamental plants is based on the use of several basic approaches: selection among seedlings of specimens that differ in a number of

characteristics from the original mother plant; vegetative propagation of mutations arising on plants; the effect on seed or vegetative material of chemical or physical mutagens, etc.

In this paper, we aimed at cold plasma application for seed treatment of perennial ornamental plant *Thuja koraiensis* Nakai to increase the germination, as well as to detect possible mutational changes in plants for obtain new breeding varieties.

2. EXPERIMENTAL SECTION

1. 1. PLASMA SETUPS FOR SEED TREATMENT

We used two plasma systems for seeds treatment: low pressure radio frequency (RF) discharge (RF plasma) as well atmospheric pressure dielectric barrier (DBD) discharge (DBD plasma).

RF plasma treatment was carried out in a planar geometry capacitively coupled 5.28 MHz plasma reactor consisting of two plane-parallel electrodes placed in a vacuum chamber [Filatova et al. 2020]. Voltage was applied to the upper electrode. Petri dish with seeds was placed on a lower electrode. Before igniting the discharge, the air was pumped from the chamber for about 7 min to reach the working pressure 200 Pa. The input power was 8.4 W.

DBD plasma ignited between two round electrodes separated from each other by a distance of 3 mm [Savastenko et al. 2022]. The upper mesh electrode with 98 mm diameter was covered by 2.0 mm quartz glass layer and connected to an alternating current power source. The lower plate electrode made of copper was grounded. The applied voltage (peak-to-peak value) was up to 25 kV with a frequency of 1 kHz. The samples to be treated were put on the grounded electrode. The power was not more than 6.2 W.

Treatment duration with both RF and DBD plasmas was 7 min.

2. 1. PLANT MATERIAL AND METHODS

Seeds of *Thuja koraiensis* Nakai harvested in the third decade of August 2021 were collected from the Central Botanical Garden of the National Academy of Sciences of Belarus (Minsk, Belarus).

The effect of treatment was assessed by seed germination tests in laboratory conditions which were started one day after the treatment. Control (untreated) and treated with RF and DBD plasmas seeds (three replicates of 100 seeds each variant) were placed in Petri dishes which were put in a climatic chamber (KK 750, POL-EKO-APARATURA, Poland) with constant light and temperature conditions (light: for 16 h at 27 ºC, darkness: for 8 h at 20°C). Seed germination was monitored for 15 days.

Then seedlings were planted in containers and placed in a heated greenhouse with a round-the-clock temperature of 22 ºC for future observation.

3. RESULTS AND DISCUSSIONS

It was found that plasma treatment had a stimulating effect on the germination of *Thuja koraiensis* Nakai seeds (Figure 1a). The treatment with RF and DBD plasmas increased the germination rate by 9.4 and 10.8% respectively, which is two times higher than in control. The treatment also affected the dynamics of germination and shortened the period of germination of the bulk of the seeds. The vast majority of plasma treated seeds germinated on the 12th day. In the control variant, less than half of seeds sprouted within the specified time periods, and the peak of seedlings occurred on the 13-14th day. The root growth parameters significantly improved in response to the cold plasma treatment. The average root length increased by 75% for RF plasma treatment and by 175% for DBD plasma (Figure 1b).

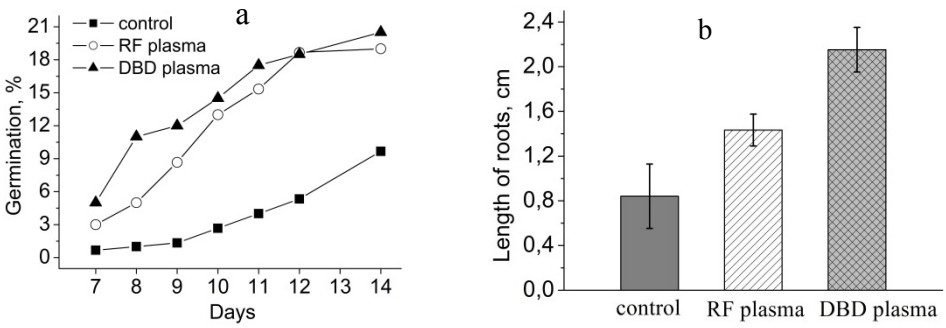

Figure 1: Germination dynamics (a) and the average root length (b) of control and plasma treated seeds of *Thuja koraiensis* Nakai.

During further observations of seedlings grown in containers in a greenhouse, samples with variegated color of needles, as well as with abnormal branching, were observed (Figure 2). It is noteworthy that the first type of anomalies in the control was encountered sporadically, the second was not detected.

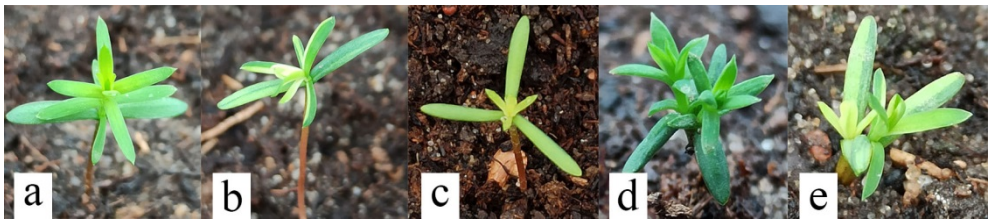

Figure 2: Seedlings of *Thuja koraiensis* Nakai (8 weeks old) in control (a) and in variants of plasma seed treatment with some morphological changes: milky white patches on the needles (b), more yellow color of the needles (c), two central shoots (d), two central shoots and milky-white patches on the needles (e).

Pauzaite et al. 2017 reported that pre-sowing treatment of Norway spruce (*Picea abies* (L.) Karst.) seeds with RF plasma had positive effects on plant development during the later stages, even despite some negative effect of treatment on seed germination. On a longer time scale (17 months after sowing) the plants of Norway spruce grown from the plasma treated seeds (during 5 and 7 min) were higher by 50–60% and had more branches (40–50%) in comparison to the control seedlings. A similar result was obtained on other perennial woody plant species − *Morus nigra* L. and *Rhododendron Smirnowii* Trautv. [see Mildaziene et al. 2016]. Seedlings of these perennials from RF plasma treated groups where inhibition of germination was the strongest also showed the best growth in later stages of development. The most negative stressor effects on seed germination were followed by the most rapid leaf growth possibly due to stress-induced stem branching. Besides, plants grown from seed treated with RF plasma showed various degrees of early branching. The most effective in causing branching was long-duration regime of RF plasma treatment (7 min): more than 30% of plants developed more than one stem, two plants had three stems, and one plant had four stems. The degree of branching correlated well with differences in numbers of leaves and total leaf surface area.

The results obtained in this paper also indicate that both RF and DBD plasma treatment of seeds can induce similar types of anomalies in *Thuja koraiensis* Nakai which may survive or even intensify in subsequent stages of plant growth.

4. CONCLUSIONS

It has been shown that plasma treatment of seeds of *Thuja koraiensis* Nakai significantly accelerates and increases germination, and also stimulates root growth. Seedlings with abnormal color of needles and shape of habitus were noted. If this trait is preserved during a longer observation, this will allow us to recommend plasma seed treatment as a new effective and ecologically friendly method for the selection of *Thuja koraiensis* Nakai plant.

References

Sera, B., Sery, M. : *Plasma Sci. Technol*. 2018, **20,** 04401.
Waskow, A., Howling, A., Furno, I. : 2021, *Front. Phys*. **9**, 617345.
Puac N., Petrovic Z., Zivkovic S, et al.: 2005, *Plasma Processes and Polymers*, eds. R. d'Agostino, P. Favia, C. Oehr and M.R. Wertheimer, Whiley, 193-203.
Mildaziene Pauzaite, G.et al. : 2016, *Bioelectromagnetics*, **37**, 536.
Pauzaite, G., Malakauskiene, A. et al.: 2017, *Plasma Process Polym.*, e1700068.
Ling Li, Jingbo Chen, et al. : 2021, *Crop Science*, **61**(4), 2827.
Filatova, I., Lyushkevich, V. et al.: 2020, *J. Physics D: Appl. Phys*., **53**(24), 24400.
Savastenko, N., Shcherbovich, A. et al.: *High Temp. Mater. Process*, **26**(2), 25.

Publ. Astron. Obs. Belgrade No. 102 (2022), 179 - 182 *Contributed Paper*

SELF-MIXING INTERFEROMETRY FOR PLASMA DIAGNOSTICS

NIKOLA GOLEŠ[1], NEDA BABUCIĆ[2], NENAD M. SAKAN[2] and MILIVOJE IVKOVIĆ[2]

[1]*Faculty of Physics, Studentski trg 12, 11001 Belgrade, Serbia*

[2]*Institute of Physics, Pregrevica 118, 11080 Belgrade, Serbia*
E-mail ivke@ipb.ac.rs

Abstract. The feature of the diode laser that it, besides producing coherent light, has an integrated photodiode, was exploited as the reference branch of interferometers in several applications. A set of continuous laser diodes, emitting at various wavelengths, was initially calibrated by measuring the mechanical motion of an external mirror mounted on a speaker, controlled by a signal generator. Afterwards, the possibility of applying this so-called self-mixing interferometer for the study of low-pressure pulsed discharge and laser-produced plasmas was investigated and assessed.

1. INTRODUCTION

Since they could be stable and coherent light sources, lasers are unavoidable in optical interferometric investigations and sensors. In contrast to most of the other laser systems, a laser diode has very large gain of active medium (Ma et al., 2013), allowing its optical resonator cavity to have an exit mirror of lesser reflection. This unique construction detail reflects both on their multi-mode regime of operation, as well as on the possibility of strongly coupling them with an external optical system. In more complex optical systems, effort is made to avoid this coupling as much as possible, usually using optical isolators, because of its influence on the inverse population in active media and hence on the laser behavior. Here, on the contrary, the coupling effect is used as a method of producing interference, an approach which was studied with gas discharge lasers for plasma electron density measurement (Rasiah, 1994). Experimental, as well as theoretical studies of the effect of strong coupling with the external resonator could be found in a variety of papers for earlier references, see (Salathé, 1979), (Kobayashi et al., 1981). Various applications of this, so called self-mixing effect, could be seen in the PhD thesis (Alexandrova, 2017), for instance.

The optical path of the self-mixing interferometer is shown on Figure 1. It is important to emphasize the fact that the only external component of the system that needed to be adjusted was the external mirror 3. The low reflectivity of the laser

diode exit mirror (numbered 2. on Figure 1), which is on the order of 20% up to 50% (in contrast to, for example, a He-Ne laser exit mirror with a reflectivity close to 99%), enables simple coupling of the external mirror, which in turn becomes part of the resonator of the more complex system.

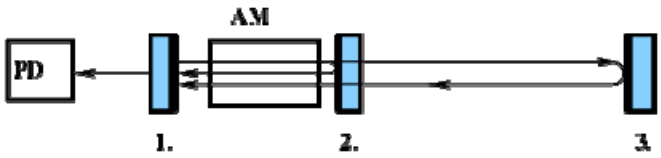

Figure 1: The simplified optical scheme of the self-mixing interferometer: AM – active medium, PD – monitoring photodiode, 1. – back mirror and 2. – front mirror are constructive parts of the laser diode, mirror 3. – external part.

2. EXPERIMENTAL RESULTS

The experiment presented here was a two-phase investigation. First, a study of the applicability and capabilities of the available diodes for the self-mixing effect detection was carried out. An external mirror (denoted by 3. on Figure 1) was mounted on the membrane of a speaker for its position to be mechanically modulated, leading to the detection of an interferometric figure on the monitoring photodiode of the laser diode module. Not all laser diodes showed equal potential for producing the self-mixing effect; the desired effect could only be observed in the case of pure continuous emitting laser diodes that are produced with integrated monitoring photodiodes. In addition, only a limited number of laser diodes was capable of producing coherence high enough to induce a measurable interference effect on the monitoring diode signal. In order to characterize a laser diode, work has been carried out to determine the conditions and limits where it can produce detectable interference (see for instance Figure 2 for the measured signals). In addition, the displacement of the speaker membrane versus time was measured from the interferograms, and the frequency of the movement of the membrane was compared to the one applied from the generator.

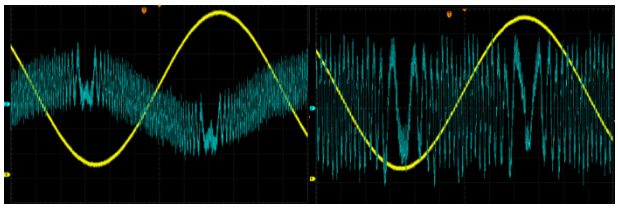

Figure 2: Self-mixing interferograms (thin blue line) for different sound frequencies applied to the speaker (thick yellow line).

The possibility of applying the laser diodes for plasma interferometry was investigated on two experimental setups, the pulsed discharge source described in detail in (Stankov et al., 2018), as well as in laser-induced breakdown spectroscopy (LIBS).

In the first step the interferometer, i.e., the external mirror, is adjusted so that an interference pattern appears in the signal on the photodiode. For easier observation of the effect measured by the interferometer, a large difference in intensity between bright and dark fringes is needed, therefore the alignment of the optical system is adjusted to produce fringes of maximum intensity. A sample interferogram of small mechanical disturbances of a properly adjusted system is shown on Figure 3. Such patterns were obtained for interferometers ranging in length from 15 cm to 50 cm, indicating that the low coherence length of the laser diodes (as compared to gas lasers) does not prevent them from being used in these applications.

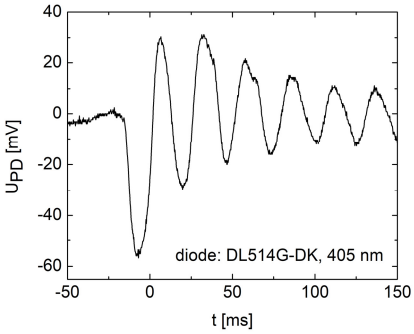

Figure 3: Interferogram of a mechanical disturbance of a properly aligned optical system.

An evaluation of the background plasma glow intensity was performed, to determine whether narrow-band filtering of the combined laser and plasma light is necessary. In the case of the pulsed discharge, the plasma background signal was several orders of magnitude greater that the intensity of the fringes, making the implementation of this diagnostic technique unattainable without additional isolation of the laser signal, which was not attempted as part of this study. However, in the case of LIBS the background glow of the plasma has minimal effect on the output signal, making it possible to test the diagnostic without modifications.

In the case of LIBS, which is suitable for testing the application of the self-mixing interferometer for the diagnostics of a spatially non-homogenous plasma, the axis of the optical setup was positioned 1 mm above a Si target irradiated by a second harmonic (532 nm) Nd:YAG laser beam, with an energy of 150 mJ and a 7 ns pulse duration. The target was positioned inside a T-shaped chamber with a diameter of 38 mm such that the distance from the window to the target was 50 mm, placed on an x-y computer-controlled stage. Due to the small dimensions of the chamber, multiple reflections of the acoustic emission waves off its walls are anticipated, see (Burger et al., 2015). All measurements were performed in air, so the glass windows of the chamber which lie on the optical path were removed. Having in mind that the plasma emission lasts on the order of tens of μs, we can conclude that the signal shown on Figure 4a is integrated, i.e., that the response time of the photodiode is too short for it to be used for plasma electron density diagnostics, even though it exhibits fringing likely arising from the changing N_e.

On the other hand, the fringes seen in the millisecond time range (Figure 4b) encourage further study of potential implementation of this diagnostic method for opto-acoustical or simple acoustical investigation of plasma propagation dynamics (Burger et al., 2015), as well as several potentially accurate methods for measuring various dynamic mechanical processes. As a control, a measurement was made with the axis of the setup positioned 3 cm above the target, outside of the plasma volume, where none of the effects on Figure 4 were observed.

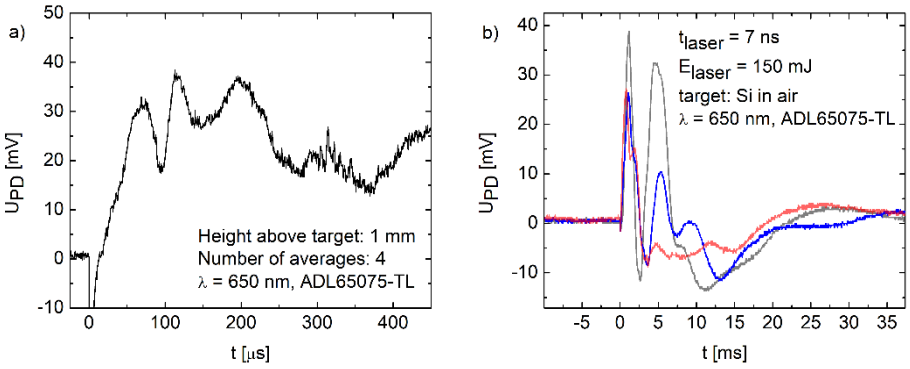

Figure 4: Photodiode signals in the LIBS setup on the a) μs and b) ms timescales.

3. CONCLUSION

The application of the self-mixing method as a means of measuring mechanical movement (disruption of setup and/or controlled movement of external mirror by a frequency generator), and for plasma diagnostics purposes, was proposed and evaluated. The requirements for laser diode characteristics, the necessity of narrow-band optical filtering, as well as the types of pulsed discharges and their characteristics which can be studied by this method (due to the limitations brought about by the response time of the integrated photodiode) were determined.

Acknowledgements

This research was funded by the Ministry of Education, Science and Technological Development of the Republic of Serbia, Contract: 451-03-68/2022-14/200024 and supported by the Science Fund of the Republic Serbia, Grant no. 3108/2021.

References

Alexandrova, A. : 2017, *Investigation into laser self-mixing for accelerator applications*, PhD thesis, University of Liverpool.
Burger, M., Nikolić, Z. : 2015, *Spectrochimica Acta Part B*, **110**, 70-78.
Kobayashi, S., Kimura, T. : 1981, *IEEE Journal of Quantum Electronics*, **17**, 681.
Ma, M., et al. : 2013, *Opt. Express*, **21**, 10335.
Rasiah, I. J. : 1994, *Review of Scientific Instruments*, **65**, 1603.
Salathé, R. P. : 1979, *Applied Physics*, **20**, 1.
Stankov, B. D., et al. : 2018, *Review of Scientific Instruments*, **89**, 053108.

Publ. Astron. Obs. Belgrade No. 102 (2022), 183 - 186 *Contributed Paper*

CHARACTERIZATION OF THE DIELECTRIC BARRIER-FREE ATMOSPHERIC PLASMA SYSTEM

MIROSLAV GULAN[1] and VLADIMIR MILOSAVLJEVIĆ[1,2]

[1]*School of Physics, Technological University Dublin, Ireland*
E-mail D14125092@mytudublin.ie

[2]*Faculty of Physics, University of Belgrade, Serbia*
E-mail vladimir@ff.bg.ac.rs

Abstract. This work presents a characterization of the new pulse plasma system that's operating at an atmospheric pressure and it be used for a material functionalization and/or surface serialization. The study includes details of developing and operating, in-house made, non-thermal, dielectric-free atmospheric plasma system. The new plasma system allows an increase in the plasma-surface interaction selectivity and reduces plasma induced damages to the surface. The plasma rig creates a plasma discharge in gap from 5 to 60 mm, and in the volume of hundreds of cm^3.

The plasma source has a pulse resonance circuit which allows the creation of a high voltage pulses with the ability to control and reduce a current of the plasma discharge. This ability allows the temperature of the treated sample's (organic or inorganic) material to be kept at room temperature. The study also includes different setting of plasma source to control the ion flux, the ion energy and the plasma chemistry. Plasma pulsing allows new domains of ion energy and radical fluxes to be reached, thereby extending the operating range of plasma generators.

1. INTRODUCTION

The impact of a gaseous plasma on a surface treatments is well known and it has been used for the last several decays. In the past, plasma systems were mainly used in a low pressure (vacuum) environment, and in the semiconductor industry, for two processes, sputtering and etching. In last several years, an atmospheric plasma systems were presented on the market, like Plasma Jets and/or Dielectric-Barrier Discharge (DBD). A plasma jet system creates plasma in a nozzle with flow gas as visible plasma stream long about 3-15 mm. The gas carrier could be argon, helium, but also an ambient air. The plasma jet systems are mainly used for local plasma treatment of a small surface areas. For treatment of the bigger surface areas, it has

been used in conjunction with a XYZ position systems. In that case, these systems are useable for bigger surface treatment, but they are also significantly slow down the treatment time, and that is an obstacle for an industrial use, Cullen and Milosavljević 2015. DBD's systems have a two metal electrodes and a dielectric material, that is between the electrodes. In reality, there are many variations of the electrodes' shape, but the basic concept remains the same, Milosavljević and Cullen 2017. The Critical point of any DBD reactor is the quality of dielectric material. Quality and homogeneity of the dielectric material is important, to be avoided a degradation of the isolation layer and the creation of arcing discharge. Inhomogeneity of dielectric material reduce lifetime of DBD system. The main function of this dielectric material is to spread the electrical charge throughout the entire plasma electrodes to increase homogeneity by creating of multiple conducting paths for the discharges to occur. There is also issues during the DBD plasma discharge, the dielectric is degrading, and it will be contaminated by the gas plasma chemistry.

Therefore, the main motivation for this work is developing an atmospheric dielectric barrier free (non-DBD) plasma system, that can produce a stable, reproducible and a homogeneity of the atmospheric plasma discharge. This plasma discharge will be at an ambient atmosphere air, i.e. without any additional gas.

2. EXPERIMENT

The atmospheric plasma system is developed as a complex system that includes: a plasma power supply unit, a high voltage transformer and plasma pin reactor (Figure 1).

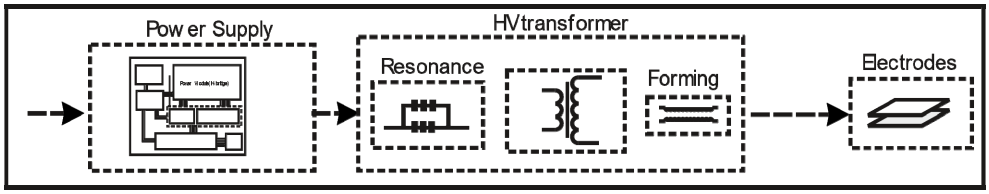

Figure 1: The Basic block diagram of the plasma system.

The Power Supply Unit (PSU) is the most complex part of the whole plasma system. There are independent logical parts implemented to combine functionality, safety, efficiency and configurability. The main parts of PSU are showed in Figure 2: Power Filter, PFC – Power Factor Correction, Internal power 24 V, Measurement and Control Module, Human Machine Interface Module, Input Output Module and Power Module with full H-Bridge.

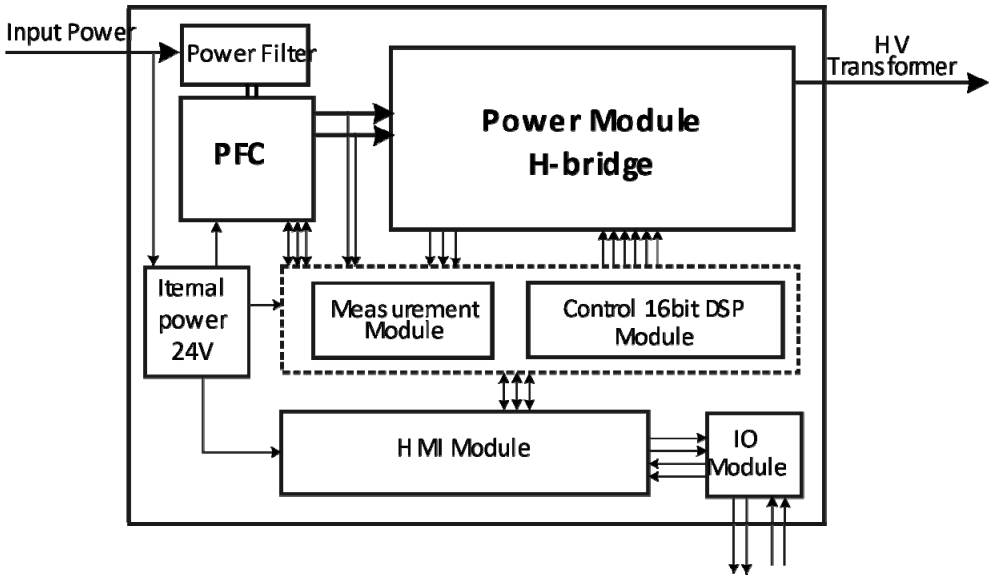

Figure 2: The Block diagram of power supply unit.

The new plasma reactor with a pin top electrode was designed (Figure 3), Gulan and Milosavljević, 2021. The pins have different lengths in the middle and at the edge of the electrode. The pins in the middle are longest and pins at the corners are the shortest. The Pins from the middle to edge of the electrode are a gradually shorter, i.e. the 3D profile of pins allows the removal of a dielectric barrier.

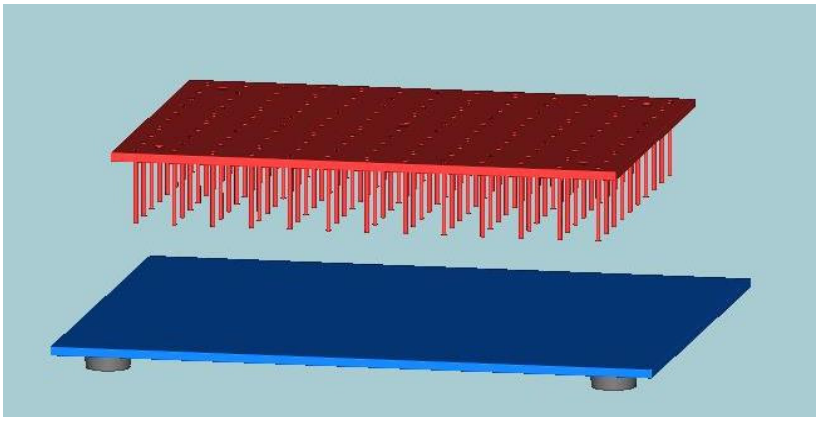

Figure 3: The electrodes of the plasma reactors.

3. RESULTS AND DISCUSSION

Figure 4 is recorded with settings: resonance frequency = 50.0 kHz, discharge frequency = 500 Hz, duty cycle = 42 % and voltage (pick-to-pick) V = 30 kV.

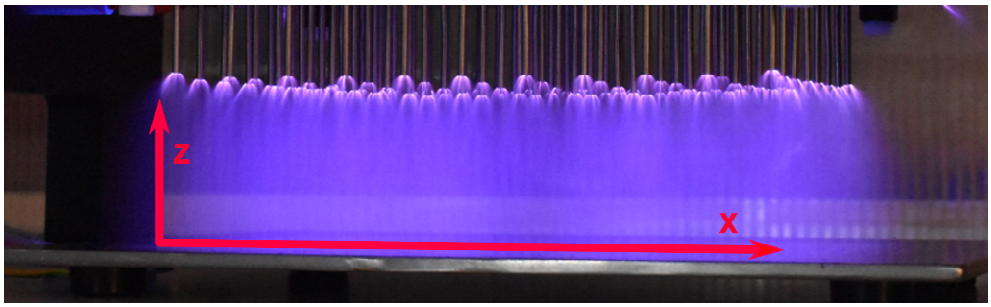

Figure 4: Plasma discharge.

Figure 5a shows a different O_3 concertation at the middle of the plasma reactor and at the edges along of X-axis. Concertation of O_3 dropped at the edges due to its interaction with the ambient air. To reach better homogeneity of O_3 along X-axis, the plastic enclosure box was used around electrodes. This plastic enclosure (Figure 5b) helps to improve homogeneity of O_3 and increase concertation of ozone for about 30 %, Gulan and Milosavljević 2022.

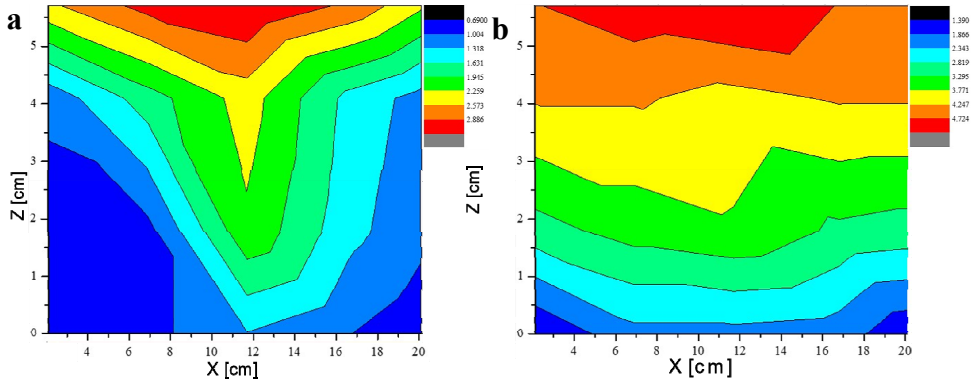

Figure 5: O3 concentration [mg/l] (a) without plastic enclosure box, (b) with plastic enclosure box.

References

Cullen, P.J., Milosavljević, V.: 2015, *Progress of Theoretical and Experimental Physics,* **2015/6**, 063J01.

Milosavljević, V., Cullen, P.J.: 2017, *Eur. Phys. J. Appl. Phys.,* **80**, 20801.

Gulan, M., Milosavljević, V.: 2021, *Eur. Phys. Lett.,* **133**, 43002.

Gulan, M., Milosavljević, V.: 2022, *International Journal Of Energy Research,* **46/5**, 6337

Publ. Astron. Obs. Belgrade No. 102 (2022), 187 - 190 *Contributed Paper*

LASER DRIVEN ELECTRON ACCELERATION BY q-GAUSSIAN LASER PULSE IN PLASMA: EFFECT OF SELF FOCUSING

NAVEEN GUPTA

Lovely Professional University Phagwara
E-mail naveens222@rediffmail.com

Abstract. A scheme for electron acceleration by self focused q-Gaussian laser pulses in under dense plasma has been presented. The relativistic increase in the mass of plasma electrons gives nonlinear response of plasma to the incident laser pulse resulting in its self focusing. Under the combined effects of saturation nature of relativistic nonlinearity of plasma, self focusing and diffraction broadening of the laser pulse, the beam width of the laser pulse evolves in an oscillatory manner. An electron initially on pulse axis and at the front of the self focused pulse, gains energy from it until the peak of the pulse reaches. When the electron reaches at the tail of the pulse, the pulse begins to diverge. Thus, the deacceleration of the electron from the trailing part of pulse is less compared to the acceleration provided by the ascending part of the pulse. Hence, the electron leaves the pulse with net energy gain. The differential equations for the motion of electron have been solved numerically by incorporating the effect of self focusing of the laser pulse

1. INTRODUCTION

Whenever we think of particle accelerators, we consider them to be meant only for research at the very edge of known physics as these enormous facilities take decades to build[1-3]. However, along with this lofty goal, though, particle accelerators are being used for decidedly more down-to-Earth projects-cancer treatments and medical sterilization, security screening, research into new materials, biological processes, and much more.

As plans are laid for the world's largest accelerator, the Superconducting Supercollider, accelerator technology is approaching" practical limits. There are two reasons. First, the forces from magnetic fields are becoming greater than the structural forces that hold a magnetic material together; the magnets that produce these fields would themselves be torn apart[10]. Second, the energy from electric fields is reaching the energies that bind electrons to atoms; it would tear electrons from nuclei in the accelerator's support structures. In this regard a new scheme of acceleration of charged particles by intense laser pulses propagating through plasmas, has gained a significant interest among researchers[4,5]. The aim of this paper is to give first theoretical investigation on laser driven electron acceleration on self focused q-Gaussian laser pulse in plasma..

2. SELF FOCUSING of LASER PULSE

Consider the propagation of a circularly polarized laser pulse with angular frequency ω_0 and wave number k_0 through a plasma with equilibrium electron density n_0. The electric filed vector of the laser pulse is given by

$$\boldsymbol{E} = A_0\, e^{\iota(k_0 z-\omega_0 t)} e^{-\frac{\left(\frac{t-z}{v_G}\right)^2}{2\tau_0^2}} (\boldsymbol{e_x} + \iota \mathbf{e_y}) \tag{1}$$

where, v_G is the group velocity of laser pulse and τ_0 is its pulse duration. The dielectric function of plasma can be written as

$$\epsilon = 1 - \frac{\omega_p^2}{\omega_0^2}$$

where,

$$\omega_p^2 = \frac{4\pi e^2}{m_e} n_0 \tag{2}$$

is the equilibrium plasma frequency, (m_e, e) being the electronic mass and charge respectively. Under the intense field of the laser pulse the oscillations of the plasma electrons become relativistic and the mass m_e of the electron in eq.(2) need to be replaced by the relativistic mass, which is related to pulse amplitude as[26]

$$m_e = m_0 \sqrt{1 + \frac{e^2}{m_0^2 c^2 \omega_0^2} A_0 A_0^\star} \tag{3}$$

Thus, in the presence of laser pulse the dielectric function of plasma gets modified as

$$\epsilon = 1 - \frac{\omega_{p0}^2}{\omega_0^2}\left(1 + \frac{e^2}{m_0^2 c^2 \omega_0^2} A_0 A_0^\star\right)^{-\frac{1}{2}} \tag{4}$$

where,

$$\omega_{p0}^2 = \frac{4\pi e^2}{m_0} n_0$$

is the equilibrium plasma frequency. Thus, the relativistic effects make the index of refraction of plasma intensity dependent which in turn due to the spatial dependence of the amplitude structure of the laser pulse, resembles to that of graded index fiber. Separating the dielectric function of plasma into linear (ϵ_0) and nonlinear (ϕ) parts as

$$\epsilon = \epsilon_0 + \phi(EE^\star)$$

we get

$$\epsilon_0 = 1 - \frac{\omega_{p0}^2}{\omega_0^2} \tag{6}$$

and

$$\phi(EE^\star) = \frac{\omega_{p0}^2}{\omega_0^2}\left\{1 - \frac{1}{\left(1+\frac{e^2}{m_0^2 c^2 \omega_0^2} A_0 A_0^\star\right)^{\frac{1}{2}}}\right\} \tag{7}$$

Now, the wave equation governing the evolution of amplitude A_0 of the laser pulse is

$$\iota\frac{\partial A_0}{\partial z} = \frac{1}{2k_0}\nabla_\perp^2 A_0 + \frac{k_0}{2\epsilon_0}\phi(A_0 A_0^\star)A_0 \tag{8}$$

In the present investigation we have used variational theory to solve eq.(8) for q-Gaussian irradiance of the laser pulse.

$$A_0(x,y,z) = \frac{E_{00}}{f}\left\{1+\frac{r^2}{qr_0^2f^2}\right\}^{-\frac{q}{2}} \tag{9}$$

Here, $E_{00}$is the axial amplitude of the pulse, q is deviation parameter and f is dimensionless beam width parameter. The evolution equation of beam width is

$$\frac{d^2f}{dZ^2} = \left(\frac{c}{\omega_0 r_0}\right)^4\left[\frac{\left(1-\frac{1}{q}\right)\left(1-\frac{2}{q}\right)}{\left(1+\frac{1}{q}\right)}\frac{1}{f^3} - \left(1-\frac{1}{q}\right)\left(1-\frac{2}{q}\right)\left(\frac{\omega_{p0}^2 r_0^2}{c^2}\right)\frac{a_0^2}{f^3}I\right] \tag{10}$$

where,

$$I = \int_0^\infty u^3\left(1+\frac{u^2}{q}\right)^{-2q-1}\left(1+\frac{\beta E_{00}^2}{f^2}\left(1+\frac{u^2}{q}\right)^{-q}\right)^{-\frac{3}{2}}du$$

$$d' = dk_0 r_0^2$$

$$u = \frac{r}{r_0 f}$$

$$Z = \frac{z\omega_0}{c}$$

$$a_0 = \frac{eE_{00}}{m_0\omega_0 c}$$

3. ELECTRON ACCELERATION

Equations of motion of electron are

$$\frac{dP_X}{dZ} = \left(1-\frac{\gamma}{P_Z}\right)\frac{a_0}{f}\left\{1\frac{(X^2+Y^2)c^2}{qr_0^2\omega_0^2f^2}\right\}^{-\frac{q}{2}}e^{-\frac{(T-Z)^2}{2\omega_0^2\tau_0^2}}\cos(T-Z) \tag{11a}$$

$$\frac{dP_Y}{dZ} = -\left(1-\frac{\gamma}{P_Z}\right)\frac{a_0}{f}\left\{1\frac{(X^2+Y^2)c^2}{qr_0^2\omega_0^2f^2}\right\}^{-\frac{q}{2}}e^{-\frac{(T-Z)^2}{2\omega_0^2\tau_0^2}}\sin(T-Z) \tag{11b}$$

$$\frac{dP_Z}{dZ} = \frac{a_0}{f}\left[-\left(\frac{P_X}{P_Z}\right)\cos(T-Z)+\left(\frac{P_Y}{P_Z}\right)\sin(T-Z)\right]\left\{1\frac{(X^2+Y^2)c^2}{qr_0^2\omega_0^2f^2}\right\}^{-\frac{q}{2}}e^{-\frac{(T-Z)^2}{2\omega_0^2\tau_0^2}} \tag{11c}$$

$$\frac{dX}{dZ} = \frac{P_X}{P_Z} \tag{11d}$$

$$\frac{dY}{dZ} = \frac{P_Y}{P_Z} \tag{11e}$$

$$\frac{dT}{dZ} = \left(\frac{\gamma}{P_Z} - 1\right) \tag{11f}$$

$$\gamma = \sqrt{1 + P_X^2 + P_Y^2 + P_Z^2} \tag{11g}$$

4. RESULTS and DISCUSSION

Eqs. (10)-(11) have been solved numerically for

$\omega_0 = 1.78 \times 10^{15}$rad/sec, $\tau_0 = 15 \times 10^{-15}$sec, $r_0 = 15\mu$m, $T(0) = 0.2$, $P_X(0) = 0.01$, $P_Y(0) = 0.01$,$P_Z(0) = 0.2$ and $q = (3, 4, \infty)$, $a_0^2 = 3$ and $\left(\frac{\omega_{p0} r_0}{c}\right)^2 = 9$.

Fig.1 depicts the variation of normalized electron energy with distance of propagation. It can be seen that initiallt the electron gain energy from the laser pulse almost linearly then after some distance of propagation its energy gets saturated with a little decrease from the maximum energy gained. Also with increase in deviation parameter q of the laser pulse the overall energy gained by the electron reduces.

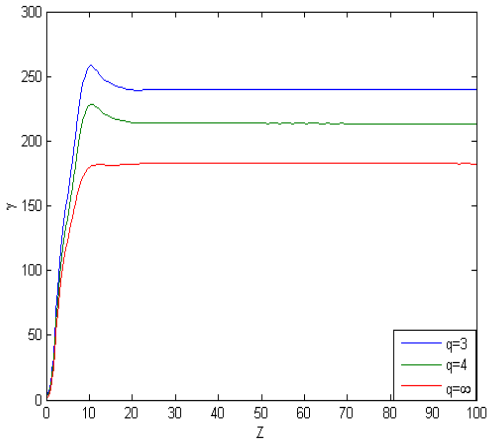

Fig.1: Evolution of electron energy with distance of propagation through plasma for $q = (3,4,\infty)$, $\left(\frac{\omega_{p0} r_0}{c}\right)^2 = 9$ and $a_0^2 = 3$.

References

Smith, C. L.:2000, Sci. Am. **283**, 70.
Rhodes, C. J. :2013, Science Progress 96, 95.
K. R. Symon, SAE Trans. 68, 157 (1960).
C. Joshi, "Plasma accelerators," Sci. Am. 294, 40 (2006).E. Esarey, C. B. Schroeder and W. P. Leemans, "Physics of laser-driven plasma-based electron accelerators," Rev. Mod. Phys. 81, 1229 (2009).

Publ. Astron. Obs. Belgrade No. 102 (2022), 191 - 194 *Contributed Paper*

CORONA MODEL FOR SURGE WAVE PROPAGATION ALONG THE TRANSMISSION LINES

MILAN IGNJATOVIC[1] , JOVAN CVETIC[2],
VERA PROTIC[3] and NEMANJA GRBIC[4]

[1]*School of electrical engineering, Bulevar kralja Aleksandra 73, Belgrade, Serbia*
E-mail ignjatovic@etf.bg.ac.rs

[2]*School of electrical engineering, Bulevar kralja Aleksandra 73, Belgrade, Serbia*
E-mail cvetic_j@etf.bg.ac.rs

[3]*School of electrical engineering, Bulevar kralja Aleksandra 73, Belgrade, Serbia*
E-mail pv130281d@student.etf.bg.ac.rs

[4]*School of electrical engineering, Bulevar kralja Aleksandra 73, Belgrade, Serbia*
E-mail gn120407d@student.etf.bg.ac.rs

Abstract. Drift-diffusion model of the corona discharge is used to simulate the charge-voltage dependence for wire conductors. Simplifications of the calculations are examined in order to implement the corona model for analysis of the surge wave propagation along the transmission lines due to atmospheric discharges.

1. INTRODUCTION

Atmospheric discharges are observed by its pronounced visual and sound effects. For the engineering practice the atmospheric discharges between clouds and ground are of the most importance, causing the damage to objects and the electronic devices and injuring the people. Lightning strokes to the parts of the energy distribution system such as transmission lines and substations can lead to interruptions in the electricity supply to a large number of people and industrial plants (see Hileman 1999). A large number of lightning strokes affect transmission lines that stretch over long distances and areas of diverse relief. Overvoltages caused by lightning discharges travel along the conductors and they can reach substations.

After the overvoltage is generated by lightning stroke into the tower or in one of the conductors, the surge waves propagate along the overhead lines. In the analysis of the propagation of voltage and current waves along the overhead line due to direct lightning stroke, the corona envelope that forms around the conductor has the prevailing effect on the change of the magnitude and the velocity of the surge pulse during the propagation. Corona discharge causes the attenuation and the

distortion of surge waves due to the losses that occur due to air ionization as well as the delay of the pulse caused by increasing the line capacitance. Part of the surge voltage wave which is above the corona threshold will propagate with a speed less than the speed of the light (see Cooray 2008).

2. CORONA MODEL

Corona is a partial discharge that occurs around the tip of sharp electrodes in air with a small curvature radius, inside the volume with a very inhomogeneous electric field. It can be described by the continuity equations for one or more types of particles involved in the discharge (see Morrow 1985). For our simulations, we used the drift-diffusion model for the particles' dynamics with four continuity equations for electrons, positive ions, O^- and O_2^- negative ions,

$$\frac{\partial n_e}{\partial t} + \vec{\nabla} \cdot \left(n_e \overrightarrow{W_e} - D\nabla n_e\right) = S_{ph} + n_e(\alpha - \eta_2 - \eta_3)\left|\overrightarrow{W_e}\right| - n_e n_p \beta + k_{det} n_{O_2^-}, \quad (1)$$

$$\frac{\partial n_p}{\partial t} + \vec{\nabla} \cdot \left(n_p \overrightarrow{W_p}\right) = S_{ph} + n_e \alpha \left|\overrightarrow{W_e}\right| - \left(n_e + n_{O^-} + n_{O_2^-}\right) n_p \beta, \quad (2)$$

$$\frac{\partial n_{O^-}}{\partial t} + \vec{\nabla} \cdot \left(n_{O^-} \overrightarrow{W_n}\right) = n_e \eta_2 \left|\overrightarrow{W_e}\right| - n_{O^-} n_p \beta, \quad (3)$$

$$\frac{\partial n_{O_2^-}}{\partial t} + \vec{\nabla} \cdot \left(n_{O_2^-} \overrightarrow{W_n}\right) = n_e \eta_3 \left|\overrightarrow{W_e}\right| + n_e \alpha \left|\overrightarrow{W_e}\right| - n_{O_2^-} n_p \beta - k_{det}., \quad (4)$$

respectively. On the right hand side of the equations (1)-(4) the terms containing the coefficients α, η_2, η_3, β and k_{det}, represent the gain and the loss of the particles due to electron impact ionization, two-body attachment, three-body attachment, the recombination and the detachment, respectively. The term S_{ph} denotes the generation of electrons and positive ions through the photoionization, whereas W_e, W_p and W_n are the drifts of electrons, positive and negative ions, respectively. The diffusion coefficient for electrons is denoted as D whereas the diffusion of heavy ions is neglected. Therefore the ionic current has only a drift component. Other details about the values of the transport and the reaction coefficients, boundary and initial conditions are given in Ignjatovic and Cvetic 2021.

This model allows a detailed analysis of the temporal evolution and the spatial dependence of the concentration of several types of particles involved in the gas discharge. Equations can be solved for two configurations of electrodes: coaxially placed wires and cylinders and the wires placed above the plane. In the case of the coaxial configuration, due to the radial symmetry, the problem is reduced to 1D equations with one radial coordinate. In the case of wire above ground that exists below the overhead lines, it is necessary to solve the equations of the drift-diffusion model in 2D geometry.

3. DISCUSSION AND RESULTS

In order to simulate the propagation of the surge wave along the overhead line, it is necessary to solve the equations of the drift-diffusion model coupled with the telegraphers' equations. The drift-diffusion model is used to calculate charge-voltage dependence (QV curve) for the conductor, which is then implemented in

the telegraphers' equations. Noda et. al. measured QV curves for overhead wire with a radius of 5 mm, which is located at height of 1.83 m above ground (Fig. 1a), for the voltage pulse amplitudes of 100-600 kV.

The corona discharge simulation requires a large number of time steps. It takes a million time steps to calculate a discharge that lasts 5 μs, so the execution of the program takes a long time, especially when coupling with the telegraphers' equations. For this reason, there is great necessity for speeding up the calculations. Therefore, corona is simulated only at a certain number of positions along the wire, and the values of the charge in the space in between are obtained by linear interpolation.

Other important goal is to try to reduce a calculation in 2D geometry to 1D equations. The simulation of corona discharge in the geometry used by Noda is performed. Entire duration of the voltage pulses is 6.5 μs. The result for electron concentration in the immediate vicinity of the wire in 1.71 μs using 2D equations is shown in Fig. 1b. In the area where the corona discharge takes place, there is a high degree of radial symmetry of the electric field, and thus the concentration of charged particles. That means that radially symmetric 1D equations can be used for the simulation, which significantly reduces the time needed for the calculations.

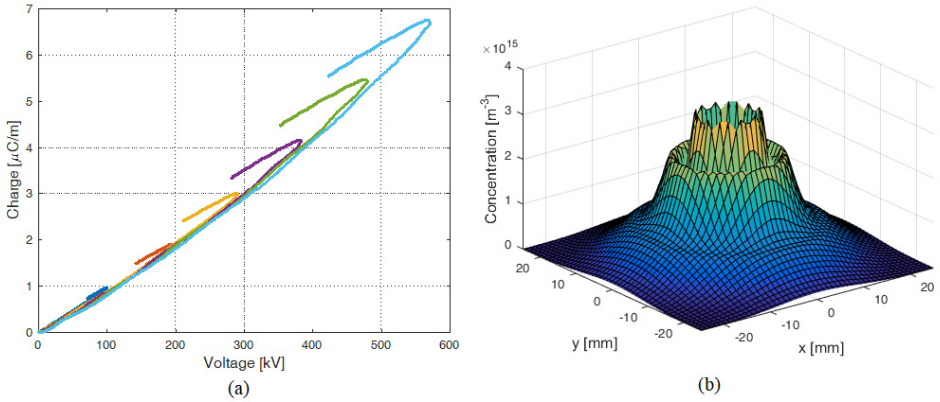

Figure 1: (a) QV curves measured by Noda, (b) Electron concentration around the wire for the 600 kV voltage pulse

In order to simplify the calculations even more, the photoionization can be neglected. All these calculation optimizations are justified, since we are not interested in detailed microstructure of the corona discharge, but only the QV curve is needed, which is an integral characteristic of the discharge. Additionally, optimization of the coefficient α is performed in order to take account the effect of streamers (see Ignjatovic et al. 2019). Due to the existence of the streamer, additional charge will be generated in the area away from the central wire in which the electric field has lower values. The modification is performed so that the coefficient α has a sufficient value for the impact ionization even when the value of the electric field drops to a certain limit, which is in this case 1.5 MV/m. In this way, we were able to obtain good agreement with the experimental measurements, as can be seen in Fig 2.

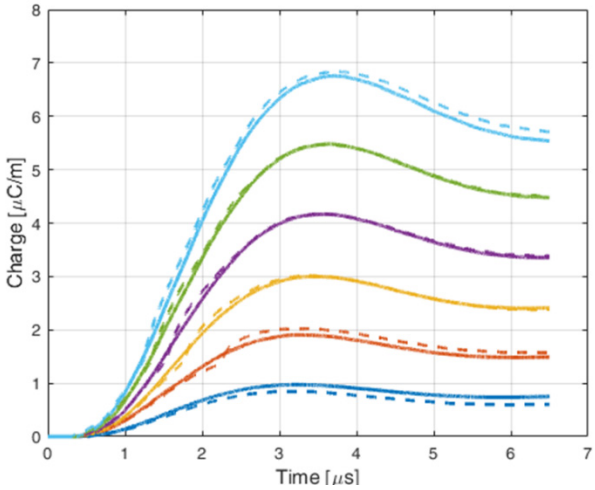

Figure 2: Measured (solid line) and calculated (dashed line) line charge density for the voltage pulses used by Noda

4. CONCLUSION

Having in mind the significant effect of the corona in the propagation of surge impulses along transmission lines, the possibilities of using drift-diffusion model for estimating the QV curves are examined. It was found that the results of 2D simulations give radially symmetric solutions of the electric field and the concentration of the particles in the vicinity of the wire. Therefore 1D equations can be used for the simulations which is less time consuming. Additionally, for the calculation of the overall generated charge, the influence of the photoionization can be neglected. With these simplifications, a very good agreement with the results of the experiments performed by Noda was obtained.

References

Cooray, V., Theethayi, N. : 2008, *IEEE Trans. on Antennas and Propagation*, **56**, 1948
Hileman, A. R. : 1999, *Insulation Coordination for Power Systems*, Boca Raton, USA
Ignjatovic, M., Cvetic, J., : 2021, Int. J. of Elec. Power and Energy Systems, **129**, 106815
Ignjatovic, M., Cvetic, J., Pavlovic, D. : 2019, Proc. of the 6th IcETRAN, pp. 103-106
Morrow, R. : 1985, *Physical Review A*, **32**, 1799
Noda T., Ono, T., Matsubara, H., Motoyama, H., Sekioka, S., Ametani, A. : 2003, *IEEE Transactions on Power Delivery*, **18**, 307

Publ. Astron. Obs. Belgrade No. 102 (2022), 195 - 198 *Contributed Paper*

POLARIZATION SPECTROSCOPY OF NEON LINES FOR ELECTRIC FIELD DISTRIBUTION MEASUREMENT IN THE CATHODE SHEATH OF A GRIMM-TYPE GLOW DISCHARGE

N. V. IVANOVIĆ[1], N. V. NEDIĆ[2], I. R. VIDENOVIĆ[2] and D. SPASOJEVIĆ[2]

[1]*University of Belgrade, Faculty of Agriculture, Nemanjina 6, 11080 Belgrade, Serbia.*

[2]*University of Belgrade, Faculty of Physics, P.O.Box 44, 11001 Belgrade, Serbia*

E-mail nikolai@agrif.bg.ac.rs

Abstract. We report on the results of the experimental study of Ne I 508,038 nm spectral line along the cathode sheath region of an abnormal glow discharge operated in neon with a small admixture of hydrogen. The line was recorded using the Stark polarization spectroscopy technique. The value of coefficient *C*, correlating the Stark shift of sigma (σ) polarized components and electric field strength, was determined and can be further used for electric field strength measurements.

1. INTRODUCTION

Atomic neon spectral lines behavior in external electric fields have been the subject of many experimental and theoretical studies (Ryde 1976, Jäger and Windholz 1984, Windholz and Neureiter 1988, Jäger at al. 1989, Ziegelbecker and Schnizer 1987). Recently, simple methods based on the analysis of the low-field quadratic Stark effect on neon lines have been developed for mapping the electric field distribution in the cathode sheath (CS) of the Grimm-type abnormal glow discharge (Majstorović at al. 2013, Šišović et al. 2014, Ivanović et al. 2017) The complex structure of the Ne I 508.038 nm spectral line was also identified (Ivanović, 2019), but so far was not studied in detail. In this work we demonstrate the use of polarized spectroscopy of the Ne I 508.038 spectral line against the known electric field strength, for determination of its shift coefficient C, so that it can be further used for the measurement of the electric field distribution in the CS.

2. EXPERIMENTAL SETUP

A modified glow discharge source was laboratory-made following the design proposed by Ferreira et al. 1980, and described in detail elsewhere (Kuraica et al. 1992, Majstorović at al. 2013, Šišović et al. 2014, Ivanović et al. 2017). The hollow anode (30 mm long with 8 mm inner diameter) has a longitudinal slot (16 mm long and 1.5 mm wide) for side-on observations along the discharge axis. The water-cooled cathode holder has an exchangeable tungsten electrode, 18 mm long and 7.40 mm in diameter.

Spectroscopic observations were performed side-on through the anode slot, in translation steps along the discharge axis of approximately 1/16 mm. The radiation from the discharge was polarized before entering the spectrometer by orienting the polarizer axis parallel or perpendicular to the discharge axis. The π-polarized component of light is linearly polarized along the electric field direction, while the σ-polarized component is circularly polarized in the plane perpendicular to the electric field. The recordings of the unpolarized profiles were carried out without the polarizer.

The radiation from the discharge is focused with an achromatic lens (focal length 75.8 mm with unity magnification) onto the 20 μm entrance slit (height restriction 2 mm) of the 2 m focal length Ebert-type spectrometer with 651 mm^{-1} reflection grating blazed at 1050 nm. The reciprocal dispersion of 0.37 nm mm^{-1} is used throughout this experiment. All spectral measurements were performed with an instrumental profile close to a Gaussian with the measured full width at half maximum (FWHM) of 8.2 pm in the second diffraction order. The signals are collected by a computer-driven CCD detector (1 x 3648 pixels, 8 μm pixel width).

3. EXPERIMENTAL SETUP

Figure 1 shows three profiles, with different polarization, of the Ne I 508.038 nm spectral line observed at the same position in the CS region. The unpolarized profile, denoted with a black line, is comprised of an unshifted component and three Stark components. The unshifted component, originated from the part of the discharge protruding through the anode slot, is emitted from the zero-field region and appears in the recorded spectra as an unshifted peak that enables us to measure the Stark shifts against it.

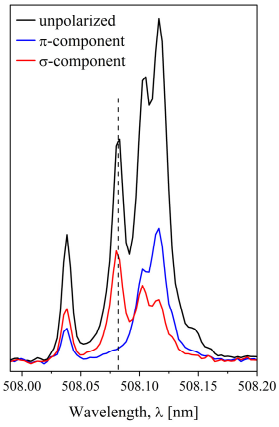

Figure 1: Unpolarized and polarized profiles of the Ne I 508.038 nm spectral line, recorded at the same axial position in the CS region.

The σ-polarized profile features an unshifted peak and one clearly separated Stark component (dashed line). Two additional peaks at the red side are not clearly

separated at lower electric fields, and therefore were not considered in the fitting process.

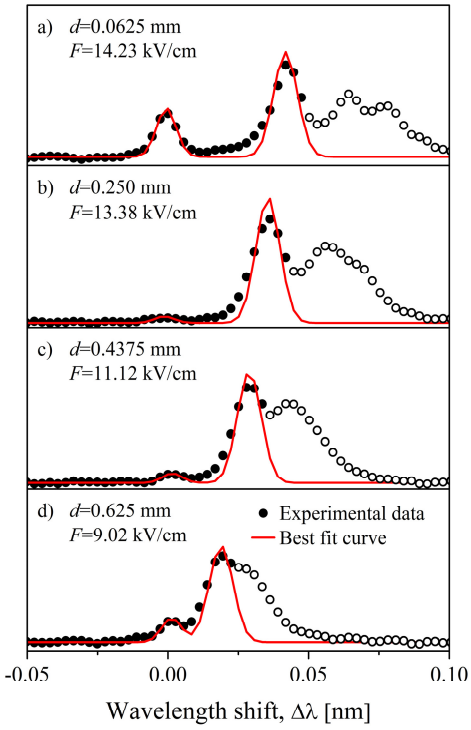

Figure 2: Experimental profiles of the Ne I 508.038 nm spectral line (dots) and their best-fit (red) curves. Hollow experimental points were discarded in the fitting process.

The profiles of the Ne I 508.038 nm spectral line recorded side-on at four different axial positions along the CS region are depicted in Fig. 2. The values of electric field at these positions are determined using the Stark shift measurements of the Ne I 507.420 nm spectral line and the calibration curve of its Stark shifts, see Ivanović et al. 2017. Upon the fitting procedure, the Stark shifts of the Ne I 508.038 nm σ-polarized component were measured relative to the unshifted component using the model function explained in detail by Ivanović et al. 2017.

The Stark shifts determined with the foregoing numerical procedure are presented in Fig. 3. The red solid line was obtained by the equation (4) given by Jäger and Windholz 1984, which in the case of small electric fields reduces to:

$$\Delta\lambda = -\lambda_0^2 C F^2 \ , \tag{1}$$

where $\lambda_0 = 508.038$ nm, yielding the C coefficient value of -0.00827 kV^{-2}cm.

4. CONCLUSION

We present a Stark polarization spectroscopy study of the Ne I 508.038 nm spectral line profiles, recorded in the cathode sheath region of the Grimm-type abnormal

glow discharge. The value of the coefficient C, correlating the Stark shift of the σ-polarized component and the electric field strength, is determined. These results expand the list of neon atomic spectral lines that can be used in spectroscopic diagnostics of the electric field strength.

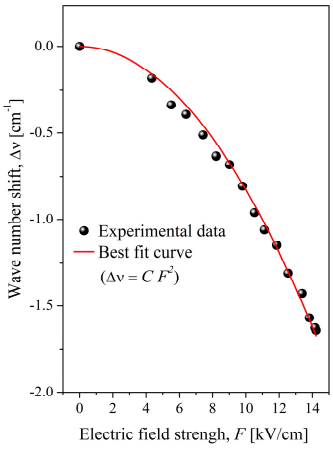

Figure 3: Dependence of the wavenumber Stark shift Δν for the Ne I 508.038 nm spectral line on the electric field strength F.

Acknowledgments

This work is supported by the Ministry of Education, Science and Technological Development of the Republic of Serbia (Grant No. 451-03-68/2020-14 /200162).

References

Ferreira, N. P., Human, H. G. C. and Butler, L. R. P. : 1980, *Spectrochim. Acta Part B*, **35**, 287.

Ivanović, N. V., Šišović, N. M., Spasojević, Dj. and Konjević, N. : 2017, *J. Phys. D: Appl. Phys.*, **50**, 125201.

Ivanović, N.V. : 2019, *Atoms*, **7**, 9.

Jäger, H. and Windholz, L. : 1984, *Phys. Scr.*, **29**, 344.

Jäger, H., Windholz, L. and Ziegelbecker, R. Ch. : 1989, *Phys. Scr.*, **40**, 740.

Kuraica, M., Konjević, N., Platiša, M. and Pantelić, D. : 1992, *Spectrochim. Acta Part B* **47**, 1173.

Majstorović, G. Lj., Ivanović, N. V., Šišović, N. M., Djurović, S. and Konjević, N. : 2013, *Plasma Sources Sci. Technol.*, **22**, 045015.

Ryde, N. : 1976, *Atoms and Molecules in Electric Fields*, Almqvist & Wiksell, Stockholm.

Šišović, N. M., Ivanović, N. V., Majstorović, G. Lj. and Konjević, N. : 2014, *J. Anal. At. Spectrom.*, **29**, 2058.

Windholz, L. : 1980, *Phys. Scr.,* **21**, 67.

Windholz, L. and Neureiter, C. : 1988, *Phys Rev.* A, **37**, 1978.

Ziegelbecker, R. Ch. and Schnizer, B. : 1987, *Z. Phys. D,* **6**, 327.

Publ. Astron. Obs. Belgrade No. 102 (2022), 199 - 202 *Contributed Paper*

THE GAS TEMPERATURE DIAGNOSTICS BY MEANS OF AlO ($B^2\Sigma^+$–$X^2\Sigma^+$) MOLECULAR BAND SYSTEM FROM THE UPGRADED ATMOSPHERIC PRESSURE PULSED DISCHARGE SOURCE IN ARGON

JOVICA JOVOVIĆ[1] and GORDANA LJ. MAJSTOROVIĆ[2]

[1]*Faculty of Physics, University of Belgrade – Studentski trg 12-16, 11000 Belgrade, Serbia*
E-mail jjovica@ff.bg.ac.rs

[2]*University of Defence, Military Academy, Generala Pavla Jurišića Šturma 33, Belgrade, Serbia*
E-mail gordana.majstorovic@va.mod.gov.rs

Abstract. In this study, the optical emission spectroscopy (OES) is applied to measure gas temperature from the upgraded needle-to-cylinder (UNTC) gas discharge source in argon driven by pulsed voltage power supply. The rotational T_{rot} temperature is obtained after the analysis of well resolved AlO ($B^2\Sigma^+$–$X^2\Sigma^+$) molecular bands at 484.2 nm and 486.6 nm (Δv=0). The T_{rot} is measured for different pulse width and duty cycle values as well. The Fortrat parabolas were constructed for the proper identification of P_2 and R_2 branch lines belonging to AlO ($B^2\Sigma^+$–$X^2\Sigma^+$) molecular bands. The results revealed T_g~1450-1800 K in the center of plasma column.

1. INTRODUCTION

The formation of metal-oxide layers (AlO, Al_2O_3, TiO etc.) in plasma-assisted processes comprises several steps such as the evaporation of electrode/target material, reaction with oxidizing particles in plasma and in afterglow and surface reactions. The Plasma Electrolytic Oxidation (PEO) and Plasma Enhanced Atomic Layer Deposition (PE-ALD) are the examples of two approaches in deposition of high-performance oxide layers. The experimental study of metal-oxide molecules contributes to plasma computation, plasma chemistry, radiative lifetimes measurements and collision quenching study (Parriger and Kornhol 2011, Johnson et al 1972, Salzberg et al 1991). In the area of astrophysics, the extensive study of molecular bands originating from the solar spectrum such as MgH, MgO, AlO, CN etc. is made (Schadee 1964 and references therein).

An interesting peculiarity of the UNTC source is the formation of di-atomic molecules in plasma such as NH, OH, AlO and CN. Having that in mind, the focus of this study is on T_g measurement by means of T_{rot} diagnostics procedure based on

normalized population distribution technique using the rovibrational distribution of AlO ($B^2\Sigma^+ - X^2\Sigma^+$,0–0) and AlO ($B^2\Sigma^+ - X^2\Sigma^+$,1–1) molecular bands. In high pressure regime, being one of the limiting cases discussed in Bruggeman et al 2014, the measured rotational temperature equals gas temperature (rotational energy transfer occurs much faster than depopulation rate of excited level).

2. EXPERIMENTAL

The schematic drawing of UNTC source and experimental setup is shown in Figure 1. The source consists of needle-type cathode (diameter 4 mm) and a cylindrical graphite anode (diameter 25 mm). The cathodes are made of aluminum (0.5 % Mg, 0.5 % Si, 0.5 % Fe and Al balance). The working gas (Ar 99.999 %) flow is measured using rib-guided glass tube flowmeter controller (0-2.5 l/min scale). The discharge is driven by pulsed voltage power supply that consist of DC power supply (Kepco, 0-2 kV, 0-100 mA), the bank of capacitors, HV switching unit (MOSFET technology) and rectangular pulses generator (2-999 μs pulse width, 0.1-100 % duty cycle), see Figure 1 in Jovović 2020. The pulsed power voltage signal, is monitored by means of 4-channel digital oscilloscope (Hantek, $f \leq$ 250 MHz, 1.4 ns rise time). During the pulse, the voltage jumps in the range 900-1300 V for 16.7 % duty cycle and 500-600 V for 3.8 % duty cycle. The radiation from UNTC source was recorded by means of 2 m Ebert type spectrometer (Carl Zeiss, O.P. f/28, an inverse linear dispersion of 0.74 nm/mm) equipped with a thermoelectrically cooled, back-thinned Hamamatsu CCD camera ($T = -10^{\circ}$C, 2048 × 512 pixels, 12 μm pixel size).

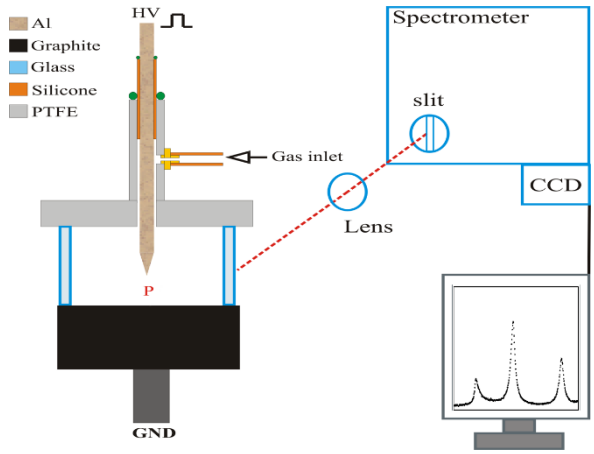

Figure 1: The cross-section of UNTC discharge source and experimental setup.

3. RESULTS AND DISSCUSSION

The P_2 branch lines of the AlO $B^2\Sigma^+$ (v'=0)–$X^2\Sigma^+$ (v''=0) (J '=17-35) are studied while the R_2 branch lines AlO $B^2\Sigma^+$ (v'=1)–$X^2\Sigma^+$ (v''=1) (J '=33-49) transition in the

range 484–488 nm are analyzed as well (Figures 2 and 3) using the procedure and spectroscopic constants listed in Herzberg 1950. Having in mind that rotational transfer coefficients become negligible if ΔE is much higher than average kinetic energy of neutrals E_{kin} (=kT), ΔE has to be the same order of magnitude as E_{kin} (Barbeau et al 1991). In our case, for AlO $B^2\Sigma^+$ ($\nu' = 1$), the energy gap between J'=33 and J'=49 rotational levels is ΔE=914 cm^{-1} and AlO $B^2\Sigma^+$ ($\nu' = 0$) the energy gap between J'=17 and J'=35 rotational levels is ΔE=574 cm^{-1}. For T_{rot} values of e.g. 1520 K and 1780 K, kT_{rot} equals 1057 cm^{-1}, or 1238 cm^{-1}, respectively. Hence, one may consider the upper levels within abovementioned J' range, to be in equilibrium with molecular ground state (Launila and Berg 2011).

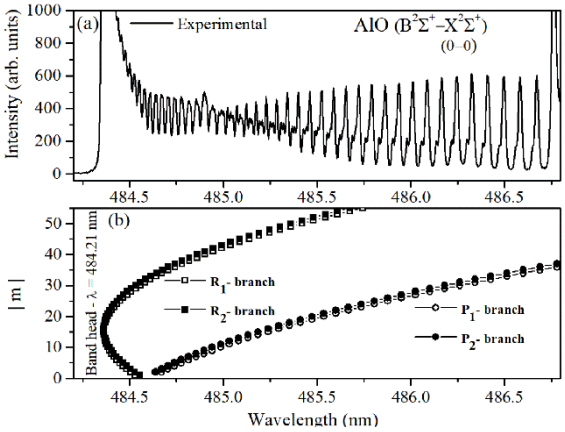

Figure 2: (a) The AlO (0−0) band at 484.2 nm recorded in the second order of diffraction grating. (b) Fortrat parabolas of the main branches of the AlO (0−0) spectrum (*m* designates the number of successive lines in each branch).

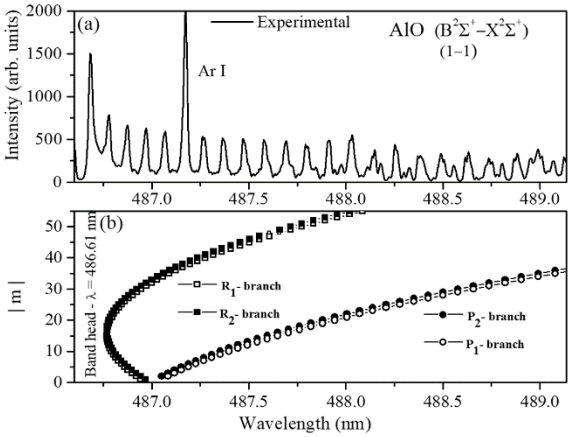

Figure 3: (a) The AlO (1−1) band at 486.6 nm recorded in the second order of diffraction grating. (b) Fortrat parabolas of the main branches of the AlO (1−1) spectrum (*m* designates the number of successive lines in each branch).

Let us mention that, for different values of pulse width (50 μs, 100 μs and 300 μs) and duty cycle (25 %, 16.7 %, 9.1 % and 4.75 %), the T_{rot} was measured using AlO ($B^2\Sigma^+ - X^2\Sigma^+$, 0–0) and AlO ($B^2\Sigma^+ - X^2\Sigma^+$, 1–1) bands as well, see Table 1. It was observed that lowering of the duty cycle induces the lowering of T_{rot} which reflects the change of T_g in plasma. It is reasonable to claim that power supply with shorter pulse width and lower pause/pulse ratio delivers the higher power into the plasma volume and consequently increases the efficiency of neutral particles heating.

AlO (0–0)	50 μs	100 μs	300 μs
25 %	1640 ± 165	1640 ± 165	1780 ± 180
16.7 %	1590 ± 160	1590 ± 160	1700 ± 170
9.1 %	1440 ± 145	1400 ± 140	1710 ± 175
4.75 %	1300 ± 130	1300 ± 130	1620 ± 165
AlO (1–1)	50 μs	100 μs	300 μs
25 %	1480 ± 150	1540 ± 155	1520 ± 155
16.7 %	1460 ± 150	1530 ± 155	1420 ± 145
9.1 %	1440 ± 145	1510 ± 155	1550 ± 155
4.75 %	1600 ± 160	1920 ± 195	1610 ± 165

Table 1: The change of T_{rot} (K) with pulse width and duty cycle.

Acknowledgement

This work is supported by the Ministry of Education, Science and Technological Development of the Republic of Serbia.

References

Parigger, C. G., Kornhol, J. O. M. : 2011, *Spectrochim. Acta A*, **81**, 404.

Johnson, S. E., Capelle G. and Broida H. P. : 1972, *J. Chem. Phys.*, **56**, 663.

Salzberg, A. P., Santiago, D. I., Asmar, F., Sandoval, D. N. and Weiner, B. R. : 1991, *Chem. Phys. Lett.*, **180**, 161.

Schadee, A. : 1964, *Bulletin of the Astronomical Institutes of the Netherlands*, **17**, 311.

Bruggeman, P. J., Sadeghi, N., Schram, D. C. and Linss, V. : 2014, *Plasma Sources Sci. Technol.*, **23**, 023001.

Jovović, J. : 2020, *Phys. Plasmas*, **27**, 053505.

Herzberg, G. : 1950, *Molecular spectra and molecular structure, vol I*, Van Nostrand-Reinhold, New York.

Barbeau, C., Baravian, G., and Jolly, J. : 1991, *Proceedings of X International Symposium on Plasma Chemistry*, Bochum.

Launila, O., Berg, J.-E. : 2011, *J. Mol. Spectroscopy*, **265**, 10.

Publ. Astron. Obs. Belgrade No. 102 (2022), 203 - 206 *Contributed Paper*

FORMATION AND HEATING OF SILICON PLASMA IN AIR UNDER PULSED BICHROMATIC LASER IRRADIATION

V. V. LUCHKOUSKI and A. N. CHUMAKOU

B.I. Stepanov Institute of Physics of the NAS of Belarus, 220072, Minsk, Independence avenue 68-2
E-mail v.luchkouski@dragon.bas-net.by

Abstract. The formation and heating of laser plasma under the irradiation of silicon in air by pulsed laser radiation with wavelengths of 355 and 532 nm at radiation power density of up to 5 GW/cm^2 has been investigated. An increased efficiency of the formation and heating of erosion plasma under bichromatic irradiation of silicon with advanced action of nanosecond pulses with wavelength of 355 nm has been established.

1. INTRODUCTION.

The efficiency of materials laser ablation in gases and formation of near-surface plasma depends on variety of parameters including intensity, laser radiation (LR) wavelength, laser pulse duration, repetition rate and order in which they follow (see Min'ko et. al. 1990, Pershin 2009, Khalin 2013). Increase in power density of LR lead to formation of near-surface plasma that start to shield sample's surface, which from one hand limits laser ablation and from other greatly contributes to newly formed surface plasma. In order to increase efficiency of materials laser ablation and heating of near-surface plasma a pulsed bichromatic laser irradiation with controlled time parameters can be used (see Chumakov et. al. 2014, Chumakov, Bosak et. al. 2014).

The goal of current work is to establish the features of formation and heating of silicon plasma in air ablated by nanosecond laser pulses of bichromatic laser irradiance with wavelengths 355 and 532 nm, controlled time interval and order in which pulses follow.

2. EXPERIMENTAL.

The installation is based on two Nd:YAG lasers and synchronization system which provide generation of paired nanosecond laser pulses with wavelengths 355 and 532 nm and duration of 18 and 15 ns respectively. Pulses follow in controlled order and time interval between them. The coaxial beam from both lasers was

formed with spectral splitter and focused on 180 μm thick silicon plate's surface in 200 μm (λ = 355 nm) and 250 μm (λ = 532 nm) diameter spot by achromatic lens (*f* = 150 mm).

Pictures of laser induced plume were taken with video camera based on ICX415AL matrix (time exposition ~ 3 ms) (see Nikonchuk et. al. 2016). Spatial resolved integral spectra of plume light were taken using diffraction spectrometer and digital video camera. Spectra were calibrated utilizing reference lines of LR with wavelengths of 532 and 632,8 nm. The emission spectra of laser plasma were registered by SL40-2 spectrometer based on TCD 1304 photodetectors within LR power density range of 0,9–5 GW/sm^2 (time exposition ~7 ms). Form of laser pulses was registered by 11HSP-V2 photodetector and Wave Surfer 510R digital oscilloscope (bandwidth 1 GHz). Laser pulse energy was measured with Ophir device by PE25BF-DIF-V2 detector.

3. RESULTS AND DISCUSSION.

Analysis of plasma's plume video pictures show that laser irradiance of silicon with wavelength 355 nm leads to ejection of vast number of condensed phase particles, which is much weaker in case of laser irradiance with λ = 532 nm (fig.1 a-b). Bichromatic irradiance with leading laser pulses of λ = 355 nm provides much more intensive plasma formation and weaker particles ejection (fig. 1, c-d).

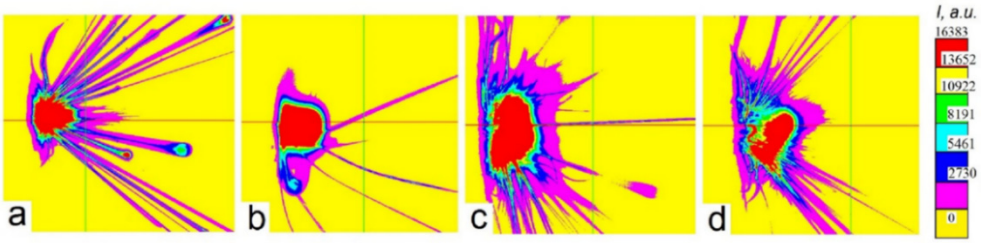

Fig. 1. – Video pictures of plasma plume induced by monochromatic (a, b) and bichromatic (c, d) laser irradiation on silicon: a – q_{355}=1,9 GW/sm^2, b – q_{532}=3,5 GW/sm^2;
c – bichromatic λ_1=355 + λ_2=532 nm, interval between pulses Δτ = –20 мкс, d – bichromatic λ_1=532 + λ_2=355 nm, interval between pulses Δτ=+30 мкс
(negative time interval corresponds with leading action of 355 nm laser pulse)

The spectra obtained with 355 nm monochromatic laser irradiance of silicon contains strongly broadened atomic (Si I 288,2 and 390,5 nm) and ionic silicon lines (Si II 385,6 and 413,1 nm) with traces of double ions (Si III 308,6 nm) and high intensity of continuous radiation (fig. 2, spectrum *1*). Bichromatic 355 + 532 nm laser irradiation of silicon initiate spectra with lowered level of continuous radiation and significant number of atomic and ionic silicon lines with traces of triple exited ions (Si IV 408,8 nm) as well as ionic N II 501,1 nitrogen line (fig. 2, spectrum 2). This indicates heating of plasma at temperature of ~20 000 K. Change

of laser pulses order to 532+355 nm leads to weaker heating of ablated plasma and to stronger ejection of particles what confirmed by weakening of double ions Si III spectral lines and absence of triple ions traces (fig. 3).

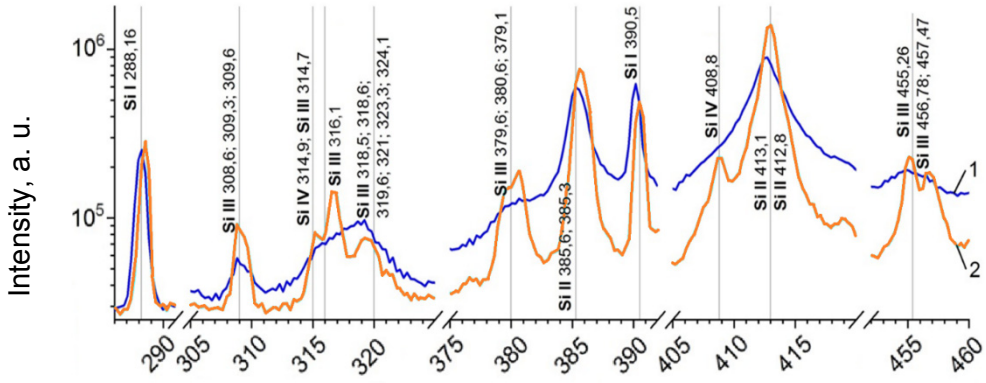

Fig. 2. – Spectra of surface plasma induced by monochromatic LI with λ=355 nm and q_{355}=4,6 GW/sm^2 (*1*) and birchromatic LI with q_{355}=1,9 GW/sm^2 + q_{532}=3,5 GW/sm^2 (Δτ=–1,4 μs) (*2*) on silicon sample in air

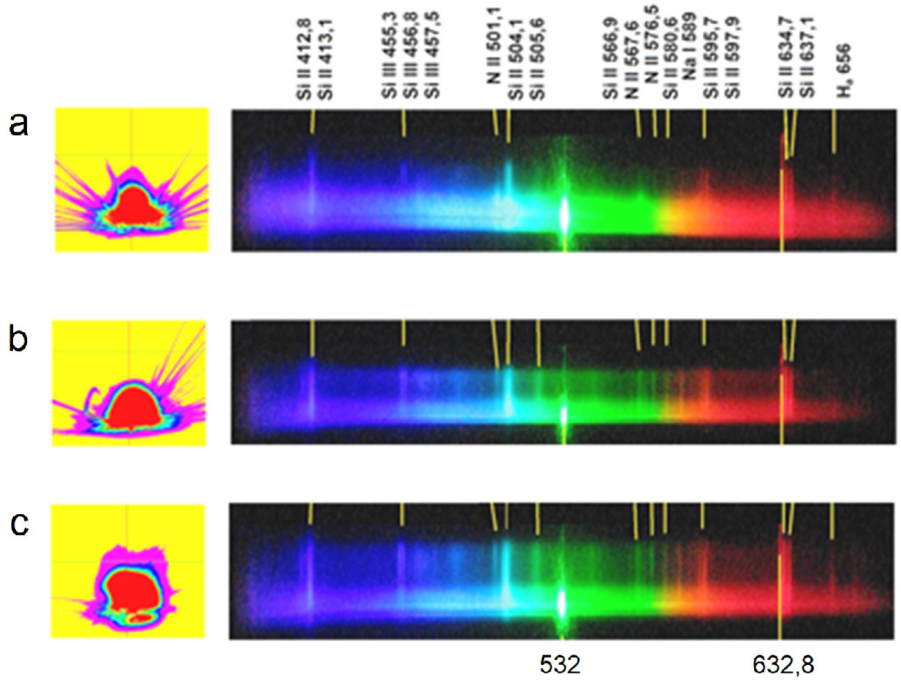

Fig. 3. – Video pictures of plasma plume and their corresponding spectra induced by bichromatic LI with q_{355}=1,9 GW/sm^2 and q_{532}=3,5 GW/sm^2 and interval between pulses Δτ=–5,5 μs (*a*), –1,3 μs (*b*) and +15 μs (*c*).

The influence of time interval from -40 to +40 μs and order of bichromatic pair of pulses on plasma parameters was evaluated based on silicon Si III 380,6 / Si II

385,6 / Si I 390,5 nm and nitrogen N II 501,1 nm spectral line's intensities ratio (fig. 4). Also, it was considered that Si II 385,6 / Si I 390,5 nm and Si III 380,6 / Si II 385,6 nm line's intensities ratio represent plasma temperature to some extent.

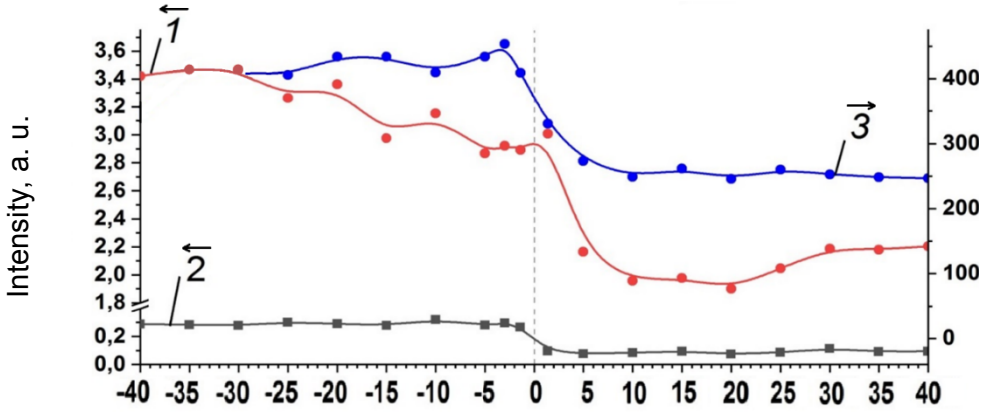

Fig. 4. – Dependence of line's intensity ratio Si II 385,6 / Si I 390,5 (*1*), Si III 380,6 / Si II 385,6 (*2*), Si II 385,6 / N II 501,1 (*3*) on time interval and order of laser pulses with wavelengths of 355 and 532 nm in silicon plasma

Analysis of dependencies *1* and *2* in fig. 4 shows comparability of Si III 380,6 nm and Si II 385,6 nm line's intensities which point on range of plasma's temperature from 11000 to 19000 K (range of "normal" temperatures for Si II and Si III spectral lines). Maximum values of dependencies *1* and *2* are reached with leading action of 355 nm laser pulse, that point on peak heating of silicon plasma with current conditions. With change of pulses order to 532 + 355 nm a raise in nitrogen's N II 501,1 nm line intensity is observed followed by decreasing of Si II 385,6 / N II 501,1 line's intensity ratio (dependence *3*, fig. 4).

4. CONCLUSION.

Formation and heating of surface plasma induced by pulsed laser irradiation of silicon with power density up to 5 GW/sm^2 in air was studied. Increase in formation and heating effectiveness of erosive plasma induced by bichromatic irradiation on silicon with leading action of 355 nm laser pulses was established.

References

Min'ko L., et. al. : 1990, *Quant. Electronics*, **17**, 1480.
Pershin S. : 2009, *Quant. Electronics*, **39**, 63.
Khalil A. : 2013, *Opt. & Laser Tech*, **45**, 443.
Chumakov A.N., et. al.: 2014, *High Temp. Material Proces*., **18**,269.
Chumakov A.N, Bosak N.A., et. al. : 2017, *J. Appl. Spectrosc*., **84**, 620.
Nikonchuk I.S., et. al. : 2016, *J. of Physics: Conf. Series*, **666**, 012021.

Publ. Astron. Obs. Belgrade No. 102 (2022), 207 - 210 *Contributed Paper*

BREAKDOWN IN SATURATED WATER VAPOR

JELENA MARJANOVIĆ[1], DRAGANA MARIĆ[1], GORDANA MALOVIĆ[1] and ZORAN LJ. PETROVIĆ[2,3]

[1]*Institute of Physics, University of Belgrade, Pregrevica 118, 11080 Belgrade, Serbia*

[2]*Serbian Academy of Sciences and Arts, Kneza Mihaila 35, 11001 Belgrade, Serbia*

[3]*School of Engineering, Ulster University, Jordanstown, County Antrim BT37 0QB, United Kingdom*

E-mail sivosj@ipb.ac.rs

Abstract. This paper presents the results of breakdown measurements in water vapour at pressures around and higher than vapour pressure for water. Breakdown voltage dependences on *pd* (*p* – pressure and *d* – electrode gap) or Paschen curves are recorded for two electrode gaps: 0.5 mm and 1 mm. Measurements were performed at room temperature of 22ºC (vapour pressure 19.8 Torr) and under conditions when the entire discharge chamber was cooled to the temperature of 8ºC (vapour pressure 8.1 Torr), in order to reach conditions where droplet formation takes place at stable discharge conditions. Paschen curves indicate that at room temperature breakdown voltages obtained at 0.5 and 1 mm agree well with the values at the centimetre electrode distances, while at the temperature of 8ºC, for pressures higher than vapour pressure, deviations occur. These deviations can be consequences of liquid droplet formation.

1. INTRODUCTION

Discharges in water and water vapour have a diverse field of application, in food, textile, and aerospace industries, for sterilization and decontamination of different surfaces and instruments in medicine, for the processing, treatment, and functionalization of materials, in biomedicine, etc. (see Stalder et al., 2006; Fumagalli et al., 2012; Rossi et al., 2009). Due to the variety of possible applications, there is a growing need to develop and design different plasma sources that can operate at atmospheric and low pressure, in vapour and in the liquid itself. A common feature of all the above-mentioned applications is the complex working environment – from a mixture of gas and vapour to an environment saturated with water vapour or humid air. In this respect, it is crucial to investigate and understand the breakdown in liquid and at the gas-liquid boundary.

Our previous studies of DC breakdown and discharges in water vapour included measurements of Paschen curves, axial emission profiles, emission spectra and Volt-Ampere characteristics at low pressures (Sivoš et al. 2015). This paper presents an investigation of the breakdown at pressures above the vapour pressure, under the conditions where condensation i.e. liquid droplets formation is expected in the discharge.

2. EXPERIMENTAL SET-UP

The schematic of the experimental setup is shown in Fig.1a) and the discharge chamber in Fig.1b). The discharge is ignited between plane-parallel electrodes that are tightly fitted inside the cylindrical teflon housing that prevents the breakdown around and behind the electrodes, ensures the parallelity of the electrodes, and fixes the electrode system itself. The electrodes are of circular cross-section, separated from each other by a ring-shaped dielectric, which also limits the volume for discharge ignition and operation. The interelectrode distance is adjustable and can be continuously changed.

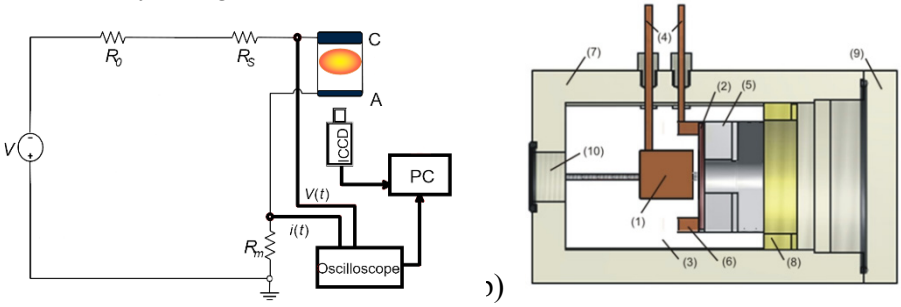

a) ›)

Figure 1: a) Schematic of the experimental setup and the electrical circuit used in measurements, and b) Cross-section of the chamber for micro-discharges with marked structural parts: (1)–stainless still cathode; (2)– transparent anode with ITO film; (3)–teflon electrodes housing; (4)–high-voltage inlets; (5)–anode mounting ring; (6)–metal contact ring; (7)–plexiglass outer cylinder; (8)–electrodes housing mounting ring; (9)–transparent chamber cover, and (10)–inlet for connection to the vacuum system.

The cathode is made of stainless steel and the anode is made of glass covered by a thin, conductive, and transparent indium-oxide film (Indium Thin Oxide coated glass). The effective diameter of the electrodes exposed to discharge is 2 mm. The electrode system with its housing is fitted inside a plexiglass cylinder, which one side is closed with a transparent lid. This design enables the ICCD recording of radial emission profiles from discharge.

Vapor is obtained from bi-distilled, deionized water in a test tube. The tube is connected to the discharge chamber by a pressure regulating valve. The other side of the discharge chamber is connected to a vacuum pump and a pressure gauge. The chamber is evacuated to low pressure ($<10^{-6}$ Torr), then water vapor is introduced into the system at a slow flow rate while monitoring that the pressure stays below the vapor pressure for water (19.8 Torr at T=22ºC, and 8.1 Torr at

T=8ºC in the case of a cooled chamber). Before measurements, the vapor is left in the system for 1-2 hours to achieve saturation of all surfaces in the chamber.

3. RESULTS AND DISCUSSION

Measurement of breakdown voltages is performed for two electrode gaps 0.5 and 1 mm and compared with Paschen curves obtained for the standard size discharge - 0.5 and 1.1 cm (Fig.2). Paschen curves for micro-discharge are measured at two temperatures 22ºC (vapor pressure is 19.8 Torr) and 8ºC (vapor pressure is 8.1 Torr). In the second case, the entire chamber was cooled to enable measurements at higher pressures than the vapor pressure. Decreasing discharge size and decreasing operating temperatures enabled us measurements at more stable operating conditions, close to a Paschen curve minimum, but above a vapour pressure for water. At room temperature (22ºC), there is good agreement between the Paschen curves recorded in standard size discharge (black and red lines) and micro-discharge (black and red diamonds).

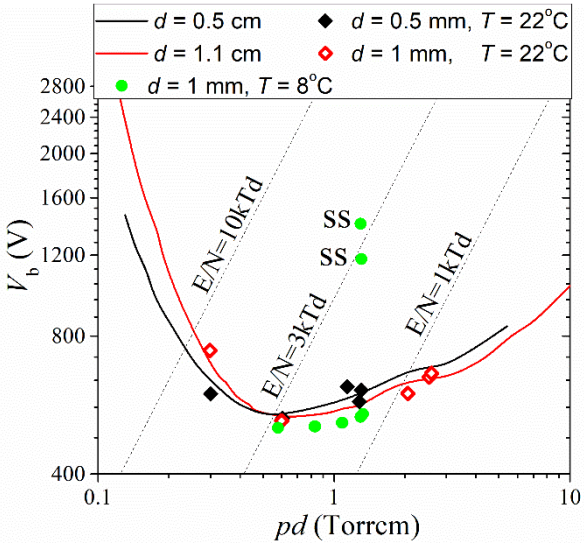

Figure 2: Comparison of the Paschen curves obtained in the chamber for standard size discharge for electrode distances of 0.5 cm (black line) and 1.1 cm (red line) and in the chamber for micro-discharges for electrode distances of 0.5 mm (black diamonds) and 1 mm (red diamonds). These measurements are done at room temperature of 22ºC. Green diamonds show breakdown voltages obtained for electrode distance of 1 mm at a temperature of 8ºC.

At micrometre interelectrode distances, the discharge was unstable, but it was possible to estimate the breakdown voltages from the relaxation oscillations (see Kuschel et al., 2011). In the case when the chamber was cooled (at 8ºC) discharge ignited and operated in the relaxation oscillations mode up to ~1.1 Torr cm. At 1.29 and 1.33 Torr cm, discharge first operated in the steady-state mode (green diamonds marked with SS), and after approximately one minute of stable

operation, it switched to the relaxation oscillations mode. Figure 3 shows the waveforms for current and voltage at pd = 1.29 Torr cm. In Fig.3a discharge operates in steady-state mode at a high voltage of ~1.4 kV while the current is 1 μA, and in Fig.3b discharge is in the oscillatory mode, where the voltage is lower for ~860 V, and the current higher for 18 μA.

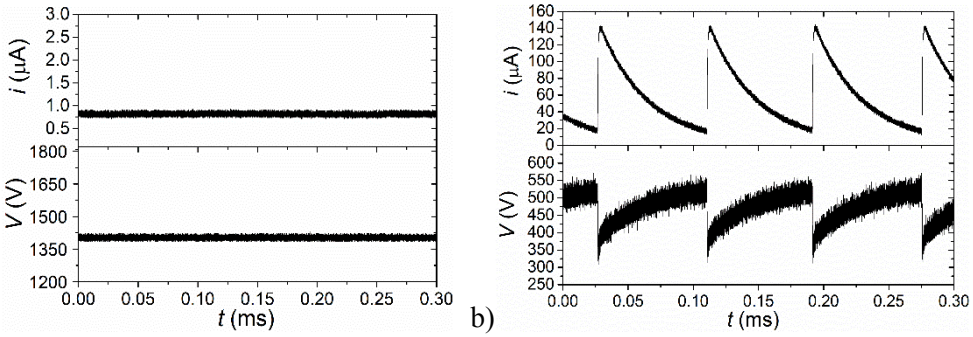

Figure 3: Voltage and current waveforms for micro-discharge in water vapor at pd = 1.29 Torr cm and d = 1 mm: a) when discharge operates in the stationary mode (i =0.8 μA, Vb = 1405 V), and b) when discharge operates in the relaxation oscillations mode (i = 19 μA, V_b = 541 V).

We assume that this behaviour is a consequence of the phase transition in the gas, and the occurrences of condensation or liquid droplets. As the chamber had to be cooled, we could not record the discharge through the transparent anode with an ICCD camera. Therefore, it could not be confirmed whether the discharge was in the Townsend mode upon breakdown. Our further investigation will include recordings of radial emission profiles of discharge, and measurements at shorter electrode gaps, in conditions when the chamber is cooled to lower the limit for the phase transition in water vapor. It must be noted that the ratio of electrode diameter and interelectrode distance should be taken into account, and maintained when reducing the electrode gap. That will limit the radial losses of charged particles to an acceptable level, and allow the application and validity of the one-dimensional Townsend theory.

Acknowledgements

The authors acknowledge support from the MESTD of Serbia.

References

Fumagalli, F., Kylián, O., Amato, L., Hanuš, J., and Rossi, F.:2012, *J. Phys. D: Appl. Phys*. **45**, 135203.

Kuschel, T., Stefanović, I., Škoro, N., Marić, D., Malović, G., Winter, J. and Petrović, Z., Lj.: 2011, *IEEE Transactions on Plasma Science* **39**, 2692.

Rossi, F., Kylián, O., Rauscher, H., Hasiwa, M., and Gilliland, D.:2009, *New Journal of Physics* **11**, 115017.

Sivoš, J., Škoro, N., Marić, D., Malović, G.and Petrović Z. Lj.: 2015, *J. Phys. D: Appl. Phys*. **48**, 424011.

Stalder, K., R., Nersisyan, G., and Graham, W., G.: 2006, *J. Phys. D: Appl. Phys*. **39**, 3457.

Publ. Astron. Obs. Belgrade No. 102 (2022), 211 - 214 *Contributed Paper*

LOOKING BEHIND THE NEGATIVE GLOW PLASMA: ESTIMATING CATHODE SHEATH PARAMETERS BY END-ON OPTICAL EMISSION SPECTROSCOPY IN A GRIMM-TYPE GLOW DISCHARGE SOURCE

N. V. NEDIĆ[1], N. V. IVANOVIĆ[2], I. R. VIDENOVIĆ[1], D. SPASOJEVIĆ[1] and N. KONJEVIĆ[1]

[1]*University of Belgrade, Faculty of Physics, P.O.Box 44, 11001 Belgrade, Serbia*
[2]*University of Belgrade, Faculty of Agriculture, Nemanjina 6, 11080 Belgrade, Serbia*
E-mail: ivan.videnovic@ff.bg.ac.rs

Abstract. A series of optical emission spectroscopy measurements of the Ne I 520.389 nm line in the Grimm-type glow discharge in pure neon has been performed in parallel from two positions: 1. from the end of the discharge, in line with the discharge axis (end-on view) and 2. side-on cathode view, at the position of the maximum external electric field F_{max} in the cathode sheath (CS), close to the cathode surface. The results collected at various conditions (pressure, voltage, current, cathode materials) show a stable linear correlation between the side-on recorded Stark component shift $\Delta\lambda_s$ at the position of maximum field F_{max} in the CS, and the end-on recorded wings broadening characteristic features shift $\Delta\lambda_e$. The obtained linear coefficient can be used to estimate the maximum CS electric field F_{max} and the CS thickness d_c within a reasonable margin of uncertainty in a standard analytical Grimm-type glow discharge source with an end-on view available only.

1. INTRODUCTION

Standard optical emission spectroscopy (OES), through the utilization of the Stark effect, successfully complements other experimental and theoretical efforts to measure the electric field distribution in the glow discharge cathode sheath (CS) and model the discharge kinetics. Starting from the early OES results in hydrogen and helium, the latest development included heavier gases like neon and argon (Majstorović et al. 2013, Šišović et al. 2014, Ivanović et al. 2017, Vasiljević et al. 2017). Conventionally used analytical Grimm-type abnormal glow discharge (GD) source with plane cathode and hollow cylindrical anode adjacent to the cathode does not allow for direct physical or optical access to the CS region for field measurements. OES discharge observations are enabled from the end of the discharge only, collecting integral light both from the bright negative glow and deep-lying low-intensity cathode sheath. In this paper we use the convenience of

our modified Grimm design with enabled both end-on and side-on view OES measurements, to systematically compare the characteristic wings broadening feature shifts in end-on spectra of the Ne I 520.389 nm spectral line with the side-on recorded profile at the position of maximum electric field F_{max} with clearly defined Stark shifted component. A verified correlation between end-on and side-on recorded profiles would enable in turn end-on determination of F_{max} in the CS and the entire CS reconstruction (electric field distribution $F(d)$ and CS thickness d_c) for the Grimm-type analytical GD sources with end-on optical observation available only. A full systematical study of this correlation is made on six neon and four argon neutral lines in Nedić et al., 2022, JAAS, DOI: 10.1039/D2JA00109H.

2. EXPERIMENTAL

A modified Grimm GD source, proposed by Ferreira et al. 1980, is improved and described in detail elsewhere (Kuraica et al. 1992, Majstorović at al. 2013, Šišović et al. 2014, Ivanović et al. 2017). It has a hollow brass anode with an 8 mm inner diameter, equipped with two parallel 16 mm long and 1.5 mm wide longitudinal slots. An exchangeable cathode sample, 18 mm long and 7.4 mm in diameter is mounted onto a water-cooled cathode holder and partially inserted into the hollow anode. This enables, besides the usual end-on view, optical observations from the side of the cathode right away from the cathode surface, and distinguishing the light emission from the cathode sheath from that originating from the negative glow. The fine-moving mechanical discharge holder allows for a spatial resolution of approximately 1/16 mm. The discharge is sustained in high-purity neon (99.999%) in the pressure range of 3-8 mbar. The light is collected by an achromatic lens (focal length 75.8 mm) and focused onto the entrance slit (2 mm in height and 20 μm width) of an Ebert-type Carl Zeiss PGS-2 monochromator (2 m focal length with reflection grating of 651 grooves/mm, blazed at 1050 nm). The OES system with reciprocal dispersion of 0.37 nm/mm in the second diffraction order introduces a Gaussian instrumental profile with the measured full width at half maximum (FWHM) of 0.013 nm. The resolved light is detected by a thermoelectrically cooled computer-driven Hamamatsu CCD camera (T = -10°C, 2068×512 pixels, 12 μm pixel size, S10140/10141 series).

3. RESULTS

Figure 1 shows the typical set of OES measurements of the Ne I 520.389 nm spectral line in this investigation: end-on recording (red line), and a series of five side-on recordings in the CS at different positions, starting from the largest Stark shift $\Delta\lambda_s$, i.e. the strongest electric field F_{max} (blue line) nearby cathode surface, and decreasing with the distance from the cathode towards the negative glow. The end-on recording, besides the strong negative glow unshifted line at λ_0, features a prominent red structure at the distance $\Delta\lambda_e$, originating from the superposition of Stark components in the CS under the integral influence of the electric field. On the other hand, the side-on spectra show a strong Stark-shifted component and a weak

unshifted line, originating from the discharge protruded through the anode observation slot into a zero-field region.

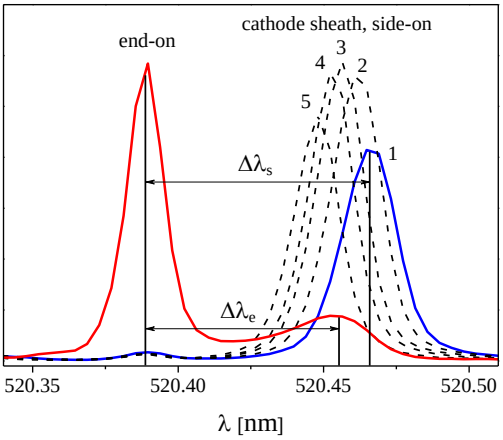

Figure 1. Ne I 520.389 nm spectral line recorded end-on (red line) and side-on in the CS at five different distances from the cathode (in 1/16 mm steps), starting from the maximum shift at F_{max} (blue line). Measured shifts, end-on $\Delta\lambda_e$, and side-on $\Delta\lambda_s$, are indicated.

The correlation between the side-on shifts $\Delta\lambda_s$ (at F_{max}) and end-on shifts $\Delta\lambda_e$ for the Ne I 520.389 nm spectral line is further investigated for various discharge conditions (voltage, current, pressure), with either tungsten or copper cathode. The results presented in Fig. 2 show that the $\Delta\lambda_s$ vs. $\Delta\lambda_e$ dependence appears linear, with the slope $k = 1.100 \pm 0.020$ for both employed cathodes.

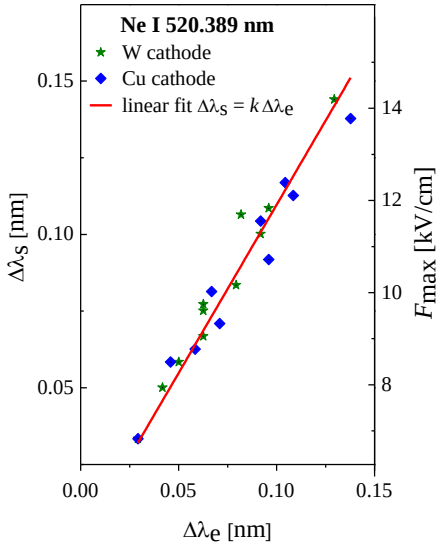

Figure 2. The side-on Stark shifts $\Delta\lambda_s$ (and corresponding F_{max}, Eq. 1) against the end-on Stark shifts $\Delta\lambda_e$ for the spectral line Ne I 520.389 nm. Each point represents different discharge conditions (pressure, current, voltage), with either tungsten or copper cathodes.

For small electric fields up to 14 kV/cm, Ivanović et al. 2017 have shown that Stark shifts of the side-on recorded Ne I 520.389 nm spectral line in the CS can be expressed as

$$\Delta\lambda_s = -\lambda_0^2\, C\, F^2 \tag{1}$$

where $C = -0.0238\ \mathrm{cm/kV^2}$ is a line-specific coefficient. The corresponding field strengths, ranging between 8 and 15 kV/cm, are also shown on the right-hand axis in Fig. 2. Therefore, a direct correlation between the end-on Ne I 520.389 nm spectra shifts $\Delta\lambda_e$ and maximum CS electric field F_{max} can be established:

$$F_{max} \approx \sqrt{-\frac{k}{C}\cdot\frac{\Delta\lambda_e}{\lambda_0^2}} \tag{2}$$

Having obtained the F_{max} in the CS, the CS thickness d_c as another important discharge parameter can be estimated using a suitable electric field distribution model (typically linear regression) and the value of applied voltage U.

4. CONCLUSION

We demonstrated the possibility of using the standard end-on view optical emission spectroscopy of the Grimm-type glow discharge source to learn more about the parameters of the low-intensity cathode sheath, "hidden" behind the bright negative glow plasma. For the Ne I 520.389 nm spectral line a stable linear correlation is found between the shifts $\Delta\lambda_e$ in end-on recorded characteristic line broadening features, and side-on measured Stark shifts $\Delta\lambda_s$, recorded at the position of the maximum electric field F_{max} in the cathode sheath.

Acknowledgment

This work is supported by the Ministry of Education, Science and Technological Development of the Republic of Serbia.

References

Ferreira, N. P., Human, H. G. C. and Butler, L. R. P. : 1980, *Spectrochim. Acta Part B*, **35**, 287.

Ivanović, N. V., Šišović, N. M., Spasojević, D. and Konjević, N. : 2017, *J. Phys. D: Appl. Phys.*, **50**, 125201.

Kuraica, M., Konjević, N., Platiša, M. and Pantelić, D. : 1992, *Spectrochim. Acta Part B* **47**, 1173.

Majstorović, G. Lj., Ivanović, N. V., Šišović, N. M., Djurović, S. and Konjević, N. : 2013, *Plasma Sources Sci. Technol.*, **22**, 045015.

Nedić, N. V., Ivanović, N. V., Videnović, I. R., Spasojević, D. and Konjević, N. : 2022, *J. Anal. At. Spectrom.*, DOI: 10.1039/D2JA00109H.

Šišović, N. M., Ivanović, N. V., Majstorović, G. Lj. and Konjević, N. : 2014, *J. Anal. At. Spectrom.*, **29**, 2058.

Vasiljević, M. M., Spasojević, D., Šišović, N. M. and Konjević, N. : 2017, *Europhys. Lett.*, **119**, 55001.

Publ. Astron. Obs. Belgrade No. 102 (2022), 215 - 218 *Contributed Paper*

DETECTION OF FAST NITROGEN AND OXYGEN ATOMS VIA EMISSION SPECTROSCOPY

B. M. OBRADOVIĆ[1], N. CVETANOVIĆ[2], I. B. KRSTIĆ[1] and M. M. KURAICA[1]

[1]*University of Belgrade, Faculty of Physics, 11001 Belgrade, Serbia*

[2]*University of Belgrade, Faculty of Transport and Traffic Engineering, 11000 Belgrade, Serbia*
E-mail nikola@ff.bg.ac.rs

Abstract. Fast atoms are generated in charge exchange reactions of ions with the molecular gas both in laboratory and astrophysical plasma. In hydrogen, they are observed in the emission spectra via Excessive line broadening. In this study, we have used a special configuration of the electrode system, to obtain energetic atoms in plasma of diatomic gases. Emission spectroscopy was used to detect the N and O fast atoms and measure their velocity. Energy analysis was performed to obtain atoms' distributions and evaluate the mean energy of atoms. This was compared to the potential energy available from the electric field. The field acceleration model, previously established for hydrogen, was extended to nitrogen and oxygen.

1. INTRODUCTION

Fast atoms are produced both in astrophysical and laboratory plasma. Exited atoms are detected in spectra with unusually high energies for heavy particles - of the order of keV. In molecular hydrogen, the process is well described via the charge exchange reaction. Specifically, the so-called field acceleration model (FAM), describes the process in which atomic and molecular ions accelerating in the electric field reach high energies, due to the low cross section for the asymmetric process (Phelps, 2011, 2009) . After the charge exchange collision occurs, a fast neutral atom is formed preserving the momentum and kinetic energy of the ion. The fast atom can then be excited in the collisions with the surrounding gas.

The Doppler shifted radiation of fast atoms, shows a distorted far wing of the line, the so-called Excessive line broadening (Cvetanović et al., 2005) of the order of ~nm. The phenomenon of excessive Doppler broadening and corresponding fast atoms was examined experimentality in detail in several types of laboratory plasma, see the references in (Cvetanović et al., 2011).

As noted above, the effect of detecting fast atoms via Doppler shift can be valid for any molecular plasma. However due to the low mass of the emitters, only hydrogen

Excessive broadening can be easily detected. In the literature, the effect was obtained so far exclusively in hydrogen plasma with exception of one paper in nitrogen (Wang et al., 2000). Here results are obtained in nitrogen and oxygen plasma.
In hydrogen discharge, three types of ions are formed H^+, H_2^+, H_3^+. The fast nitrogen and oxygen atoms are produced via similar mechanisms but mostly from the atomic ion collision with slow molecule (Phelps, 1991; Stebbings et al., 1963). In all cases, the fast atom is excited mostly through the process of collisions with molecular gas. The spontaneous emission then gives Doppler shifted radiation by $\Delta\lambda$.

2. EXPERIMENTAL SETUP

The experimental setup consists of a hollow cathode discharge chamber, gas control and pressure system, power supply and the optical detection system. The detailed scheme can be found in Ref. (Cvetanović et al., 2011), though a different spectrometer is used in this experiment. A gas flow of about 300 cm^3/min of nitrogen or oxygen was sustained at a selected pressure. by means of a needle valve and a two-stage mechanical vacuum pump. To run the discharge, a 0–2.5 kV voltage stabilized power supply is used. The discharge image was projected by a lens to the entrance slit of 1-m monochromator. At the exit of the monochromator, radiation was detected using a two-dimensional ICCD camera. The instrumental profile half-width was measured to be FWHM=0.035 nm.

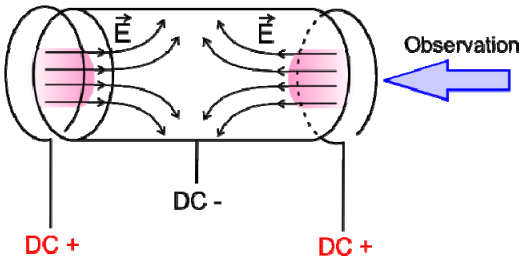

Figure 1: Schematics of the hollow-cathode discharge. The sheath electric field is shown.

The plasma reactor itself is a hollow-cathode discharge, with a cylindrical cathode and a round wire anode set further from the cathode cylinder, see Fig. 1. Both anode and cathode have the diameter of 10 mm. The distance between the edge of the cathode cylinder and the anode wire is 3 mm. Below the pressure of 1 mbar the discharge operates in the so-called low-pressure regime. Namely, at pressure below 1 mbar, the negative glow is notably extracted from the cathode cylinder, so the sheath (or cathode fall) fills the gap to the anode ring thus making the electric field vector coincide with the central axis of the cathode cylinder (Fig 1). To sustain this field configuration the applied discharge voltage must be increased.

Additional feature of our electrode system is that it has two wire anodes on each side of the cathode cylinder. This construction of the discharge electrodes enabled engaging either one of the anodes or both, if required. Effectively, this changes the direction of the field in respect to the detector i.e., direction of observation, see Fig. 1. This enabled observation of very small Doppler shift of the moving particles since the change of the field direction creates asymmetry of the measured spectral line.

3. RESULTS

It was determined that reduction of pressure extends the mean free path of the ions thereby creating faster atoms. Low pressure was chosen in here in order to maximize the shift in the spectrum. The nitrogen spectrum was measured for two groups of lines: 818-825 nm and the NI ($3p^4D \rightarrow 3s^4P$) triplet transition at 868 nm. The asymmetric broadening is ≈0.2 nm but it can still be observed since the asymmetry of each spectral line changes from "red" to "blue" with the electric field reversal. To obtain the velocities of the emitting N atoms, transition NI ($3p^4P \rightarrow 3s^4P$) at 822 nm is chosen and recorded at lower pressure, see Figure 2. It can be seen that in the case of nitrogen the maximum velocity reached is ≈100 km/s.

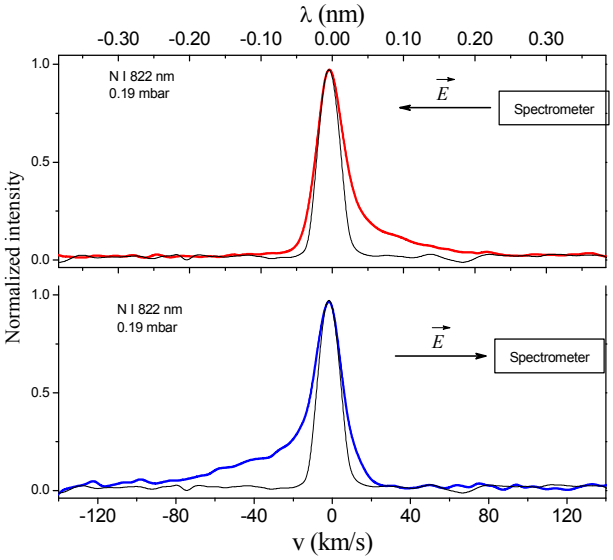

Figure 2: Nitrogen NI ($3p^4P \rightarrow 3s^4P$) 822 nm shown in the velocity scale. The instrumental profile is shown for comparison.
Conditions: U=1300 V, p=0.19 mbar, I=1.2 mA.

Detecting fast atoms in oxygen plasma is even more difficult due to the even larger atom mass (M(O)=16). The spectrum of the notable OI 777 nm triplet for two field directions is shown in Figure. 3. The spectrum measured from the Geisler tube, with line profiles close to instrumental profile, is shown to clearly note the small asymmetry in the line profile. The spectral observation of oxygen fast atom in a discharge was not published so far. Again, the difficulty lies in very small Doppler shift. The spectral line in the velocity scale is shown in Fig.8.

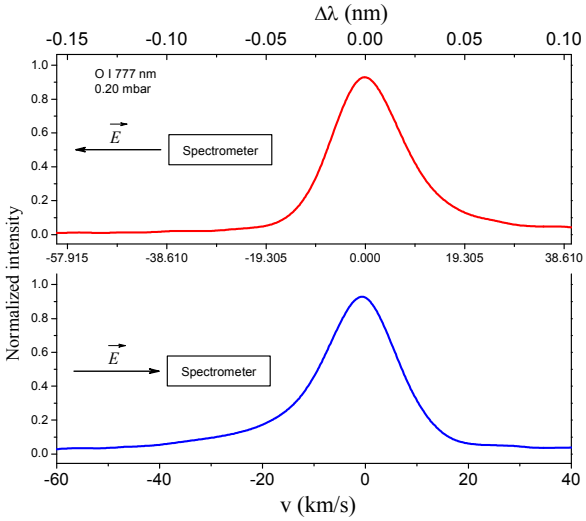

Figure 3: Oxygen triplet OI ($3p^5P \rightarrow 3s^5S$) 777.4 nm shown in the velocity scale. Conditions: U=1000 V, p=0.17 mbar, I=0.7 mA.

Using variable transformation, energy distribution of atoms can be obtained. The mean kinetic energy was calculated at 252 eV for nitrogen and 145 eV for oxygen atoms. The maximum kinetic energy for both gases corresponds to about ~80% of the available potential energy from the electric field, respectively.
Therefore, the detection of fast atoms in nitrogen and oxygen discharge was successfully demonstrated. Energy analysis can be performed and the FAM model can be well extended to these gases.

References

Cvetanović, N., Kuraica, M.M., Konjević, N., 2005. J. Appl. Phys. 97, 033302.
Cvetanović, N., Obradović, B.M., Kuraica, M.M., 2011.. J. Appl. Phys. 110, 073306.
Phelps, A. V., 2011.: Plasma Sources Sci. Technol. 20, 043001.
Phelps, A. V., 2009.: Model. Phys. Rev. E 79, 066401.
Phelps, A. V., 1991:. J. Phys. Chem. Ref. Data.
Stebbings, R.F., Turner, B.R., Smith, A.C.H., 1963.: J. Chem. Phys. 38, 2277–2279.

Publ. Astron. Obs. Belgrade No. 74 (2022), 219 - 222 *Contributed Paper*

ANALYSIS OF PRINTED CIRCUIT BOARD LIBS DATA USING DEEP LEARNING

M. S. RABASOVIC[1], B. P. MARINKOVIC[1] and D. SEVIC[1]
[1] *Institute of Physics, University of Belgrade, Pregrevica 118, 11080 Zemun, Serbia*
E–mail majap@ipb.ac.rs

Abstract. The laser-induced breakdown spectroscopy (LIBS) is a method often used for monitoring the selective removal of thin layers by laser. In this way it is possible to achieve rapid prototyping of printed circuit boards. We show that it is convenient to use deep learning algorithm on LIBS data to obtain an indication that copper layer is fully removed.

1. INTRODUCTION

Rapid prototyping of printed circuit boards can be achieved by laser ablation. One of the possible approaches to this process was presented in Rabasovic et al. 2016. We have used the laser-induced breakdown spectroscopy (LIBS) as a convenient method both for ablation and for monitoring the selective removal of thin layers by laser. In Rabasovic et al. 2016 the LIBS data were analyzed by using correlation coefficients. Nowadays, availability of more and more fast computers, capable of machine learning, moves the analysis algorithms from simple numerical calculation towards the more sophisticated artificial intelligence methods. Our initial efforts for machine learning analysis of LIBS printed circuit board data, using principal component analysis are presented in Sevic et al. 2020. Interesting applications of machine learning algorithms for analysis of LIBS data are presented in Boucher et al. 2015, Moros et al. 2013, Serranoa et al. 2014. State of the art approaches to the problem are reviewed in Porızka et al. 2018, Vrabel et al. 2020; Zhang et al. 2022. In this paper we study the spectral data by using the deep learning algorithm.

2. ARTIFICIAL NEURAL NETWORKS AND DEEP LEARNING

Artificial neural networks (ANNs) mimic the human brain through a set of algorithms. They consist of input layer, hidden layers and output layer. A neural network that consists of more than three layers can be considered a deep learning algorithm, or a deep learning network.

Because of increasing computer efficiency more and more sophisticated machine learning algorithms become extensively used. The data set of certain structure is used to "train" the machine to learn some specific characteristics of input data. Then, machine could be used to recognize and identify these characteristics in newly presented

data of similar structure and nature.

3. EXPERIMENTAL SET-UP AND METHODS

Our experimental setup is and its applications for elemental analysis using LIBS, including several ways of processing spectra, are described in detail in Rabasovic et al. 2012, Rabasovic et al. 2014, Rabasovic et al. 2019, Sevic et al. 2011. The data analyzed here were obtained by experimental setup described in Rabasovic et al. 2016; at that time we have calculated the correlation coefficients of measured spectra to identify the moment of achieving the full removal of copper layer by laser ablation. In Sevic et al. 2020 we have implemented the PCA to achieve automatic recognition of the instant when laser ablation of copper layer has been finished and the laser starts damaging the composite substrate of printed circuit board. Here, to achieve the same goal, we use deep learning network. We use Solo + MIA software package (Version 9.0, Eigenvector Research Inc, USA).

4. RESULTS AND DISCUSSION

Plasma breakdown optical spectra of printed circuit board at the start, when only copper is ablated; and when the substrate is fully exposed, are shown in Fig. 1. Their differences could be seen by a naked eye.

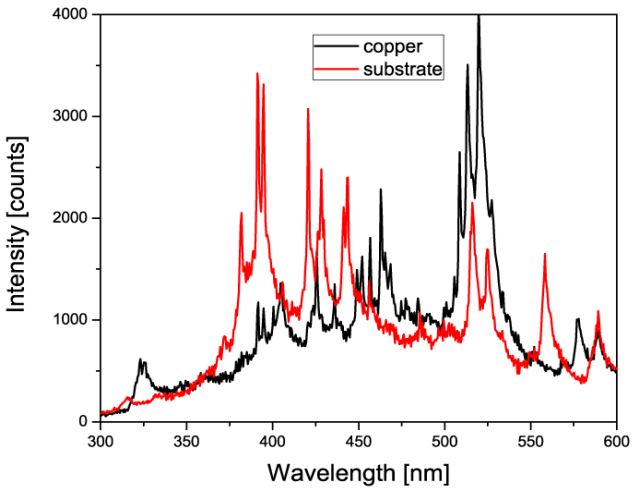

Figure 1: Plasma breakdown optical spectra of printed circuit board at the start, when only copper is ablated; and when the substrate is fully exposed.

At the beggining of the ablation process the peaks observed were neutral Cu lines at 510.55, 515.32, 521.82, and 578.21 nm. The prominent line was Cu I at 521.82 nm.

The presence of characteristic emission lines corresponding to the substrate was an indication to restrict the ablation zone and minimize the damage to the substrate. Any of the prominent lines such as Al I (394.39 nm, 396.19 nm), Ca I (422.64 nm, 616.2 nm), Ca II (393.43, 396. 88 nm), and Na I (589.15 nm) can be used as an indicator of the substrate.

We have trained the deep learning neural network with measured spectra corresponding to ablation of copper layer with 10, 50, 200 and 500 laser shots. We have adopted that output of network should produce the numbers between 1 and 100, corresponding very roughly to percent of laser ablation of copper. If output is higher of, say threshold of 90, then the laser shots should be stopped on that spot and laser beam should be moved further.

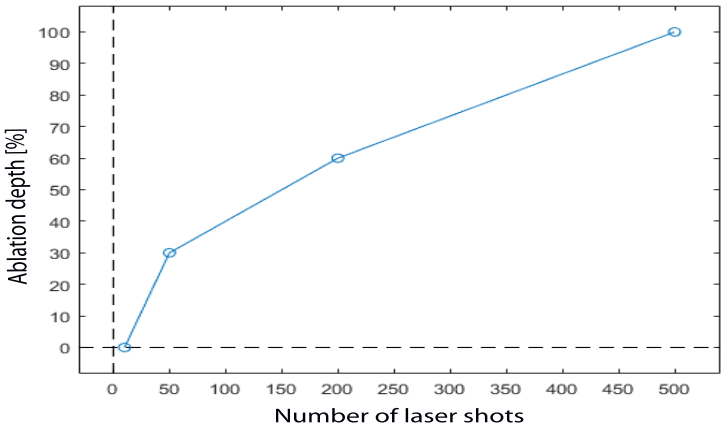

Figure 2: Training of deep neural network.

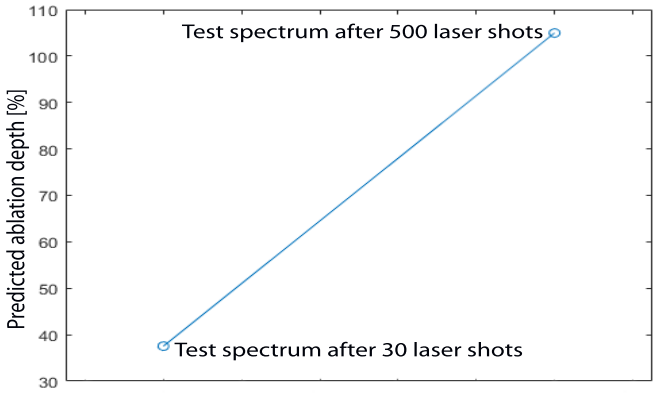

Figure 3: Two tests of trained deep neural network.

We have tested the network with spectra not presented before to the computer; and as expected, the predicted ablation level corresponded roughly to the functional dependence shown in Fig. 2. Two examples are shown in Fig. 3.

5. CONCLUSION

Rapid prototyping of printed circuit boards can be achieved by using laser ablation and LIBS. We have analyzed the LIBS data of printed circuit board by using deep learning algorithm. In our previous analyses we have used the correlation coefficients and PCA to identify the moment when laser ablation reaches the composite substrate of printed circuit board. Now, we have shown that it is possible to automatically detect the instant when the copper layer is fully ablated by deep learning network.

Acknowledgment

This work was financially supported by the Institute of Physics Belgrade, through the grant by the Ministry of Education, Science, and Technological Development of the Republic of Sebia

References

Boucher T.F., Ozanne M.V., Carmosino M.L., Dyar M.D., Mahadevan S., Breves E.A., Lepore K.H., Cleggc S.C. : 2015 *Spectrochimica Acta Part B* **107** 1.

Ann. Acad. Sci. Fennicae. Ser. A. I. Math.-Phys. **37** 1.

Loeve, M. : 1948 *Processus stochastiques et mouvements Browniens, Paris: Gauthier-Villars.*

Moros J., Serrano J., Gallego F.J., Macıas J., Laserna J.J : 2013 *Talanta* **110** 108.

Porízka P., Klus J., Hrdlicka A., Kepes E., Prochazka D., Hahn D.W., Kaiser J.: 2017 *J. Anal. At. Spectrom.* **32**, 277.

Rabasovic M.S., Sevic D., Pejcev V., Marinković B.P. : 2012 *Nucl. Instrum. Meth. B* **279**, 61.

Rabasovic M.S., Marinković B.P., Sevic D. : 2014 *IEEE Transactions on Plasma Science* **42**, 2388.

Rabasovic M.S., Sevic D., Lukac N., Jezersek M., Mozina J., Gregorcic P. : 2016 *Appl. Phys. A* **122**, 186.

Rabasovic M.S., Rabasovic M.D., Marinkovic B.P., Sevic D. : 2019 *Atoms* **7**, 6.

Serranoa J., Moros J., Sánchez C., Macías J., Laserna J.J : 2014 *Analytica Chimica Acta* **806** 107.

Sevic D., Rabasovic M.S., Marinkovic B.P. : 2011 *IEEE Trans. on plasma science* **39**, 2782.

Sevic D., Rabasovic M.S., Gregorcic P., Rabasovic M.S., Marinkovic B.P. : 2020 Publ. Astron. Obs. Belgrade No. 99, 117-120.

Vrabel J., Kepes E., Duponchel L., Motto-Ros V., Fabre C., Connemann S., Schreckenberg F., Prasse P., Riebe D., Junjuri R., Gundawar M.K., Tan X., Porízka P., Kaiser J. : 2020 *Spectrochimica Acta Part B* **169**, 105872

Zhang D., Zhang H., Zhao Y., Chen Y., Ke C., Xu T., He Y: 2022 *Applied Spectroscopy Review* **57** (2) 89-111.

Publ. Astron. Obs. Belgrade No. 102 (2022), 223 - 226 *Contributed Paper*

APPLICATION OF ARTIFICIAL NEURAL NETWORK IN THE ANALYSIS OF THE SPECTRA FROM LASER ABLATION COMBINED WITH FAST PULSE DISCHARGE

NENAD M. SAKAN, MILICA L. VINIĆ, VLADIMIR A. SREĆKOVIĆ, IVAN TRAPARIĆ and MILIVOJE R. IVKOVIĆ

Institute of Physics Belgrade, University if Belgrade, Pregrevica 118, Belgrade, Serbia
E-mail nsakan@ipb.ac.rs

Abstract. The presented work investigates the application of artificial neural networks (ANN) onto spectral classification. The goal of the work was to determine the type of unknown spectra on the basis of a train dataset with the usage of several types of basic ANN. The numerical procedures we are developing, for LIBS analysis of the plasma-facing components of the fusion reactor, was tested on the classification of spectra from different soil or ore types. The data source is a laser ablation combined with fast pulse discharge, the method proposed for the reactor wall analysis. The success in it's application has shown not only that the ANN is usable in case of classification of type of spectra but it presents a step forward making of expert system for the more complex equipment.

1. INTRODUCTION

Classification and determination is a common field for the usage of machine learning. The artificial neural networks (ANN) are most powerful machine learning algorithms (Mishra et. al. 2017). As a test case the simplest shallow and deep neural networks has been selected. As a merit a experimental data from laser ablation assisted plasma source for the cases of clay soil and tile brick are used. The goal was to test if the ANN could achieve precision in determining of the appropriate analyzed material as well as type of plasma as an emitter, and as such to prove the usability of ANN method for the fast classification of the recorded spectra. The test dataset was collected with the advanced, laser ablation combined with fast pulse discharge, enhanced LIBS technique (Vinić et al., 2014).

The main contributions of this research work are as follows:

- We compared the applications of the four ANN of different complexities.
- Utilized the ANN of deep type.

In the flowing section we have described the experimental setup and discussed the results and the future steps.

2. EXPERIMENTAL SETUP

The laser induced breakdown spectroscopy (LIBS) has evolved to a mature technique for the analysis of various samples, from gaseous up to underwater samples. The work has been carried out in order to enhance the emissivity of plasma, the introducing a second pulse, in the case of dual pulse LIBS (DP-LIBS). This technique has made improvement in detection limit and a DP-LIBS is now comparable to other more mature spectroscopy techniques and as such is adopted as a standard spectroscopy technique. The other way of enhancement of the detection limit is fast spark discharge enhanced LIBS, it also has a possibility to excite harder to excite elements such as carbon, chlorine, sulphur and fluorine.

The experimental setup is shown on Figure 1. The investigated material (1.) is irradiated by the 100-mJ nanosecond pulse Molectron model MY-34 Nd-YAG laser (2). The plasma is formed on the sample, as well as inside the fast spark discharge. The radiation is analyzed spectrally as well as temporally with the Andor technology, model Shamrock 303-i spectroscope, coupled with the Andor iStar iCCD camera, model DH 720 -18F-03 (position 3). The time delay for the start of collection a spectral data is determined by the delay unit (4). The electrical behavior of the spark as well as total emissivity is monitored and recorded on the oscilloscope (5). The spark discharge unit consists of capacitor (7), and current probe (8). The photodiode (9) monitores the emissivity of produced plasma.

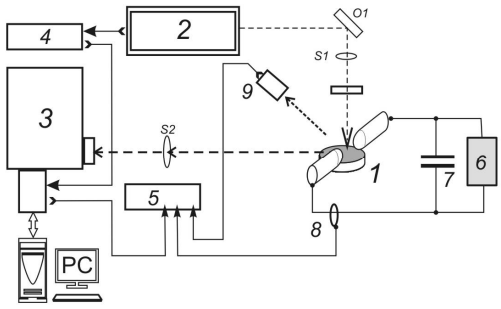

Figure 1: Experimental setup of the system for the laser ablation of the sample material spectroscopy: 1. - investigated material pill, 2. - Nd-YAG laser, 3. - spectroscope with coupled iCCD camera, 4. - delay unit, 5. - oscilloscope, 6. - high voltage supply , 7. - capacitor bank , 8. - current probe.

The set of measurements for clay soil and tile bricks are selected. In the initial time at the delay of 0.1 us, only the LIBS phase of the plasma is visible, in the later recorded spectra, 0.6 us delay, the ablated material is inside spark discharge that was triggered by the LIBS phase plasma. So, the four classes of spectra are recorded and used for ANN training, they are denoted here as clay-LIBS, clay-spark, tile-LIBS and tile-spark. For more details on the technique as well as achieved improvement of the signal to noise ratio please consult (Vinić et al., 2014).

3. ANN THEORY AND TOPOLOGY

The artificial neural network application in various areas of spectroscopy is in growth, from environmental applications up to the analysis of LIBS extraterrestrial probes on Mars rover (Sun et al. 2021). In the literature the LIBS spectroscopy as a tool for determining a lead concentration in soil (Zhao et al. 2019) is coupled with ANN. It is a trend in progress for environmental and geophysical analysis (Tingting et al., 2020). Usually, the package of proven machine learning kit is used, for instance Google kit Keras (https://keras.io/) is often used in LIBS specific applications (Hao et al., 2020), in this work a Keras implementation of feed forward and deep feed forward ANN was made for the investigation of the usability of ANN presented in this manuscript.

4. RESULTS AND DISCUSSION

The prediction was made on the basis of available experimental data set. The selection was made to throw individual CCD lines of data in order to have artificial dataset enlargement with the different areas of plasma observed as well as different noise composition. The random choice of two thirds of the data was used to train the ANN while the one thirds was used to test the prediction.

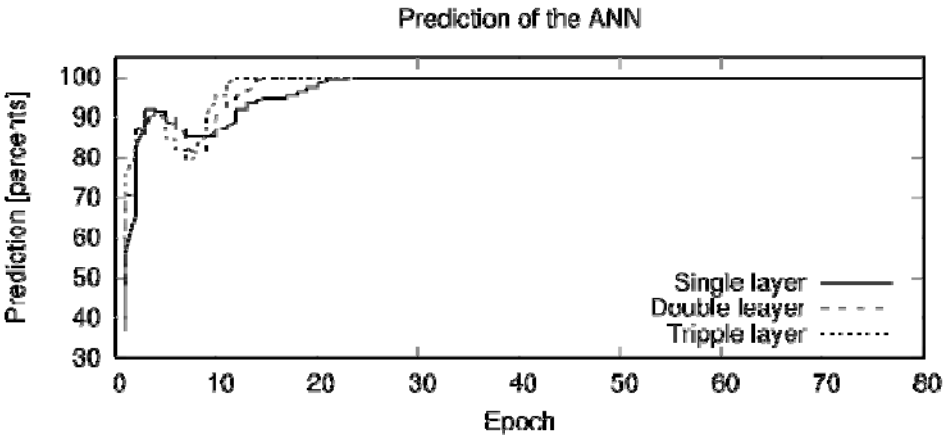

Figure 2: Artificial neural network prediction of the spectra type

The input layer is determined with the dimensionality of input data, so for the available data set the input layer consists of 9927 input neurons. The prediction space consists of four individual outcomes, so the output layer consists of four vectors: [1 0 0 0] – clay-LIBS; [0 1 0 0] – clay-spark; [0 0 1 0] – tile-LIBS; and [0 0 0 1] – tile-spark. The output layer of ANN consists of four neurons belonging to each output vector. Three networks were compared, simplest one consists of only one hidden layer of 15000 neurons, the two layers one with additional 512 neuron second hidden layer, and third one, most complex, consisting of three hidden dense layers of 15000,

1200 and 256 neurons consequently. The output of four consecutive runs was recorded for each of the three investigated ANN. The output outcome was shown on Figure 2. The most complex ANN consist of three hidden dense layers is the one that converged fastest towards the 100% prediction. It could be seen that the process of selection of investigated spectra could be conducted with the help of ANN.

5. CONCLUSIONS AND PERSPECTIVES

From the presented results it is possible to make several conclusions, as first it could be seen that the determination of target type as well as plasma condition, as an emitter could be achieved with ANN successfully. The further conclusion is made by the analysis of the convergence, the more complex, deep ANN, could be more usable for investigation of the further applicability of the method. More over, the third one, is that the sensitivity on the type of emitter, the type of plasma with the ablated material, could lead to more advanced application of inverse methods, to enable prediction of the emitted spectra based on input variables as laser energy, buffer gas, pressure, composition of target and so on.

The paths for the further development, enlarging the data base of the training sets in order of making a more precise determination of the investigated spectra category, the outcome could be enlarged sensitivity on both target material composition as well as plasma conditions. In the case of large training set the interpolation of the known cases is more precise so the inverse problem could be tested. The other result could be more sensitive selection between the spectra that could not be easily dissolved by human eye or the in depth analysis of data could be both time and effort consuming process. Finally, a set of trained ANN could be generated for the in field usage for the specific tasks, e.g. the path towards the production of expert systems.

Acknowledgements

The research was funded by the Ministry of Education, Science and Technological Development of the Republic of Serbia, Contract: 451-03-68/2022-14/200024 and supported by the Science Fund of the Republic Serbia, Grant no. 3108/2021

References

Chen T., et al. (2020), TrAC, **133**, 116113
Hao Y., et al. (2020), *Sensors*, ***20***(5), 1393
Mishra, C. et. al. (2017), *IAES International Journal of Artificial Intelligence* 6.2 : 66
Sun C. et al. (2021), Sci Rep **11**, 21379
Vinić M. and Ivković M., (2014), IEEE Trans. Plasma Sci., **42**, no. 10, 2598
Zhao Y et al. (2019), Appl. Spectrosc., **73**(5), 565

Publ. Astron. Obs. Belgrade No. 102 (2022), 227 - 230 *Contributed Paper*

FEATURES OF THE HeI 492.2 nm LINE PROFILE REGISTERED AT DIAGNOSTICS OF DC AND STREAMER DISCHARGES

L. V. SIMONCHIK and A. V. KAZAK

Institute of Physics of the NAS of Belarus, Minsk, Belarus
E-mail l.simonchik@ifanbel.bas-net.by

Abstract. Formation of the registered profile of the HeI 492.2 nm line during diagnostics of cathode drop of DC normal glow discharge in atmospheric pressure helium depending on the parameters of the optical system and sharp gradients of the electric field strength are shown. Obtained results are used for interpretation of experiment results in streamer discharges.

1. INTRODUCTION

Recently, Stark polarization spectroscopy of the helium line HeI 492.2 nm has been widely used to study helium plasma jets at atmospheric pressure, excited by pulsed and alternating currents [see Sretenović et al. 2014, 2019; Mirzaee et al. 2021]. However, the published experimental results do not reproduce the large amplification of the electric field predicted by simulations [see Norberg et al. 2015; Babaeva et al. 2019]. The main reason for this, apparently, is the insufficient temporal resolution, enhanced by the possible instability of the discharge ignition time, as well as an inadequate interpretation of the formation of the recorded profile of the HeI 492.2 nm line. In this work, we will consider how the recorded profile of the HeI 492.2 nm line is formed depending on the parameters of the optical system and sharp gradients of the electric field strength in pulsed and direct current discharges.

2. MODEL EXPERIMENT

A DC normal glow discharge at atmospheric pressure in helium was ignited in a sealed chamber between a flat copper cathode and a weakly rounded tungsten anode [see Arkhipenko et al. 2000]. Using an optical system consisting of two achromatic objectives with focal lengths of 110 and 210 mm, a 2-fold magnified discharge image was focused in the plane of the entrance slit of a MDD-500x2 (Solar) high-resolution scanning monochromator. With two diffraction gratings of 1800 lines/mm, the inverse linear dispersion is 0.52 nm/mm, and the instrumental

profile has a Gaussian shape with a full half-width of about 0.02 nm. A film polarizer was installed between the objectives. To reduce the aperture of the optical system, a slit with a width of 2–3 mm was used. The emission spectrum was recorded using a U2C-14T3 CCD array and a personal computer.

Experimental parameters: discharge current 0.4 mA, helium flow 1 l/min, discharge gap 10 mm, the aperture of the optical system in the axial direction about 0.025, the entrance slit of the monochromator 40 μm (spatial resolution about 20 μm). The profile of the HeI 492.2 nm line, registered at the distance about 20 μm from cathode surface, is shown in Figure 1*a* (circles). The position of the Stark π-components with instrumental profile for a constant field of strength E_0 = 27 kV/cm, in accordance with the data of [see Foster 1927], are shown here too.

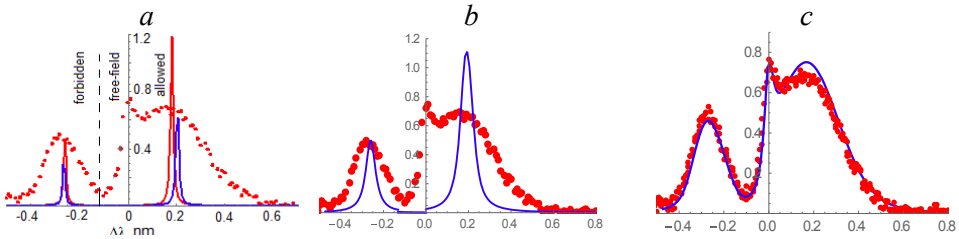

Figure 1: Experimental (circles) and calculated profiles of the HeI 492.2 nm line at E_0 = 27 kV/cm: no broadening (*a*), nonelectrical (*b*) and electrical (*c*) broadenings

In order to approximate the experimental profile of the HeI 492.2 nm line, it is necessary to take into account the broadening of the Stark components, which is caused by external factors of an electrical and non-electrical nature when acting on an emitting atom. Estimates show that the main non-electrical reasons for the broadening of the spectral line components in the region of the cathode drop in the potential of a normal glow discharge in helium at atmospheric pressure under the conditions of this experiment can be van-der-Waals (with a half-width of ~ 0.05 nm), Doppler (~ 0.01 nm) and instrumental (~ 0.02 nm) broadening. The largest half-width w_L = 0.05 nm of them is given by the van-der-Waals broadening, which has a Lorentz's profile. The broadening of the Stark components caused by electric fields can be caused by fluctuations of the discharge current and charged particles, as well as a large gradient of the cathode potential drop within the spatial resolution of the optical system.

In Figure 1*b-c* (solid curves) show how the calculated profile of the HeI 492.2 nm line will change when taking into account nonelectrical (*b*) and electrical (*c*) broadening mechanisms. In case of nonelectrical mechanisms (Figure 1*b*), simulation was performed at E_0 = 27 kV/cm and van der Waals broadening with a half-width of 0.05 nm. A difference is observed with the experimental profile both in the widths of the allowed and forbidden components and in their intensity. The same situation will be observed with the predominance of Doppler or instrumental broadening, as well as for the resulting profile when convolving three profiles determined by these three broadening mechanisms.

In case in Figure 1*c*, we taken into simulation the parameters: constant electric field E_0 = 27 kV/cm; fluctuating electric field with value of E_G = 15 kV/cm, caused by the random generation of anode spots; broadening of the Stark components, similar to the broadening of the unshifted component w_L = 0.05 nm. As you can see, calculated profile of the helium line is in satisfactory agreement with the experimental one. Thus, only three parameters are needed for the simulation. The broadening of the Stark components w_L can be characterized by the half-width of the unshifted component to the left of its center.

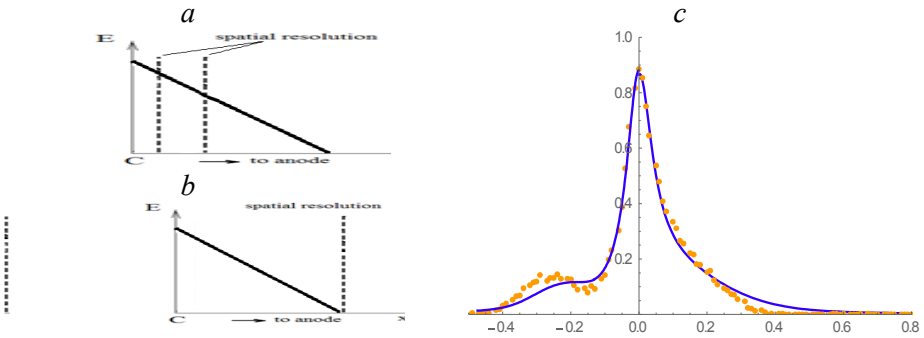

Figure 2: Influence of the spatial resolution on the recorded profiles of the helium line.

The recorded profile of the HeI 492.2 nm line near the cathode surface depends on the spatial resolution (Figure 2). Figure 2*a* schematically shows the position of the image of the entrance slit (vertical dashed lines) and the distribution of the electric field strength for case of Figure 1*c*. Let us increase the entrance slit of the monochromator to 150 μm so that the entire region of the cathode potential drop falls into the monochromator (Figure 2*b*). It can be seen that the recorded profile of the line has changed significantly (Figure 2*c*, circles). The broadening of the Stark components is determined in this case by an instrumental profile with a half-width of ~ 0.09 nm. The calculated profile of the helium line, obtained by summing the Stark profiles for intensities from 0 to the maximum value, satisfactorily corresponds to the experimental one (Figure 1*c*). When recording line profiles near the cathode surface, the choice of aperture is very important as well.

3. EXPERIMENTS IN THE STREAMER DISCHARGES

Let us interpret the profile of the HeI 492.2 nm line in the case of rapidly changing fields, namely, in the case of a slower streamer (9×10^3 m/s and 4×10^4 m/s) [see Sretenović et al. 2014] and a fast streamer (2.5×10^5 m/s) [see Mirzaee et al. 2021]. In the first case, the streamer or a part of it with the maximum field is in the field of view (Figure 3*a*). The registered profile is shown in Figure 4*b* (circles). The profile was approximated by analogy with Figure 2*c*. Calculation parameters: E_{max} = 19 kV/cm, half-width 0.07 nm, relative intensity of the unshifted component is

about 0.15. In blue in Figure 3*b* shows the forbidden and allowed components, red - unshifted, black line - total profile. Here, the dashed lines show the profiles from [see Sretenović et al. 2014]. Although in terms of wavelengths these profiles correspond to our approximation, they are symmetric, and their half-width is more than 0.12 nm, and its justification in [see Sretenović et al. 2014] is not given. The field strength in terms of the distance between the maxima is only about 11 kV/cm.

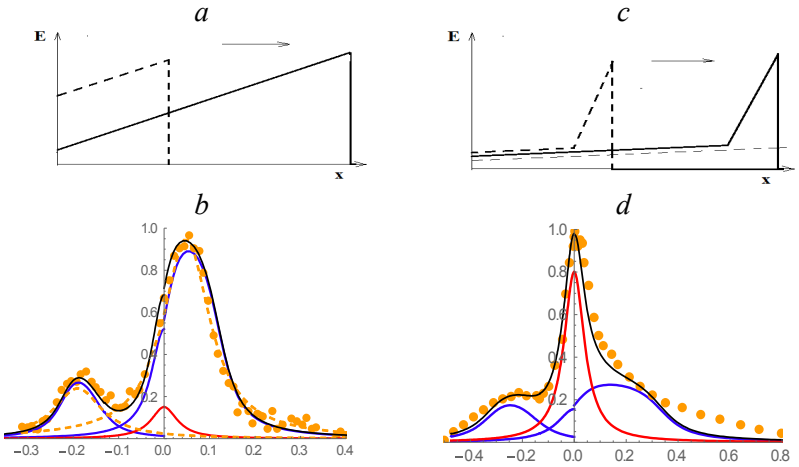

Figure 3: Line profiles of HeI 492.2 nm for slow and fast streamers.

In the case of a fast streamer [see Mirzaee et al. 2021], the distance equal to the spatial resolution, the streamer spreads about 0.2 ns. However, the registration time in this case was 4 ns. In Figure 4*c* shows schematically how a streamer appears, passes, and disappears from the field of view. During the registration time, only a small part of the radiation will fall on the region with high field strength. The registered profile of the HeI 492.2 nm line [see Mirzaee et al. 2021]] is shown in Figure 3*d* (circles). Calculation parameters: E_{max} = 40 kV/cm, half-width 0.08 nm, relative intensity of the unshifted component about 0.75. The calculated profile is represented by a solid black curve. It is seen that the approximated profile satisfactorily corresponds to the experimental one from the side of the forbidden component. From the side of the allowed component, there is less compliance.

References

Sretenović, G.B., Krstić, I.B., et al.: 2014, *J. Phys. D: Appl. Phys.,* **47**, 102001.

Sretenović, G.B., Guaitella, O., et al.: 2019, *Plasma Sources Sci. Technol.,* **28,** 055010.

Mirzaee, M., Simeni, M.S. and Bruggeman, P.J.: 2021, *Physics of plasmas*, DOI: 10.1063/5.0021837.

Norberg, S.A., Johnsen, E. and Kushner, M.J.: 2015, *J. Appl. Phys.,* **118**, 013301; 2016, *J. Phys. D: Appl. Phys.,* **49**, 185201.

Babaeva, N.Y., Naidis, G.V., et al.: 2019, *Plasma Sources Sci. Technol.,* **28**, 095006.

Arkhipenko, V.I., Zgirovskii, S.M., et al.: 2000, *J. Appl. Spectrosc.,* **67**, 910.

Foster, J. S., 1927, *Proc. R. Soc. London* A., **117**, 137.

Publ. Astron. Obs. Belgrade No. 102 (2022), 231 - 234 *Contributed Paper*

TEMPERATURE ESTIMATION IN THE EARLY STAGE OF LASER INDUCED PLASMA FORMATION RELAYING ON BLACK BODY RADIATION

MILOŠ SKOČIĆ, NIKODIN NEDIĆ, DEJAN DOJIĆ, LUKA RAJAČIĆ and SRDJAN BUKVIĆ
University of Belgrade, Faculty of Physics, Studentski Trg 12-16, 11000 Belgrade, Serbia
E–mail skocic@ff.bg.ac.rs

Abstract. We present experimental results of cooper plasma temperature measured in first couple of nanoseconds at the beginning of the laser-induced breakdown experiment. The experiment is conducted by Nd:YAG laser for two irradiances: 1.5×10^{11}, 3.0×10^{11} W/cm^2. The results indicate that LIP is in the state close to thermodynamic equilibrium while the laser illuminates the target. The values for temperature obtained from analysis of continuous spectrum are in agreement with the data available in the literature.

1. INTRODUCTION

Laser induced plasma (LIP) has been the subject of intensive research in recent decades (Hanh and Omenetto, 2010). LIP is created when the powerful pulsed lasers illuminate solid targets, liquids, and gaseous media. Depending on laser energy and pulse duration elementary processes taking place during illumination of targets are essentially different. For common nanosecond lasers interacting with metallic targets the process starts with heating of the solid target, followed by melting and evaporation of the target material (Bogerts et al. 2003, Lutey 2013, Singh and Narayan,1996). Due to high temperature the illuminated area of the target becomes bright with dominantly continuous spectrum. The evaporated material expands, absorbs laser radiation, heats up, and becomes a high-density plasma emitting in most cases continuous spectrum (Skocic et al., 2022).

The aim of this paper is to study plasma temperature evolution in the early stage of LIP when the laser still illuminates the plasma. All results are obtained by analyzing the continuous spectrum emitted by the plasma slice, see Fig.1.

2. EXPERIMENTAL SETUP

The experimental setup consist of a homemade chamber with high purity flat copper sample placed inside the chamber. The chamber is filed up with residual atmosphere at pressure ~ 0.02 mbar. To prevent drilling of the sample chamber is mounted on computer controlled x-y-z translation stage. The plasma was created by a focused laser beam from pulsed Nd:YAG, EKSPLA NL311-SH-TH, laser. Duration of the

pulse (fundamental harmonic at 1064 nm wavelength) was 5.6 ns with repetition rate of 1 Hz. The spatial intensity profile of the laser spot on the target's surface had a top-hat form. The diameter of the spot was 0.2 mm. Dispersion system is based on Andor Shamrock SR-163 spectrograph with intensified CCD camera (2048 512 pixels) Andor iStar DH740-18F- 03, cooled down to 20 ^{0}C, as the detection system. The spectral range covered by the CCD chip, in this configuration, is from 200 nm to 750 nm. The plasma plume is projected on the entrance slit of the spectrograph with the collimating lens, with unity magnification, see Fig.1, left panel. The radiometric calibration (chamber window + collecting lens + optical fiber + CCD) is done relying on deuterium spectral lamp provided by StellarNet for UV and tungsten lamp for visible spectrum. Appropriate set of filters is used to prevent overlapping of the spectra coming from different spectral orders. The laser controller provides trigger signal which precedes actual firing of the Nd:YAG laser for $\sim$5 μs. In this way, the CCD camera can record the very beginning of the heating of the metal surface when the intensity of the laser is far below its maximum intensity.

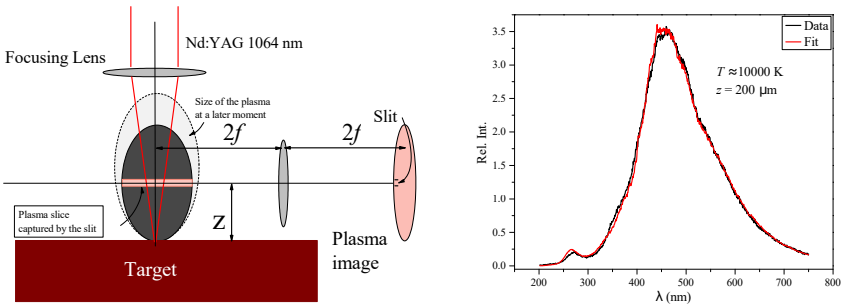

Figure 1: **Left:** Details of the experimental setup. The target is illuminated by the 1064 nm Nd:YAG harmonic. The optical system projects the image of the plasma on the spectrograph entrance slit, with unit magnification. **Right:** The black line represents the spectrum $I_r(\lambda)$ recorded by iCCD camera. The red line is the best fit of the product of Planck's spectrum $I_P(\lambda, T)$ and calibration curve $C(\lambda)$.

3. FITTING PROCEDURE

The radiometric calibration is conducted for the current experimental setup. With $C(\lambda)$ we denote calibration curve which is related to recorded spectrum $I_r(\lambda)$ and emitted spectrum $I_e(\lambda)$ in the following way: $I_r(\lambda) = I_e(\lambda)C(\lambda)$. It follows that

$$I_e(\lambda) = I_r(\lambda)/C(\lambda). \tag{1}$$

Comparing $I_e(\lambda)$ with black-body spectrum characterized by Plancks relation $I_P(\lambda, T)$:

$$I_P(\lambda, T) = \frac{A}{\lambda^5} \frac{1}{\exp(hc/\lambda kT) - 1}, \tag{2}$$

where A is a fitting constant, h is Planck's constant, c is speed of light, k is Boltzmann's constant, λ is wavelength, and T is temperature, one can estimate temperature of the emitter. However, due to noise present in $I_r(\lambda)$ and $C(\lambda)$ the ratio $I_r(\lambda)/C(\lambda)$ is for some recordings prone to large scatter at the end of intervals making fitting procedure inaccurate. A simple way to overcome this difficulty is to multiply Planck's spectrum by the calibration curve $I_p(\lambda, T)C(\lambda)$, and compare it, in sense of the least-squares method, with recorded spectrum $I_r(\lambda)$; see Fig.1, right panel. The best fit curve is obtained by minimizing $\sum_\lambda \left(I_r(\lambda) - I_P(\lambda, T)C(\lambda)\right)^2$ where T is a temperature, the only fit parameter.

4. RESULTS AND DISCUSSION

Fig.2 provides an overview of our results. On the panel a) temporal profile of the ND:YAG laser is given. On the panels b) and c) we present temperatures for different positions from the target, for three distinct times. Different z values represent plasma slices at the position z, and width of 50 μm. Black squares, red circles and blue triangles stand for three different times, in respect to the trigger signal, at which the measurement is conducted. The times of measurements are marked with corresponding colors on the panel a). Values for temperature on panel b) are for laser irradiance of 1.5×10^{11} W/cm^2, and values on panel c) are for irradiance of 3.0×10^{11} W/cm^2.

For temperatures above 15 000 K, according to Planck's law, maximum of emission is in the UV part of the spectrum, at wavelengths below the detection range of the setup. In this case the fitting procedure relies only on the points from the red wing of Plancks curve, resulting generally in lower accuracy. Typical values of the relative errors associated to the temperature are ~ 20 %.

There is a noticeable difference between the two graphics (Fig.2 panel b) and c)), for two different laser irradiances. On the panel b), it can be seen that the temperature reaches a maximum at $t \approx 0$ ns, and then the plasma cools down. While the panel b) shows that the temperature of the plasma reaches a maximum value for $t \approx 4$ ns. This could be explained by the fact that plasma formed with a higher irradiance has higher density and therefore it can absorb laser radiation in later times much more intensively. Generally, the values for temperature are in reasonable agreement with the results from the model (Bogaerts et al., 2003).

5. CONCLUSION

In this work we present a technique for measurement of copper plasma temperature at the very beginning of the laser induced breakdown experiment, while laser still irradiates the plasma. The experiment is conducted by Nd:YAG laser for two irradiances: 1.5×10^{11}, and 3.0×10^{12} W/cm^2 at the residual atmosphere of 0.02 mbar. It is found that temperature plasma is in the interval 5000 - 60000 K. These values are in agreement with the data available in the literature obtained from the numerical simulations.

6. ACKNOWLEDGMENTS

This work is part of Project No. 451-03-68/2022-14/200162 supported by the Ministry of Education, Science, and Technological Development of the Republic of Serbia.

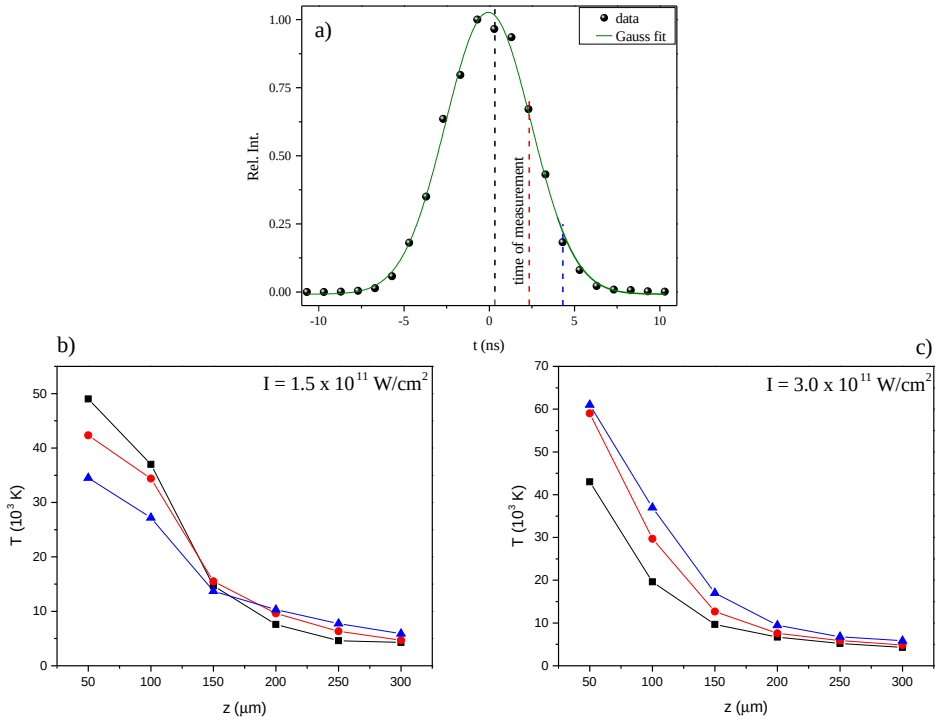

Figure 2: **Panel a)**: Black dots are measured Nd:YAG laser intensity in respect to the trigger signal. Green line is the best fit of to the Gauss function. Dashed lines represents the times at which the measurement was performed. The colors of the dashed lines are correlated with the colors of the points in panels b) and c). **Panel b) and c)** Set of temperatures for three time delays measured at different positions in respect to the target, for two laser irradiances.

References

Bogaerts A., Chen Z., Gijbels R., Vertes A. : 2003, *Spectrochimica Acta Part B*, **58**, 1867.
Hahn D. W., Omenetto N. :2010, *Applied Spectroscopy*, **64** 335.
Lutey A. :2013, *J. Appl. Phys.*, **14**, 083108.
Singh R. K., Narayan J. : 1990, *Phys.Rev. B*, **41**, 13.
Skocic, M., Dojic, D., Bukvic, S., :2022, *Phys. Rev. E*, (105), 045211

Publ. Astron. Obs. Belgrade No. 102 (2022), 235 - 238 *Contributed Paper*

STUDY OF PLASMA-FLOW INTERACTION IN LOW TEMPERATURE PLASMA JETS

G. B. SRETENOVIĆ, P. S. ISKRENOVIĆ, V. V. KOVAČEVIĆ, B. M. OBRADOVIĆ and M. M. KURAICA

University of Belgrade, Faculty of Physics, PO Box 44, 11001 Belgrade, Serbia
E-mail sretenovic@ff.bg.ac.rs

Abstract. The influence of the plasma generation and propagation in an atmospheric pressure plasma jet on the gas flow is experimentally studied. Two plasma action mechanisms have been identified and quantified: electrohydrodynamic force mechanism and thermal mechanisms due to fast localized heating. These two mechanisms appear to be counterbalancing or supporting, in dependence on the experimental conditions. Besides, it was shown that plasma can cause decrease of the gas velocity, probably depending on the dominant presence of the negative or positive ions in the jet. The complexity of the experimental conditions, such as initial gas flow, applied voltage shape and polarity, has been systematically studied and the results of these investigations are presented in this manuscript in a form of the main conclusions.

1. INTRODUCTION

Gas flow may be induced or modified by plasma. This fact inspired work on the development of efficient plasma flow control devices and detailed studies of flow generating mechanisms. Additionally, plasma devices attracted attention of scientists and engineers due to their positive features, such as fast control and absence of the motion of the mechanical parts. The influence of the plasma on the gas flow parameters in atmospheric pressure plasma jets is also documented by many studies utilizing the different methods (Darny et al., 2017; Iseni et al., 2019; Oh et al., 2011). This article is devoted to the presentation of our efforts on the quantitative determination of the flow changes induced by plasma and on the identification of plasma-flow interaction mechanisms (Sretenović et al., 2021, 2018).

2. EXPERIMENTAL SETUP

Two types of helium atmospheric pressure plasma jets were used in this study. Both plasma jets have the same electrode geometry, see Figure 1. The powered electrode is placed inside the glass tube, while the grounded electrode is wrapped around it. Both plasma jets worked with helium that freely flowed into the ambient

air. The only, but crucial difference was the use of different power supplies. The first power supply was laboratory-made power source operating at 12.65 kHz of sinusoidal voltage signal with variable amplitude and the second one pulsed high voltage power supply both with positive and negative polarities (pulse duration 3 μs, rise and fall time 1 μs, frequency 1- 5 kHz, voltage 2-11 kV). The plasma jets were pointed downwards.

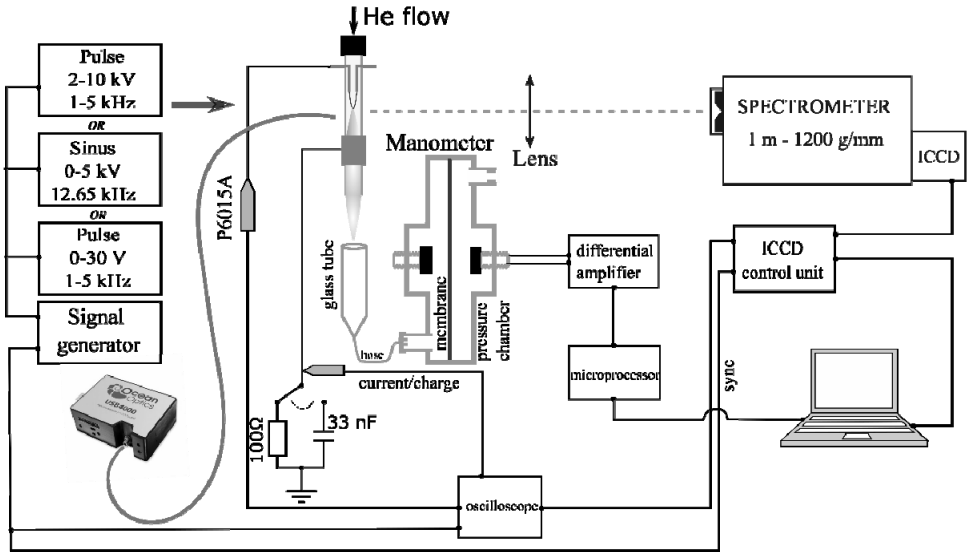

Figure 1: The scheme of the experimental setup.

The apparatus for the flow change measurements was a laboratory made manometer with the membrane and electrooptic sensors for the membrane movement detection, also depicted in Figure 1 (Iskrenović et al., 2020). The experiment was supported by the electrical and spectroscopic measurements.

3. RESULTS

The manometer operating range and sensitivity are flexible and may be set by a proper selection of the material and thickness of the membrane. For the current study, rubber and latex membranes were used, which enabled sensitivity of 0.4 Pa in a pressure range 1-20 Pa for the latex membrane and 1 Pa in a pressure range 1-140 Pa for the rubber membrane, see calibration curves in Figure 2. The first graph presented in Figure 2 (a) demonstrate the sensitivity of the sole. Figure 2 (b) presents the response of the manometer for the flow changes in the experimental configuration presented in Figure 1. The gas flow is controlled using Omega FMA-2606A mass flow controller. The device enabled observation of the flow changes caused by plasma in plasma jets.

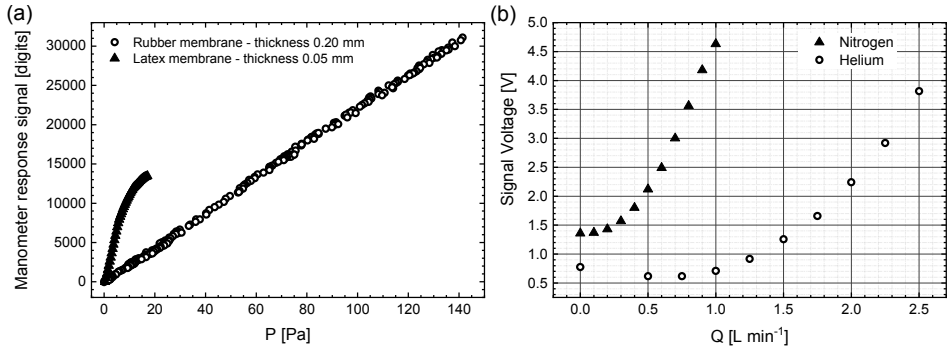

Figure 2*:* Calibration curves of the manometer for: (a) different membranes and (b) different gases flowing through the tube of the plasma jet.

The influence of the discharge on the gas flow is studied for helium flow ranging from 0.75 to 2.0 l min^{-1} for different applied voltages of the sinusoidal plasma jet. Applied voltages ranged from the breakdown voltage of the inter-electrode discharge to the maximal voltage where discharge is relatively stable. For a part of the voltage range, the discharge consists only of dielectric barrier discharge between the HV electrode and the isolated grounded ring. When the voltage becomes high enough, the plasma jet exceeds the glass tube. The results presented in Figure 3 show the gas flow increase that depends on the applied voltage value.

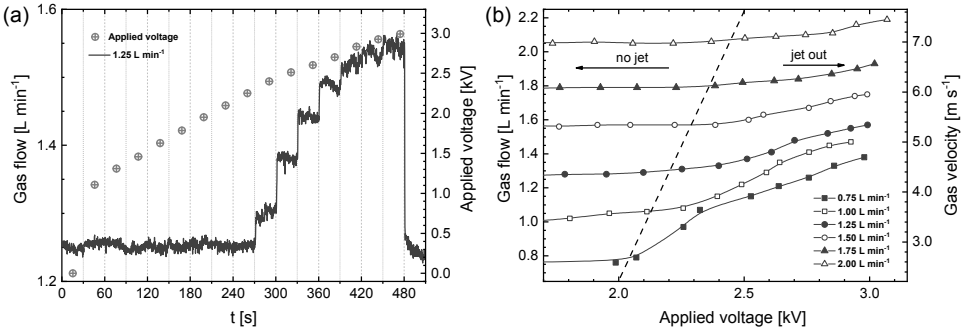

Figure 3: Influence of the plasma on the gas flow for the sinusoidal helium plasma jet. (a) Raw signal for the initial flow rate of 1.25 $Lmin^{-1}$. (b) Flow changes for the different flow rates and the different applied voltages.

In order to identify the mechanisms of the plasma-flow interaction and separate the dominant effects, the same discharge cell is supplied with voltage pulses of different polarity. The results are presented in Figure 4. Interestingly, besides the expected increase of the gas flow rate with the applied voltage, the evident decrease is recorded for some experimental conditions. In some cases, the change of the sign of the flow change is evidenced for the same voltage polarity, but different voltage values. These findings indicated that there are at least two

competitive plasma-flow interaction mechanisms under the studied experimental conditions.

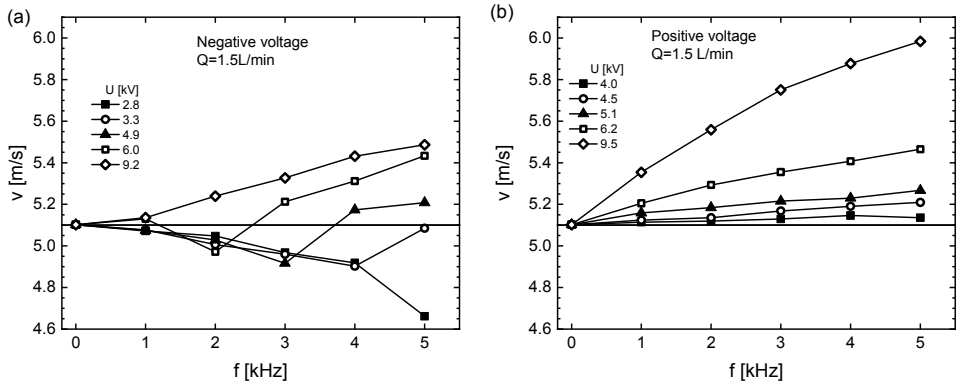

Figure 4: Influence of the plasma on the gas flow in the pulsed helium plasma jet for different applied voltages for: (a) negative and (b) positive voltage.

There are three basic plasma-flow interaction mechanisms: electrohydrodynamic (EHD), thermal, and magnetohydrodynamic (MHD). Having in mind low current in plasma jets, MHD effect may be neglected and the most probable two effects considered in the further investigations were EHD and thermal effect. EHD effect is due to the collisions of the charged particles that move under the influence of the electric field end collide with the neutral particles transferring the momentum. The thermal effect is due to the fast heating of the localized area due to the input of the electrical energy that induces acoustic pressure waves, which finally affects the global flow. In case of the used plasma jets, the rapid localized heating appears close to the high voltage electrode that acts as cathode when supplied with the negative voltage pulses. The experimental simulation of the fast localized heating of the high voltage electrode is performed through its pulsed Joule heating and the measurement of the heating effect. It is found that pulsed heating of the high voltage electrode causes overall gas flow increase. Furthermore, it is concluded that EHD force may induce both increase and the decrease of the total gas flow.

References

Darny, T., Pouvesle, J.-M., Fontane, J., Joly, L., Dozias, S., Robert, E.: 2017. *Plasma Sources Sci. Technol.* **26**, 105001.

Iseni, S., Pichard, C., Khacef, A.: 2019. *Appl. Phys. Lett.* **115**, 034102.

Iskrenović, P.S., Sretenović, G.B., Kuraica, M.M.: 2020. *Measurement* 108916.

Oh, J.-S., Olabanji, O.T., Hale, C., Mariani, R., Kontis, K., Bradley, J.W.: 2011. *J. Phys. D. Appl. Phys.* **44**, 155206.

Sretenović, G.B., Iskrenović, P.S., Kovačević, V. V., Kuraica, M.M.: 2021. *Appl. Phys. Lett.* **118**, 124102.

Sretenović, G.B., Iskrenović, P.S., Krstić, I.B., Kovačević, V. V., Obradović, B.M., Kuraica, M.M.: 2018. *Plasma Sources Sci. Technol.* **27**, 07LT01.

Publ. Astron. Obs. Belgrade No. 102 (2022), 239 - 242 *Contributed Paper*

SPECTROSCOPIC CHARACTERIZATION OF LASER-INDUCED PLASMA ON DOPED TUNGSTEN

BILJANA STANKOV[1], MARIJANA R. GAVRILOVIĆ BOŽOVIĆ[2], JELENA SAVOVIĆ[3] and MILIVOJE IVKOVIĆ[1]

[1]*Institute of Physics, University of Belgrade, Pregrevica 118, 11080 Belgrade, Serbia*

[2]*Faculty of Engineering Sciences, University of Kragujevac, Sestre Janjić 6, 34000 Kragujevac, Serbia*

[3]*Vinca Institute of Nuclear Sciences, University of Belgrade, Mike Petrovića Alasa 12-16, 11000 Belgrade, Serbia.*

E-mail ivke@ipb.ac.rs

Abstract. In this paper, the dependence of plasma characteristics, excitation temperature, and electron number density on the presence of fusion relevant doping elements (La and Th) in tungsten is evaluated and compared with a pure tungsten sample. It was found that different doping elements have little to no influence on plasma temperature, while electron number density seems to be more sensitive to the doping element type.

1. INTRODUCTION

The properties of tungsten, i.e., high melting point, high thermal conductivity, and low tritium retention, make it a promising material for fusion-related applications. On the other hand, its high Z number limits allowed concentration in plasma, which, with poor machinability, explosion dust potential, and irradiation-induced transmutations, pose a significant challenge for stable and safe operation. Although a large variety of tungsten grades and alloys already exist, numerous attempts to further optimize these materials are ongoing, Waseem et al., 2016. Investigations are needed to address many different issues related to the plasma-facing material (PFM) performance when exposed to thermal loads, neutron irradiation, and the plasma, Pintsuk et al. 2019. Erosion of tungsten under high localized thermal loads occurring during plasma disruption, vertical displacement events (VDEs), and the edge-localized mode (ELM) have an analogy with W erosion during laser ablation, Oderji et al. 2016. Following this analogy, the present research was undertaken to study plasma properties produced by laser ablation of pure and doped tungsten

(with La and Th) using optical emission spectroscopy methods. Both doping elements are relevant for fusion technology, Gietl et al., 2022, and Raj et al., 2022. The idea is to get insight into the dependence of plasma characteristics on different doping elements present in tungsten targets, which is essential for clarifying the impact of these elements in fusion-related applications.

2. EXPERIMENTAL SETUP

Different tungsten targets (pure W; 98,5%W+1.5%La_2O_3, 98%W+2%ThO_2) were placed on the PC controllable x-y table. A Q-switched Nd:YAG pulsed laser (Quantel, λ = 532 nm, energy 40 mJ, pulse duration 0.6 ns) was used to induce plasma on the target. The laser beam was focused on a target using a lens of 10 cm focal length. Light emitted from a plasma was collected with a fiber optic cable (Ø = 400 μm) and detected using an imaging spectrometer Shamrock 303 Andor equipped with the Andor iStar DH734 camera. The iCCD camera was operated in the full-vertical binning mode and controlled using a pulse generator (DDG 535, Stanford Research Systems). Delay was set to 0.5 μs, and the gate used was 2.5 μs. All measurements were performed in an argon atmosphere at 10 mbar pressure.

3. RESULTS

Typical spectra obtained with the employed setup are shown in Fig 1.

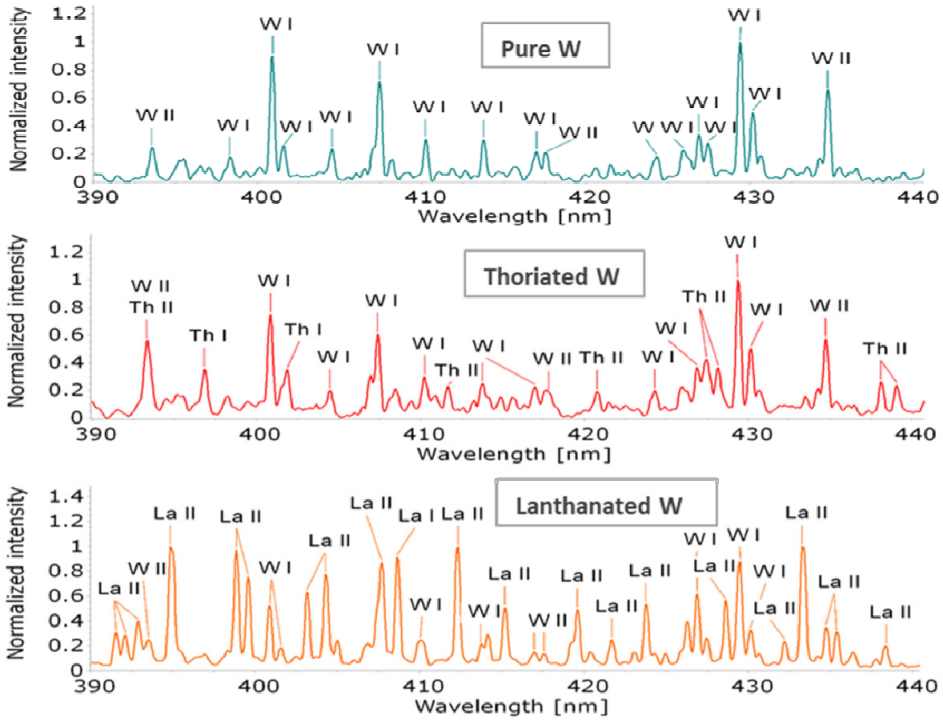

Figure 1: Characteristic LIBS spectra of pure and doped tungsten samples.

The most dominant lines belong to neutral and singly ionized tungsten for all target materials. These rich spectra of tungsten were suitable for excitation temperature determination by a Boltzmann plot method. An example of a Boltzmann plot for a pure tungsten target is given in Fig 2. The excitation temperature, T_{exc} calculated from the lines of singly ionized W was 13500K±1000K, slightly higher than the calculated temperature using neutral W lines (12300K±900K). The observed difference in temperature values obtained from a neutral atom and ion emissions is expected for spatially integrated measurements. As explained by J.A. Aguilera et al., 2004, in that case, the Boltzmann plots of neutral atoms and ions provide two different apparent excitation temperatures that correspond to the respective population averages of the local electronic temperature in the plasma. For all target materials, the obtained temperature values were similar (within the measurement uncertainty), implying an insignificant influence of doping elements on the plasma temperature.

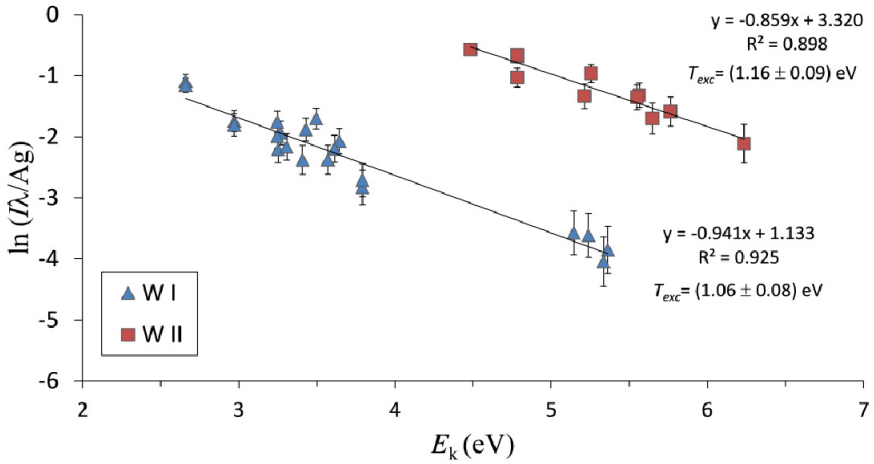

Figure 2: Boltzmann plot used to determine excitation temperature in LIBS plasma induced on a pure tungsten target.

For electron number density, N_e, estimation, a Stark broadening of the H_α line was used, Fig. 3. Based on the FWHM of the H_α spectral line and using the approximative formula (1), N_e was calculated. The results are shown in Table 1.

$$N_e[m^{-3}] = 10^{23} * (w_{SA}[nm]/1.098)^{1.47135} \quad (1)$$

Table 1: Electron number density determined using Stark broadening of H_α line.

Target	H_α	N_e (10^{22} m^{-3})
Pure W	0.503	2.84
Thoriated W	0.557	3.37
Lanthanated W	0.510	2.91

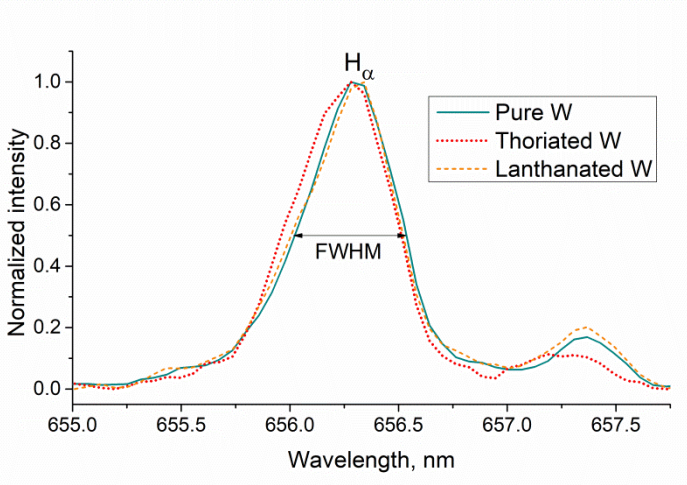

Figure 3: Stark broadened H_α line profiles used to evaluate N_e.

4. CONCLUSION

Different doping elements seem to have a negligible impact on laser-induced plasma excitation temperature. Electron number density shows slightly higher values in the case of thoriated W compared both to pure and lanthanated tungsten. A possible reason for this is the lower energy needed for significant erosion of thorium doped tungsten, already observed in experiments with tungsten-based cathodes, Casado et al., 2002. For a deeper understanding of the influence of doping elements on plasma properties, temporally and spatially resolved measurements are needed and are currently underway.

Acknowledgements

The research was funded by the Ministry of Education, Science and Technological Development of the Republic of Serbia, Contract numbers: 451-03-68/2022-14/200024 and 451-03-68/2022-14/200017, and supported by the Science Fund of the Republic of Serbia, Grant no. 3108/2021.

References

Oderji H.Y., Farid N., et al.: 2016, *Spectrochimica Acta Part B*, **122**, 1.
Pintsuk G., Hasegawa A.: 2019, *Comprehensive Nuclear Materials 2nd edition*, Elsevier.
Waseem O., Ryu H.J.: 2016, *Nuclear Material Performance*, Chapter 7, InTech.
Aguilera J.A., Aragón C.: 2004, *Spectrochimica Acta Part B*, **59**, 1861.
Gietl H., et al. 2022 *Journal of Alloys and Compounds*, **901**, 163419.
Raj D., Kannan U.: 2022, *Annals of Nuclear Energy*, **174**, 109162.
Casado E., Colomer V., et al.: 2002, *J. Phys. D: Appl. Phys*., **35**, 992.

Publ. Astron. Obs. Belgrade No. 102 (2022), 243 - 246 *Contributed Paper*

MODELING OF STARK SPECTRAL LINE BROADENING BY MACHINE LEARNING ALGORITHMS

IRINEL TAPALAGA[1], IVAN TRAPARIĆ[2], NORA TRKLJA BOCA[1], JAGOŠ PURIĆ[1] and IVAN P. DOJČINOVIĆ[1]

[1]*University of Belgrade, Faculty of Physics, P. O. Box 44, 11000 Belgrade, Serbia*

[2]*University of Belgrade, Institute of Physics, Pregrevica 118, 11080 Belgrade, Serbia*

E-mail nora@ff.bg.ac.rs

Abstract. Stark broadening caused by free electrons in plasma and its dependence on atomic parameters available in NIST and Stark-b atomic databases has been investigated using a new method based on the machine learning (ML) approach. The correlation parameter obtained by artificial intelligence (AI) is slightly better than the one obtained by classical methods, but the scope of application is much wider. ML algorithms successfully identified quantum nature by analyzing atomic parameters. The biggest issue of classical analysis, which is infinite spectral line broadening for high ionization stages, was resolved by AI with a saturation tendency.

1. INTRODUCTION AND THEORETICAL BACKGROUND

Stark broadening of spectral lines of neutral atoms and ions is used in science for a number of problems in various physical conditions (see Tapalaga et al. 2022). Recent research indicates the importance and usefulness of searching for possible types of regularities in the framework of a Stark broadening investigation. Still, existing tables with calculated and measured Stark widths have a big lack of data. There is a need for Stark widths data in the wide range of chemical elements, plasma temperature and electron densities. In this paper a correlation between Stark broadening and environment parameters, such as the ionization potential of the upper level of the corresponding transition, electron density and temperature, will be investigated using modern ML algorithms. If this method proves to be accurate enough, the process of calculating the value of Stark widths will be significantly accelerated and facilitated.

The general formula for Stark width calculation in the impact approximation (see Griem 1974) is very complicated, it cannot be resolved exactly, so it is useful

to use different approaches in the calculation. The regularity approach which correlates Stark width of spectral line (ω) expressed in [rad/s], electron density (N_e), electron temperature (T_e) and positive value of electron binding energy on the upper level of the transition (χ), expressed in [eV], is given by Puric and Scepanovic 1999. (Eq. 1)

$$\omega = Z_e^k a N_e f(T_e) \chi^{-b} \tag{1}$$

where Z_e = 1, 2, 3... for neutrals, singly charged ions, ... respectively and it represents the rest core charge of the ionized emitter and a, b and k are coefficients independent of electron concentration and ionization potential for a particular transition and the rest core charge of the emitter.

It is expected that spectral series within an isoelectronic sequence show regularity behavior because a wide range of atomic/ionic parameters depend on the electron number. In the last decade we have investigated Stark broadening regularities within spectral series of individual elements, individual isoelectronic sequences and within two spectral series of isoelectronic sequences simultaneously. The present investigation goes one step further and analyses all elements for which there are available data needed for Stark broadening investigation, simultaneously, using machine learning approach. The aim is to find the best possible model which correlates Stark width of spectral line with all available parameters for transition of interest (atomic parameters and environmental parameters).

2. DATASET CREATION AND DATA CLEANING

In order to create dataset, two public repositories connected with atomic spectroscopy are used. First one is Stark B database, see Sahal-Brechot et al. 2020, where the parameters of Stark broadening for different emitters are given. The features taken from this database are: chemical element, ionization stage, upper and lower level of spectral transitions, Stark broadening, the environment temperature and electron density in environment. For analysis purpose, Stark widths expressed in angstroms are converted in radian per second.

To ensure better results we enriched features taken from Stark B database with ones taken from NIST Atomic Spectra database (see Kramida et al. 2019): binding energy of both upper and lower transition levels, ground level energy, total angular momentum quantum number (*J)* of both upper and lower transition level, as well as principal (*n)* and orbital (*l)* quantum numbers and ionization energy. The algorithm for connecting those two databases to form our own works is described below. For every transition connected with certain chemical element, we take the electronic configuration of both upper and lower levels from Stark B database. Then we look for that particular element in NIST database and compare the electronic configurations. If they match, then we take the binding energy of those levels, their

principal quantum number, orbital quantum number and total angular momentum quantum number and finally the ionization energy of that atom.
After data cleaning, dataset contains 53 emitters and 34973 spectral lines and follows a normal distribution.

3. MODEL CREATION AND TRAINING

For model creation and training, public Python package Sci-kit learn is used. Four models have been created, every being Pipeline with two steps. In each object of Pipeline class, the first step was data scaling using StandardScaler, and in second step we made our predictions with defined model. Considered models were: Linear Regression, Decision Tree Regressor, Random Forest Regressor and Gradient Boosting Regressor. The dataset was split into training and test dataset using train test split method, leaving 25% of the data for testing. To rank the performance of models, we used best Coefficient of Determination, R^2, value obtained after GridSearchCV algorithm finished. As a result, we got that the best R^2 value was for Random Forest Regressor having $R^2 = 0.95$ for n estimators = 100. Random Forest is a learning method that operates by constructing a large number of decision trees during the training process, see Tapalaga et al. 2022. It is simple to use and shows high performance for a wide variety of tasks, making it one of the most popular ML algorithms in different sciences. Random forests are an effective tool in predicting new data, in our case new atomic parameters.

4. RESULTS

The Random Forest model is used to calculate Stark broadening data for spectral series within neutral lithium Li I, see Tapalaga et al. 2022. Fig 1. shows the dependence of the Stark width (ω) on the reciprocal value of the electron binding energy at the upper level of the transition (χ^{-1}) for 2s-np and 3s-np transitions within lithium atom. Calculated Stark widths (red lines) for transitions within analyzed series are represented with existing known values of Stark widths data at the same graphs (see Fig. 1). The functional dependence obtained using the ML algorithm describes the quantum structure of the energy levels of lithium atoms. From the model lines (red lines) it can be concluded that the model successfully (within the error) indicates the quantum nature of atomic transitions and that other results do not make physical sense, but only jumps.

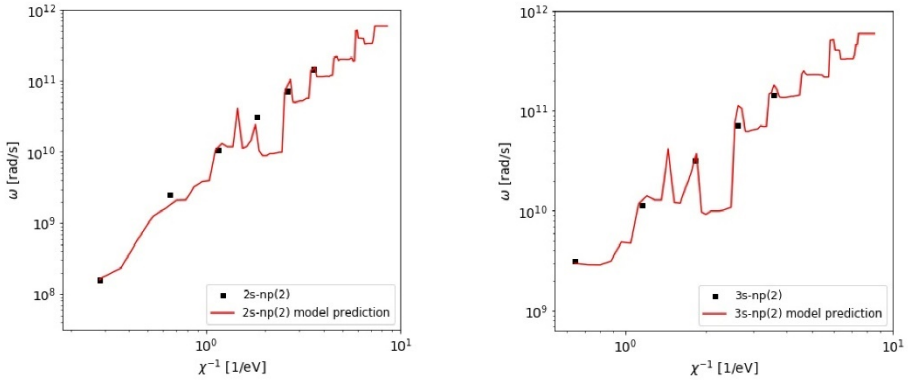

Figure 1: Stark widths regularities within 2s-np and 3s-np spectral series of Li I ($T = 30000$ K, $N_e = 10^{20}$ m^{-3})

5. CONCLUSION

Analysis of spectral data on Stark broadening for 53 different emitters and 34973 lines by ML algorithms was done with more success than it was previously done by classical methods of data analysis. Random forest has scored an average of $R^2 = 0.95$ which makes it an excellent choice for Stark broadening calculations. With standard known methods for Stark width calculation, it is not possible to calculate Stark widths for levels for which energy values of the closest perturbing levels are missing, but ML algorithms enable calculation in these situations, too.

References

Griem, H.R. : 1974, *Spectral Line Broadening by Plasmas*, Academic Press, New York

Kramida A, Ralchenko Yu, Reader J and NIST ASD Team (2019). NIST Atomic Spectra Database (version 5.7.1), [Online]. Available: https://physics.nist.gov/asd [Tue Mar 24, 2020]. National Institute of Standards and Technology, Gaithersburg, MD.

Purić, J., Šćepanović, M. : 1999, *Astrophys. J*, **521**, 490.

Sahal-Brechot S., Dimitrijević M. S., Moreau N. (2020) STARK-B database, [online]. Available: http://stark-b.obspm.fr [February 20, 2020]. Observatory of Paris, LERMA and Astronomical Observatory of Belgrade

Tapalaga, I., Traparić, I., Trklja Boca N., Purić, J., Dojčinović, P. I. : 2022, *Neural Computing and Application*, **34**, 6349

Publ. Astron. Obs. Belgrade No. 102 (2022), 247 - 250 *Contributed Paper*

SPECTROSCOPIC DETERMINATION OF THE DEGREE OF DISSOCIATION OF HYDROGEN IN THE GLOW DISCHARGE

M. M. VASILJEVIĆ[1], G. LJ. MAJSTOROVIĆ[2], I. R. VIDENOVIĆ[1] and D. SPASOJEVIĆ[1]

[1]*University of Belgrade, Faculty of Physics, 11001 Belgrade, P.O. Box 44, Serbia*

[2]*University of Defence, Military Academy, 11105 Belgrade, Pavla Jurišića Šturma 33, Serbia*

E-mail gordana.majstorovic@va.mod.gov.rs

Abstract. The optical emission spectroscopy technique is used to measure the degree of dissociation of hydrogen along the axis of cylindrical abnormal glow discharge parallel (side-on) to the copper cathode surface in hydrogen - argon mixture at low pressure. The degree of dissociation is determined from the intensity ratio of the H_γ line and the diagonal Fulcher-α bands, while the electric field strength distribution in the cathode sheath region is determined from the measured Stark shifts of the experimental profiles of the hydrogen Balmer gamma line H_γ.

1. INTRODUCTION

Within a growing number of applications, Glow Discharge Sources (GDS) are successfully used as excitation sources for analytical spectroscopy of metal and alloy samples, see e.g. Jakubowski et al. 2003 and Broekaert 2003. Most GDS applications are based on the original design described by Grimm 1968, with both direct current (DC) and radio frequency (RF) excitations.

The knowledge of discharge parameters, like the degree of dissociation of molecular hydrogen in hydrogen and hydrogen-containing low-temperature plasmas, is of common interest in basic research, industrial applications, and understanding the outer space phenomena, see Lavrov et al. 2006.

In this study, the optical emission spectroscopy (OES) technique is used to estimate the degree of dissociation of a hydrogen-argon mixture in a low-pressure Grimm-type glow discharge. For this purpose, the hydrogen H_γ line and emission spectra of the $d^3\Pi^-_u \rightarrow a^3\Sigma^+_g$ system are recorded and analysed in the cathode sheath region of the discharge.

2. EXPERIMENTAL

A detailed description of a modified Grimm GDS is given in Majstorović et al. 2013 and thus, only a few important details will be mentioned here. The experiment was realized in a hydrogen-argon (5% vol. Ar) mixture; further details can be found in Vasiljević et al. 2020.

The axial intensity distribution of radiation has been observed side-on through the anode slot, see Figure 1. The discharge tube was translated in approximately 0.25 mm steps. The light from the discharge was focused with an achromatic lens (focal length 75.8 mm) with unity magnification onto a 20 μm entrance slit (height restriction 2 mm) of 2 m focal length Ebert type spectrometer with 651 g/mm reflection grating blazed at 1050 nm. For the line shape measurements, the reciprocal dispersion of 0.37 nm/mm is used throughout this experiment. All spectral measurements were performed with an instrumental profile very close to Gaussian form with measured full width at half maximum (FWHM) of 8.2 pm.

Thermoelectrically cooled Hamamatsu CCD (2048 × 506 pixels, pixel size 12 × 12 μm, -10 ºC) was used as a radiation detector, and the collected data were transferred to and processed by a PC.

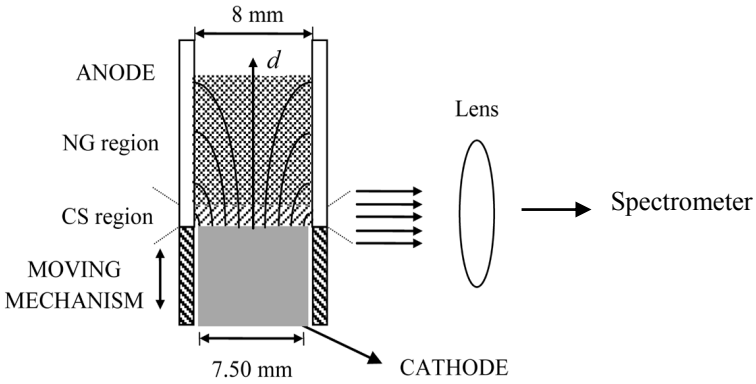

Figure 1: Schematic diagram of the central part of the Grimm GD for side-on observations. Symbols: CS – cathode sheath region, NG – negative glow region.

3. RESULTS AND DISCUSSION

Some recent studies, e.g., Fantz et al. 2006 and Dang et al. 2016, suggest that the ratio of the intensity of the hydrogen Balmer gamma line and Fulcher-α system is a proper value for estimation of the degree of dissociation of hydrogen. It is well known that the atomic hydrogen density is correlated with the Balmer line emission, while the molecular density is correlated with the emission of molecular radiation (Fulcher-α band transition: $d^3\Pi^-_u \rightarrow a^3\Sigma^+_g$, $v' = v'' = 0–3$, $\lambda = 590–645$ nm). The ratio of the emission rate coefficients for H_γ and H_2 is found almost independent of the electron temperature T_e and barely dependent on electron density n_e if 5×10^{16} m^{-3} < n_e < 5×10^{18} m^{-3}, see e.g. Fantz et al 2006 and references therein. Thus, the intensity ratio, H_γ /H_2, is considered suitable for the determination of the density ratio [H] / [H_2] in our GDS as well.

In Figure 2 we present recorded rotational bands belonging to the H_2 Fulcher-α diagonal bands. From the recorded spectra, it is evident that the lines of P, Q and R branch in the visible 590-645 nm wavelength region (wavelength data taken from Crosswhite 1972), are well resolved and have a high signal to noise ratio. In this

study we used the intensities of all lines of the electronic transition $d^3\Pi^-_u, v' \rightarrow a^3\Sigma^+_g, v''$ ($v'=v''=0,1,2,3$), see Vasiljević et al. 2020.

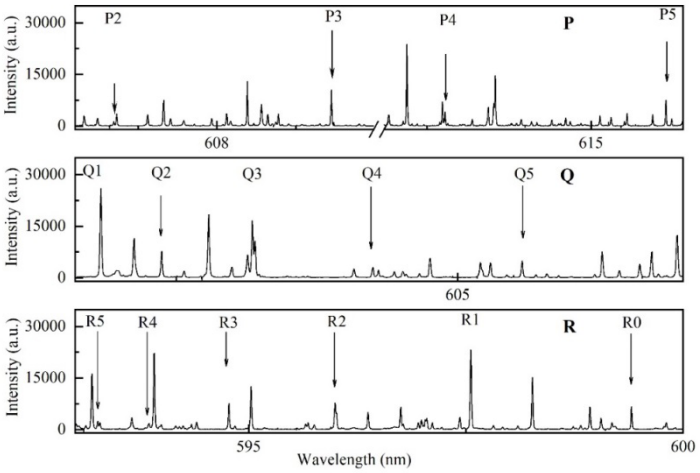

Figure 2: Emission spectra of the rotational lines for the $d^3\Pi^-_u, v'=0 \rightarrow a^3\Sigma^+_g, v''=0$ band, P, Q and R-branches, recorded in the second order of diffraction grating. Experimental conditions: cooper cathode GDS in H_2+5%Ar at p = 4.5 mbar; I = 13.4 mA; U = 646 V.

The intensity ratio, according to Fantz et al. 2006 and Dang et al. 2016 is:

$$\frac{I_\gamma}{I_{Ful.}} = \frac{X_\gamma^{eff}}{X_{H_2.}^{eff}} \frac{[\mathrm{H}]}{[\mathrm{H_2}]}, \quad (1)$$

where $[\mathrm{H}]$ and $[\mathrm{H_2}]$ are the number densities of hydrogen atoms and molecules and $\frac{X_\gamma^{eff}}{X_{H_2}^{eff}}$ is the ratio between the effective emission rate for the H_γ line and Fulcher-α system molecular radiation calculated according to the collisional radiative model (Fantz et al. 2006). Owing to the high resolution spectrometer, we were able to determine the intensity of the Fulcher-α band. The value for $\frac{X_\gamma^{eff}}{X_{H_2}^{eff}}$ was taken from Figure 5 in Fantz et al. 2006, and the ratio $\frac{I_\gamma}{I_{H_2}}$ was calculated to determine $\frac{[\mathrm{H}]}{[\mathrm{H_2}]}$. Using the relationship between the neutral particle density ratio and the degree of dissociation from Lavrov et al. 2006 and Dang et al. 2016 we estimated the degree of dissociation expressed as:

$$\mathrm{D} = \frac{[H]}{[H]+2[H_2]} = \frac{\frac{[H]}{[H_2]}}{\frac{[H]}{[H_2]}+2}. \quad (2)$$

The electric field strength measurement is performed using the value of the Stark shift coefficient s for the chosen Stark component, and its Stark shift $\Delta\lambda=\Delta\lambda_{p\text{-}p}/2$; here, $\Delta\lambda_{p\text{-}p}$ is peak-to-peak distance, measured on the recorded line shape between the two strongest Stark components that are equally shifted, one to the red, and the other to the blue wavelength side. The so-obtained electric field

distributions were fitted using the linear regression and the results suggest that the thickness of the CS region is around 1.75 mm, which is in good agreement with the result obtained using the H_α line published in Vasiljević et al 2020.

Presented results show that the degree of dissociation doesn't vary a lot through the CS region and decreases around the edge with the negative glow region. The thickness of the CS region is used when showing the changes in the intensity and degree of dissociation in Figure 3.

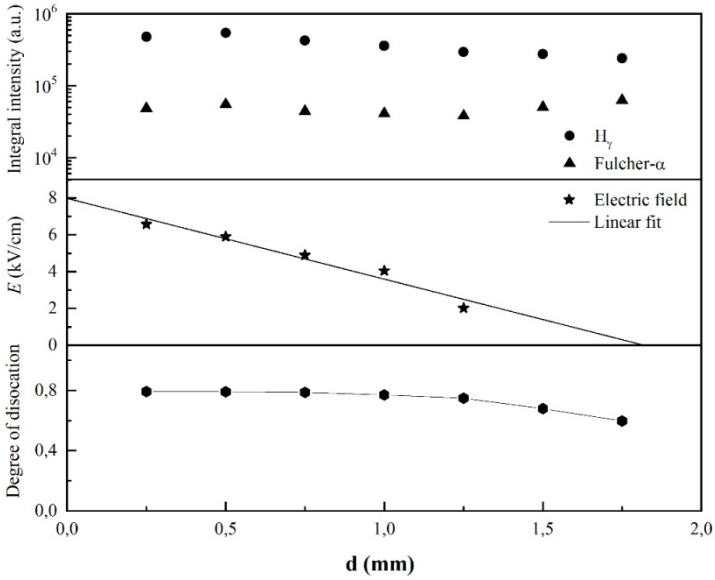

Figure 3: The dependence of: (a) Relative intensity of H_γ line and Fulcher-α bands ($v'=v''=$ 0, 1, 2, 3) (b) Electric field strength and (c) Degree of dissociation, all upon the distance from the cathode. Experimental conditions: cooper cathode Grim GD in H_2+5%Ar at p = 4.5 mbar; I = 13.4 mA; U = 646 V.

Acknowledgments

This work is supported by the Ministry of Education, Science and Technological Development of the Republic of Serbia.

References

Broekaert J. A. C. : 2003, *Glow Discharge Plasmas in Analytical Spectroscopy*, Marcus R. K. and Broekaert J. A. C., New York: Wiley.

Dang J. J., Chung K-J., Hwang Y. S. : 2016, *Rev. Sci. Instrum.*, **87**, 053503.

Fantz U., Falter H., Franzen P., Wunderlich D., Berger M., Lorenz A., Kraus W., McNeely P., Riedl R., Speth E. : 2006, *Nucl. Fusion*, **46**, S297.

Grimm W. : 1968, *Spectrochim. Acta B*, **23,** 443.

Jakubowski N., Bogaerts A. and Hoffmann V. : 2003, *Atomic Spectroscopy in Elemental Analysis*, Sheffield: Cullen M, Blackwell Publishing.

Lavrov B. P., Pipa A. V. and Röpcke J. : 2006, *Plasma Sources Sci. Technol.*, **15**, 135.

Majstorović G. Lj., Ivanović N. V., Šišović N. M., Djurović S., Konjević N. : 2013, *Plasma Sources Sci. Technol.*, **22**, 045015.

Vasiljević M. M., Majstorović G. Lj., Spasojević D., Konjević N. : 2020, *J. Quant. Spectrosc. Radiat. Transfer*, **254**, 107195.

Publ. Astron. Obs. Belgrade No. 102 (2022), 251 - 254 *Contributed Paper*

COMPARISON OF BIOCOMPATIBILITY OF ORGANIC POLYMERS MODIFIED IN VARIOUS TYPES OF NON-TEMPERATURE PLASMAS

TATIANA VASILIEVA[1], ELENA NIKOLSKAYA[2], MICHAEL VASILIEV[3], NIKITA YABBAROV[2], MARIA SOKOL[2], MARIIA MOLLAEVA[2] and MARGARITA CHIRKINA[2]

[1]*Moscow Institute of Physics and Technology, Institutsky per., 9, Dolgoprudny, Moscow region 141700 Russia*
E-mail vasileva.tm@mipt.ru

[2]*N.M. Emanuel Institute of Biochemical Physics RAS, Kosygina str., 4, Moscow 119991 Russia*
E-mail elenanikolskaja@gmail.com

[3]*Joint Institute for High Temperatures of Russian Academy of Sciences (JIHT), Izhorskaya str., 13, Bd.2, Moscow 125412 Russia*
E-mail vasilev.mn@mipt.ru

Abstract. Application and perspectives of plasma chemical rectors generating cold hybrid plasma for polymeric materials biocompatibility improvement are considered. Oxygen hybrid plasma was produced by joint action of a continuous or intermittent electron beam and a capacity coupled RF-gas discharge (13.56 MHz) on gaseous media at moderate pressures. Oxygen-containing functional groups were formed on the poly(ethylene terephthalate) surface, which increased its hydrophilicity. The plasma-treated polymers turned out to be noncytotoxic and biocompatible. Fibroblasts 72 h survival on hybrid plasma-modified poly(ethylene terephthalate) films was higher in comparison with control cells cultured on untreated polymers and substrates treated in RF-discharge only.

1. INTRODUCTION

For the effective use of polymers and plastics in biology and medicine, their preliminary modification and functionalization is often needed and therefore the development of new technologies for polymeric surfaces engineering is of great research and commercial importance.

Among the several techniques for the surface modification of polymeric materials, non-temperature plasmas are of the most frequently applied [see Sui et al. 2021; Zanini et al. 2020], since they offer a large number of advantages over conventional methods like mechanical abrasion, wet chemical cleaning, etching,

etc. By the introduction of hydrophilic or hydrophobic groups the plasma-stimulated surface activation modifies the surface energy and the water wettability of polymers, affecting their adhesive interface bonding [see Fattah. 2019], binding of specific active molecules [see Soygun et al. 2020], antibacterial properties [see Ozge et al. 2014], and integration with living tissues [see Ozge et al. 2014; Rezaei et al. 2016].

The objective of the study was to compare the chemical composition and biocompatibility of the surface of poly(ethylene terephthalate) (PET) films treated in hybrid plasma, generated by joint action of a continuous or intermittent electron beam (EB) and RF-gas discharge on gaseous media at moderate pressures.

2. HYBRID PLASMA CHEMICAL REACTOR

PET films were modified in the hybrid plasma chemical reactor as it was described earlier in Vasiliev et al. 2019. All experiments were carried out using oxygen of the spectroscopic grade as a plasma gas at a pressure of P_m = 1.5 Torr and other parameters were as follows:

- the EB accelerating voltage, E_b = 30 kV;
- the EB current I_b = 1.5 mA
- the RF-frequency 13.56 MHz and the RF-power 10 W;
- gas flow rate 5 sccm (standard $cm^3 \times min^{-1}$);
- treatment time was 10 min.

Under these conditions, the material temperature did not exceed 40 ºC. The stability of the conditions was ensured by automatic control systems of the plasma chemical reactor.

The main hybrid reactor advantages are as follows:

1. The reaction volume is uniform and doesn't contract with the increase of the plasma generating gas pressure to values at which the RF-discharge is filamentary or does not glow at all;

2. Electron beam scanning can instantly control the reaction volume geometry, while active plasma particles concentrations can be controlled by the beam power independently, which allows to accurately localize the RF-discharge on the desirable polymer surface zone. On the other hand, the EB scanning, and the control of both the EB parameters and the plasma media characteristics prevent local overheating of the treated polymer. As a result, areas within which physical, chemical and functional properties change abruptly (structured patterns) or smoothly (gradient materials) can be formed on the surface. Experimental results that confirm these possibilities can be found in our papers [Vasiliev et al. 2019; Vasilieva et al. 2021].

3. EXPERIMENTAL RESULTS

The hybrid plasma treatment resulted in oxygen-containing polar hydroxyl, carbonyl, and carboxyl groups formation in the PET surface layers. Surface free

energy increase and wettability enchantment up to 1.5-2 times in comparison with original PET were observed as well. The changes in the chemical composition of the polymeric surface together with the rise of its hydrophilic properties associated with the improvement of compatibility of the plasma-modified PET films with living cells and tissues.

The biological tests of plasma-treated PET samples were performed on BJ-5ta line of immortalized human fibroblasts cell culture, which is commonly used for assessment of the new materials cytotoxicity and biocompatibility.

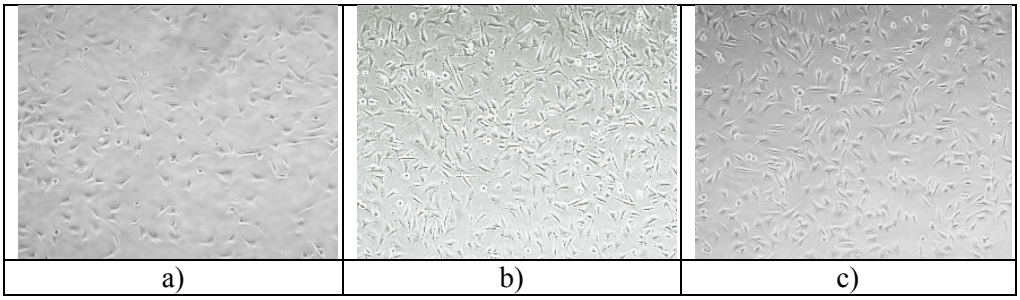

Figure 1: The optical microscopic images of the fibroblasts BJ-5ta after 48 h of their culturing on: a) – original PET; b) - PET treated in oxygen hybrid plasma; c) – blank culture sample.

In optical microscopic images, the fibroblasts spreading on the PET samples modified in oxygen hybrid plasma was observed (Figure 1) after 48 hours of their cultivation. The cells were exhibiting a flattened morphology that demonstrated good adherence to the polymeric surface. The normal cell morphology and proliferation patterns, which can also be seen in Figure 1 are similar to those of the negative control (blank culture), prove the noncytotoxic effect of the plasma-modified PET.

The MTT [3-(4,5-dimethylthiazol-2-yl)-2,5-diphenyltetrazolium bromide] colorimetric assay did not also show any cytotoxic effect of PET modified in oxygen hybrid plasma. For instance, a tendency to a better cell growth was observed on hybrid plasma-modified samples after 72 h in comparison with the original PET films (the positive control) and PET substrates treated in RF-discharge only. This trend was confirmed by the colorimetric measurements of the individual values of fibroblast survival on single PET substrates (Figure 2): the optical densities of the supernatants obtained from cells incubated with hybrid plasma-modified PET samples were significantly increased with respect to the ones for the positive controls as well as for polymers after RF-discharge processing. Thus, the hybrid plasma and hybrid type plasma chemical reactors seem to be perspective for obtaining biocompatible polymers for tissue engineering and regenerative medicine.

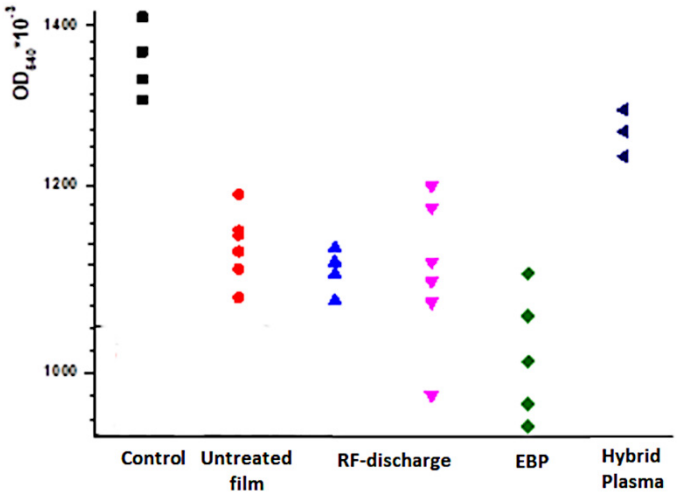

Figure 2: Individual values of the survival of BJ-5ta fibroblasts cultivated on PET films for 72 h in 24-well culture plates in comparison with the average survival value of control cells culture in the absence of PET films.
The average survival was assessed as the absorbance of biosamples measured at wavelength $\lambda = 540$ nm ($OD_{540}\times10^{-3}$).

References

Fattah, E. A. : 2019, *Coatings*, **9**, 228.
Ozge, O., Nesrin, H. : 2014, *J. Biomater. Tissue Eng.*, **4**, 479.
Rezaei, F., Shokri, B., Sharifian, M. : 2016, *Appl. Surf. Sci.*, **360**, 641.
Soygun, K., Tamam, E., Dogan, A., Keskin, S. : 2020, *Niger. J. Clin. Pract.*, **23**, 1266.
Sui, S., Li, L., Shen, J., et al. : 2021, *Polym. Eng. Sci.*, **61**, 506.
Vasiliev, M., Vasilieva, T., Aung Miat Hein : 2019, *J. Phys. D: Appl. Phys.*, **52**, 335202.
Vasilieva, T., Vasiliev, M. : 2021, *IEEE Transac. Plasma Sci.*, **49**, 3307.
Zanini, S., Papagni, A., Vaghi, L., et al. : 2020, *Coatings*, **10**, 135.

Section 4.

GENERAL PLASMAS

ACTION-SPECTROSCOPIC STUDIES OF TRANSIENT CARBON-RICH MOLECULAR IONS

SVEN THORWIRTH, OSKAR ASVANY, and STEPHAN SCHLEMMER
I. Physikalisches Insitut, Universität zu Köln, Köln, Germany
E–mail sthorwirth@ph1.uni-koeln.de

Abstract. Carbon-rich material is of importance in diverse scientific areas such as material science, structural chemistry, theoretical chemistry and astrochemistry. In space, carbon–rich molecular chains both in their neutral and charged forms are abundant ingredients of molecular clouds and circumstellar shells. In this talk, recent efforts towards laboratory spectroscopic characterization of positively charged carbon-rich molecular ions will be presented. These species were observed as products of electron impact ionization of suitable precursor gases using infrared/millimeter-wave techniques and 22-pole ion trap instruments in combination with a collection of action spectroscopy schemes. Low-resolution studies were performed using infrared photo dissociation (IRPD) of ion-rare gas clusters (Figure 1). High spectral resolution was obtained when using laser induced inhibition of complex growth (LIICG), rotational state selective attachment of helium and infrared-millimeter wave double resonance techniques (see, e.g., Asvany and Schlemmer 2021, for a recent review).

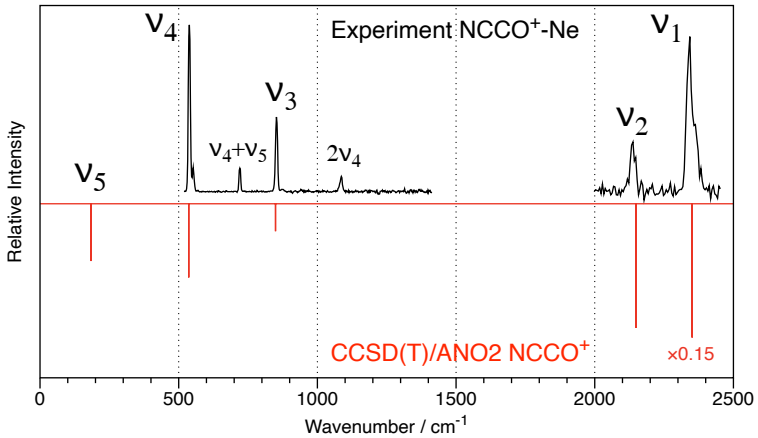

Figure 1: IRPD spectrum of the weakly bound complex of the linear $NCCO^+$ molecular ion and one Ne atom obtained with the FELion apparatus (Jusko et al. 2019) connected to the Free Electron Laser for Infrared eXperiments, FELIX, vs. a calculated stick spectrum of the bare $NCCO^+$ ion.

References

Asvany, O., Schlemmer, S. : 2021, *Phys. Chem. Chem. Phys.*, **23**, 26602.
Jusko, P., Brünken, S., Asvany, O., Thorwirth, S., Stoffels, A., van der Meer, L., Berden, G., Redlich, B., Oomens, J. Schlemmer, S., : 2019, *Faraday Discuss.* **217**, 172.

Publ. Astron. Obs. Belgrade No. 102 (2022), 258 *Topical Invited Lecture*

LINE SHAPE MODELING FOR MAGNETIC FUSION AND ASTROPHYSICAL PLASMAS: AN OVERVIEW OF RECENT RESULTS

J. ROSATO, Y. MARANDET, I. HANNACHI and R. STAMM

Aix-Marseille-Université, CNRS, PIIM, Campus de Saint-Jérôme, F-13397 Marseille Cedex 20, France
E-mail joel.rosato@univ-amu.fr

Abstract. A selection of problems related to the modeling of Stark broadening is considered, for astrophysical and laboratory plasma diagnostic applications. At the atomic level, a proper description of a line shape requires the ion microfield evolution be accounted for during the time of interest of the transition under consideration; this is the so-called ion dynamics issue. In addition, the lines presenting a structure such as Hβ can exhibit an asymmetry due to presence of multipolar interactions, which is significant at high density regimes and must be retained in calculations. Some observed spectra from magnetized plasmas also exhibit lines with a Zeeman triplet structure due to both linear and quadratic terms in the Hamiltonian, which must also be retained in calculations. We give a review of these problems and present new spectra calculations. A focus is put on plasma conditions relevant to stellar atmospheres and magnetic fusion experiments. We present calculations and also report on line shape fittings which have been performed for diagnostic applications. We have recently developed models for retaining the effect of collective electric fields on the line shapes of hydrogen. Langmuir waves are an example of such fields which are present in equilibrium and can be strongly amplified by density gradients or by beams of fast electrons. We present results of a computer simulation showing the changes in the line shape resulting from electronic Langmuir waves with a magnitude of the order of the mean plasma microfield.

DESCRIBING THE MATEMATICAL METHODS FOR CALCULATING BASIC PHYSICAL PARAMETERS OF THE GAUSSIAN-ROTATIONAL (GR) MODEL

ANTONIOS ANTONIOU[1, 2], EMMANUEL DANEZIS[2], DIMITRIOS STATHOPOULOS[2, 3], EVAGELIA LYRATZI[2, 3] and DIMITRIOS TZIMEAS[2]

[1]*University of the Peloponnese, Department of Informatics and Telecommunications, Akadimaikou G. K. Vlachou Street, GR-221 31 Tripoli, Greece*
E-mail a.antoniou@uop.gr

[2]*University of Athens, Faculty of Physics, Department of Astrophysics, Astronomy and Mechanics, Panepistimioupoli, Zographou, 157 84 Athens, Greece*
E-mail ananton@phys.uoa.gr, edanezis@phys.uoa.gr, dstathopoulos@phys.uoa.gr, elyratzi@phys.uoa.gr, dtzimeas@phys.uoa.gr

[3]*Eugenides Foundation, 387 Sygrou Av., 175 64, Athens, Greece*

Abstract. Our research group developed Gaussian-Rotational (GR) model and A.S.T.A. software that can analyze the complex DAC/BAL (Discrete Absorption Components/Broad Absorption Lines) profiles, which we observe in the spectra of Hot Emission Stars and Quasars, to individual components. By applying a series of strict fitting criteria, we analyze each DAC/BAL to the uniquely determined number of components it consists of; our method guarantees the uniqueness of the best fit. For every absorption component, we calculate the radial (Vrad) and rotational (Vrot) velocity, the FWHM, the random velocities of the ions (Vrand), the optical depth at line center (τ_0), and the column density (N). Notice that, in the final line function, we can apply all the known distributions, which contribute to the peculiar profile of the studied spectral line. In this paper, we present the mathematical methods for applying of the Gaussian, Lorentzian, and Voigt distribution to the final line function, as well as the calculation of the FWHM and the random velocities in each of the above mentioned distributions. Additionally, we present the so-called problem of the "Partial Coverage of the Radiation" and a mathematical method of its solution.

ANALYSIS OF ADIABATIC PROCESSES IN MULTILEVEL N-POD QUANTUM SYSTEMS FROM THE PERSPECTIVE OF RIEMANNIAN GEOMETRY

A. CININS[1], M. S. DIMITRIJEVIĆ[2], V. A. SREĆKOVIĆ[3], K. MICULIS[1,4], N. N. BEZUGLOV[1,5] and A. N. KLYUCHAREV[5]

[1]*Institute of Atomic Physics and Spectroscopy, University of Latvia, LV-1004 Riga, Latvia*

[2]*Astronomical Observatory, Volgina 7, 11060 Belgrade 38, Serbia*
E-mail mdimitrijevic@aob.rs

[3]*Institute of physics, University of Belgrade, P.O. Box 57, 11001, Belgrade, Serbia*

[4]*Moscow State Engineering Physics Institute, Kashirskoe shosse 31, 115409, Moscow, Russia*

[5]*Saint Petersburg State University, St. Petersburg 199034, Russia*

Abstract. Population transfer between quantum levels in atomic and molecular systems with slowly (adiabatically) changing parameters (internuclear distances, intensities of external control fields, etc.) is traditionally described within the formalism of adiabatic or so-called dressed states. In this formalism, the quantum dynamics of a system is determined by the nonadiabatic coupling operator and critically depends on the structural features of the adiabatic energy diagram. In contrast to the case of an avoided crossing where population transfer is localized in Landau-Zener points, the dynamics of mixing permanently degenerate adiabatic states requires studying the entire time interval of the process, thus significantly complicating the theoretical methods used.

Focusing on a tripod excitation scheme, we demonstrate that adiabatic evolution of an N-pod system for a given sequence of laser excitation pulses $\Omega_j(t)$ can be interpreted as Riemannian parallel transport [1] of the state-vector along the surface of a (N-1)-dimensional Bloch sphere. This approach presents a convenient tool for analysis of adiabatic quantum processes.

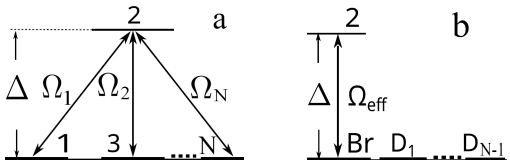

Figure 1: (a) Energy level diagram of a N-pod system and (b) the relevant set of (N-1) degenerate adiabatic D-states.

References

[1] Arnold V. I. 1978, *Mathematical Methods of Classical Mechanics*, Springer New York.

MATTER DISTRIBUTION IN NEARBY GALAXIES

MILENA JOVANOVIĆ

Astronomical Observatory of Belgrade, Volgina 7, 11060 Belgrade, Serbia
E-mail milena@aob.rs

Abstract. In this work we determine the Baryonic Mass Function (BMF) for a representative sample of nearby galaxies for which very detailed observations are available. The galaxy sample is based on the THINGS survey of neutral atomic hydrogen. From these types of observations it is possible to derive the rotation curve, and thus the total dynamical mass up to relatively large radii. Furthermore, in combination with IR observations, we simultaneously fit dynamical mass with observed stellar mass, the neutral gas component, and dark matter (DM) models, following Jovanović 2017. Stellar mass is scaled with the mass-to-light ratio, which is a factor of great interest in this work, and it is either kept free or fixed in the models. The DM component is implemented in the ΛCDM framework, which is a dominant cosmological paradigm entailing cold dark matter CDM and a cosmological constant Λ. Two ΛCDM profiles are used – pseudo-isothermal sphere and Navarro-Frank-White model. Having determined dynamical, stellar, gas, and dark matter mass we construct mass functions for our sample. By adding all contributions from baryonic components in a given mass range we derive the BMF. Additionally, we compare our Galactic environment with a BMF constructed for a larger volume (Papastergis et al. 2012), and discuss the Milky Way's placement on the BMF as well. Surprisingly, we find that while the Milky Way is typical for its immediate environment, it is not at all typical when the larger volume is considered.

References

Jovanović, M: 2017, *MNRAS*, **469**, 3564.
Papastergis, E., Cattaneo, A., Huang, S., Giovanelli, R. & Haynes. M. P.: 2012, *Astrophys. J.*, **759**, 138.

DEVELOPMENT OF A TIME-DOMAIN PIPELINE FOR DETECTING BINARY SUPERMASSIVE BLACK HOLES IN THE UPCOMING LEGACY SURVEY OF SPACE AND TIME (LSST)

V. RADOVIĆ[1] and A. KOVAČEVIĆ[2],D. ILIĆ [1], R. STREET [3] , L. Č. POPOVIĆ, [1,2,4], M. NIKOLIĆ [1]
N. ANDRIĆ MITROVIĆ [1], I. ČVOROVIĆ-HAJDINJAK [1]

[1] *Deaprtment of Astronomy, University of Blegrade, Studentski trg 16, 11000 Belgrade, Serbia*
E–mail rviktor@matf.bg.ac.rs

[2]*Fellow of Chinese Academy of Sciences President's International Fellowship Initiative (PIFI)*

[3] *Las Cumbres Observatory, 6740 Cortona Drive, Suite 102,Goleta, CA 93117, USA*

[4] *Astronomical Observatory, Volgina 7, 11060 Belgrade, Serbia*

Abstract.

The Vera C. Rubin Observatory's Legacy Survey of Space and Time (LSST) will radically change our view of the universe as it will continuously be observing around 18 000 squared degrees of the southern sky. It is expected that LSST will detect an unprecedented sample of Active Galactic Nuclei (AGNs), approximately around 300 million. However, obscuration and host-galaxy dilution will restrain AGN selection so that the final sample will consist of up to 20 million active supermassive black holes. The study of AGN variability is going to be one of the main investigation tasks which will be done by the LSST, as it is expected that millions of well-sampled, multicolor light curves will be available.

The LSST community has accepted two in-kind contributions from the Serbian AGN group (SER-SAG). One of them is a time-domain periodicity mining pipeline, whose primary objective is the detection of oscillation signals from the plasma environment of close binary supermassive black holes in the LSST light curves.

The pipeline will be written as a Python-based, open-source application whose output will be the extracted light curve periodic properties (periodicities, uncertainties, and periods likelihood). Additionally, the program will provide at least four different time-domain algorithms, as well as parametric and non-parametric preprocessing unit of the input LSST light curves. Furthermore, a catalog of robust close binary candidates for the next generation gravitational wave observatories focused on detecting the nano Hertz gravitational waves will be prepared.

Our in-kind contribution began in January 2022, and in this talk, we will present half-yearly updates on its advancement. We will demonstrate the pipeline's initial testing and the plan for future actions. By analyzing massive LSST AGN variability data, we expect to find or usefully constrain the uncertain frequency of close binary SMBHs.

RECENT PROGRESS ON ACTION SPECTROSCOPY OF LOOSELY BOUND HYDROGEN-HELIUM COMPLEXES

SALOMON, T. [1], BRACKERTZ, S. [1], ASVANY, O. [1], SAVIĆ, I. [2], GERLICH, D. [3], and SCHLEMMER, S.[1]

[1] *I. Physikalisches Institut, Universität zu Köln, Zülpicher Str. 77, D-50937 Köln, Germany*
E–mail salomon@ph1.uni-koeln.de

[2] *Department of Physics, Faculty of Sciences, University of Novi Sad, Novi Sad, Serbia*

[3] *Department of Physics, Technische Universität Chemnitz, D-09107 Chemnitz, Germany*

Abstract. Recent progress on action spectroscopy of loosely bound Hydrogen-Helium complexes will be presented on the example of He-H_3^+. The ro-vibrational predissociation spectrum of He-H_3^+ has been recorded via excitation of the ν_2 vibrational mode of the H_3^+ sub-unit in the 22-pole ion trap experiment COLTrap. The spectrum of bare H_3^+ consists of only a few ro-vibrational lines each for the para and ortho nuclear spin configuration, respectively. Instead, the spectrum of the complex is very rich (several hundred lines) even at the low temperature (4 K) of the trap experiment. Part of this complexity is associated with the (almost) free internal rotation of H_3^+. The experimental results are compared to theoretical predictions of ro-vibrational spectra on the basis of *ab initio* calculations of the He-H_3^+ potential energy surface (see Harding et al. 2022). The energy levels result in transitions which agree in many cases with experimental results within a few wavenumbers. In particular the typical band structures of a P- and R-branch associated with an effective diatomic complex seen in the experimental and predicted spectrum help in assigning the rich spectrum. Moreover, an experimental energy term diagram is reconstructed from the observed transitions which can be compared to the rather accurate theoretical predictions. The influence of the Coriolis interaction resulting from the H_3^+ internal rotation in a rotating He-H_3^+ frame will be discussed.

References

Harding, M. E., Lipparini, F., Gauss, J. , Gerlich, D. , Schlemmer , S. ,van der Avoird, A. : 2022, *J. Chem. Phys.*, **156**, 144307.

Publ. Astron. Obs. Belgrade No. 102 (2022), 265 - 268 *Contributed Paper*

WINGED DRAGN SOURCE FROM LEAHY'S ATLAS: 3C 315

A. ARSENIĆ[1], D. BORKA[1], P. JOVANOVIĆ[2] and V. BORKA JOVANOVIĆ[1]

[1] *Department of Theoretical Physics and Condensed Matter Physics (020), Vinča Institute of Nuclear Sciences - National Institute of the Republic of Serbia, University of Belgrade, P.O. Box 522, 11001 Belgrade, Serbia*
E–mail byebyenoob@gmail.com
E–mail dusborka@vinca.rs
E–mail vborka@vinca.rs

[2] *Astronomical Observatory, Volgina 7, P.O. Box 74, 11060 Belgrade, Serbia*
E–mail pjovanovic@aob.rs

Abstract. The goal of this paper is to inspect the flux density as well as the spectral index distribution of 3C 315, an X-shaped radio source with a steep spectrum core. To this end we used publicly available data and images of the source at different frequencies (specifically 1646 MHz and 2695 MHz, as well as Leahy's atlas of double radio-sources). We found that synchrotron radiation is the dominant radiation mechanism over most of the area of 3C 315 with an average spectral index α of 0.956.

1. AN ATLAS OF DRAGNS AND WINGED SOURCE 3C 315

Double Radio Sources Associated with Galactic Nuclei (DRAGNs) are large radio structures which result from processes in Active Galactic Nuclei (AGN) and manifest as double radio sources.

The closest 85 of these DRAGNS from the 3CRR sample were compiled into an atlas (Leahy et al. 2013), along with highly detailed radio images of the sources and basic information concerning each one. The sources in this atlas have been subjects of many studies and plenty of observations at a multitude of frequencies have been made available, making them perfect candidates for the type of research conducted in this paper.

1. 1. 3C 315

The radio source 3C 315 was first listed in the Third Cambridge Catalogue of Radio Sources, where the number after 3C indicates its position in the dataset (cross-identifications: 3C 315; 4C +26.47; PKS 1511+26; B2 1511+26; LQAC 228+026 002). What distinguishes this source and makes it interesting are a few of its characteristics.

Firstly, it is an X-shaped (winged) radio source, meaning it has two sets of double lobes angled with respect to each other. This is a result of a rotation in the axis of the jets, which again might result from reorientations of the supermassive black hole in the center of the host galaxy in the aftermath of black hole merger.

DRAGN 3C 315 does not contain any true hotspots, apart from a weak hotspot in the far-side of the north-western lobe. However as an X-shaped radio galaxy it would still be classified as an FR-II radio galaxy.

The host galaxy of 3C 315 is highly elongated in the north west - south east direction (de Koff el al. 2000) and accompanied by an elliptical galaxy, both of which are located inside a cluster, which allows for the environment to play a role in the evolution of this object.

Lastly, 3C 315 is a steep spectrum core source, which means the core actually consists of a pair of lobes much like the outer kiloparsec sized lobes. These inner lobes have a flux density - frequency relation described by a power law (much like the outer lobes), from where the name is derived.

We used observations of 3C 315 at two different frequencies, 1646 MHz (21 cm) and 2695 MHz (11 cm) (see Alexander & Leahy 1987). In Figure 1 we present the flux density distribution at the two frequencies over the area of the source, where the lower boundaries of the source were determined to be contours $S_{\nu,min} = 0.002$ Jy at 1646 MHz and $S_{\nu,min} = 0.0022$ Jy at 2695 MHz. These lower limits are in agreement with contours drawn at 3.5 times the standard deviation of the background noise.

In Figure 2 the same data is shown, but on a 3D graph for additional clarity. The most distinguishing feature is the bright steep spectrum core in the center of the source and it is surrounded by the relaxed structure of the four lobes surrounding it. In the 2695 MHz image much of the north-east section of the structure is lost in the noise.

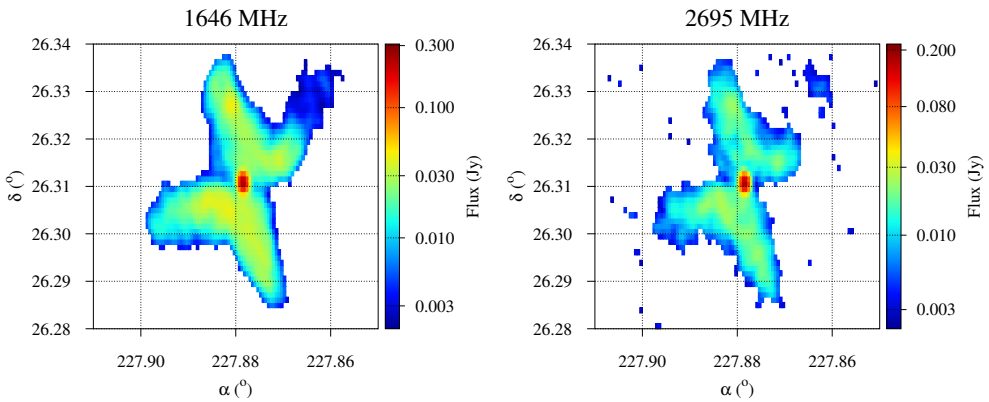

Figure 1: Flux density distribution of 3C 315 at 1646 MHz (left) and 2695 MHz (right). The areas with flux density levels below the lowest contour have been coloured in white.

2. DISTRIBUTION OF SPECTRAL INDICES BETWEEN 1646 AND 2695 MHz

In radio sources, the flux density S_ν dependence on frequency is characterized with the power-law relation $S_\nu \propto \nu^{-\alpha}$, where α is called the 'spectral index' and is easily obtainable by measuring the flux density at different frequencies and taking the negative slope of the above relation, resulting in:

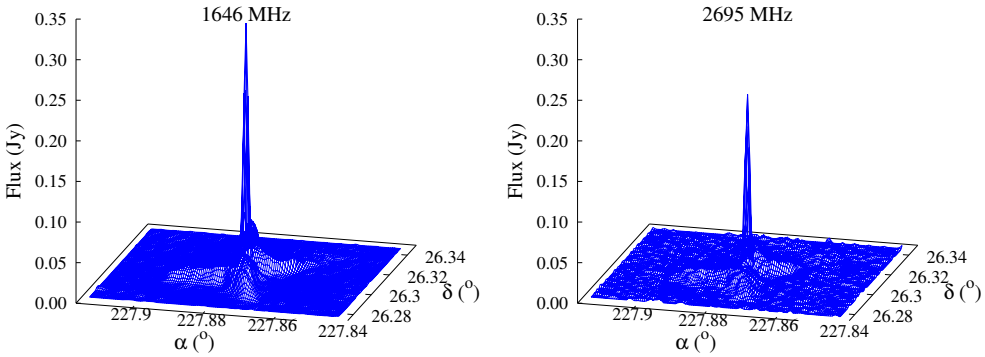

Figure 2: 3D plot of 3C 315 flux density distribution at 1646 MHz (left) and 2695 MHz (right).

$$\alpha = -\frac{\log\left(\frac{S_{\nu_1}}{S_{\nu_2}}\right)}{\log\left(\frac{\nu_1}{\nu_2}\right)}. \tag{1}$$

The spectral index can be used to classify radio sources and understand the origin of radio emission. More specifically, if $\alpha > 0.1$ the emission is non-thermal (synchrotron) in origin, meaning it does not depend on the temperature of the source, and for $\alpha < 0$ it is thermal (depends only on the temperature of the source) in origin.

In Figure 3 we present the spectral index map of 3C 315, derived from the flux density distributions at 1646 and 2695 MHz. The calculation methods we used and developed were first published in Borka (2007), and further elaborated in Borka Jovanović (2012) and Borka Jovanović et al. (2012).

It should be noted this is the first time such a spectral index map (i.e. its distribution over entire source) for this source has been shown. As can be seen, the spectral index is positive (with an average value of 0.956, which aligns with earlier studies such as Northover (1976)) over almost the entirety of the area of 3C 315, indicating that non-thermal emission is the dominant emission mechanism. The only region with a significantly negative spectral index is the far end of the north-east lobe with a mean spectral index of -0.35, which would imply thermal emission as the origin. It should also be mentioned that the spectral index is on average higher along the south west - north east axis, which would confirm these are more aged lobes from previous AGN activity.

3. CONCLUSION

We obtained the flux density of 3C 315 at 1646 MHz (21 cm) and at 2695 MHz (11 cm), and provided the spectral index distribution derived from these two frequencies for the first time. At both frequencies the core dominates the flux density distribution, while the rest of the structure is relaxed with no obvious hotspots. In the spectral index map the difference between the core and lobes is much less pronounced. Synchrotron

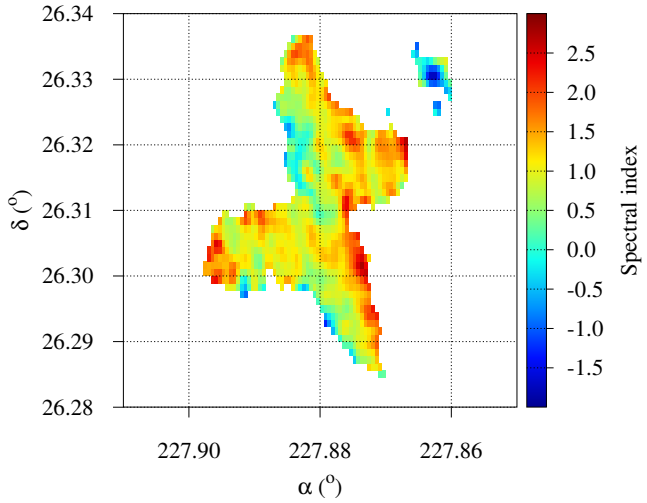

Figure 3: Spectral index map of 3C 315, obtained by combining 1646 MHz and 2695 MHz image data.

radiation is the dominant emission mechanism over the majority of the area of the source with an average spectral index of 0.956, with the exception of the north-eastern section where the spectral index is primarily negative with a mean value of −0.35.

The results of this study will be helpful for understanding the evolutionary process of the 3C 315 radio source.

Acknowledgments. This work is supported by Ministry of Education, Science and Technological Development of the Republic of Serbia. P.J. wishes to acknowledge the support by this Ministry through the project contract No. 451-03-68/2022-14/200002.

References

Alexander, P., Leahy, J.P.: 1987, *Mon. Not. R. Astron. Soc.*, **225**, 1.
Borka, V.: 2007, *Mon. Not. R. Astron. Soc.*, **376**, 634.
Borka Jovanović, V.: 2012, *Publ. Astron. Obs. Belgrade*, **91**, 121.
Borka Jovanović, V., Borka, D., Skeoch, R., Jovanović, P.: 2012, *Publ. Astron. Obs. Belgrade*, **91**, 255.
de Koff, S., Best, P., Baum, S.A., Sparks, W., Röttgering, H., Miley, G., Golombek, D., Macchetto, F., Martel, A.: 2000, *Astrophys. J. Suppl. Series*, **129**, 33.
Leahy, J.P., Pooley, G.G., Riley, J. M.: 1986, *Mon. Not. R. Astron. Soc.*, **222**, 753.
Leahy, J. P., Bridle, A.H., Strom, R.G.: 2013, An Atlas of DRAGNs, An Atlas of DRAGNs - online: http://www.jb.man.ac.uk/atlas/
Northover, K.J.E.: 1976, *Mon. Not. R. Astron. Soc.*, **177**, 307.

Publ. Astron. Obs. Belgrade No. 102 (2022), 269 *Contributed Paper*

HIGHER ORDER NON-LINEAR DUST ION ACOUSTIC (DIA) SOLITARY WAVES IN PLASMAS WITH WEAK RELATIVISTIC EFFECTS IN ELECTRONS AND IONS

S. DAS[1] and D. C. DAS[2]

[1]*Department of Mathematics, Central Institute of Technology Kokrajhar, BTR, Assam 783370, India*
E-mail s.das@cit.ac.in

[2]*Department of Mathematics, Barnagar College, Sorbhog, Barpeta 781317, India*
E-mail ph20maths1002@cit.ac.in

Abstract. In this new investigation of higher order non-linear dust-ion acoustic (DIA) waves with negative dust charges and weakly relativistic ions and electrons in the plasma, only compressive DIA solitons of interesting characters are established through the modified Korteweg-de Vries (mKdV) equation which is derived through standard perturbation technique. It is found that the amplitude of the solitons increases for smaller streaming speed to ions and electrons with the increment of dust to ion density ratio, whereas it is opposite for higher streaming speed of ions and electrons. It is also found that the amplitude of the compressive solitons remains unaffected and linearly increases with the enhancement of dust charges in the plasma. Finally, application of this study to astrophysical and space plasma are discussed briefly.

References

Kalita, B.C., Das, S. : 2014, *Astrophysics and Space Science*, **352**(2), 585.
Mamun, A. A., Cairns, R. A., & Shukla, P. K. : 1996, *Physics of Plasmas*, ***3***(7), 2610.
Mamun, A. A., Mannan, A. : 2021, *Waves in Random and Complex Media*, 1-12.
Kalita, B. C., Bhattacharjee, D. : 2020, *Plasma Physics Reports*, **46**(10), 1004.
Kalita, B.C., Das, S. : 2017, *Journal of Plasma Physics*, **83**(5), 905830502.

Publ. Astron. Obs. Belgrade No. 102 (2022), 271 - 274 *Contributed Paper*

DECOMPOSITION OF THE BLENDED Hα+[N II] LINES IN SPECTRA OF THE ACTIVE GALACTIC NUCLEI TYPE 1.8-2

J. KOVAČEVIĆ-DOJČINOVIĆ[1], I. DOJČINOVIĆ[2], M. LAKIĆEVIĆ[1] and L. Č. POPOVIĆ[1,3]

[1] *Astronomical Observatory, Volgina 7, 11060 Belgrade, Serbia*
E–mail jkovacevic@aob.bg.rs

[2] *Faculty of Physics, University of Belgrade, Studentski Trg 12, Belgrade, Serbia*

[3] *Faculty of Mathematics, University of Belgrade, Studentski Trg 16, Belgrade, Serbia*

Abstract. Here we present the procedure for decomposition of the blended [N II]+Hα wavelength band in spectra of Active Galactic Nuclei (AGN) Type 1.8-2, which could be the sum of the three strong wing components of narrow [N II] and Hα lines, hidden broad Hα component, or all these combined. For establishing this procedure and for setting the line parameter constraints in decomposition, we use the results of the outflow kinematics analysis done on the large AGN sample. We apply this procedure to the sample of 219 AGN spectra with blended [N II]+Hα, to demonstrate the complex and sophisticated decomposition and to check its physical validity.

1. INTRODUCTION

Active galactic nuclei (AGNs) are very strong sources of energy. Enormous amount of energy is radiated during the process of accretion of matter around a super-massive black hole in an AGN center. This process is followed by the gravitationally bounded motion of the emitting gas and appearance of gas outflows. The main characteristics of AGN spectra are strong emission lines. In the case of the AGNs Type 2, only narrow emission lines are present. The core of narrow lines dominantly originates from the gravitationally bounded gas, while outflow emission contributes in the narrow lines wings (Kovačević-Dojčinović et al. 2022, hereafter KD22). In AGNs Type 1.9 and 1.8, beside narrow lines, some broad lines are present, which originate from gravitationally bounded gas closer to the black hole. In the case of the AGNs Type 1.9 it is broad Hα, and in the case of the AGNs Type 1.8, the broad Hα and Hβ lines are present in spectra (see Osterbrock & Ferland 2006).

It seems that distinguishing between AGNs Type 2 or AGNs Type 1.9/1.8 is not always simple, since in some objects typically classified as Type 2 AGNs, [N II]6548, 6583 Å and Hα lines overlap, making the blended [N II]+Hα wavelength band. In these spectra, one cannot be sure without very careful spectroscopic analysis whether the blended [N II]+Hα is the sum of the three strong wing components of narrow

[N II] and Hα lines, or hidden broad Hα component (see Woo et al. 2014, Oh et al. 2015, Eun et al. 2017), or even a mixture of the two.

The correct decomposition of the blended [N II]+Hα wavelength band is important, since in the case of the presence of the broad Hα, its line parameters could be used for estimation of the black hole mass (M_{BH}), following the virial theorem (Greene & Ho 2005). On the other hand, the wing components of the narrow lines originate from the outflowing gas, which is not gravitationally bounded (KD22) and potential misinterpretation of the sum of the three wing components of the narrow [N II] and Hα as broad Hα could lead to fake estimation of M_{BH}.

In this work we will present the procedure for decomposition of the blended [N II]+Hα in spectra of Type 1.8-2 AGNs. The procedure is established using the outcomes of the outflow kinematics investigation on the large sample of AGN spectra, which is described in KD22.

2. THE SAMPLE AND ANALYSIS

For this research we used the sample of AGN spectra obtained from Sloan Digital Sky Survey (SDSS) Data Release 14. The spectra were chosen to have high signal-to-noise ratio and presence of the several narrow emission lines (see details in KD22). Using these selection criteria, we obtained 577 predominantly Type 2 AGNs, but also with the possible presence of Type 1.9 and Type 1.8 AGN spectra. Afterwards, we kept in the sample only the objects with blended [N II]+Hα wavelength band, which makes $\sim$40% of initial sample, i.e. 219 objects.

In these objects, the spectra were corrected for Galactic reddening, redshift and host-galaxy contribution (see KD22). Then, [O III]4959, 5007 Å, Hβ and [S II] narrow lines were fitted with two component Gaussian model - one Gaussian which fits the core of the line and the other which fits the wings of the line and represents the outflow emission. In this way, we got the data about the outflow contribution in the other lines in spectra, which will be used in [N II]+Hα decomposition procedure.

3. PROCEDURE FOR DECOMPOSITION OF THE BLENDED Hα+[N II] lines

KD22 analyzed the outflow kinematics following several narrow emission lines ([O III], Hβ, Hα, [N II] and [S II]) in AGN sample where [N II] and Hα lines do not overlap, i.e. could be fitted independently, without any fitting constrains. They found that: shifts and widths of wing components (which represent the outflow contribution) correlate between all analyzed emission lines, specially between Hα and [N II] lines, where they follow one-to-one relationship. The shifts of [S II] wing components, are also in strong correlation and follow one-to-one relationship with shifts of the Hα and [N II] wing components, but the wing component widths are sistemically smaller. On the other hand, the widths and the shifts of the [O III] wing components are sistemically larger than the same of the Hα and [N II] lines.

These results imply that the outflow kinematics systemically affects the line profiles in AGN spectra, but it reflects with different strength in profiles of different lines, and therefore multiple lines should be analyzed as one system in order to achieve physically correct spectral decomposition of blended [N II]+Hα wavelength band. In accordance with this findings, following procedure is established.

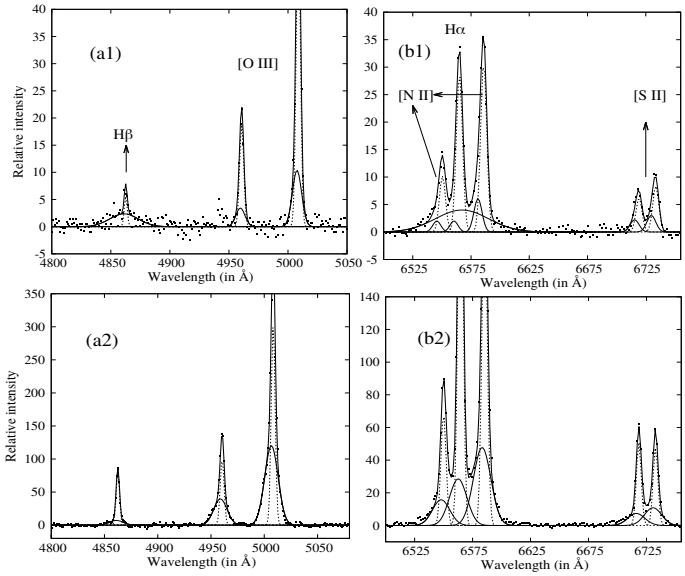

Figure 1: Example of decomposition of blended [N II]+Hα as mixture of the wing components and broad Hα (a1, b1) and as the sum of the three strong wing components (a2, b2). The wing components and broad Hα are denoted with solid line, and core components with dotted line.

In the case if there is no flux that extends significantly out of the [N II] doublet, i.e. the presence of the broad Hα in the blended [N II]+Hα wavelength band is uncertain, we propose to:

(1) Check if the broad Hβ is present. If it is present in the spectrum, the broad Hα component should be included as well. Hα and [N II] wing components should be additionally included (with reduced fitting parameters as defined below) if obvious asymmetry is present in narrow lines.

(2) If [O III] lines have no wing components detected, or if they have weak and narrow wing components (their width is not much broader than the width of the [O III] core), that implies that the broad Hα dominantly fits blended [N II]+Hα, and Hα and [N II] wing components should be included only if needed to fit the shape of the narrow lines.

(3) Contrary, if the [O III] lines have strong and broad wing components, then we expect that the sum of the three wing components of [N II] and Hα dominates in the blended region. Therefore, the blended [N II]+Hα should be fitted with the three wing components using the following fitting constraints.

shift Hα wing = shift [N II] wing = shift [S II] wing.

width Hα wing = width [N II] wing.

If there are no [S II] wing components detected, then the shift of Hα and [N II] wing components is one free parameter. Following empirical results from KD22, it is recommended to keep Hα and [N II] wing component widths to do not exceed much the width of the [O III] wing component. If the fit with three wing components, limited with the mentioned fitting constraints, cannot accurately describe the shape

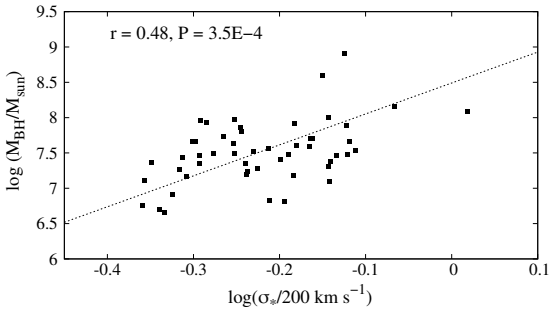

Figure 2: M_{BH} estimated using broad Hα vs. stellar velocity dispersion σ_*. σ_* - M_{BH} relation of Kormendy & Ho (2013) is denoted with dashed line.

of the complex [N II]+Hα wavelength band, then the broad Hα should be included.

The objects where the presence of the broad Hα is certain (the flux extend distinctly from both sides of the [N II] doublet) should be fitted with one broad component, and the wing components should only be included if narrow lines show asymmetry. In the case where they are needed, the wing components should be fitted with parameter constraints as defined above.

4. RESULTS OF THE DECOMPOSITION

By applying this procedure of decomposition in our sample of 219 AGNs with blended [N II]+Hα, we found that 55 objects ($\sim$25% of sample) belong to the Type 1.9/1.8 AGNs, i.e. they have hidden the broad Hα line in blended [N II]+Hα. The rest of objects are Type 2 AGNs with strong wing components whose sum could be misinterpreted as broad Hα, as also noticed in Woo et al. (2014) and Eun et al. (2017). The detected broad Hα lines have Full Widths at Half Maximum (FWHMs) in the range of 2050-10600 km s^{-1}. The examples of decomposition are shown in Figure 1.

In order to check validity of [N II]+Hα decomposition in 55 objects where the broad Hα is detected, we estimated M_{BH} using the parameters of the broad Hα line (see Greene & Ho 2005) and we compared the obtained values with σ_* - M_{BH} relation (see Kormendy & Ho 2013). We found that estimated masses follow well σ_* - M_{BH} relation with scatter up to $\sim$0.5 dex (see Figure 2), while the correlation coefficient between estimated M_{BH} and σ_* is r=0.48, P=3.5E-4. These results imply that presented procedure gives the physically correct decomposition of the blended [N II]+Hα wavelength band.

References

Eun, D., Woo, J.-H. & Bae, H.-J.: 2017, *ApJ*, **842**, 5
Greene, J. E. & Ho, L. C.: 2005, *ApJ*, **630**, 122.
Kovačević-Dojčinović, J., Dojčinović, I., Lakićević, M., Popović, L.Č.:2022, *A&A*, **659**, 130.
Kormendy, J., Ho, L.C.: 2013, *ARA&A*, **51**, 511.
Oh, K., Yi, S.K., Schawinski, K., Koss, M., Trakhtenbrot, B., Soto, K.: 2015, *ApJS*, **219**, 10
Osterbrock, D., Ferland, G., 2006, Astrophysics of gaseous nebulae and active galactic nuclei, Sausalito, CA: University Science Book
Woo, J.-H., Kim, J.-G., Park, D., Bae, H.-J., et al.: 2014, *JKAS*, **47**, 167.

THE EFFECT OF NEGATIVE IONS ON WEIBEL INSTABILITY IN THE PRESENCE OF LARGE AMPLITUDE ELECTROSTATIC WAVES

AMIT KUMAR[1] and JYOTSNA SHARMA[1*]

[1]*Department of Physics, Amity School of Applied Sciences, Amity University Haryana, Manesar, Gurugram-122051, India*
Email[1] ak8689049@gmail.com
Email[1]* amit.kumar9@s.amity.edu

Abstract. In the present manuscript, the effect of a large amplitude Langmuir wave on the Weibel instability in the presence of negative ions with an electron beam is studied. The electromagnetic (EM) perturbation couples with the Langmuir wave and give rise two Langmuir side bands and the Langmuir wave enhanced the growth rate over its linear value. The growth rate scales as one half power of the beam velocity and in the presence of negative ions the growth rate is calculated. Here, the author observed that the growth rate of Weibel instability strongly depends on plasma frequency of negative ions. Our theoretical work may find applications in the astrophysical plasmas, laboratory plasmas, laser produced plasmas, microwave breakdown of dilute gases, energy transportation etc. Our work can be used for generation of magnetic field in space, supernovas and galactic cosmic rays also.

References

Gruzinov, A. and E. Waxman, E.: 1999, Astrophys. J. **511,** 852.
Medvedev, M. V., and Loeb, A.: 1999, Astrophys. J. **526,** 697.
Schlickeiser, R. and P. K. Shukla, P. K.: 2003, Astrophys. J. **599,** L57.
Medvedev, M. V., Silva, L.O., Fiore, M., Fonseca, R.A., and Mori, W.B.: 2004, Astrophys. J. **37,** 533.
Medvedev, M. V., Silva, L.O., Kamionkowski, M.: 2006, Astrophys. J. **642,** L1.
Weibel, E.S.: 1959, Phys. Rev. Lett. **2,** 83.
Nerush, E.N., Serebryakov, D. A. and Kostyukov, I. Y.: 2017, Astrophys. J. **851,** 129.
Pegoraro, F., Bulanov, S.V., Califano, F. and Lontano, M.: 1996, Physica Scripta. **T63,** 262.
Califano, F., Pegoraro, F., and Bulanov, S.V.: 1997, Phys. Rev. E. **56,** 963-969.
Califano, F., Pegoraro, F., and Bulanov, S.V., and Mangeney, A.:1998, Phys. Rev. E. **57,** 7048-7059.

Publ. Astron. Obs. Belgrade No. 102 (2022), 277 - 280 *Contributed Paper*

THE CHEMI-RECOMBINATION PROCESSES IN ALKALI-METAL ASTROPHYSICAL AND LOW-TEMPERATURE LABORATORY PLASMAS: RATE COEFFICIENTS

V. A. SREĆKOVIĆ[1], L. M. IGNJATOVIĆ[2], V. VUJČIĆ[2] and M.S. DIMITRIJEVIĆ[2,3]

[1]*Institute of Physics Belgrade, University of Belgrade, Pregrevica 118, 11080 Belgrade, Serbia*
E-mail vlada@ipb.ac.rs

[2]*Astronomical Observatory, Volgina 7, 11060 Belgrade, Serbia*
E-mail mdimitrijevic@aob.rs

[3]*Observatoire de Paris, PSL Université, CNRS, Sorbonne Université, F-92195 Meudon, France*

Abstract. In this contribution, some collisional processes i.e. chemi-recombination processes in alkali-metal low-temperature plasmas are investigated. The spectral rate coefficients which involve alkali metals, as well as corresponding data on species, are calculated as a function of quantum numbers and temperatures. The presented results can be of interest for laboratory plasmas as well as for the research of chemistry of different stellar objects with various astrophysical plasmas.

1. INTRODUCTION

Collisional processes which include atoms and molecules in geo-cosmical plasmas constantly attract the attention of scientists (see e.g. Sreckovic et al. 2020; Klyucharev et al. 2007; Ignjatovic et al. 2020). Among these processes, those which produce highly excited Rydberg atoms are of particular interest (Gnedin et al. 2009; Mihajlov et al. 2011; Sreckovic et al. 2018a). Primarily this can be attributed to a group of chemi-recombination (CR) processes (Mihajlov et al. 2003, Sreckovic et al. 2018b). In a series of papers of Mihajlov and coworkers' CR processes involving hydrogen and helium have been studied from the point of view of their effect on the optical (spectral line shapes) and kinetic properties of weakly ionized laboratory and astrophysical plasmas. This contribution is a continuation of this research.

Here we will consider the following chemi-recombination processes,

$$A_2^+ + e \Rightarrow A^*(n) + A \qquad (1a)$$
$$A + A^+ + e \Rightarrow A^*(n) + A \qquad (1b)$$

where A and A^+ are alkali (Li or Na) atoms and ions in their ground states, and A_2^+ is molecular-ion in the ground electronic state.

The importance of chemi-recombination (eqs. (1a)– (1b)) and chemi-ionization processes in a geo-cosmic plasma, is determined by comparing corresponding fluxes. This is performed under the standard assumption that in photosphere plasmas $Te = Ta = T$, where Te and Ta are the electron and atom temperatures and T is their common value. Under this assumption, the deviation from LTE in a given plasma is manifested through the departure of the excited atom state populations from Boltzman's distribution. Therefore, it is necessary to take into account all processes which can influence the excited atom state populations, particularly ionization/recombination processes.

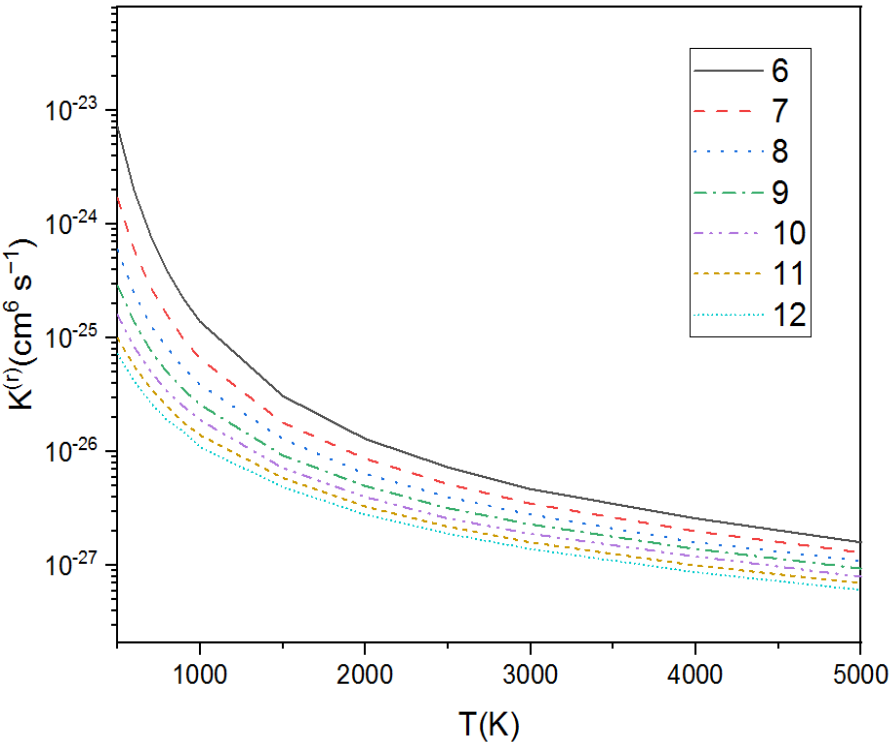

Figure 1: Total chemi-recombination rate coefficients for processes (1) for the case A=Li, with 500 K < T < 5000 K and for principal quantum numbers 6 < n < 12.

Total chemi-recombination rate coefficients can be defined as the sum of the partial ones describing both processes (1a) and (1b):

$$K_r^{(tot)} = K_r^{(a)} + K_r^{(b)} \qquad (2)$$

For details see e.g. Mihajlov et al. 2003, 2011. The rate coefficients for the chemi-recombination (CR) processes are calculated for a wide region of temperatures and the principal quantum numbers. The obtained data are needed for modeling and research of cool stars, lithium stars, sodium clouds around Io cometary tails, and primordial gas containing Li atoms and ions (Gnedin et al., 2009), etc.

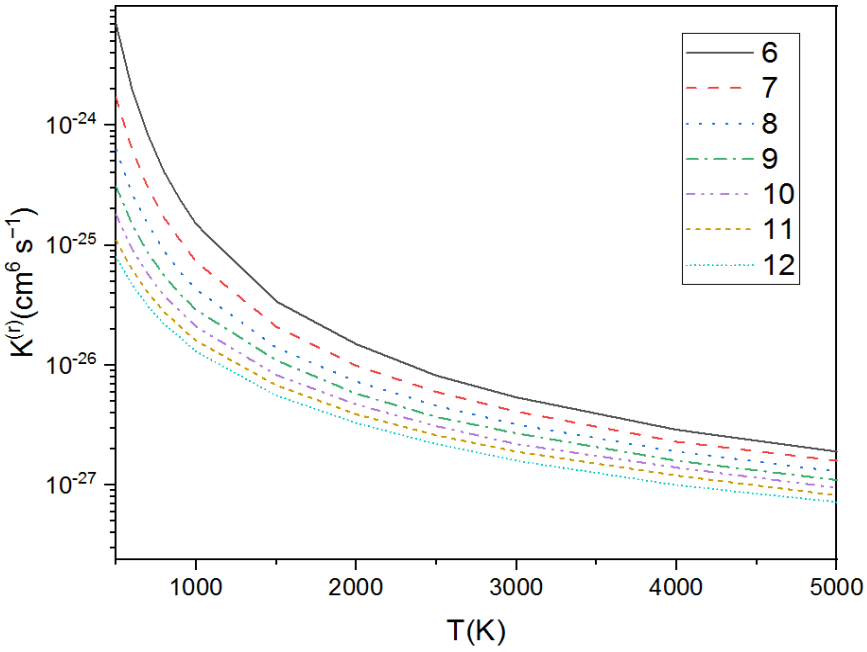

Figure 2: Total chemi-recombination rate coefficients for processes (1) for the case *A*=Na, with 500 K < T < 5000 K and for principal quantum numbers 6 < n < 12.

2. RESULTS AND APPLICATION

We give the total rate coefficients for CR processes for sodium and lithium cases (*A*=Na, Li) for principal quantum numbers $6 \leq n \leq 12$ in a wide region of temperatures $500\ K \leq T \leq 5000\ K$.

The total CR rate coefficients $K_r^{(tot)}(n,T)$ are shown in Figs. 1 and 2 for the cases of Li and Na. The results presented here show the influence of chemi-recombination processes (1) in populating the highly excited atoms in non-equilibrium alkali plasmas in broad ranges of parameters. It can be observed that the total rate coefficient for all cases decreases with increasing temperature and the coefficient decreases with increasing principal quantum numbers.

3. SUMMARY

The results presented here show the influence of chemi-recombination processes (1) in populating the highly excited atoms in non-equilibrium alkali plasmas in broad ranges of parameters. Therefore, these processes have to be included in all collisional radiative models dealing with such plasmas. Generally, the obtained results have potential astrophysical use in the improvement of chemistry and modeling of different layers of weakly ionized geo-cosmical plasmas of the atmospheres of various stars and cosmic objects (Sreckovic et al. 2014; Mihajlov 2011, Sreckovic et al. 2020). The results are also important in theoretical and laboratory spectroscopic plasmas research, industry, and technology application.

Acknowledgments

The authors acknowledge the support from the Institute of Physics, Belgrade, which was made possible by grants from the Ministry of Education, Science and Technological Development of the Republic of Serbia (including contract no 451-03-68/2022-14/200287)

References

Gnedin, Y. N., Mihajlov, A. A., Ignjatovic, L. M., et al.L 2009. *New. Astr. Rev.*, **53**, 259

Ignjatović, L.M.; Srećković, V.; Dimitrijević, M.: 2020, *Contrib. Astron. Obs. Skaln. Pleso*, **50**, 187.

Mihajlov, A. A., Ignjatović, L. M., Dimitrijević, M. S., & Djurić, Z.: 2003, *Astrophys. J., Suppl. Ser.*, **147**(2), 369.

Mihajlov, A. A., Ignjatović, L. M., Srećković, V. A., et al.: 2011, *Astrophys. J., Suppl. Ser.*, **193**(1), 2.

Klyucharev, A. N., Bezuglov, N. N., Matveev, A. A., et al.: 2007, *New. Astr. Rev.*, **51**, 547.

Srećković, V.A.; Mihajlov, A.A.; Ignjatović, L.M.; Dimitrijević, M.S.: 2014, *Adv. Space Res.*, **54**, 1264.

Srećković, V. A., Dimitrijević, M. S., Ignjatović, L. M., et al.: 2018a, *Galaxies*, **6**(3), 72.

Srećković, V. A., Dimitrijević M. S. and Bezuglov N. N.: 2018b, *Atoms* **7**.1, 3.

Srećković, V. A., Ignjatović, L. M., & Dimitrijević, M. S.: 2020, *Molecules*, **26**(1), 151.

The Workshop on X-ray and VUV Interaction with Biomolecules in Gas Phase (XiBiGP)

Publ. Astron. Obs. Belgrade No. 102 (2022), 283

PHOTOFRAGMENTATION OF THE RADIATION THERAPY ENHANCERS: CAN WE MAKE BETTER ONES?

M. BERHOLTS[1], P. H. W. SVENSSON[2], L. PIHLAVA[3], A. VLADYKA[3], J. NISKANEN[3], I. UNGER[2], K. KOOSER[1], C. STRÅHLMAN[4], P. ENG-JOHNSSON[5], L. SCHWOB[6], A.-L. VIELI[2], O. BJÖRNEHOLM[2], C. CALEMAN[2,7], R. LINDBLAD[8] and E. KUKK[3]

[1]*Department of Physics, Tartu University, EST-50411 Tartu, Estonia*
E-mail: marta.berholts@gmail.com

[2]*Department of Physics and Astronomy, Uppsala University, SE-75120 Uppsala, Sweden*

[3]*Department of Physics and Astronomy, Turku University, FI-20014 Turku, Finland*

[4]*Department of Materials Science and Applied Mathematics, Malmö University, SE-20506 Malmö, Sweden*

[5]*Department of Physics, Lund University, SE-22100 Lund, Sweden*

[6]*Deutsches Elektronen-Synchrotron DESY, DE-22607 Hamburg, Germany*

[7]*Center for Free-Electron Laser Science, DESY, DE-22607 Hamburg, Germany*

[8]*Department of Chemistry-Ångström, Uppsala University, SE-75121 Uppsala, Sweden*

Abstract. In this progress report, we show the results of two mass spectrometric experiments performed on a set of nitroimidazole-based radiosensitizers, medications that enhance radiation damage to the cancerous cells (Itälä et al. 2019 and 2020, Rockwell et al. 2009). We have incorporated a heavy element (Br and/or I) into the structure to introduce an additional function to the radiosensitizer. The idea here is that heavy element absorption hotspot locally enhances the radiation dose by generating secondary X-rays, photo- and Auger electrons, while the other part of the molecule produces sensitization-relevant species upon fragmentation (radicals originating from nitro group). Potentially it could increase the positive outcome from the radiation therapy, minimizing negative effects on normal cells. It is often difficult to interpret the results of clinical trials in the context of fundamental physical and chemical processes. Therefore, fundamental investigations on isolated molecules are crucial to determine directly the relationship between the structure of the radiosensitizer and its fragmentation outcome after X-rays absorption. We compare the results with non-halogenated references to evaluate the differences in the fragmentation dynamics using such methods as photoelectron-photoion-photoion coincidence (performed at MAX IV, FinEstBeAMS beamline) and near edge X-ray absorption mass spectrometry (performed at BESSY II, UE52_PGM beamline).

References

Itälä, E.; Myllynen, H.; Niskanen, J.; González-Vázquez, J.; Wang, Y.; Ha, D. T.; Denifl, S.; Kukk, E. 2019, *J. Phys. Chem. A*, **123 (14)**, 3074–3079.

Itälä, E.; Niskanen, J.; Pihlava, L.; Kukk, E. 2020, *J. Phys. Chem. A*, **124 (27)**, 5555–5562.

Rockwell, S.; Dobrucki, I. T.; Kim, E. Y.; Marrison, S. T.; Vu, V. T. 2009, *Curr. Mol. Med.*, **9 (4)**, 442–458.

Publ. Astron. Obs. Belgrade No. 102 (2022), 284 - 285

THE "LEGO BRICKS" OF LIFE: A GAS-PHASE STUDY OF DIPEPTIDES

L. CARLINI, P. BOLOGNESI, J. CHIARINELLI, G. MATTIOLI, A. CASAVOLA, M. C. CASTROVILLI, V. VALENTINI, A. DE STEFANIS, E. M. BAUER, E. MOLTENI, D. SANGALLI and L. AVALDI

Istituto di Struttura della Materia, ISM-CNR, 00015 Monterotondo Scalo, Roma, Italy

Abstract. Linear (*ℓ*-) and cyclo (*c*-) dipeptides, obtained by linking two aminoacids via one/two peptide bonds, are the smallest and simplest peptides present in nature. They are one of the most important classes of biomolecules active in many relevant biological processes. Their use in the development of therapeutics[1] as well as for innovative preparation methods of nanomaterials[2] have made these compounds the object of widespread interest since the 50s of the previous century. It has also been proposed that *c*-dipeptides may have played a role in the emergence of life in the early universe[3] thanks to both their capability to withstand radiation and to produce crucial intermediates for the development of peptide chains[4]. Moreover, *ℓ*- and *c*-dipeptides containing an aromatic aminoacid in the side chain are of interest for the study of the dynamics involving energy and charge transfers[5] in bio-systems.

In this talk, our results on the study of *ℓ*- and *c*-dipeptides (*ℓ*-PheAla, *c*-GlyPhe, *c*-TrpTrp and *c*-TrpTyr) by mass spectrometry and photoelectron-photoion coincidence experiments (PEPICO) in the gas-phase will be presented.

Combining several different experimental techniques (mass spectrometry, infrared and Raman spectroscopy, and thermogravimetric analysis) with tight-binding and ab initio simulations, we provided evidence that the linear PheAla dipeptide can turn into the cyclic one via 'intramolecular' peptide bond formation accompanied by water release[6] (Figure 1, left panel). This irreversible cyclization mechanism, catalyzed by water and driven by temperature, occurs in the condensed phase. This process can be considered as a very efficient strategy to improve the dipeptide stability by turning the comparatively fragile *ℓ*-structure into the robust and more stable cyclic one.

In the case of *c*-GlyPhe, *c*-TrpTrp and *c*-TrpTyr, valence photoemission (PES) measurements and a systematic ab-initio study implemented with different computational tools has allowed a detailed investigation of the electronic energy levels of themolecules[7]. Then PEPICO experiments have been performed at the CIPO beamline of Elettra synchrotron radiation facility. The correlation between the electronic distribution of the molecular orbitals and the fragments yields has been investigated by comparing the PES spectrum and the PEPICO relative ions yields (Figure

2, right panel). The calculated branching ratios of the main fragments provided information on the fragmentation pathway channels versus binding energy (BE) as well as approximate onset for the production of specific fragments and correlation among the different channels.

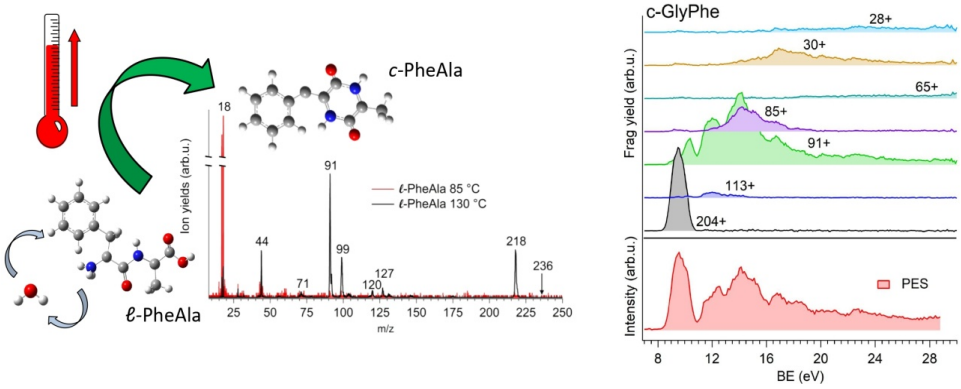

Figure 1: *Left panel* - Photoionization mass spectra of ℓ-PheAla measured at 85 (red line) and 130 °C (black line) with 21.22 eV incident radiation. A non-linear emission of water, with a dramatic increase at about 85 °C lasting several hours has been detected. At 130 °C the mass spectrum is dominated by the m/z fragments assigned to the *c*-structure. The linear parent (m/z=236) has never been observed throughout the heat-up of the sample. *Right panel* - The state-selected fragmentation of *c*-GlyPhe molecule studied by PEPICO experiments in the BE range from the ionization threshold up to 30 eV. In the bottom panel the the PES spectrum is shown while in the other panels the PEPICO relative yields for several m/z fragments are reported.

Acknowledgments

COST (European Cooperation in Science and Technology) Action CA18212−Molecular Dynamics in the GAS phase (MD-GAS) and PRIN Project 20173B72NB "Predicting and controlling the fate of biomolecules driven by extremeultraviolet radiation".

References

[1] Zorzi, A. et all., *Curr. Opin. Chem. Biol.* 2017, **38**, 24−29.
[2] Ziganshin, M. A. et all., *Phys. Chem. Chem. Phys.* 2017, **19**, 13788−13797.
[3] Ying, J. Et all., *Sci. Rep.* 2018, **8**, 936.
[4] Barreiro-Lage, D. et all.,*J. Phys. Chem. Lett.* 2021, **12**, 7379−7386.
[5] R. Weinkauf et al, *J. Phys. Chem.* 1995, **99**, 11255-11265.
[6] Carlini, L. et all., *J. Phys. Chem. B* 2022, **126**, 2968−2978.
[7] Molteni E. et all., *Phys. Chem. Chem. Phys.*, 2021, **23**, 26793.

Publ. Astron. Obs. Belgrade No. 102 (2022), 286

ULTRAFAST DYNAMICS OF PHOTO-EXCITED MOLECULES AT FERMI FREE ELECTRON LASER

M. DI FRAIA

Elettra-Sincrotrone Trieste S.C.p.A.
E-mail michele.difraia@elettra.eu

Abstract. Static and time-resolved studies of atomic and molecular targets by means of VUV and soft X-ray spectroscopy have greatly benefited from the advent of new experimental methods and from the interplay between complementary light sources. Spectral quality, tunability, low timing jitter between pump-and-probe pulses, are ideal specifications for light sources devoted to this class of experiments. These specifications are met by the seeded Free Electron Laser FERMI in Trieste [Allaria et al. 2015, Finetti et al. 2017]. FELs allow femtosecond time-resolved experiments with a much higher brightness than HHG sources, opening new opportunities for pump-and-probe experiments especially at higher photon energies. In the framework of atomic and molecular dynamics studies the Low Density Matter beamline [Lyamayev et al. 2013] of FERMI, celebrating 10 years of operation, offers a variety of consolidated spectroscopic techniques. Recent highlights will be presented in this progress report: the complete evolution of the photoinduced ring-opening reaction occurring in thiophenone molecules [Pathak et al. 2020]; how the synergy between experimental results and advanced quantum chemistry calculations allow one to go beyond the usually accepted picture of the ring-opening reaction of 1,3-Cyclohexadiene [Travnikova et al. 2022]; time-resolved photoelectron circular dichroism (TR-PECD) spectroscopy at the carbon edge on fenchone molecules [Facciala' et al. 2022].
The combination of above achievements with recent machine and endstation upgrades expands the possibilities for studying the dynamics of small biological molecules.
The results of these studies originate from the joint effort of many international laboratories and of a large number of researchers, whose work is gratefully acknowledged**.**

References

Allaria E. et al. : 2015 *J. Synchrotron Rad*, **22**, 485–49.
Finetti, P. et al. : 2017, *Phys. Rev. X*, **7**, 021043.
Lyamayev, V. et al. : 2013, *J. Phys. B*, **46**, 164007.
Pathak S. et al. : 2020, *Nat. Chem.*, **12**, 795–800.
Travnikova O. et al. : 2022, *Submitted*.
Facciala' D. et al. : 2022, *Submitted*.

Publ. Astron. Obs. Belgrade No. 102 (2022), 287

EUROPEAN SYNCHROTRON AND FEL USER ORGANISATION: CURRENT CHALLENGES AND PROSPECTS (COST ACTIONS)

BRATISLAV P. MARINKOVIĆ

Institute of Physics Belgrade, University of Belgrade, Pregrevica 118, 11080 Belgrade, Republic of Serbia
E-mail Bratislav.marinkovic@ipb.ac.rs

Abstract. European Synchrotron and Free Electron Laser User Organisation (ESUO) represents all users of synchrotron and free electron-laser facilities in Europe, see ESUO webpage. At present, users from 31 European member states and European associated countries are represented by ESUO national delegates, among them is also a Serbian delegate who has been appointed by Optical Society of Serbia (OSS). In December 2018, the ESUO-Serbia has been established as a section of a National Organization of OSS. One of the major achievements of the ESUO-Serbia was an organization of the First ESUO Regional Workshop as a satellite meeting of the international conference *Photonica* held in Belgrade on 28th August 2019. Current challenges (e.g. the absence of Trans-National Access) and prospects of the ESUO (e.g. ESUO as a legal entity) will be discussed at this workshops, that is going to happened just after the 18th General Assembly of ESUO in SOLEIL synchrotron in August 2022. Also, some of the COST Actions related to the networking of a research preferentially done at synchrotron facilities will be reviewed.

Figure 1: ESUO official standard logo.

References

ESUO webpage: https://www.esuo.eu/
ESUO-Serbia webpage: http://uranus.ipb.ac.rs/~esuo-serbia/

Publ. Astron. Obs. Belgrade No. 102 (2022), 288

SURFACE PROPENSITY OF SMALL ORGANIC BIOMOLECULES IN VAPOUR-WATER INTERFACE BY XPS

ALEXANDRA MOCELLIN[1],

MARINHO RRT[1], BJORNEHOLM O[2], NAVES DE BRITO A[3]

[1]*University of Brasilia, UnB Brasília- DF Brazil*
alexandra.mocellin@gmail.com

[2]*Upssala University, UU, Upssala Sweden*

[3] *Campinas University, UNICAMP, Campinas SP Brazil*

Abstract. Aqueous interfaces are crucial in, e.g., environmental sciences, biology, and technology. One example of this is biointerfaces, i.e., interfaces between cells, biological tissue or organic material with another biomaterial or inorganic/organic material. The structure and properties of such biointerfaces depend on the interactions between biomolecules and surfaces. A second example is the liquid−vapor interface of water, which is of tremendous importance in the atmosphere. One powerful tool to study the surface propensity of solvated molecules is X-ray photoelectron spectroscopy (XPS). This probe combines the chemical selectivity and surface sensitivity. For amino acids, XPS has previously been applied to aqueous solutions of glycine, revealing a high selectivity to the different pH-dependent charge states, see Otosson et al. 2011. Recently, it has also been shown that cysteine, in which −SH constitutes a third titratable group, exhibits different protonation states at the aqueous surface as compared to the bulk, see da Silva 2015. In this presentation, I will show XPS studies in aqueous solutions of amino acids, with different size chains and compositions, see Mocellin et al. 2017. Moreover, as the vapor phase outside the liquid effectively acts as a very hydrophobic surface, the water-vapor interface is a useful model for hydrophobic interfaces, and the results may therefore also have significance for hydrophobic biointerfaces.

References

da Silva, A. M.; Mocellin, A; et al: 2015 *J. Phys. Chem. Lett.,* **6**, 807.
Mocellin, A; Gomes, AHA; et al., 2017 *J. Phys. Chem. B,* **121**, 4220.
Ottosson, N.; Børve, K. J.; et al. 2011 *J. Am. Chem. Soc*., **133**, 3120.

AUTHORS' INDEX

SPIG 2022 PROGRAMME

Belgrade, Serbia, September 05 – 09, 2022

All indicated times are given in the Central European Summer Time (CEST) zone.

Monday 5th September 2022 **SPIG 2022 (day 1)**	
	XiBiGP Workshop
09:00-09:30	***Registration***
09:30-09:40	**Hall B: Opening and Introduction** Aleksandar Milosavljević and Christophe Nicolas (SOLEIL)
09:40-10:00	*European Synchrotron and FEL User Organisation: Current Challenges and Prospects (COST Actions)* **Bratislav Marinković**, Institute of Physics Belgrade, Serbia **[Regular]**
	***Session 1, Hall B**, Chair: Aleksandar Milosavljević*
10:00-10:20	*Ultrafast dynamics of photo-excited molecules at FERMI Free Electron Laser* **Michele di Fraia,** Elettra-Sincrotrone Trieste, Italy **[Virtual]**
10:20-10:40	*UV-induced processes in DNA* **Lara Martínez-Fernandez,** Universidad Autónoma de Madrid, Spain **[Virtual]**
10:40-11:00	*The 'LEGO bricks' of life: a gas-phase study of dipeptides* **Laura Carlini,** CNR-ISM, Italy **[Virtual]**
11:00-11:20	*Photofragmentation of the radiation therapy enhancers: can we make better ones?* **Marta Berholts,** Tartu University, Estonia **[Virtual]**
11:20-12:00	***Coffee break***
	***Session 2, Hall B**, Chair: Sergio Diaz-Tendero*
12:00-12:30	*Plasmon-induced chemical reactions on noble metal nanoparticles studied by synchrotron XPS and surface-enhanced Raman scattering* **Ilko Bald,** University of Potsdam, Germany **[Virtual]**
12:30-12:50	*Valence band structure of isolated biomolecule-functionalized gold nanoparticles* **Jelena Pajović,** Faculty of Physics, University of Belgrade, Serbia **[Regular]**
12:50-13:10	*Determination of the Adenine-Thymine binding energy* **Sebastian Hartweg,** Synchrotron SOLEIL, France **[Virtual]**
13:10-13:30	*In the search of peptide prebiotic building blocks: Studying the fragmentation of photoionized Diketopiperazines* **Darío Barreiro-Lage,** Universidad Autónoma de Madrid, Spain **[Regular]**
13:30-15:30	***Lunch break***
	***Session 3, Hall B**, Chair: Lucas Schwob*
15:30-16:00	*VUV and soft X-ray interactions with trapped biomolecular ions* **Thomas Schlathölter,** University of Groningen, Netherlands **[TBC]**
16:00-16:20	*Covalent bond formation within clusters: a pathway for the synthesis of complex molecules in the interstellar medium* **Yoni Toker,** Bar Ilan University, Israel **[Regular]**
16:20-16:40	*To be announced* **Kaja Schubert,** DESY, Germany **[Virtual]**
16:40-17:00	*X-ray absorption spectroscopy and mass spectrometry of protonated ATP molecule* **Aleksandar Milosavljevic,** Synchrotron SOLEIL, France **[Regular]**
17:00-17:30	***Coffee break***
	***Session 4, Hall B**, Chair: Christophe Nicolas*
17:30-18:00	*An overview on the recent liquid-jet PES developments* **Bernd Winter,** Fritz Haber Institute of the Max Planck Society, Germany **[Virtual]**

18:00-18:20	*Surface propensity of small organic biomolecules in vapour-water interface by XPS* **Alexandra Mocellin,** Institute of Physics, Brasil **[Virtual]**
18:20-18:40	*Electronic structure and solvation effects from core and valence photoelectron spectroscopy of serum albumin* **Jean Philippe Renault,** University Paris Saclay, France **[Virtual]**
18:40-19:00	*First (e,e) coincidence measurements at PLEIADES beamline on solvated benzoate in water using a new magnetic bottle time-of-flight spectrometer* **Jerome Palaudoux ,** Sorbonne Université, France **[Virtual]**
19:30-22:00	***Welcome cocktail (Gallery of Science and Technology, SASA)***

All indicated times are given in the Central European Summer Time (CEST) zone.

Tuesday 6th September 2022
SPIG 2022 (day 2)

PL *– Plenary lecture: 35+10 min*	***TL*** *– Topical lecture: 25+5 min*	***PR*** *– Progress Report: 15+5 min*

08:45-09:00	***Opening, Chairs:*** *V. Srećković, D. Ilić, B. Obradović, J. Cvetić*	
	Plenary Session 1, Hall A, *Chair: V. Srećković & D. Ilić*	
09:00-09:45	**Sven Thorwirth** (Germany), Action-spectroscopic studies of transient carbon-rich molecular ions **[Regular]**	
09:45-10:30	**Sergio Diaz-Tendero** (Spain), Ultrafast dynamics of ionized molecules and molecular clusters in the gas phase **[Regular]**	
10:30-11:00	***Break & Chat Room***	
	Plenary Session 2, Hall A, *Chair: B. Obradović*	
11:00-11:45	**Ryo Ono** (Japan), Measurement and simulation of atmospheric-pressure streamer discharge **[Virtual]**	
11:45-14:30	***Break***	
	Hall A - Parallel Session: *Chair: N. Simonović*	***Hall B - Parallel Session*** *Chair: D. Borka*
14:30-15:00	**Stojan Madzunkov** (USA), Utillization of Electric Dipole Fields in protection from GCR and SEPs **[Regular]**	**Jiri Limpouch** (Czech Republic), High-power laser interactions with low density porous materials and their applications **[Virtual]**
15:00-15:30	**Gregory Boyle** (Australia), Thermalisation time of electron swarms in Noble gases for uniform electric fields **[Virtual]**	**Minna Patanen** (Finland), Electron-ion coincidence experiments with electron and photon ionization **[Virtual]**
15:30-16:00	**Mikhail Pinchuk** (Russia), Control of guided streamer propagation and interaction with substrate in helium atmospheric pressure plasma jet **[Regular]**	**Violeta N. Nikolic** (Serbia), Spectroscopic investigation of the influence of NO3- anions on the crystallization of the SiO2 matrix **[15:30-15:50] [Regular]**
16:00-16:30	**Aranka Derzsi** (Hungary), Surface processes in low-pressure capacitively coupled plasmas **[Regular]**	**Dejan Dojić** (Serbia), Measurements of continuous optical spectrum during nanosecond laser pulse **[15:50-16:10] [Regular]**
		Milivoje Hadžijojić (Serbia), Study of two dimensional crystals by rainbow scattering effect **[16:10-16:30] [Regular]**
16:30-17:00	***Break & Chat Room***	
	Hall A - Parallel Session *Chair: S. Tošić*	***Hall B - Parallel Session*** *Chair: M. Trtica*

17:00-17:30	**Vasco Guerra** (Portugal), Coupled kinetics in CO2-N2 plasmas **[Regular]**	**Nikola Starčević** (Serbia), Ion-crystal rainbow interaction potential in channeling **[17:00-17:20] [Regular]**
17:30-18:00	**Teodora Velcheva Kirova** (Latvia), Numerical investigations of the impact of the magnetic field of radiation on amino acids **[Regular]**	**Jovan V. Ciganovic** (Serbia), Action of pulsed lasers on titanium target: surface effects **[17:20-17:40] [Regular]**
18:00-18:30	**Lucas Schwob** (Germany), X-ray action spectroscopy of gas-phase biomolecular ions **[Virtual]**	**Dušan Popović (Serbia),** Picosecond pulsed laser ablation of silicon single crystal **[17:40-18:00] [Virtual]**
18:30-20:00	***Poster session (1)*** Poster presentation – ***Hall A*** *(Chair: D. Borka)*	

All indicated times are given in the Central European Summer Time (CEST) zone.

Wednesday 7th September
SPIG 2022 (day 3)

PL *– Plenary lecture: 35+10 min* | ***TL*** *– Topical lecture: 25+5 min* | ***PR*** *– Progress Report: 15+5 min*

	Plenary Session 3, Hall A, *Chair: D. Marić*	
09:00-09:45	**Darryl Jones** (Australia), Electron spectroscopies for probing electronic structure and collision dynamics **[Virtual]**	
09:45-10:30	**James Sullivan** (Australia), Experiments with positrons - from fundamental to applied science **[Virtual]**	
10:30-11:00	***Break & Chat Room***	
	Hall A - Parallel Session *Chair: G. Poparić*	***Hall B - Parallel Session*** *Chair: V. Srećković*
11:00-11:30	**Nicolina Pop** (Romania), Dissociative recombination and excitation of molecular cations by electron-impact in cold plasmas: Application to H 2+ , BeH+ and their isotopomers **[Regular]**	**Stéphane Béchu** (France), Investigation of the ro-vibrational levels of H2/D2 molecules by VUV-absorption spectroscopy for the production of H-/D- negative ions for fusion application **[Virtual]**
11:30-12:00	**Saša Dujko** (Serbia), Electron transport, transient plasmas and high-energy phenomena in planetary atmospheres **[Regular]**	**Joel Rosato** (France), Line shape modeling for magnetic fusion and astrophysical plasmas: an overview of recent result **[Virtual]**
12:00-12:20	**Milan Ignjatovic** (Serbia), The influence of corona discharge on the lightning surge propagation along the transmission lines **[Regular]**	**N. N. Bezuglov** (Russia), Analysis of adiabatic processes in multilevel n-pod quantum systems from the perspective of riemannian geometry **[Virtual]**
12:30-14:30	***Break /SPIG Committee meeting at 13h***	
	Hall A - Parallel Session *Chair: V. Milosavljević*	***Hall A - Parallel Session*** *Chair: L. Č. Popović*
14:30-15:00	**Djordje Spasojević** (Serbia), On the application of iterative kinetic model for diagnostics of abnormal glow discharges in noble gases **[Regular]**	**Teresa Belmonte Sainz-Ezquerra** (Spain), What can plasma spectroscopy do for astronomers? Measuring atomic parameters of astrophysical importance **[Virtual]**

15:00-15:20	**Danilo Delibasic** (Serbia), Relative importance of the electron continuum intermediate state in single-electron capture into any state of fast protons from helium-like atomic systems. **[Regular]**	**Antonios Antoniou (Greece)**, Describing the Mathematical Methods for Calculating Basic Physical Parameters of the Gaussian-Rotational (Gr) Model **[Virtual]**
15:20-15:40	**Leo Sala** (Czech Republic), Interaction of ionizing radiation with DNA nanostructures **[Regular]**	**Thomas Salomon** (Germany), Recent Progress on Action Spectroscopy of loosely bound Hydrogen-Helium complexes **[Regular]**

All indicated times are given in the Central European Summer Time (CEST) zone.

Thursday 8th September 2022
SPIG 2022 (day 4)

PL *– Plenary lecture: 35+10 min* | ***TL*** *– Topical lecture: 25+5 min* | ***PR*** *– Progress Report: 15+5 min*

	***Plenary Session 4, Hall A**, Chair: M. Trtica*	
09:00-09:45	**Jorn Bonse** (Germany), Laser-induced periodic surface stuctures, mechanisms, applications, and unsolved problems **[Virtual]**	
09:45-10:30	**Marie-Lise Dubernet** (France), Towards a Global Network for Laboratory Astrophysics Activities and Data **[Virtual]**	
10:30-11:00	***Break & Chat Room***	
	***Plenary Session 3, Hall A,** Chair: V. Guerra*	
11:00-11:45	**Lawrence Overzet** (USA), Measurements of RF plasma re-ignition: RF-IV and PROES **[Virtual]**	
11:45-14:00	***Break***	
	Hall A - Parallel Session *Chair: M. Škorić*	***Hall B - Parallel Session*** *Chair: J. Cvetić*
14:00-14:30	**Nathan Garland** (Australia), When fusion plasmas get cool: A need for more atomic physics in classical fusion models **[TBC]**	**Pavel Dvorak** (Czech Republic), Higher harmonic frequencies of discharge voltage and current in capacitively coupled discharges **[Regular]**
14:30-15:00	**Mohammed Koubiti** (France), Application of machine-learning to spectroscopic line emission by hydrogen isotopes in fusion devices for isotopic determination and prediction **[Virtual]**	**Milica Vasiljević** (Serbia), Determination of the electric field strength in glow discharges using argon spectral lines. **[Regular]** 14:30-14:50
15:00-15:40	***Break & Chat Room***	
	Hall A - Parallel Session *Chair: V. Milosavljević*	***Hall B - Parallel Session*** *Chair: D. Ilić*
15:40-16:00	**Amit Kumar** (Serbia), Design, development and characterization of atmospheric plasma system for wastewater treatment **[Regular]**	**Viktor Radovic** (Serbia), Development of a time-domain pipeline for detecting binary supermassive black holes in the upcoming Legacy Survey of Space and Time (LSST) **[Virtual]**

16:00-16:20	**Nenad Selaković** (Serbia), Mass spectrometry of plasma jet and application of electrical discharges operating at atmospheric pressure in biomedicine **[Regular]**	**Milena Jovanovic** (Serbia), Matter distribution in nearby galaxies **[Virtual]**
16:20-17:00	***Break & Chat Room***	
	Hall A - Parallel Session *Chair: I. Savić*	***Hall B - Parallel Session*** *Chair: I. Mančev*
17:00-17:20 CET	**Marija Puač** (Sebia), Modeling of radio frequency breakdown by Monte Carlo technique **[Regular]**	**Smita Omkarnath Ganguly** (Sweden), Fragmentation of core-ionized adamantane molecule **[Regular]**
17:20-17:40 CET	**Madhusree Roy Chowdhury** (France), VUV Photoionization and Fragmentation of cyano-PAHs **[Regular]**	**Dale Muccignat (Australia)**, Simulating the feasibility of using liquid micro-jets for determining electron-liquid scattering cross-sections **[Virtual]**
17:40-20:00	**Poster session (2)** - Virtual poster presentations - ***Hall A*** *(Chair: N. Cvetanović)* [*Optional: 3min presentation per poster]	
20:30 -	**Conference dinner and Closing**	

Friday 9th September 2022 SPIG 2022 (day 5)	
10:00-17:00	**Excursions (optional, info at registration desk)**
17:00	**Departure**

LIST OF POSTERS

No	Session	Title	Authors
1.	1.1.	Total cross section measurements for electron scattering on methyl formate ($HCOOCH_3$) molecule: methylation effect	Natalia Tańska, Kuba Wójcik, Sylwia Dylnicka, Elżbieta Ptasińska-Denga, Czesław Szmytkowski and Paweł Możejko
2.	1.1.	Dissociation of N_2 by electron impact in RF electric field	V. Stanković, M. Ristić, R. Ranković, M. Aoneas, M. Vojnović and G. B. Poparić
3.	1.1.	Rate coefficients for O_3^+ dissociation to O^+ and O_2^+ by electron impact	M. M. Vojnović, M. M. Ristić and D. S. Belić
4.	1.1.	Photoelectron energy spectra in sequential two-photon ionization of hydrogen by gaussian and half-gaussian laser pulses	N. S. Simonović, D. B. Popović, A. Bunjac
5.	1.2.	Single-electron capture from He by fast alpha particles	Nenad Milojević, Danilo Delibašić Ivan Mančev

6.	1.3.	Reduced mobility of H+ ions in n-butanol gas	Željka Nikitović and Zoran Raspopović
7.	1.3.	Excitation of $^1\Sigma^+_u$ and $^1\Pi_u$ states and ionization of CO_2 in DC electric field	Violeta V. Stanković, Mirjana M. Vojnović, Miroslav M. Ristić, Sava M.D. Galijaš and Goran B. Poparić
8.	1.3.	Formation and propagation of streamers in CF_3I-SF_6 gas mixtures	J. Atić, D. Bošnjaković, I. Simonović, Z.Lj. Petrović and S. Dujko
9.	1.3.	Electron transport coefficients in CO: Scanning drift tube measurements and kinetic computations	S. Dujko, D. Bošnjaković, M. Vass, I. Korolov, P. Hartmann, N. Pinhao, D. Loffhagen and Z. Donko
10.	1.3.	Third-order transport coefficients for electrons in C_3F_8	I. Simonović, D. Bošnjaković, Z.Lj. Petrović and S. Dujko
11.	2.1.	The time-symmetric description of electron exchange in ion-ion collision	S. M. D. Galijaš, V. M. Milosavljević and G. B. Poparić
12.	2.1.	Analytical expression for stopping force acting on a slow charged particle moving parallel to a thick graphene-sapphire-graphene structure	Ana Kalinić, Ivan Radović, Lazar Karbunar, Vito Despoja and Zoran L. Mišković
13.	2.1.	Bohmian dynamics of positrons channeled through a chiral carbon nanotube	M. Ćosić, M. Hadžijojić, and N. Nešković
14.	2.1.	Study of graphene by rainbow scattering effect	M. Hadžijojić and M. Ćosić
15.	2.1.	The influence of the ion-target parameters on the size of the surface nanohillocks created by an impact of highly charged ions	N. N. Nedeljković, M. D. Majkić, M. A. Mirković, I. Stabrawa, D. Banaś
16.	2.1.	Effect of the ionic type on the shape of the nanostructures created by an impact of slow highly charged ions on gold surface	M. D. Majkić, N. N. Nedeljković M. A. Mirković,
17.	2.2.	Influence of carbon ions of different multiplicity on regimes of promising laser technologies for the deposition of diamond-like carbon nanocoatings	V.K.Goncharov, G.A.Gusakov, M.V.Puzyrev
18.	2.3.	Elemental analysis of austenitic steel by calibration-free laser-induced breakdown spectroscopy (CF-LIBS)	I. Traparić, M. Jovanović, M. Kuzmanović, M. Ivković

19.	2.3.	ODS+Hf and AISI 316L steel surface variations at high laser intensity, 1013 W/cm^2, in air and vacuum: comparative study	M. Trtica, J. Stasic, X. Chen and J. Limpouch
20.	2.3.	Silicon spalling destruction and ablation in air under bichromatic laser radiation	A.N. Chumakov, V.V. Luchkouski and I.S. Nikonchuk
21.	2.3.	Features of silicon ablation in air under the influence of Nd:YAG laser harmonics	A.N. Chumakov, V.V. Lychkovsky, I.S. Nikonchuk
22.	2.3.	Investigation of properties of yttrium vanadate YVO_4 films	N.A. Bosak, A.N. Chumakov, L.V. Baran, V.V. Malyutina-Bronskaya, T.F. Raichonok, A.A. Ivanov, V.V. Kiris, E.M. Dyatlova, A.A. Shevchenok, A.V. Buka, A.S. Kuzmitskaya
23.	2.3.	Treatment of steel 16MnCr5 and steel 42CrMo4 by plasma flow generated in magnetoplasma compressor	Nora Trklja Boca, Žarko Z. Mišković, Radivoje M. Mitrović, Bratislav M. Obradović, Milorad M. Kuraica
24.	2.3.	Combining plasma-assisted synthesis of metal oxide nanoparticles with thin films deposition	Natalie Tarasenka, Vladislav Kornev, Alena Nevar, Mikhail Nedel'ko, Anton Radomtsev and Nikolai Tarasenko
25.	2.3.	Perspective on the use of nanoparticles to improve the tea CO2 based LIBS analytical performances: copper nanoparticles for NELIBS analysis of polypropylene	S. Živković, J. Petrović, M. Momčilović, M. Radenković, N. Krstulović, J. Car, D. Palasti, F. Casian Plaza and G. Galbács
26.	2.3.	Analytical prediction and numerical analysis of plasma mediated ablation of skin tissue samples with nanosecond-to-femtosecond laser pulses	H. Delibašić, Marković, V. Petrović and I. Petrović
27.	2.3.	Pulsed laser assisted fabrication of Co-doped ZnO nanocrystalline layers on a glass substrate	Natalie Tarasenka, Vladislav Kornev, Svetlana Pashayan, and Nikolai Tarasenko
28.	3.1.	The gas temperature diagnostics by means of AlO (B2Σ+–X2Σ+) molecular band system from the upgraded atmospheric pressure pulsed discharge source in argon	Jovica Jovović, Gordana Lj. Majstorović
29.	3.1.	High-resolution spectroscopy of astrophysically relevant molecular ions	O. Asvany, S. Thorwirth, P. C. Schmid, T. Salomon, and S. Schlemmer

30.	3.1.	Polarization spectroscopy of neon lines for electric field distribution measurement in the cathode sheath of a Grimm-type glow discharge	N. V. Ivanović, N. V. Nedić, I. R. Videnović and D. Spasojević
31.	3.1.	Analysis of printed circuit board LIBS data using deep learning	M.S. Rabasovic, B.P. Marinkovic, D.Sevic
32.	3.1.	Spectroscopic determination of the degree of dissociation of hydrogen in the glow discharge	M. M. Vasiljević, G. Lj. Majstorović I. R. Videnović and D. Spasojević
33.	3.1.	Spectroscopic characterization of laser-induced plasma on doped tungsten	Biljana Stankov, Marijana R. Gavrilović Božović, Jelena Savović and Milivoje Ivković
34.	3.1.	Features of the HeI 492.2 nm line profile registered at diagnostics of DC and streamer discharges	L.V. Simonchik and A.V. Kazak
35.	3.1.	Temperature estimation in the early stage of laser induced plasma formation relaying on black body radiation	Milos Skocic, Nikodin Nedic, Dejan Dojic, Luka Rajacic, Srdjan Bukvic
36.	3.1.	Formation and heating of silicon plasma in air under pulsed bichromatic laser irradiation	V.V. Luchkouski and A.N. Chumakou
37.	3.1.	Self-mixing interferometry for plasma diagnostics	Nikola Goleš, Neda Babucić, Nenad M. Sakan and Milivoje Ivković
38.	3.1.	Study of plasma-flow interaction in low temperature plasma jets	G. B. Sretenović, P. S. Iskrenović, V.V. Kovačević, B. M. Obradović and M. M. Kuraica
39.	3.1.	Application of artificial neural network in the analysis of the spectra from laser ablation combined with fast pulse discharge	Nenad M. Sakan, Milica L. Vinić, Vladimir A. Srećković, Ivan Traparić, and Milivoje R. Ivković
40.	3.1.	Detection of fast nitrogen and oxygen atoms via emission spectroscopy	B.M. Obradović, N. Cvetanović, I.B. Krstić and M.M. Kuraica
41.	3.1.	Modeling of Stark spectral line broadening by machine learning algorithms	Irinel Tapalaga, Ivan Traparić, Nora Trklja Boca, Jagoš Purić and Ivan P. Dojčinović

42.	3.2.	Looking behind the negative glow plasma: estimating cathode sheath parameters by end-on optical emission spectroscopy in a Grimm-type glow discharge source	N. V. Nedić, N. V. Ivanović, I. R. Videnović, D. Spasojević and N. Konjević
43.	3.2.	Corona model for surge wave propagation along the transmission lines	Milan Ignjatovic, Jovan Cvetic, Vera Protic, Nemanja Grbic
44.	3.2.	Breakdown in saturated water vapor	Jelena Marjanović, Dragana Marić, Gordana Malović and Zoran Lj. Petrović
45.	3.3.	Comparison of biocompatibility of organic polymers modified in various types of non-temperature plasmas	Tatiana Vasilieva, Elena Nikolskaya, Michael Vasiliev, Nikita Yabbarov, Maria Sokol, Mariia Mollaeva, Margarita Chirkina
46.	3.3.	Characterization of the dielectric barrier-free atmospheric plasma system	Miroslav Gulan and Vladimir Milosavljević
47.	3.3.	The effect of plasma seed treatment on germination and early growth of thuja koraiensis nakai plants	I.I. Filatova, V.A. Lyushkevich, S.V. Goncharik, U.I. Torchyk, Y.V. Kandratau, M.O. Slesarenka
48.	3.3.	Laser driven electron acceleration by q-Gaussian laser pulse in plasma: effect of self focusing	N. Gupta
49.	4.2.	Winged DRAGN source from Leahy's atlas: 3C 315	A. Arsenic, D. Borka, P. Jovanovic and V. Borka Jovanovic
50.	4.2.	Decomposition of the blended Hα+[N II] lines in spectra of the active galactic nuclei type 1.8-2	Jelena Kovačević-Dojčinović, Ivan Dojčinović, Maša Lakićević and Luka Č. Popović
51.	4.2.	The chemi-recombination processes in alkali-metal astrophysical and low-temperature laboratory plasmas: rate coefficients	V.A. Srećković, L.M. Ignjatović, V. Vujčić, M.S. Dimitrijević
52.	4.2.	Higher order non-linear dust ion acoustic (dia) solitary waves in plasmas with weak relativistic effects in electrons and ions	S. Das and D. C. Das
53.	4.2.	The effect of negative ions on Weibel instability in the presence of large amplitude electrostatic waves	Amit Kumar, Jyotsna Sharma

ACKNOWLEDGEMENT

31st SUMMER SCHOOL AND INTERNATIONAL
SYMPOSIUM ON THE PHYSICS OF IONIZED GASES

is organized by

University of Belgrade – School of Electrical Engineering

University of Belgrade – Faculty of Physics

Serbian Academy of Sciences and Arts

University of Belgrade,
School of Electrical Engineering

University of Belgrade,
Faculty of Physics

Serbian Academy
of Sciences and Arts

and

with the support of the

**Ministry of Education, Science and Technological Development,
Republic of Serbia**

Republic of Serbia
Ministry of Education,
Science and Technological
Development

sponsored by

EPJ D
Atomic, Molecular, Optical and Plasma Physics

SOLEIL
SYNCHROTRON

RoentDek
Handels GmbH
Supersonic Gas Jets
Detection Techniques
Data Acquisition Systems
Multifragment Imaging Systems

SPECS™

technical organizer

PANACOMP - Zemlja čuda d.o.o.